LBL-36065
UC-401

# BRIDGING THE PRESSURE GAP: IN SITU ATOMIC-LEVEL INVESTIGATIONS OF MODEL PLATINUM CATALYST SURFACES UNDER REACTION CONDITIONS BY SCANNING TUNNELING MICROSCOPY

BRIAN JAMES MCINTYRE
Ph.D. Thesis

DEPARTMENT OF CHEMISTRY
University of California

and

MATERIALS SCIENCES DIVISION
Lawrence Berkeley Laboratory
University of California
Berkeley CA 94720

MAY 1994



This work was supported by the Director, Office of Energy Research, Office of Basic Energy Sciences, Materials Sciences Division, of the U.S. Department of Energy under Contract No. DE-AC03-76SF00098

The dissertation of Brian James McIntyre is approved:

Chair — Date April 5, 1994

Date April 13, 1994

Date April 20, 1994

Date April 22, 1994

University of California at Berkeley

1994

## DISCLAIMER

Dedicated to my mother, Marian
and the memory of my father,
John Dorsey McIntyre

## TABLE OF CONTENTS

Page

## LIST OF ILLUSTRATIONS

Figure Page

# ACKNOWLEDGMENTS

I would like to extend my sincere grattitude to my advisors, Professor Gabor Somorjai and Dr. Miquel Salmeron. I will always be indebted to them for providing the opportunity to perform research in their groups. Their enthusiastic support and guidance while allowing me to work on research problems which were of interest to me is something for which I am most grateful.

I would especially like to acknowledge the past and present members of the Somorjai and Salmeron groups with whom I've been fortunate to interact, their help and friendship have been invaluable to me. In particular I would like to thank the people with whom I have worked directly. These include Jim Dunphy, Uwe Schröder and Philippe Sautet. Jim's friendship and willingness to allow me to repeatedly invade his chamber for the HPSTM sample preparations as well as a few UHV experiments is something for which I am most grateful. Without Uwe's persistance, much of the tip catalysis work which came about through a rewarding partnership we had during his stay at Berkeley would not have been accomplished. Finally, Philippe's extraordinary patience in showing me how to carry out ESQC calculations of STM images is most appreciated. Other people who deserve special mention for their help and friendship include Anna Lio, Sean Newman, Heather Galloway, Frank Ogletree, Gang-yu Liu, Carmen Morant, Qing Dai, Francis Wolf, Junfei Zheng, Jim Powers, Sabrina Fu, Colette Knight and Istvan Böszörményi.

I would like to thank the technical staff at the Lawrence Berkeley Laboratory and in the Berkeley Chemistry department for all their help and expertise in the construction and subsequent modifications of the HPSTM system. The facilities and the support staff at UCB and LBL are the best one could hope to work with.

My thanks go to Anna Lio, Heather Galloway and Uwe Schröder for critically reviewing various sections of this thesis.

Finally, I am especially grateful to my family for all of their love and support. In particular, I believe that in learning from my father's relentless drive and inspiration, in combination with my mother's extraordinary patience and creativity, I have been able to work through (or around) my own challenges, which has allowed me to bring this chapter of my life to a successful close.

This work was supported by the Director, Office of Energy Research, Office of Basic Energy Sciences, Materials Science Division of the U.S. Department of Energy under Contract No. DE-AC03-76SF00098. Additional support was provided by a gift from Union Carbide, South Charleston, WV.

Berkeley, April 1994

# CHAPTER 1

# INTRODUCTION

From a fundamental perspective, the study of surfaces is of great interest because surfaces represent a rather special kind of defect in the solid state. Much of our understanding of solids is based on the fact that they are, in essence, perfectly periodic in three dimensions. The introduction of a surface breaks this periodicity in one direction, often resulting in changes of physical structure and properties. To this end, achieving an understanding of surfaces has become of paramount importance in gaining insight to solid state properties and ultimately to "real world" phenomena.

Perhaps the most common motivation for modern surface studies is the goal of improving heterogeneous catalysis in terms of being able to customize catalysts so that they will display improved performance in any useful combination of improved activity, selectivity, and longer catalyst lifetime. A particularly important attribute of catalyst science is the fact that improved catalysts can easily be translated into new industrial technologies. For this purpose, it is essential to understand how catalysts work. Once this is established, then it may be possible to incorporate this knowledge into the development of superior catalysts.

The problems of understanding catalytic processes in a microscopic or atomic way are formidable. Industrial processes frequently operate at high temperatures and pressures, and the catalysts are in the form of highly dispersed powders. These powders frequently involve platinum, iridium, and related precious metals on oxide supports. Of all catalyst materials, platinum is perhaps the most versatile. Some of its uses include petroleum reforming, carbon monoxide oxidation in automotive exhaust systems, and ammonia oxidation for fertilizer production [1].

As a result, the catalytic behavior of platinum has been studied extensively and two general approaches have been taken in an effort to elucidate the working atomic structure and composition of the active catalyst surface. The first approach involves the study of catalytic reactions on dispersed, high surface area catalysts as a function of catalyst pretreatment and particle size. In general, these studies involve catalyst systems which have at best ill-defined compositions and structures. Because of this, it is difficult to make detailed conclusions from these investigations.

The second approach involves the study of reactions catalyzed on small area ($\sim$ 1-2 $cm^2$) model catalysts including single crystal surfaces and polycrystalline foils. This approach originated in this laboratory and came about through the development of surface sensitive electron and ion spectroscopic and diffraction techniques [2,3]. With these techniques, it is possible to obtain atomic and molecular information about surface composition, structure, electronic structure, the local chemical environments of surface atoms, and various other physical and chemical characteristics of material surfaces and adsorbates. However, these techniques are limited by the fact that they require large mean free paths and the surfaces must remain clean or stable for long periods of time, thus restricting their use to ultrahigh or near ultrahigh vacuum environments. Therefore, it is not possible to carry out *in situ* studies using this approach, rather, model catalysts can only be studied before and after high pressure reactions.

In attempt to understand how reactions progress on surfaces on the atomic-scale, intense effort has been directed toward the development of methods which combine the benefits of controlled, ultrahigh vacuum (UHV) atomic-level surface analysis, and *in situ* (high pressure and high temperature) catalytic reaction measurements. Perhaps one of the most popular approaches is the use of high pressure isolation cells [4], which allow samples that have been characterized by UHV techniques to be exposed, intermittently, to high pressures and high temperatures, while in the same apparatus. Unfortunately, it is not

possible to combine, simultaneously, the benefits of these two regimes. As a result, our information on the atomic-level structure of surfaces and their adsorbates while under high pressure and temperature reaction conditions is very limited.

The demonstrated capability of the scanning tunneling microscope (STM) to probe the topography and electronic structure of surfaces and adsorbate layers with atomic resolution makes it a powerful tool in the study of surface chemistry. Chemistry is a local phenomenon: adsorption is usually site-specific, reactions occur at particular "active sites," the reaction products may be different at different sites, etc. Since most conventional surface-analytical and structural techniques average over surface areas usually containing more than $10^{12}$ atomic sites, site-specific information is difficult to obtain. One of the features which distinguishes scanning tunneling microscopy (STM) from other surface-analytical techniques is its demonstrated capability to probe the geometric and electronic structure of surfaces with real-space atomic resolution [5]. Scanning tunneling microscopy has made dramatic advances in many areas of surface science since its introduction by Binnig and Rohrer in 1981-82 [6]. Recent work has shown the possibile uses of STM for the direct observation of dynamic processes such as adatom diffusion [7], chemical reactions [8], and adsorbate restructuring of surfaces [9]. Scanning tunneling microscopy is also rapidly becoming important in the characterization of not only model surfaces but also catalysts [10].

The aim of the work presented in this thesis is to take advantage of STM's capacity for operation under wide-ranging environments to monitor catalyst structures as well as the structure of adsorbate molecules while under atmospheric pressures of reactant gases and variable temperatures consistent with catalytic reaction conditions.

This thesis is divided into three distinct sections which discuss the motivation, theory and current progress in STM technique and its applications for catalysis research; the development and construction of a novel STM apparatus for *in situ* investigations of

model catalyst surfaces under conditions of high temperatures and pressures; and new results for adsorbate-induced restructuring of Pt(110) in high pressures of hydrogen, oxygen, and carbon monoxide, for sulfur atoms adsorbed on Pt(111), for coadsorbate-induced compression of sulfur atoms by carbon monoxide molecules on Pt(111), for theoretical modeling of the STM experiment by the use of electron scattering calculations, for hydrocarbons adsorbed on Pt(111) in various high pressure environments and temperatures, and for chemical interactions between the tip of the STM and surface during catalytic reaction conditions.

In the first section, chapter 2 provides a general overview of the state of the art for STM theory, technique and instrumentation, and describes the current role of STM in the field of catalysis science and shows how this work fits in. In the second section, chapter 3 describes, in detail, the design, construction and operation of the High Pressure STM (HPSTM) that was developed in the course of this research as well as the UHV system which was at least partially involved in much of the work. The final part of this thesis is concerned with new results by *in situ* STM investigations. Chapter 4 discusses investigations of the stability of the platinum (110) single crystal surface upon exposure to atmospheric pressures of hydrogen, oxygen, or carbon monoxide. The remainder of the chapters will be concerned primarily with adsorbate and coadsorbate structures. Chapter 5 describes results from UHV studies of sulfur on Pt(111). The Pt(111)-($\sqrt{3}$X$\sqrt{3}$)R30°-sulfur structure was used as a protectant during *in vacuo* sample transfer from the UHV system to the HPSTM and served as the starting surface for the HPSTM investigations on Pt(111). Chapter 5 also presents the results of an *in situ* investigation of the coadsorbate-induced compression of sulfur atoms by carbon monoxide molecules and subsequent restructuring of the Pt(111) surface by carbon monoxide. Also presented in this chapter are experimental results showing sulfur diffusion and theoretical modeling of experimental images as a function of tip structure and general tunneling conditions by an electron

scattering method developed recently [11,12]. Chapter 6 presents results showing the coadsorbate-induced recontruction of Pt(111) by sulfur and CO. Chapter 7 shows results from investigations of the stability of propylene on Pt(111) and the morphology of decomposition products as a function of atmospheric environment (hydrogen, $H_2$/propylene, and CO) and sample temperature (300K-900K). Clusters of carbonaceous material were formed as a result of various decomposition pathways. Chapter 8 concludes with an investigation of an effect observed during the course of this research in which a platinum STM tip acts as a catalyst, hydrogenating (or oxidizing) carbonaceous fragments on the surface of the Pt single crystal when under hydrogen (or oxygen) gas environments.

[1] G.A. Somorjai, "Chemistry in Two Dimensions: Surfaces", Cornell University Press, Ithaca 1981.

[2] G.A. Somorjai, "Chemistry in Two Dimensions: Surfaces", Cornell University Press, Ithaca 1981.

[3] G. Ertl, J. Kuppers, Low Energy Electrons in Surface Chemistry, Verlag-Chimie, Germany, 1974.

[4] D.W. Blakely, E.I. Kozak, B.A. Sexton, and G.A. Somorjai, J. Vac. Sci. Technol. **13**, 1091 (1976).

[5] G. Binnig, H. Rohrer, Ch. Gerber, and E. Weibel, Phys. Rev. Lett. **49**, 57 (1982).

[6] G. Binnig, H. Rohrer, Ch. Gerber, and E. Weibel, Phys. Rev. Lett. **49**, 57 (1982).

[7] J. C. Dunphy, P. Sautet, D.F. Ogletree, O. Dabbousi, and M.B. Salmeron, Phys. Rev. B. **47**, 2320 (1993).

[8] Ph. Avouris, R. Wolkow, Phys. Rev. Lett. **60**, 1049 (1988).

[9] J. Wintterlin and R.J. Behm, *Scanning Tunneling Microscopy I*, edited by H. J. Güntherrodt and R. Wiesendanger, Springer Series in Surface Sciences Vol. 20 (Springer-Verlag, Berlin, 1992), Chap. 4.

[10] F. Besenbacher, E. Lægsgaard, I. Stensgaard, P. Stoltze, and H. Topsøe, Catalysis Letters **8**, 273 (1991).

[11] P. Sautet and C. Joachim, Phys. Rev. B **38** (1988) 12238.

[12] P. Sautet, O. Eisenstein and E. Canadell, Chem. Mater. **1** (1989) 225.

# CHAPTER 2

# OVERVIEW OF SCANNING TUNNELING MICROSCOPY (STM)

## 2.1 Principles of STM operation

Scanning Tunneling Microscopy is based upon the quantum effect of electron tunneling between two solids through a classically forbidden energy barrier. Its equivalent in solid state physics is the metal-oxide-metal tunnel junctions where the oxide is substituted by vacuum. The STM probes surfaces by moving a sharp tip (often W or Pt-Rh wire) to within a few angstroms of the surface to be imaged. The electrons in the tip and surface are restricted to move in their respected interiors as a result of the potential barrier at the surface. The potential barrier is due to positive nuclear charges and neighboring electron rearrangements. In quantum mechanics, electrons are not completely confined within the potential barrier, but rather the amplitude of the electron wavefunction decays exponentially away from the surface. The decay length $\frac{1}{\kappa}$ may be estimated from the following expression:

$$\kappa = \left[\frac{2\phi M_e}{\hbar} + K_{\parallel}^2\right]^{\frac{1}{2}}$$

where $\phi$ is the work function or barrier height for electrons at the Fermi level and $K_{\parallel}$ is the component of the surface electron wave vector parallel to the surface. The tunneling current may be described as follows:

$$I \propto e^{-2s\kappa}$$

where s is the distance between the tip and surface measured from the crossing points of the Fermi level and the potential as shown in Fig. 2.1. This is the simplest case of one-dimensional tunneling through a barrier of height $\phi$. It is the exponential

of one-dimensional tunneling through a barrier of height $\phi$. It is the exponential relationship between the tunneling current I and distance s that gives rise to the high resolution of the STM. For example, for a work function value of 4eV, $\kappa^{-1}$=1 Å and a change in s of 1 Å varies I by about a factor of 10. Simmons [1] derived a complete equation for the current density, through a one-dimensional square barrier, which was later corrected by Payne, *et al* [2], that includes the effect of biasing of the tip by an amount V relative to the surface and the different work function values of tip and sample. The average barrier height used to estimate the decay length $\kappa^{-1}$ can be estimated by:

$$\Phi = \frac{1}{2}\left(\phi_{tip} + \phi_{sample}\right) - \left(E - \frac{eV}{2}\right)$$

for electrons tunneling into states at the energy E above the sample Fermi level for negative tip bias and where $\phi_{tip}$ and $\phi_{sample}$ are the workfunctions of the tip and sample, respectively. In the end, it is clear that for small bias voltages (v), the tunnel current is proportional to $Ve^{-1.025\phi^{\frac{1}{2}}s}$ where $\phi$ is in eV and s is in Å.

$$I = Bexp(-2\kappa s)$$
$$\kappa = \frac{\sqrt{2m}}{\hbar}\sqrt{\bar{\phi}} = A\sqrt{\bar{\phi}}$$

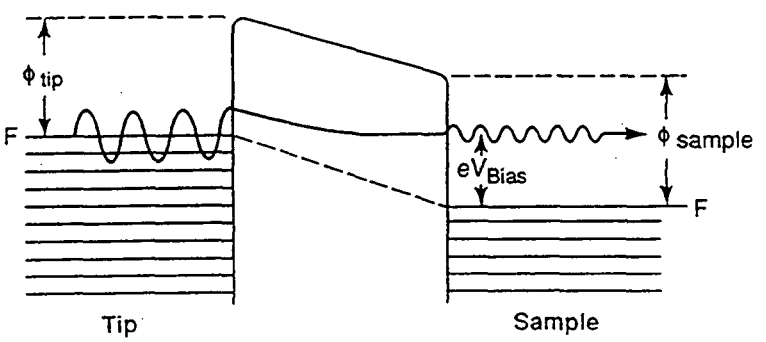


Given:

$A = 1.025\mathring{A}^{-1}eV^{-1/2}$

$\bar{\phi} \sim 4eV$

$eV_{Bias} \approx 1V$

Varying s by $1\mathring{A}$ changes I by an order of magnitude.

Figure 2.1. Schematic of one-dimensional tunneling barrier.

The previously described square well tunneling model is the simplest one for the tunneling microscope. To get more realistic results an STM theory must take into account the electronic structure of both the tip and the substrate. The roles of the filled density of states for the cathode and of the empty density of states for the anode are fundamental to the STM experiment and must be included when determining the nature and the meaning of the images obtained. Tersoff and Harmann [3] approach this problem by assuming an ideal tip represented by an s-wave function at a small bias voltage. Putting this 'tip' into a first-order perturbation expression, they obtain a tunnel current as follows:

$$I = \frac{2\pi e}{\hbar} \sum_{L,R} f(E_L)[1 - f(E_R + eV)] |\mathcal{H}_{LR}|^2 \delta(E_L - E_R)$$

where $\mathcal{H}$ is the tunneling matrix element, $\mathcal{H}_{LR} = \begin{Bmatrix} \mathcal{H}_L \\ \mathcal{H}_R \end{Bmatrix}$, f(E) is the Fermi factor, V is the voltage across the barrier, $E_L$ is the energy of the filled cathode states L, and $E_R$ is the energy of the empty anode states R. Bardeen showed [4] that $\mathcal{H}_{LR}$ can be written in a form requiring knowledge only of the wavefunctions of the two electrodes separately. Specifically,

$$\mathcal{H}_{LR} = \frac{\hbar^2}{2m_e} \int d\bar{S} \cdot (\psi_L^* \bar{\nabla} \psi_R - \psi_R \bar{\nabla} \psi_L^*)$$

where $\psi_R$ and $\psi_L$ are the electrode wavefunctions and the integral is over any plane in the barrier region. At this point, the surface and tip wavefunctions can be expanded to obtain;

$$I \propto V_x D_t(E_f) \cdot e^{2\kappa R} \cdot \rho(r_0, E_f)$$

with

$$\rho(r_0, E_f) \approx \sum_{\upsilon} |\psi_\upsilon(r_0)|^2 \delta(E_\upsilon - E)$$

where $\rho(r_0, E_f)$ is the total charge density at $r_0$ contributed by the states near the Fermi energy that take part in tunneling, $D_t(E_f)$ is the tip density of states and R is the

radius of the spherical wave tip state. The important point here is that the tunneling current is defined by the surface density of states at the tip position. This provides the basis for the spectroscopic capabilities of STM allowing, in principle, atomic scale density of states measurements.

## 2.2 STM technique

Anatomically, the STM is quite simple. Fig. 2.2 shows a basic STM design with magnified views of the tip and sample [5]. The square bars represent piezoelectric ceramics. Applying electric fields to these ceramics result in deformation of unit cells, thus providing precise, frictionless mechanical motions. After bringing the tip close to the surface so that the tunnel current can be measured, the tip is rastered across the surface while sensing the current. By using an electronic feedback loop, tunnel current can be maintained which affords a number of modes for operation. These include **topographic** [6,7,8] (or constant current), **current** [9] (or constant height), and a few other modulation modes, including **barrier height** $\left(\frac{dI}{dZ}\right)$. Figure 2.3(a) shows the basic **topographic** mode of operation. In this mode, the tunnel current is kept constant by varying the tip-sample distance as the tip scans over the surface. The height is plotted versus the tip position. The vertical resolution is often < 0.1Å while the lateral resolution is commonly about 1 Å. The topographic mode is the most widely used method of imaging, as it works well for samples which are not atomically flat. Figure 2.3(b) describes the current mode of imaging. In the current mode, the Z feedback loop is slowed down such that the tip is scanned on a plane over the surface and the tunnel current is monitored. The image in this case is a function of the tunnel current and the tip position. The advantage is primarily one of speed, since only the electronics and not the Z feedback control are employed.

Scan rates are commonly on the order of 1 KHz. Corresponding scan rates for topographic mode are 1 Hz. The major disadvantage of using current mode is that the surface must be atomically flat. Binnig, *et al.* [10] first demonstrated that a modulation of the tip-surface distance will produce a component in the tunneling current proportional to the tunneling barrier height:

$$\frac{dI}{dZ} \propto I\phi^{\frac{1}{2}}$$

The barrier height $\phi$ is closely related to the workfunction of the sample. The major difference between the two is that the workfunction is an averaging property of the surface where $\phi$ is a local property. Experimentally, the barrier height method is described in Fig. 2.3 (c). The tip is oscillated with a sinusoidal signal as the tip moves over the surface in a topographic fashion.

The three types of imaging techniques discussed above are termed contrast methods. In an attempt to be more quantitative with respect to electronic structure, work is ongoing with the intent of understanding exactly how these images relate back to the surface. In order to completely characterize a surface, much effort is being placed into the development of reliable Scanning Tunneling Spectroscopy (STS) techniques. It is evident [11,12] that STM has the unique ability to perform atomically resolved electron spectroscopy. The methods at this point are extremely varied (and for the most part ambiguous), and won't be discussed here, except to say that they most successful generally involve some sort of spatially resolved local I-V spectra [13].

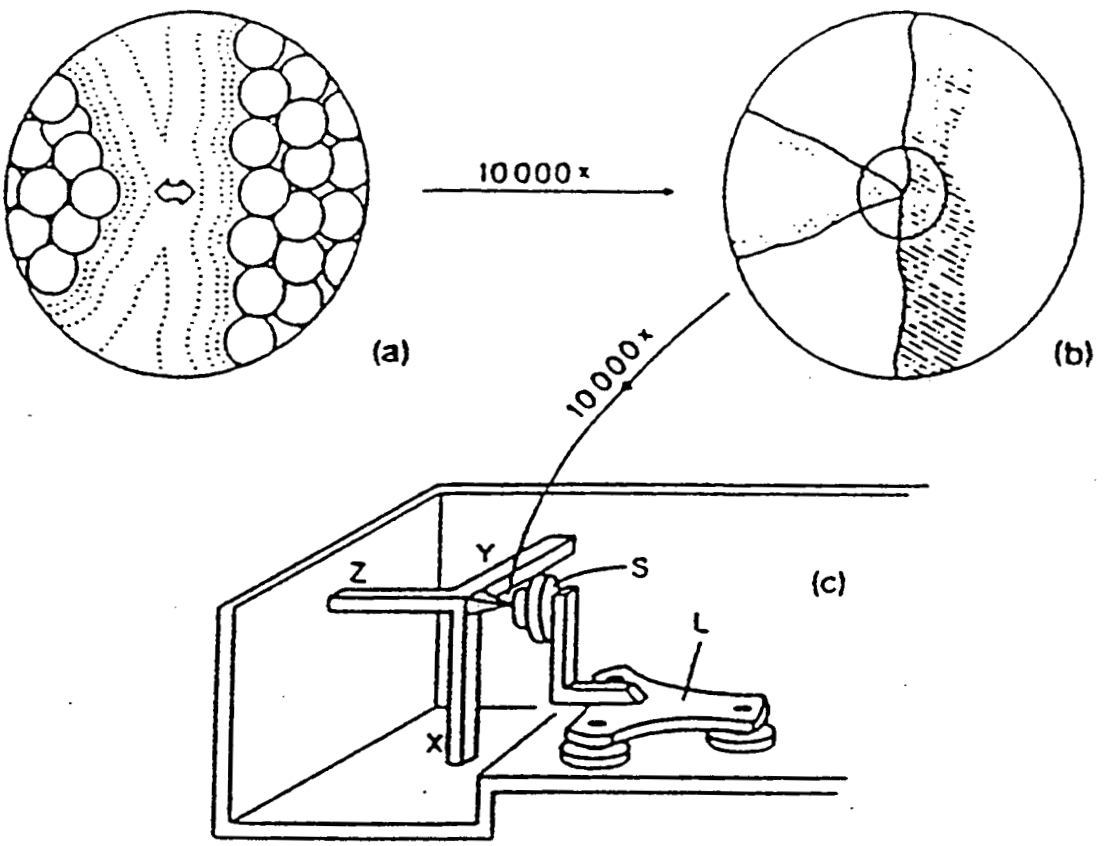


Figure 2.2. Original Zurich STM design [14]. (a) Apex of the tip (left) and surface (right) at a magnification of about $10^8$. The circles indicate atoms, the dotted lines correspond to electron density contours. The path of the tunnel current is given by the arrow. (b) Scaled down by a factor of $10^4$, the tip (left) appears to touch the surface (right). (c) STM with rectangular piezoelectric drives X, Y, Z of the tunnel tip, and 'louse' L (electrostatic motor) for rough positioning of sample S.

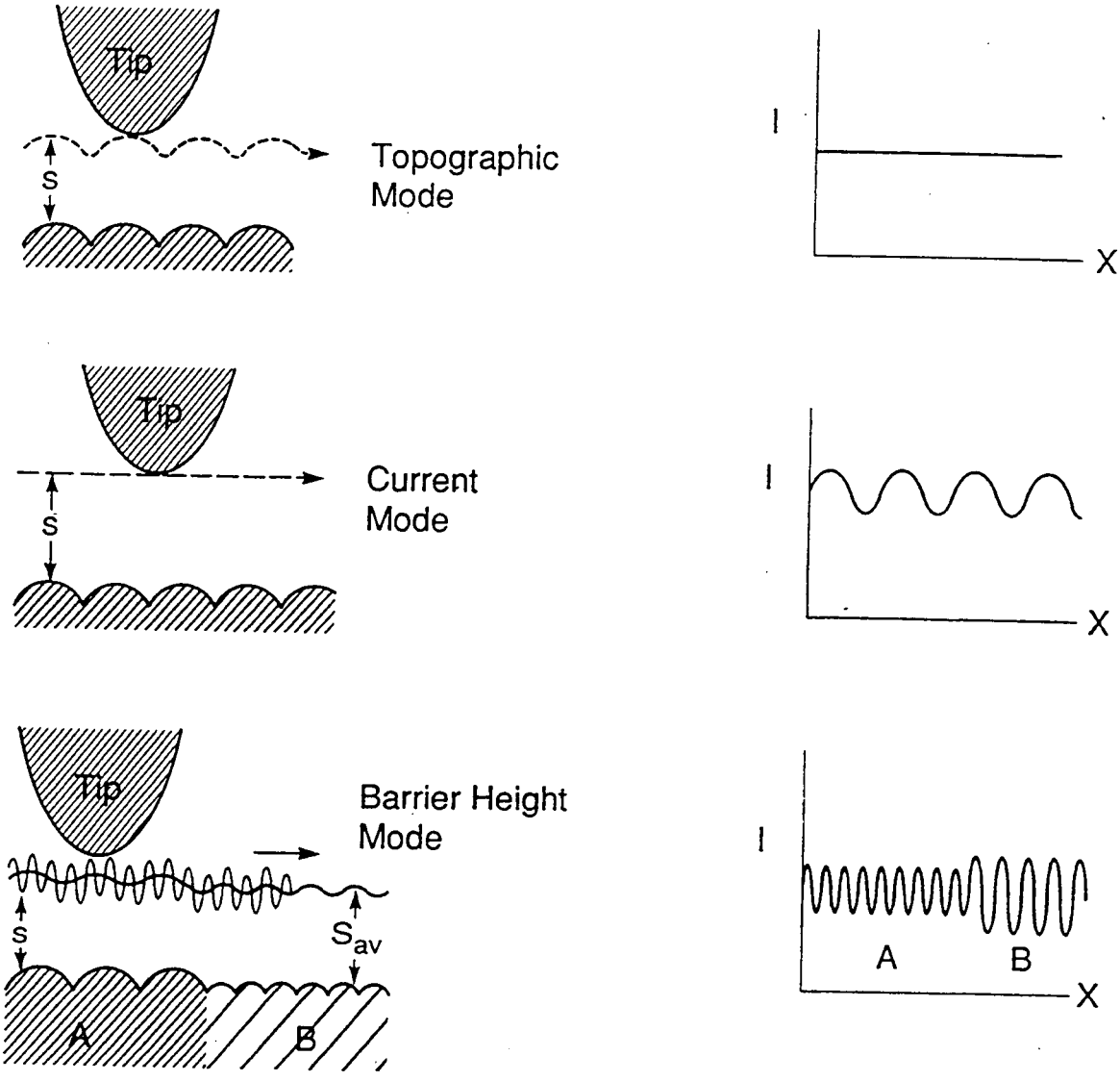


Figure 2.3. (a) Schematic representation of topographic (or constant current mode) of imaging. The cartoon on the left shows how the tip is moved over the surface. The graph on the right gives indication as to why this technique is termed 'constant current' imaging. (b) Schematic representation of current (or constant height mode). (c) Representation of barrier height imaging. In this case the tip is modulated as it is scanned over the surface in topographic mode.

## 2.3 STM as a tool for catalysis research

Scanning tunneling microscopy is rapidly becoming an important tool in the investigation of model catalyst surfaces. Single crystals having well defined crystallographic orientations are often prepared as such model catalysts so that surfaces may be studied with regards to reactivity and overall chemisorptive properties. Typically, the structures of these crystals are probed with Low Energy Electron Diffraction (LEED). However, because LEED is a diffraction technique, it is relatively insensitive to disorder. In fact, combined STM and LEED studies have shown that for some metal systems, distinct LEED patterns are obtainable with terrace widths as small as 20 Å [15]. As a result, crystals with a chemically significant number of steps can go undetected by LEED. As of yet, however, very little work has been done with STM to study surface stability and faceting which are key to understanding surface thermodynamic properties. Since the invention of STM, the bulk of the science has been done on semiconducting surfaces. The reasons for this, among others is that these are the subjects of importance to its inventors. Another primary reason is that metals are more difficult to image. This is a result of the reduced electronic corrugation (approximately a factor of 10) in the surface unit cells. In metals, the free nature of the electrons in the conduction bands, make the surface electronically smooth. As a result, atomic resolution of metals is much more difficult to achieve. Even so, atomic resolution has been obtained on the close-packed (111) surfaces of Au[16], Al[17], Cu[18], Ag[19], and Pt[20]. As well, a significant amount of atomically resolved work has been carried out on more open ((110), (100)) and reconstructed surfaces.

### 2.3.1 Chemisorption on metals

In comparison to the entire body of literature concerning structural determinations of adsorbates on metals, there have been relatively few STM investigations of metal chemisorption systems. The vast majority of adsorbate structural studies to date have been performed using such surface sensitive methods as low energy electron diffraction (LEED) or ion scattering techniques. However, it is clear that STM is rapidly becoming an important tool for structural determination, especially for the immense number of chemisorptive systems which either show very complicated order or are at best locally ordered. In any case, the importance of chemisorption in surface processes is well known and should provide sufficient incentive for further research.

Several reviews of the STM literature have been published, including those of Ogletree and Salmeron [21], Golovchenko [22], Hansma and Tersoff [23], Binnig and Rohrer[24], and Demuth, *et al.* [25] but with the large number of STM groups and commercially available STM systems, the amount of STM results has increased exponentially in the past few years. Below is a short description of some of the adsorbate-substrate systems which have been studied with STM.

Barò, *et al.* [26] obtained the first STM image of a non-metallic adsorbate on a metal surface in UHV. They were able to recognize the 2x1 reconstruction of O/Ni(100). Van de Walle, *et al.* imaged the p(2x2)2H overlayer on Ni(111) [27]. The graphite-like superlattice was attributed to two hydrogen atoms per unit cell adsorbed in different surface sites. Kuk, *et al.* studied the H/Ni(110) system [28]. These authors showed that the reconstruction of the Ni surface induced by the adsorption of H can be resolved and appears as tetramers of Ni atoms formed as a result of combined row pairing and missing

[001] rows. While the adsorbate H atoms were never resolved, the effect of their presence was quite obvious.

Sulfur chemisorption has been studied on a large number of substrates including Re [29], Mo [30], Pd [31], Pt [32,33], Cu [34], and Ni [35]. Adsorbed oxygen on the Al(111) surface was found to create atomic scale depressions at -40 mV sample bias and 16 nA tunnel current in agreement with several theoretical studies [36]. This serves to keep in mind that the vertical coordinate of the image is not at all obvious. Another example of this type is O on GaAs (Stroscio, *et al.* [37] ), here, the presence of the O atom produces a long-range screening effect of localized charge. This screening effect is associated with local band bending producing an image with a depression or protrusion depending upon the bias voltage. Oxygen has also been studied on Cu (111)[38], (100) [39] and (110) [40, 41, 42, 43, 44], Ni(110) [45], Ni(100) [46] Ag(110) [47], Ru(0001) [48], and $Cu_3Au(100)$ [49]. As a result of these studies, in combination with numerous electron diffraction and ion scattering studies Besenbacher, *et al.* have observed a number of general trends for the chemisorption of oxygen on the Cu, Ni, and Ag vicinal surfaces [50]:

- On all the (110) surfaces of Cu, Ni, and Ag and on the Cu(100) surface, oxygen initiates a restructuring of the metal surface, and the driving force for the resulting O-induced reconstruction appears to be the formation of -Metal-O-rows along the [001] direction.

- Oxygen induces no reconstruction of the (100) surfaces of Ni and Ag, and instead O chemisorbs in the four-fold hollow sites, resulting in the p(2x2) and the c(2x2) lattice-gas overlayer structures.

- The mass transport for the O-induced reconstructions differs significantly. The Cu(100) forms a true missing-row structure, whereas the (nx1) structures on the (110)

surfaces of Cu, Ni, and Ag all are of the added-row type where the metal atoms are supplied from step edges or by digging troughs on terraces.

• On Cu(111) and Ag(111), no ordered structures exist at room temperature, but after O adsorption at elevated temperature, ordered structures have been identified. All observed structures are explained as coincidence structures between the underlying (1x1) lattice and a thin oxide-like layer, associated with the (111) plane of $Cu_2O$ and $Ag_2O$ respectively.

• The subsurface/bulk oxidation does not start before a critical coverage is established, at least locally, and there is a strong tendency for island formation in the oxidation reaction.

In the studies of Ni(100) and Ru(0001), the presence of oxygen was observed to modify the behavior of metal (Ni on Ni(100) and Au or Cu on Ru(0001), respectively) epitaxial growth. The presence of oxygen in the $Cu_3Au(100)$ alloy was observed to force the alloy to terminate with a Cu plane, forming a c(2x2)-O structure.

Carbon has been studied on the Pt(111) [51], Ni(100) [52], Ni(111) and Ni(110) [53], and Ni(771) [54] surfaces. It was observed that for the Pt(111) surface, the carbon formed a graphitic overlayer which exhibited the asymmetric height of the alternating C atoms which is reminiscent of the situation for bulk HOPG. In the case of Ni(100), low coverages of C were observed to induce a radial displacement of the surrounding Ni atoms of $\approx$ 0.1 Å. Above a local critical coverage, C induces a disorder-order transition to a reconstructed phase, and the STM results show a coordinated 0.55 Å lateral displacement of the topmost Ni atoms, resulting in a (2x2)p4g symmetry for the reconstruction. In this study, the C atoms were imaged as $\approx$0.3 Å depressions, consistent with theoretical calculations for a C atom adsorbed on a jellium surface under similar tunneling conditions.

Nitrogen has been observed to induce a (2x3) reconstruction on the Ni(110) surface [55]. In the case of $Cu_3Au(100)$ [56], nitrogen was observed to produce similar effects as

the case of oxygen adsorption, namely producing a Cu terminated surface plane with the nitrogen adsorbed in the four-fold hollow sites.

Well ordered iodine structures have been resolved on Pt(111) and (100) by STM [57, 58]. In contrast to standard UHV preparation, these surfaces were initially cleaned in electochemical cells, followed by annealing in a hydrogen flame and cooled in a nitrogen atmosphere containing iodine. These studies provided the first convincing evidence that surfaces can be made atomically clean and that ordered structures can be produced and characterized in environments other than UHV. Since the results of Schardt, *et al.* was published, the field of solid-liquid interfaces has undergone a process of rapid growth. This is an exceedingly important area in electrochemistry and many important results have already emerged.

The study of molecular chemisorption on metals has also received some attention from the STM community. One early study which was performed and compared to dynamic LEED calculations was that of CO and benzene coadsorbed on Rh(111) [59]. The c($2\sqrt{3}$x4)rect overlayer observed by STM correlated well with the LEED analysis. Lippel, *et al.* observed that STM images of isolated Cu-phthalocyanine molecules on a Cu(100) substrate exhibit atomic scale features which agree well with Hückel molecular-orbital calculations [60,61]. Hallmark, *et al.* performed near atomic-resolution STM studies of naphthalene on Pt(111) producing very interesting results of adsorbate organization [62]. Hallmark, *et al.* also performed a systematic STM study of related organic molecules on Pt(111) in attempt to determine whether it is possible to distinguish molecules which are electronic or structural isomers of one another [63]. They found that the electronic isomers naphthalene and azulene can be recognized, as can three structural isomers of monomethylazulene, as well as dimethyl- and trimethylazulene. Molecularly resolved studies have also been performed on the ethylene/Pt(111) system [64]. Land, *et al.* found that at room temperature the molecules diffused around the surface too quickly

to be resolved, however, by cooling to temperatures below 180 K, the ethylene and ethylidyne species could be resolved and distinguished between one another.

High diffusion rates of atoms and molecules on metal surfaces has prevented some systems from being resolved at room temperature. Specifically, low coverages of CO on Pt surfaces have not been atomically resolved at low temperatures, however their presence is clearly observed in the case of the CO-induced structural transformation of Pt(110) [65]. In this work, Gritsch, *et al.* directly observed the removal of the (2x1) missing-row reconstruction by adsorption of CO.

### 2.3.2 STM studies of dynamic systems

The STM is not only well suited for studying static surfaces, but has the potential to be extremely useful for monitoring the dynamics of local surface structures during surface reactions. This could conceivably allow for direct determination of the local activity on a surface and/or observation of changes in surface structures inflicted by reactions such as corrosion processes, or adsorbate-induced reconstructions.

Real-space observation of surface reactions has already been achieved for simple systems such as the dissociation of ammonia on Si(111) [66], the oxidation of Cu(110) [67], and the conversion of ethylene to ethylidyne on Pt(111) [68].

Dynamic information has also been obtained with the STM. In particular, quantitative diffusion rates have been obtained from STM images through a variety of methods. These include measuring the change in shape of features [69], observing changes in collective atomic structures (i.e. changes in the number or shape of islands) and comparing to Monte Carlo simulations [70], observing single atom hops from image sequences [71], and comparing 'diffusion related noise' with correlation functions [72].

## 2.4 Conclusions

The ultimate goal of structural catalyst science is the determination of the geometric and electronic structure of the catalyst during reaction. These conditions often mean environmental pressures of several atmospheres of reactant gases and temperatures of several hundred degrees Celsius. Atomic-scale investigations have been impossible or very difficult with present day techniques. As a result, our present knowledge of atomic-level structures of catalysts is largely limited to those which are stable in ultrahigh vacuum before and after reaction.

The demonstrated capability of the scanning tunneling microscope (STM) to probe the topography and electronic structure of surfaces and adsorbate layers with atomic resolution makes it a powerful tool in the study of surface chemistry. The aim of the work presented in the following chapters is to take advantage of STM's capacity for operation under wide-ranging environments to monitor catalyst structures as well as the structure of adsorbate molecules while under atmospheric pressures of reactant gases and variable temperatures consistent with catalytic reaction conditions.

To this end, the development of a specialized High Pressure and variable temperature STM (HPSTM) will be described and experimental results will be presented which provide, for the first time, atomic-scale, real space information on the structure of model catalysts and their adsorbates while under environmental pressures of reactant gases.

[1] J.G. Simmons, J. Appl. Phys. **34**, 1973, (1963).

[2] M.C. Payne, and J.C. Inkson, Surf. Sci. **159**, 485, (1985).
[3] J. Tersoff, and D.R. Harmann, Phys. Rev. Lett., **50**, 1998, (1983).

[4] J. Bardeen, Phys. Rev. Lett. **6**, 57, (1961).

[5] G. Ertl, J. Kuppers, Low Energy Electrons and Surface Chemistry, Verlag-Chemie, 1974, Germany.

[6] G. Binnig, H. Roher, Surf. Sci., **126**, 236 (1983).

[7] G. Binnig, H. Rohrer, Ch. Gerber, and E. Weibel, Phys. Rev. Lett., **50**, 120, (1983).

[8] G. Binnig, H. Rohrer, Ch. Gerber, and E. Weibel, Phys. Rev. Lett., **49**, 57, (1982).

[9] A. Bryant, D.P.E. Smith, and C.F. Quate, Appl. Phys. Lett., **48**, 832, (1986).

[10] G. Binnig, H. Rohrer, Ch. Gerber, and E. Weibel, Surf. Sci., **131**, L379, (1983).

[11] R.S. Becker, J.A. Golvochenko, and B.S. Schwartzentruber, Phys. Rev. Lett., **55**, 987, (1985).

[12] G. Binnig, K.H. Frank, H. Fuchs, N. Garcia, B. Rehl, H. Rohrer, F. Salvan, and A.R. Williams, Phys. Rev. Lett., **55**, 991, (1985).

[13] R.J. Hamers, R.M. Tromp, and J.E. Demuth, Phys. Rev. Lett. **56**, 1972, (1986).

[14] G. Binnig and H. Rohrer, Surf. Sci. **152-3**, 17 (1985).

[15] M. Salmeron, B. Marchon, S. Ferber, and D.S. Kaufman, Phys. Rev. B., **35**, 6, (1987).

[16] V. M. Hallmark, S. Chiang, J. Rabolt, J. Swolen, and R. Wilson, Phys. Rev. Lett., **59**, 2879 (1987).

[17] J. Wintterlin, J. Wiechers, Th. Gritsch, H. Hofer, and R.J. Behm, J. of Microscopy, **152**, 423, (1988).

[18] D. Chambliss, and R. Wilson, Bull. of American Phys. Soc., **35**, 579, (1990).

[19] R. Berndt, J.K. Gimzewski, and R.R. Schlittler, Ultramicroscopy, **42-44**, 528, (1992).

[20] M. Bott, M. Hohage, T. Michely, and G. Comsa, Phys. Rev. Lett. **70**, 1489 (1993).

[21] F. Ogletree, and M. Salmeron, Progress in Solid State Chemistry, Pergamon Press, Oxford, U.K., (1991).

[22] J.A. Golovchenko, Science, **232**, 48, (1986).

[23] P.K. Hansma and J. Tersoff, J. of Applied Physics, **61**, 1, (1987).

[24] G. Binnig and H. Rohrer, Rev. of Modern Physics, 59, 615, (1987).

[25] J.E. Demuth, U.K. Koehler, and R.J. Hamers, J. of Microscopy, **152**, 299, (1988).

[26] A.M. Barò, G. Binnig, H. Rohrer, Ch. Gerber, E. Stoll, A. Baratoff, and f. Salvan, Phys. Rev. Lett., **52**, 1304, (1984).

[27] G.F.A. Van de Walle, H. Van Kempen, P. Wyder, and C.J. Flipse, Surf. Science, **181**, 27, (1987).

[28] Y. Kuk, P. Silverman, and H. Nguyen, Phys. Rev. Lett. **59**, 1452, (1987).

[29] R.Q. Hwang, D.M. Zeglinski, A. Lopez Vazquez-de-Parga, D.F. Ogletree, and M. Salmeron, Phys. Rev. B, **44**, 1914, (1991).

[30] J.C. Dunphy, P. Sautet, D.F. Ogletree, and M.B. Salmeron, J. Vac. Sci. Technol. A **11**, 1975, (1993).

[31] A.J. Gellman, J. Dunphy, and M. Salmeron, Langmuir, **8**, 534, (1992).

[32] V. Maurice and P. Marcus, Surf. Sci. **262**, L59, (1992).

[33] B.J. McIntyre, M. Salmeron, and G.A. Somorjai, to be published.

[34] S. Rousset, S. Gauthier, O. Siboulet, W. Sacks, M. Belin, and J. Klein, J. of Vac. Sci. and Technol. A, **8**, 302, (1988).

[35] L. Ruan, I. Stensgaard, F. Besenbacher, and E. Lægsgaard, Phys. Rev. Lett., **71**, 2963, (1993).

[36] J. Wintterlin, H. Brune, H. Hofer, and R.J. Behm, Appl. Physics A, **A47**, 99, (1988).

[37] J.A. Stroscio, R.M. Feenstra, and A.P. Fein, Phys. Rev. Lett., **58**, 1668, (1987).

[38] I. Stensgaard, L. Ruan, F. Besenbacher, F. Jensen and E. Lægsgaard, Surf. Sci., **269/270**, 81, (1992).

[39] F. Jensen, F. Besenbacher, E. Lægsgaard and I. Stensgaard, Phys. Rev. B, **42**, 9206, (1990).

[40] D.J. Coulman, J. Wintterlin, R.J. Behm and G. Ertl, Phys. Rev. Lett. **64**, 1761, (1990).

[41] Y. Kuk, F.M. Chua, P.J. Silverman and J.A. Meyer, Phys. Rev. B, **41**, 12393, (1990).

[42] F. Jensen, F. Besenbacher, E. Lægsgaard, and I. Stensgaard, Phys. Rev. B **41**, 10233, (1990).

[43] R. Feidenhans'l, F. Grey, M. Nielsen, f. Besenbacher, F. Jensen, E. Lægsgaard, I. Stensgaard, K.W. Jacobsen, J.K. Nørskov and R.L. Johnson, Phys. Rev. Lett. **65**, 2027, (1990).

[44] D.J. Coulman, J. Wintterlin, J.V. Barth, G. Ertl and R.J. Behm, Surf. Sci. **240**, 151, (1990).

[45] L. Eirdal, F. Besenbacher, E. Lægsgaard and I. Stensgaard, Ultramicroscopy, 42-**44**, 505, (1992).

[46] E. Kopatzki, S. Günther, W. Nichtl-Pecher, and R.J. Behm, Surf. Sci. **284**, 154, (1993).

[47] T. Hashizume, M. Taniguchi, K. Motai, H. Lu, K. Tanaka and T. Sakurai, Jpn. J. Appl. Phys. **30**, L1529, (1991).

[48] J. Schröder, C. Günther, R.Q. Hwang and R.J. Behm, Ultramicroscopy, **42-44**, 475, (1992).

[49] H. Niehus and C. Achete, Surf. Sci. **289**, 19, (1993).

[50] F. Besenbacher and J.K. Nørskov, Progress in Surf. Sci. **44**, 5 (1993).

[51] D.F. Ogletree, D.M. Zeglinski, G. Somorjai, W. Siekhaus, and M. Salmeron, March meeting of the APS, New Orleans, LO, (1988).

[52] C. Klink, L. Olesen, F. Besenbacher, I. Stensgaard, E. Lægsgaard and N.D. Lang, Phys. Rev. Lett., to be published.

[53] S. Harada and M. Goda, J. Vac. Sci. Technol. A **8**, 308, (1990).

[54] O. Haase, R. Koch, M. Borbonus and K.H. Rieder, Ultramicroscopy, **42-44**, 541, (1992).

[55] M. Voetz, H. Niehus, J. O'Connor, and G. Comsa, Surf. Sci. **292**, 211, (1993).

[56] H. Niehus and C. Achete, Surf. Sci. **289**, 19, (1993).

[57] B.C. Schardt, S. Yau, and F. Rinaldi, Science, **243**, 1050, (1989).

[58] R. Vogel and H. Baltruschat, Surface Sci. **259**, L739 (1991).

[59] H. Ohtani, R.J. Wilson, S. Chiang, and C.M. Mate, Phys. Rev. Lett., **60**, 2398, (1988).

[60] J.K. Gimzewski, E. Stoll, and R.R. Schlittler, Surf. Sci., **181**, 267, (1987).

[61] P.H. Lippel, R.J. Wilson, M.D. Miller, Ch. Wöll, and S. Chiang, Phys. Rev. Lett., **62**, 171, (1989).

[62] V.M. Hallmark, S. Chiang, J.K. Brown, and Ch. Wöll, Phys. Rev. Lett. **66**, 48, (1991).

[63] V.M. Hallmark, S. Chiang, K.-P. Meinhardt and K. Hafner, Phys. Rev. Lett., **70**, 3740 (1993).

[64] T.A. Land, T. Michely R.J. Behm, J.C. Hemminger, and G. Comsa, Appl. Phys. A, **53**, 414 (1991).

[65] T. Gritsch, D. Coulman, R.J. Behm, and G. Ertl, Phys. Rev. Lett., **63**, 1086 (1989).

[66] R.J. Hamers, Ph. Avouris, and F. Bozso, Phys. Rev. Lett., 59, 2071 (1987).

[67] F. Besenbacher, F. Jensen, E. Lægsgaard, K. Mortensen, and I. Stensgaard, J. Vac. Sci. Technol. B **9**, 874 (1991).

[68] T.A. Land, T. Michely, R.J. Behm, J.C. Hemminger, and G. Comsa, Appl. Phys. A **53**, 414 (1991).

[69] D.A. Sommerfeld, R.T. Cambron, and T.P. Beebe, Jr., J. Phys. Chem. **94**, 8926, (1990).

[70] H. B. Elswijk, A.J. Hoeven, E.J. van Loenen, and D. Dijkkamp, J. Vac. Sci. Technol. B **9**, 451 (1991).

[71] R.M. Feenstra, A.J. Slavin, G.A. Held, and M.A. Lutz, Phys. Rev. Lett., **66**, 3257 (1991).

[72] J.C. Dunphy, P. Sautet, D.F. Ogletree, O. Dabbousi, and M.B. Salmeron, Phys. Rev. B, **47**, 2320.

# CHAPTER 3

# EXPERIMENTAL METHODS

## 3.1 Introduction

The nature of STM is such that in order to maximize the amount of information obtained from an STM experiment, it is necessary to have some idea about the atomic-scale composition and structure of the surface. By the same token, it is commonly observed that even though such surface structure and composition sensitive techniques as Auger electron spectroscopy (AES) and low energy electron diffraction (LEED) indicate that on a large scale the surface appears to be clean and well ordered, the STM experiment shows that this is not the case. STM's capability of real-space atomic resolution of surfaces have shown researchers that the surfaces which they originally thought to be largely 'perfect single crystal surfaces' by other surface sensitive techniques are in fact full of imperfections (such as steps, kinks, vacancies, and interstitial defects). Because of this, it is clear that extreme care is necessary for proper surface preparation and characterization prior to performing STM experiments.

This chapter describes in detail, the High Pressure Scanning Tunneling Microscope (HPSTM) system which was designed and constructed as part of this work. Also included are descriptions of the experimental vacuum techniques, sample preparation and characterization methods and conditions for the experiments performed in this thesis.

## 3.2 High Pressure STM (HPSTM) Apparatus

This section describes in detail the design and construction of a Scanning Tunneling Microscope (STM) which is contained in a reactor cell and allows *in situ* operation throughout a wide range of pressures and temperatures. This STM is capable of imaging in pressures ranging from ultrahigh vacuum up to several atmospheres. Samples can also be easily moved in and out of the STM cell in a small separate vacuum transfer chamber for external characterization and treatment. The equilibration time and stability of the microscope after temperature changes was determined at atmospheric pressures, by monitoring the evolution of atomically resolved images of Highly Oriented Pyrolytic Graphite (HOPG) at temperatures ranging from 300 to 425K. The STM's stability when flowing gases are used instead of stationary pressures was also examined.

In order to operate an STM in variable pressure (ultra-high vacuum (UHV) - atmospheric) and variable temperature (300 - 425 Kelvin) conditions, several critical design parameters must be considered, including: thermal drift for variable temperature operation, material compatibility, sample transfer in and out of STM, sample preparation, vibrational isolation, and variable pressure control and monitoring. In overcoming these design criteria, a specialized version of the STM was developed.

### 3.2.1 Microscope head design

The STM head consists of 2 concentric piezoelectric tubes [1] (piezos) and an anodized aluminum sample holder, (Figs. 3.1, 3.2 and 3.3). Typically the piezoelectric tubes' outer electrodes are sectored into four quadrants providing x-y motion. In the case of the outermost tube which controls the approach of the sample to the tip it is not necessary to sector the piezo as it is only used for z-displacement. The outermost piezo is

soldered [2] to an anodized aluminum tube (which has an electroless nickel coating at the solder joint) and provides large scale displacement of the sample by means of fast and slow length changes that cause the inertial translation of the sample holder. The inner piezo which controls scan/offset of the tip has 8 sectors in total (x+ offset, x- offset, y+ offset, y- offset, x+ scan, x- scan, y+ scan, and y- scan). The z offset is summed to all four offset sectors and the inner electrode is used as the z signal (the z displacement in the feedback loop).

Because of its symmetry around the z-axis, this design provides thermal compensation in the x and y directions. This is particularly important for variable temperature work. The head assembly is held mounted to the anodized heating shroud by machine screws. This was done in order to maximize the efficiency of the inertial approach, however it may be possible to eliminate this mechanical connection and have the head assembly held in place by silicone O-rings [3]. This design eliminates the need for adhesives which are often undesirable for several reasons: they tend to reduce mechanical stability, are reactive in many gaseous environments, are not vacuum compatible, are not capable of joining dissimilar materials, or are not capable of withstanding variable temperature operation. This design also has the advantage that the microscope can be disassembled and repaired easily. Aside from the piezoelectric transducers, machine screws, and silicone cord, the STM head is made of aluminum which has the advantage of having a high thermal conductivity and low reactivity. A 0.0005-in.-thick (0.0010-in.-thick can also be used) gold foil strip [4] is attached to the anodized aluminum sample support tube [5], providing electrical contact to the stainless steel sample holder by frictional contact. Because of its thickness, the foil does not interfere with the sample motion, allowing sample transfer. Tip wires [6] are held in a 0.75 in. long section of a stainless steel hypodermic needle [7] which is glued [8] to a small ceramic collar. This needle/collar assembly is also glued to the end of the scan/offset piezo. Electrical contact

to all piezo sectors, the tip assembly, and gold bias foil is provided by 0.006-in.-diameter Kapton coated copper wire [9] which is soldered to each electrode. To the other end of the wires are attached gold pins [10]. Smaller diameter (0.003 in.) wire may also be used, however in any case it is important to be careful when stripping the Kapton insulation from the ends. One method which has proven to be successful is to use a small butane lighter. The insulation turns black and is easily wiped off. A teflon pin holder which is attached to the back of the heating shroud allows for a modular connection of the STM head to the STM housing. In this configuration the STM may be disconnected from the housing without disrupting the feedthru connections. With this design, atomic resolution images were obtained of Au(111)/mica which is known to have an atomic corrugation of approximately 0.3 Å (see Fig. 3.4) [11]. Also, with a high mechanical resonance frequency, the microscope is able to obtain images with very high tip scan rates. Fig 3.5 is a large scale (1000 Å x 1000 Å) image of Au(111)/mica which was obtained in 1.02 seconds. In this image the monatomic step structure of the gold is clearly resolved. This design has proven to be very stable as images have been routinely obtained where the vertical resolution is better than 0.1 Å.

The mechanical frequency characteristics of the STM head were determined by measuring the electrical signal generated in one sector of the piezo tube while it is being excited by a signal applied to another sector [12]. In this test, a sine wave voltage of varying frequency was applied to one sector, while the frequency response in which the other sector resonated were monitored with a phase-sensitive lock-in amplifier. As there are 9 outside sectors total (8 for the scan/offset tube and 1 for inertial approach), there are a large number of possible permutations. Generally, it was found that the configuration which gave the lowest resonance occurred when monitoring a scan piezo sector while applying a sine wave voltage to its two neighboring sectors. In this geometry, the response of the scan piezo sector was measured while the sine voltage with a 5 V rms was

applied over a frequency range of 100 Hz to 15 KHz to the neighboring sectors. Typically, resonances were observed to occur around 9 - 12 KHz. An example from an earlier HPSTM head design is shown in Fig. 3.6. This plot shows a small resonance in the sector at 4 KHz and much larger resonances at 8 KHz.

The head is enclosed (except for the sample introduction opening) in an anodized aluminum heating shroud. For temperature dependent studies under pressures of gases, the entire head is heated resistively to a constant thermal gradient, after which the sample is imaged. This method eliminates the problem of uncompensated thermal expansions due to non-uniform temperature gradients within the head. Unfortunately, this method also limits the maximum temperature to the temperature at which the piezos depolarize. One would prefer to use the heating method currently in use in UHV variable temperature STM experiments, which is to heat only the sample and thermally shield the microscope. Unfortunately, initial experiments with this geometry in atmospheric pressures of gases proved that the thermal conduction through the gas environment created instabilities which were too great to allow STM experiments.

To illustrate the capabilities of this instrument, Highly Oriented Pyrolytic Graphite (HOPG) was imaged while increasing the background pressure of argon. The microscope was able to maintain atomic resolution while increasing the pressure of argon from $5x10^{-9}$ Torr up to 1 atmosphere. In principle, the microscope is capable of imaging in pressures ranging up to several hundred atmospheres [13], however, as the reaction cell is fitted at present with viewports which are not capable of withstanding large internal pressure differences, experiments have not been attempted in pressures above 2 atmospheres. As many images as desired could be obtained at any given pressure, as the gas introduction control was remarkably good. In fact, the microscope is stable enough that it has been possible to image while under flowing gas conditions (approximately 50 ml/s). In principle, there is no limitation to the rate of flow, so long as it is not turbulent.

Images of HOPG have also been obtained at atmospheric pressures and elevated temperatures. Figure 3.7 shows a time lapsed series of current images of HOPG taken at 425 Kelvin over a twenty minute time period, with a 10 minute separation between images. The temperature was measured by placing an alumel/chromel thermocouple against the edge of the alumina sample holder tube. From previous thermocouple experiments, it was determined that this location consistently recorded the lowest temperature of the entire head assembly, but was always within two degrees of the sample temperature. The first image, (Fig. 3.7(a)) shows significant drift, although rows of atomic structure in the x-direction are resolved. The second image, taken 10 minutes later, (Fig. 3.7(b)) shows the drift slowing down such that structure along the y-direction begins to appear. The third image, (Fig. 3.7(c)) was taken 10 minutes after the previous one and approximately 1 hour after heating commenced and shows HOPG clearly resolved in both the x and y directions. This type of drift in the first images is to be expected as the tip is scanning much faster in the x-direction than in the y-direction. It has been found that the microscope usually requires 1 hour for thermal equilibration before imaging can take place after each temperature change. The STM head is controlled by electronics designed in this laboratory, a modified version of these electronics are available commercially [14]. The software used for data acquisition and analysis is also developed in this laboratory and available commercially[15].

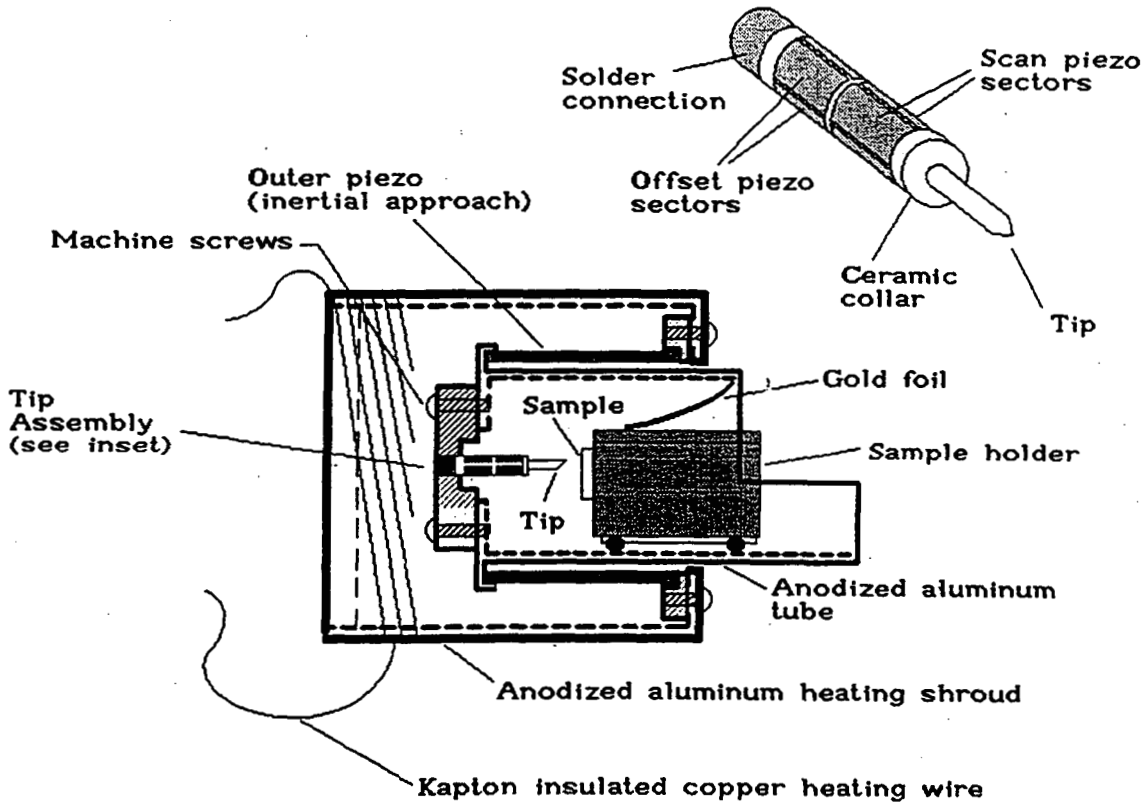


Figure 3.1 Cross-sectional schematic of STM head (side view). The piezos are soldered to the supports and the entire assembly is attached to the heating shroud by machine screws, making a very stable head assembly. The sample car rests on sapphire balls inside an anodized aluminum tube and is provided bias voltage by contact with a hanging gold strip.

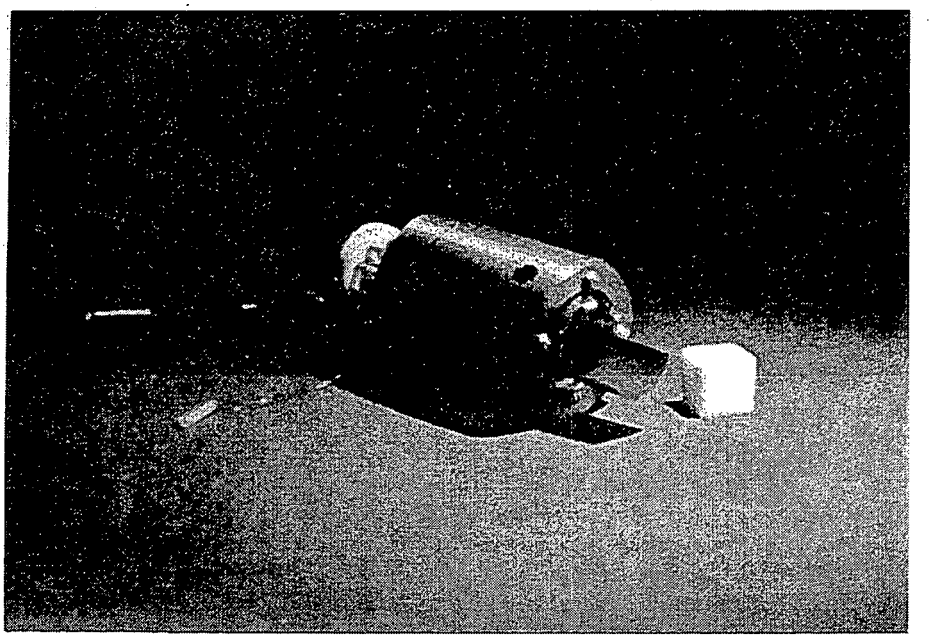

Figure 3.2. Photograph of HPSTM head, (sugar cube is approx. 1 cm. on a side).

Figure 3.3. (following page) Photograph of HPSTM head, heating shroud, and housing.

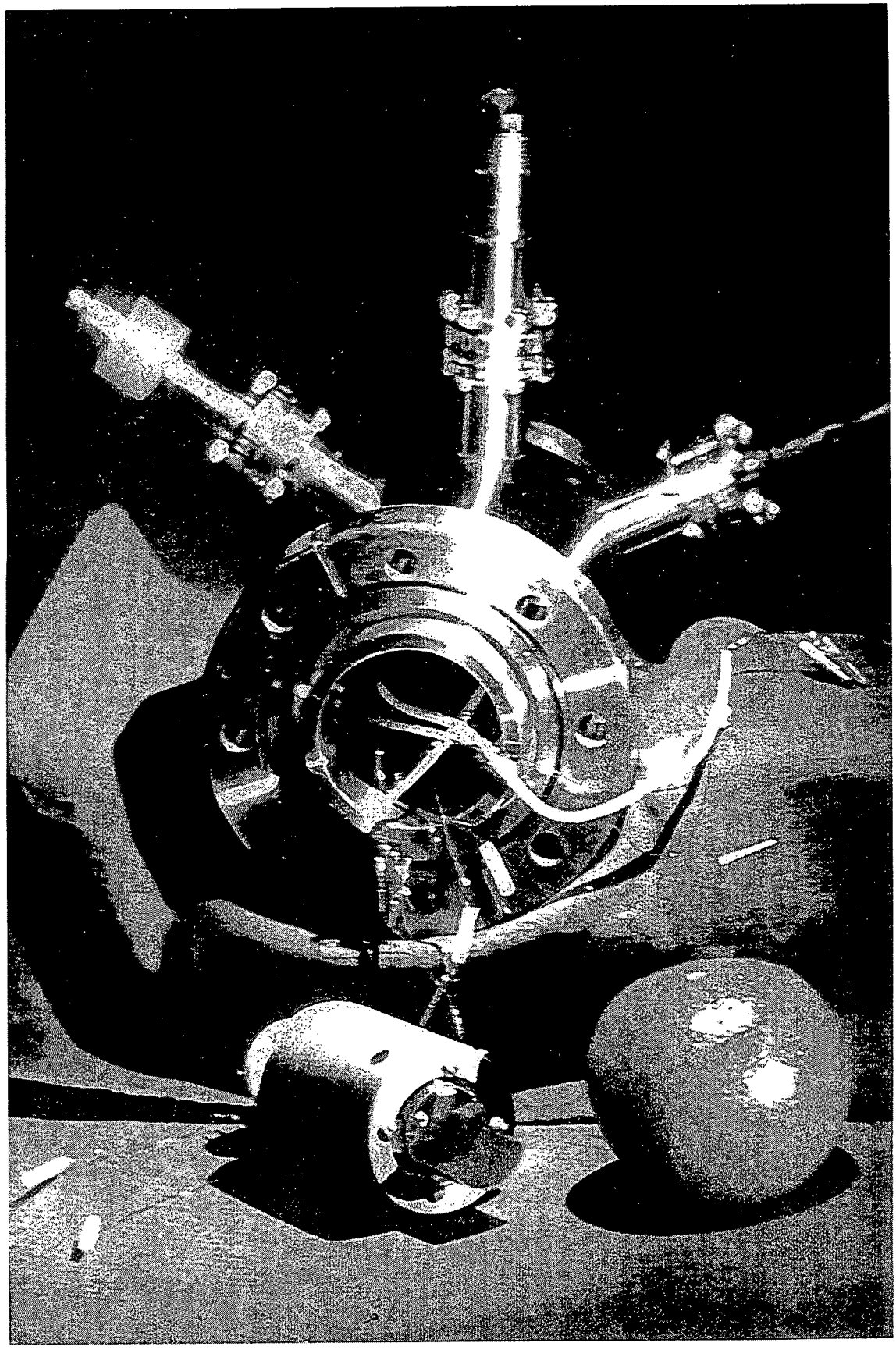

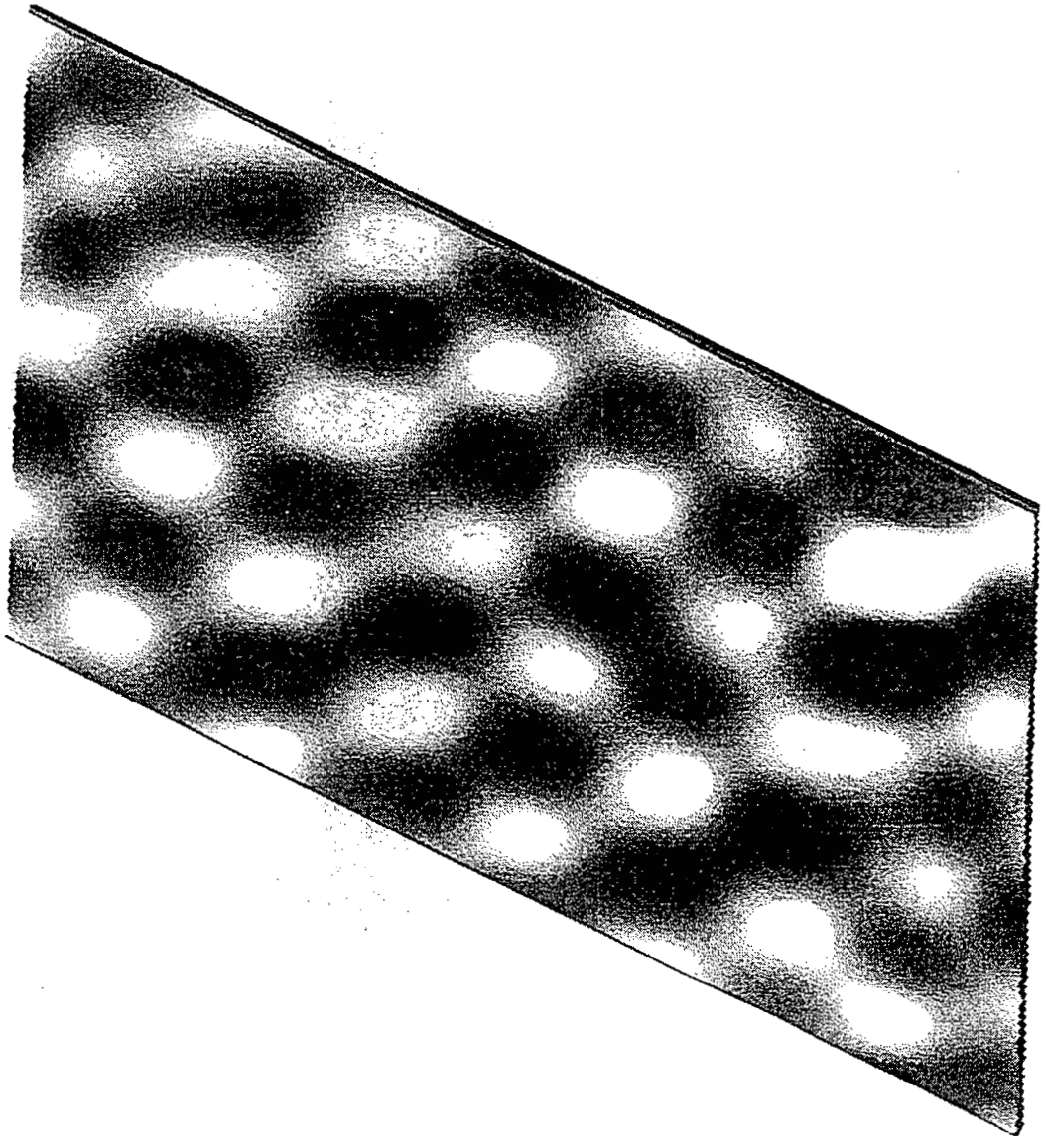

Figure 3.4. STM current image showing atomic structure of Au(111) supported on mica. Image size: 26 Å x 180 Å , dz $\approx$ 1 nA, $V_{bias}$ = 0.02 V

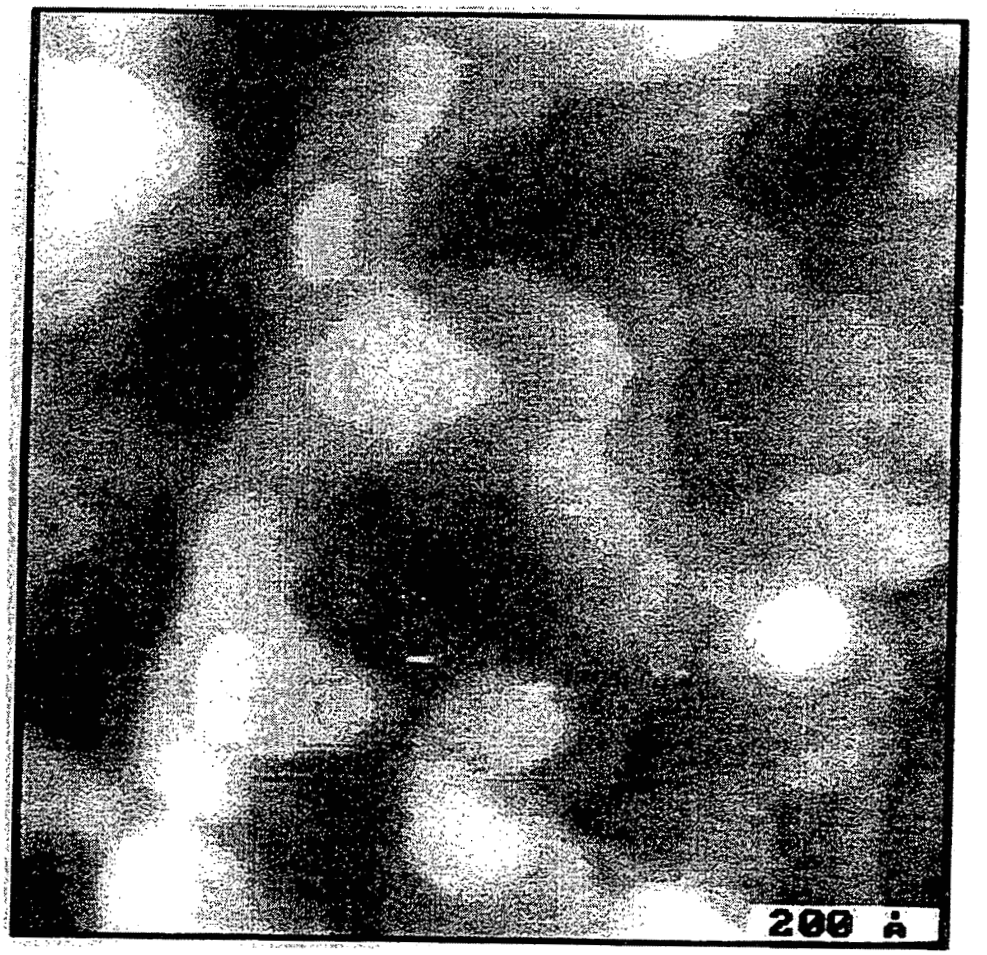


Figure 3.5. A large scale (1000 Å x 1000 Å) image of Au(111)/mica which was obtained in 1.02 seconds. In this image the monatomic step structure of the gold is clearly resolved. This design has proven to be very stable as images have been routinely obtained where the vertical resolution is better than 0.1 Å.

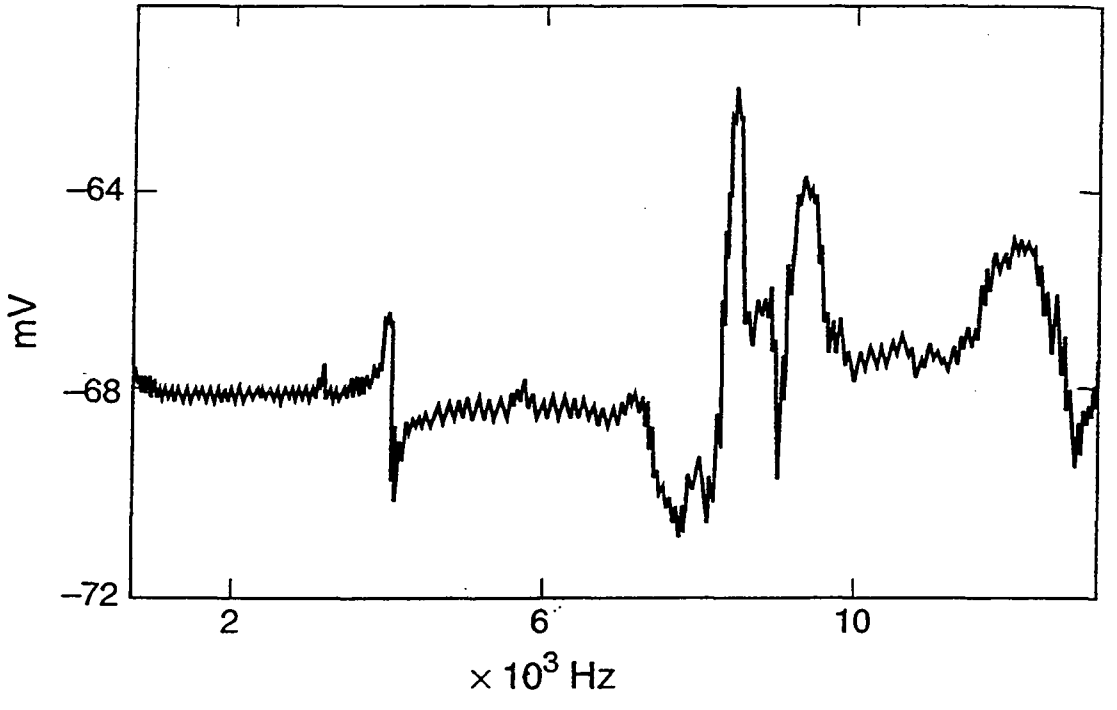


Figure 3.6. Voltage vs. frequency response of a y-scan piezo sector upon excitation of x-scan piezo sectors with sine voltage of 5 V rms. The frequency was scanned from 100 Hz to 15 KHz. The voltage response baseline was flat below 1 KHz. A small excitation can be seen at 4 KHz with larger resonances beginning at 8 KHz. The voltage response was recorded with a phase sensitive lock-in amplifier. This plot is from an earlier HPSTM design.

Figure 3.7. (following page) Current images of Highly Oriented Pyrolytic Graphite (HOPG) obtained in 1 atmosphere nitrogen at 425 Kelvin. The series of images are time lapsed to show the thermal drift decrease as the microscope reaches thermal equilibrium. (a.) Taken approximately 45 minutes after heating commenced, showing wavy rows of atomic structure indicating a significant amount of thermal drift. Image size: 20 Å x 20 Å. (b.) Taken 10 minutes after the first image (a.), showing a reduced drift rate as atomic structure along the y-direction begins to appear. Image size: 20 Å x 20 Å. (c.) Taken 65 minutes after heating commenced and 10 minutes after (b.), showing atomic resolution clearly resolved in both the x and y directions. Image size: 50 Å x 50 Å.

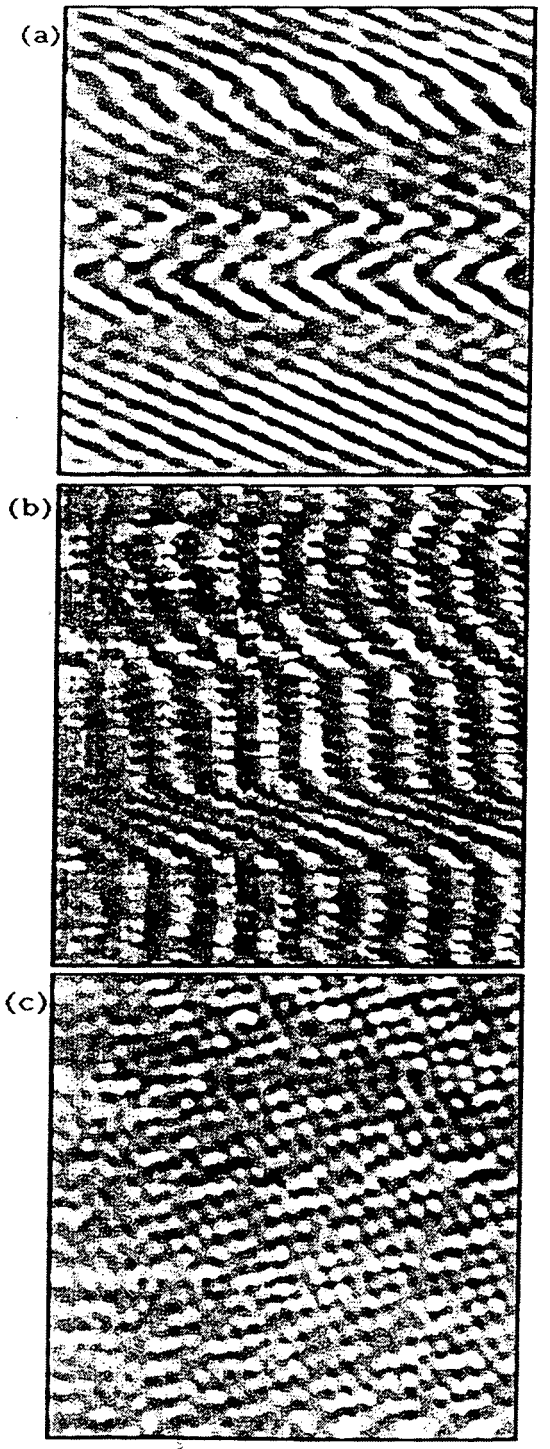
(a)
(b)
(c)

### 3.2.2 Cutting, etching, soldering, and re-polarizing piezos

Piezos are relatively easy to cut and sector and, as often a customized configuration is necessary for a particular application, it is usually cheaper and faster to cut and etch the piezos in the lab.

Piezoceramic companies generally charge for piezos by the piece, therefore it is generally cost efficient to purchase piezo pieces which are multiples of the length actually required for a particular application (unless there are requirements that the ends of the tubes be metallized). Cutting piezos to a desired length is a simple process which requires a low speed diamond saw having a thin blade. For small (0.125" diameter) piezos it is best to glue them to a microscope glass slide using Duco® cement. After cutting, the Duco® cement is easily dissolved in acetone and any rough edges can be removed with fine sandpaper (wet/dry sandpaper works very well). The glass slide is then attached to the mounting assembly of the diamond saw and can be easily manipulated to allow the desired cut. Cutting piezos with larger diameters usually requires the piezos to be securely attached with wax to a hollow mandrel (glass is probably best but brass can also be used). A mandrel is a small rod which has one end machined down to slightly less than the inside diameter of the piezo tube). Warming the mandrel on a hot plate, blocking wax, commonly used in (and borrowed from) glass shops, is melted over the machined end of the mandrel. The piezo is then attached and the heat is turned off and the wax is allowed to set.

Once cut, the piezos are ready for etching, again it is necessary to securely mount the piezo in some fashion which allows access to all areas of the piezo for resist coating, handling, and etching. This is usually accomplished by use of a brass mandrel. In this configuration the whole external electrode surface is exposed for sectoring. One should take care not to allow wax on the outside surface of the piezo as this usually results in an uneven coating of the resist and makes etching more difficult. Once mounted, the piezos

can be presectored using micro-circuit board tape [16] (otherwise the sectoring can be achieved using a razor blade and a steady hand following the resist coating).

The piezos are then coated with Miccroshield® [17] etch resist. This resist is usually too concentrated for easy application and requires some dilution with acetone (be careful not to stir too vigorously or small bubbles will form in the resist mixture which usually result in the formation of pinholes. Other resists can be used, however it is necessary to test to make certain they will withstand the highly acidic etch necessary to remove the nickel coating. It was found that perhaps the easiest method of obtaining an even coating of the resist was to immerse the piezo in the Miccroshield® resist (rather than painting which usually left brush streaks).

After sectoring, the piezos are immersed in a 1:1:1 (by volume) solution of sulfuric acid, nitric acid, and de-ionized water (remember to add the acid to the water!). In preparing this etch solution, it will be very warm initially and it is necessary to let it cool to at least room temperature before immersing the piezo, otherwise the etching will be too vigorous and the resist is likely to fail (putting the etch solution in a refrigerator helps (especially with other etch resists). Also, when using brass mandrels, be sure to coat the brass with resist as it will also react with the etch solution.

It should be noted that for STM head assembly, piezo soldering was found to produce the most mechanically stable microscope head. In addition, piezos could be exchanged relatively easily (as opposed to gluing which often resulted in extensive efforts to remove glue from the joints of the support rings). It was found that soldering to aluminum pieces could be done if the pieces had an electroless coating of nickel at the solder joints [18]. In order to solder the piezos, a heating plate was used and the piece was heated to approximately 200° C (the heating configuration was done in whatever order which minimized the heating of the piezo itself). While the use of the Eutector 157 solder flux was necessary, it should also be minimized as it is highly corrosive. One

should take particular care to protect anodized aluminum pieces from this flux as the anodization will be removed quite efficiently (teflon tape works well to protect the inertial approach tube).

Once assembled (especially after piezo soldering), and often during the course of experiments, it is useful to re-polarize the piezos to regain the maximum displacement per volt. Also it should be mentioned that occasionally a light coating of graphite [19] should be applied to the inertial approach tube and sapphire balls of the sample holder for optimum inertial approach. Routine re-polarization is also often desirable in order to maintain a constant calibration (within a few percent) over long periods of time. This can be very easily accomplished by applying a voltage of 30 - 40 Volts per 0.001 in. wall thickness with the negative polarity applied to the inside of the piezo tube. Piezo manufacturers recommend this be applied at room temperature for 8-12 hours. Re-polarization can be achieved more quickly using higher voltages or if the piezo is at an elevated temperature (such as during bakeout).

### 3.2.3 HPSTM Reaction Cell.

The STM is housed in a small stainless steel vacuum chamber (approximately 2 Liters) containing an ion pump [20] and detachable turbopump station [21] (see Fig. 3.8 and 3.9). Thus, the chamber can also be pumped down to UHV. The reactor cell has an infrared spot heater [22] which allows samples to be heated up to 1400 Kelvin in atmospheric pressures. This allows a number of *in situ* high pressure sample preparations that otherwise could not be performed for lack of an external heating source. The chamber is fitted with variable leak valves, ion and convectron tube gauges [23] for gas introduction and control, as well as an electron bombardment heater. This system is also equipped with a quadrupole mass spectrometer [24] which can be differentially pumped

for gas analysis while the chamber is pressurized. Finally, the chamber has a turbopumped airlock for *in vacuo* sample transfer to and from a nearby UHV chamber [25] capable of performing Auger electron spectroscopy (AES), low energy electron diffraction (LEED), and STM.

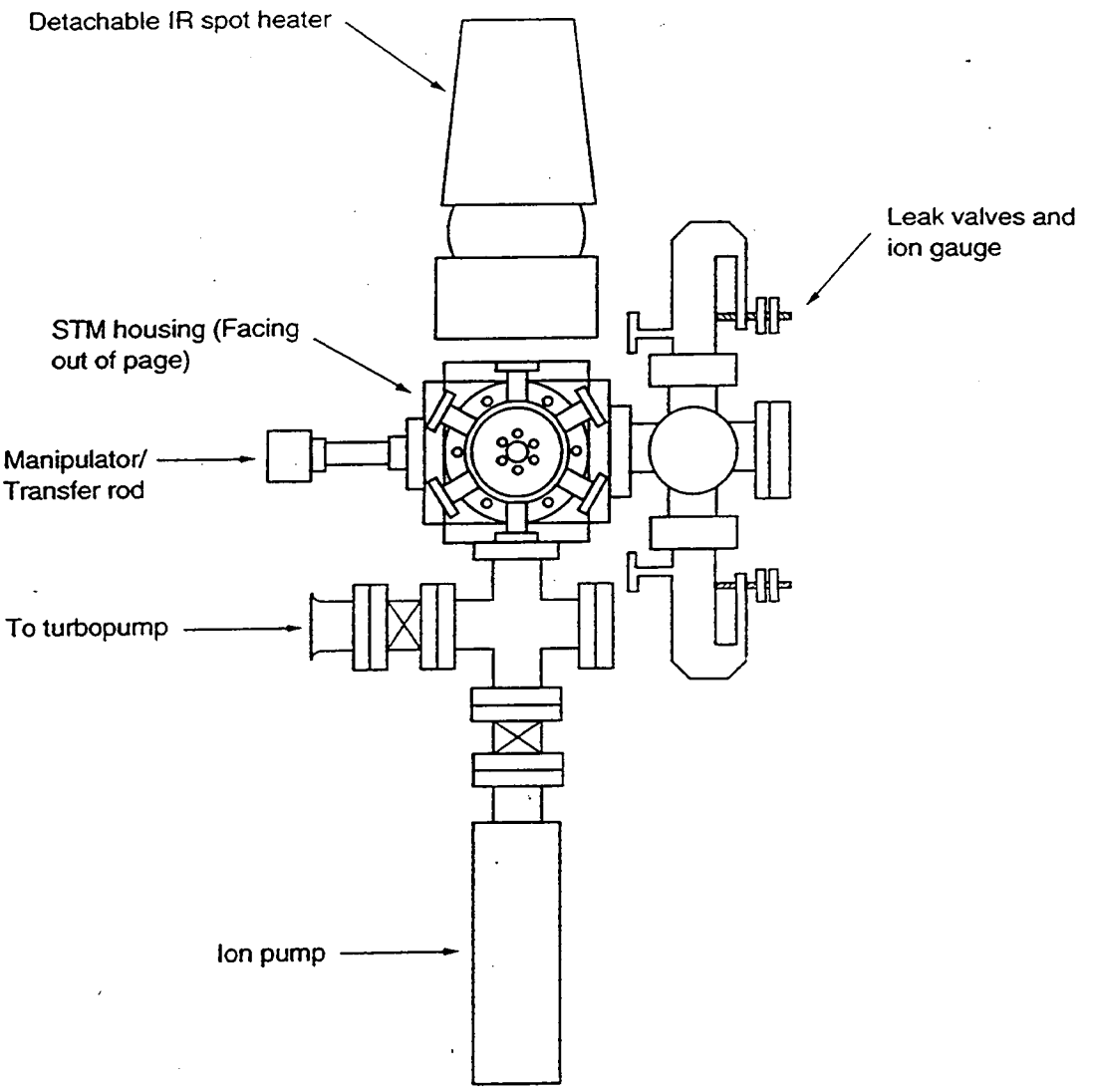


Figure 3.8. Schematic of HPSTM Reaction Chamber. The STM housing is facing out of the page. To the left of the STM housing is the transfer rod/electron bombardment heater. The transfer chamber is not pictured.

Figure 3.9. (Following page) Photograph of HPSTM Reaction Chamber.

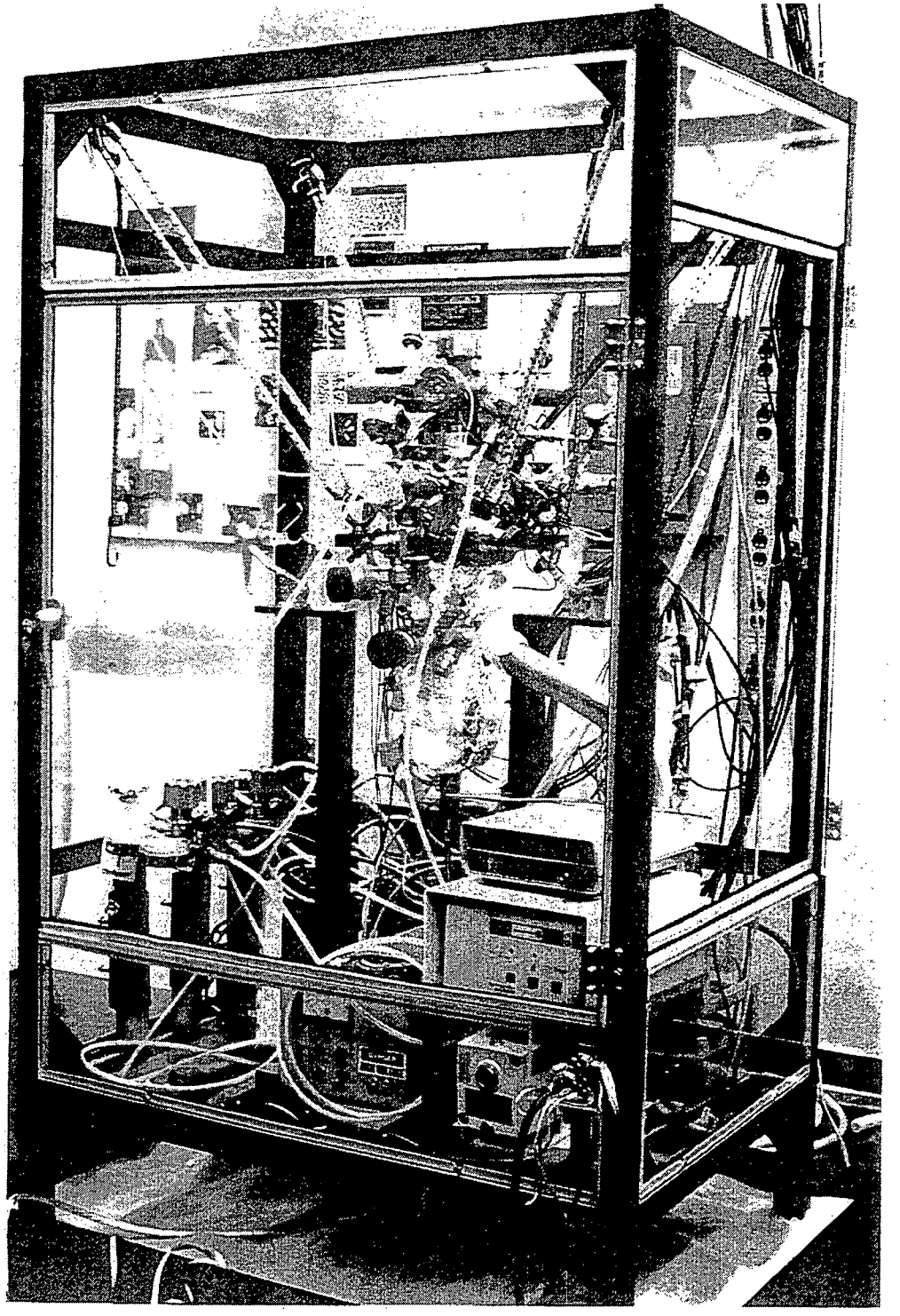

### 3.2.4 Vibration Isolation.

This instrument uses three stages of vibration isolation. One stage is used for the in-vacuum instrument assembly. The STM head is contained in a series of concentric damping plates separated by silicone cord. The reactor cell is supported by a series of elastic cords. These elastic cords are attached to an extruded aluminum frame which is suspended in a sand bath. The elastic cords are 3/8-in-diameter and arranged such that the chamber is level and has a resonance between 1-2 Hz. The frame housing is encased in Lucite [26] sheeting in order to damp acoustical noise. This method of vibration isolation has been found to be quite effective and cost efficient.

### 3.2.5 Sample Transfer.

The system has two mechanisms of sample transfer. The reaction cell is equipped with a differentially pumped manipulator/transfer rod which allows the sample to be transferred in and out of the STM. This assembly is equipped with a built in electron bombardment heater, and is also capable of placing the sample at the correct focal point for heating by the infrared spot heater. The second transfer mechanism is a vacuum transfer cell. This cell consists of a 2 3/4" Tee to which an internal magnetic transfer rod assembly is attached at one end and a gate valve with a quick flange at the other. Hanging down from the cell is an 8 L/sec. ion pump. After transfer of the sample from the STM to the manipulator/transfer rod, the sample can then be removed from the reactor cell, placed in the vacuum cell, and transferred *in vacuo* to a separate UHV chamber. Currently, samples can be transferred while maintaining pressures $< 10^{-7}$ Torr.

### 3.2.6 Initial tests with Pt(110)

After the graphite tests described above, the stability of the Pt(110) surface was investigated in various environments. Following sample cleaning and characterization in a neighboring UHV chamber, the Pt(110) surface was transferred *in vacuo* to the reaction cell. The sample was cleaned by heating to 900 K in $10^{-5}$ Torr of $O_2$, a procedure previously tried in the UHV chamber and proven to produce clean, well ordered Pt(110) surfaces with (3x1) periodicity. This surface was then exposed to and imaged in various pressures of oxygen and hydrogen. Analysis with the mass spectrometer showed that the most efficient method of switching from one gas to another is to pump the chamber with the turbopump to 1 x $10^{-6}$ Torr and then introduce the new gas. Since impurity levels in the compressed gas cylinders were not better than 1 ppm, it was not necessary to bake out the reaction cell before changing gases. Figure 3.10 is a topographic image of the Pt(110) reconstructed surface in 1 x $10^{-6}$ Torr hydrogen and at room temperature. The vertical columns in this image are missing row reconstructions. This image is 84 Å x 177 Å and shows the surface as having nested reconstructions or areas with small (2x1) or (3x1) reconstructions separated by larger reconstructions. Small patches of (1x1) structure are also observed [27]. Figure 3.11 shows a topographic image of the reconstructed Pt(110) surface which was obtained at 425 Kelvin in 1.6 atmospheres of hydrogen. Missing row reconstructions are clearly visible, as are some defects, the image is 230 Å X 220 Å, dz = 20 Å. The surface at 425 Kelvin appears to be similar to the surface at room temperature and atmospheric pressures of hydrogen. In general, the surface in hydrogen exhibits a large number of nested, missing row ((nx1) for n=3,4,5,6,7) reconstructions.

In another example, Figure 3.12 shows a topographic image of the same Pt(110) surface in 1.7 atmospheres of oxygen at 425 Kelvin. The image size is 540 Å x 430 Å, dz

= 10 Å and does not show the small scale structure observed when the surface is exposed to hydrogen. Instead, a larger (100-300 Å) scale structure is present, that shows high corrugation in the direction perpendicular to the compact [$\bar{1}$10] rows of Pt atoms. Holes (black spots) are also evident in many of the high temperature images and are not understood, but may be due to the presence of impurities on the surface. They appear to have corrugations ranging from 1 Å up to 20 Å.

While the images shown are not necessarily of the same area of the surface, they are representative of those obtained in their respective environments. Images of Pt(110) have been taken in a variety of environments and temperatures and will be discussed in more detail in the next chapter.

These results indicate that indeed this instrument is capable of imaging the atomic-scale structure of the surface in high pressure and temperature gas environments. It also demonstrates the usefulness of these types of studies, by showing the sensitivity of the Pt(110) surface to the gas environment in equilibrium.


Figure 3.10. Topographic image of the Pt(110) surface in 1 x $10^{-6}$ Torr hydrogen and room temperature. The vertical columns in the image are missing row reconstructions. (2x1) and (3x1) reconstructions are clearly resolved along with larger nested reconstructions. Image size: 84 Å x 177 Å, dz = 1 Å.

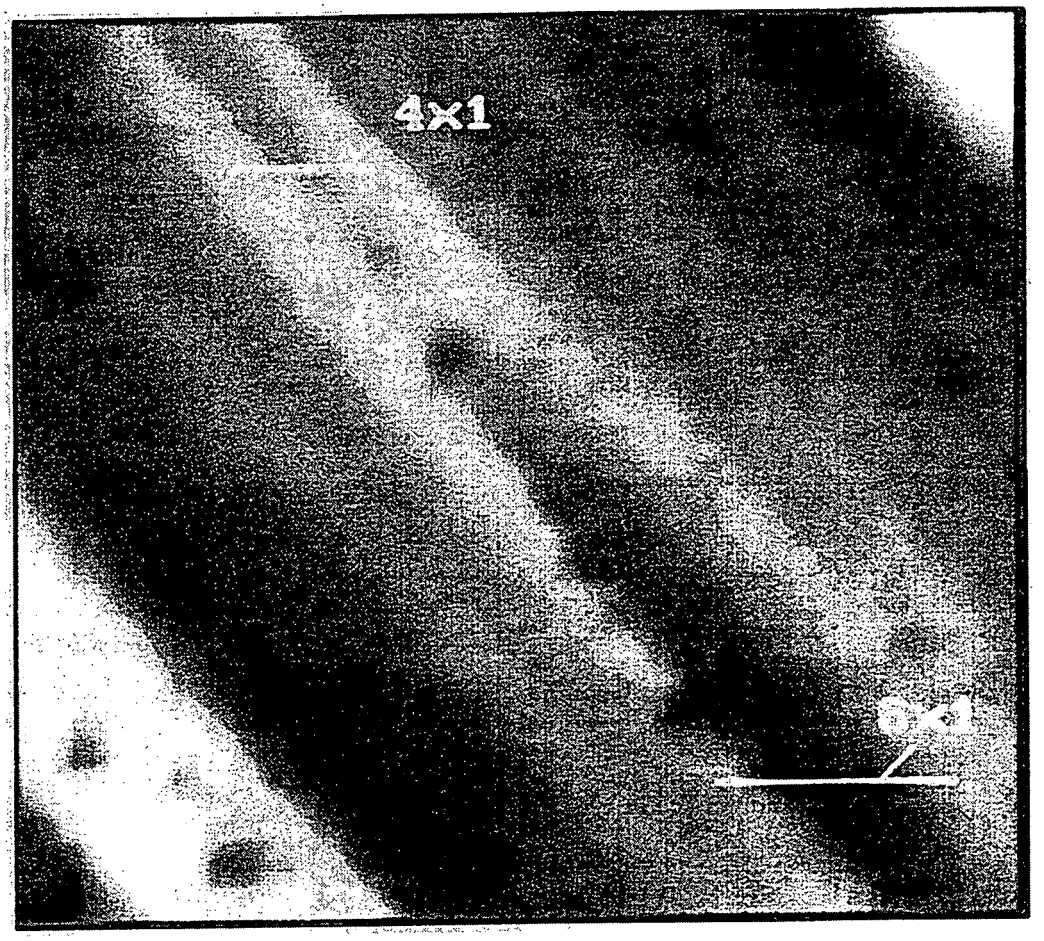


Figure 3.11.Topographic image of the Pt(110) surface in 1.6 atmospheres of hydrogen and at 425 Kelvin. Missing row reconstructions are clearly evident. Image size: 230 Å x 220 Å, dz = 20 Å.

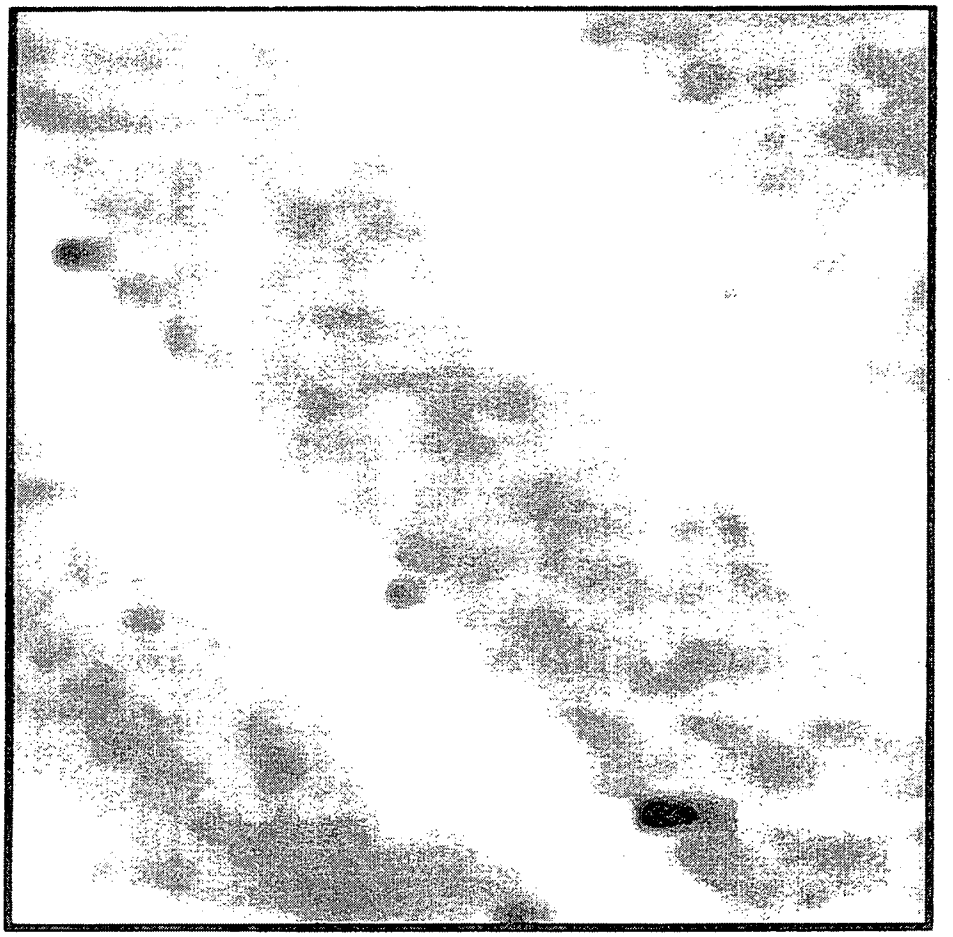

Figure 3.12.Topographic image of the Pt(110) surface in 1.7 atmospheres of oxygen and at 425 Kelvin. The image does not show the small scale missing row reconstructions, however, there is some large (100 - 300 Å) scale structure present. The presence of the holes (black spots) is not understood but could be due to the presence of impurities. The image size is 540 Å x 430 Å, dz = 10 Å.

### 3.2.7 Summary

The design of a specialized STM and reactor system in which samples may be imaged while exposed to pressures ranging from UHV to atmospheric, and temperatures up to 425 Kelvin has been described. Initial results on the Pt(110) surfaces and Au(111) thin films clearly demonstrate the stability of the instrument and the possibilities of extending the range of environments in which it is now possible to observe the atomic structure of surfaces and adsorbates.

## 3.3 UHV Apparatus

The sample preparation for the high pressure STM experiments and the experiments described in chapters 5 & 6 were performed using the ultrahigh vacuum (UHV) system shown schematically in Fig. 3.13. The basic features of this system are:

• UHV chamber with a base pressure of $< 1 \times 10^{-10}$ Torr. The belljar is a commercially available model (Varian) pumped by an ion pump. The chamber is equipped with a turbomolecular pump for initial pumpdown and sample transfer in and out of UHV through an airlock. The system is also equipped with a titanium sublimation pump which was used occasionally when it was necessary to increase the pumping speed of reactive gases.

• A modified commercial crystal manipulator allowing off-axis x,y,z motion and rotation of the sample. The manipulator is equipped with an electron bombardment heater capable of sample heating to 2000 °C.

• A single-pass cylindrical mirror analyzer with a glancing incidence electron gun for performing Auger Electron Spectroscopy.

- Electron optics for performing Low Energy Electron Diffraction (LEED).
- Ar+ ion sputtering gun for cleaning of the surface.
- Sample cooling by thermal contact with a liquid nitrogen cooled copper block.
- A quadrupole mass spectrometer (UTI 100C) for analysis of background gases.
- Four leak valves for controlled leaking of gases into the UHV chamber.

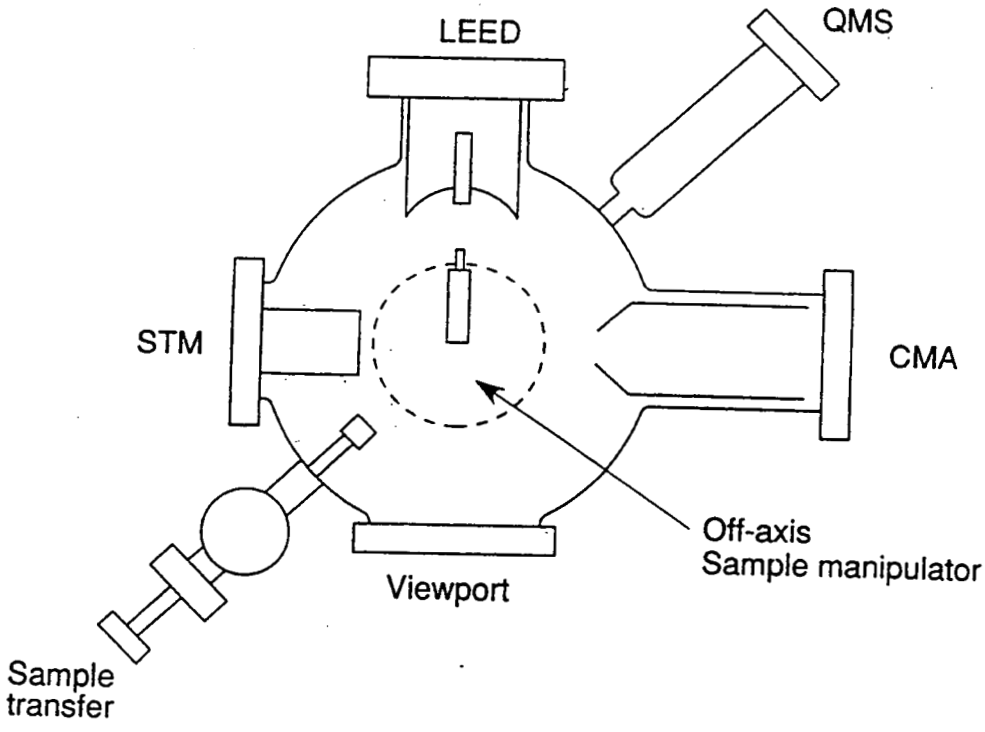


Figure 3.13. Schematic of UHV system.

### 3.3.1 Auger spectroscopy

The theory of the Auger process has been described in detail in a number of articles and books [28,29]. The experiment is performed by having a beam of high energy electrons incident on the surface ionizing atoms to create core holes. The excited state ion can then decay either by X-ray emission or by an auto-ionization process in which an electron from a higher lying level decays into the core hole simultaneously ionizing a second electron into the continuum. The kinetic energy of the detected electron is determined by the various energy levels involved in the process and is characteristic of the various energy levels involved in the process and is characteristic of the atom from which it originated.

Auger data were obtained using the glancing incidence electron gun for excitation and the cylindrical mirror analyzer (CMA) as the detector. Auger Electron Spectroscopy (AES) was most commonly used to detect impurities. In this mode the electron beam was incident at ~60° from the crystal normal at 1.5 KeV and ~ 20 μA. The CMA pass energy was modulated at ~ 17.4 KHz with a 5 V peak-to-peak modulation. The signal current was decoupled and detected with a lock-in amplifier.

Auger spectra obtained in this mode provided a quick check of surface cleanliness and was also used in some cases as a rough estimate of adsorbate coverage (generally within a few percent of a monolayer). AES was particularly useful for this as platinum has relatively weak Auger transitions and therefore most of the common contaminants were easily detected. Silicon contamination is more difficult to detect directly as its main AES transition overlaps with Pt, however its presence could be detected by checking for the presence of oxygen.

### 3.3.2 Low energy electron diffraction

In the Low Energy Electron Diffraction (LEED) experiment, a monochromatic beam of electrons is directed onto a flat, single crystal surface. Some of the electrons are back scattered and can be detected by any number of techniques, in this case a fluorescent screen was used. Due to their wave character, some of the back-scattered electrons will be diffracted and will appear as spots on the screen. The diffraction pattern gives a reciprocal space representation of the two dimensional surface periodicity. In addition to the two dimensional periodicity of the surface, some three dimensional information can be determined from an extensive analysis of the LEED spot intensities. Since electrons of 50-500 eV can only penetrate the first 2-3 layers of the surface, the intensity of the scattered electron beams depends on their energy. An analysis of the LEED spot intensities versus electron energy can thus be used to give information about distances normal to the surface. Detailed discussions of the LEED experiment can be found in numerous publications including G. Ertl, *et al.* [30] and M.A. Van Hove, *et al.* [31].

The LEED experimental apparatus used in this work is a relatively simple one which is commercially available (Varian). This work has used LEED primarily to check long range order on the surface before and after performing STM experiments.

## 3.4 Materials and sample preparation

Most of the experiments described in this thesis were conducted on the platinum (110) and (111) crystal faces. The platinum crystals were previously grown from a melt of high-purity zone-refined platinum. the platinum crystals were then oriented by Laue X-ray back-diffraction and cut with a diamond saw. After cutting, the crystals were polished using diamond pastes to approximately 1 micron followed by final polishing in an alumina

[32] slurry using a syntron [33] mechanical polishing apparatus. At this point the crystals were introduced into the UHV system for final cleaning and preparation.

The crystals used were cylindrical discs, approximately 5 mm in diameter and 0.75 mm thick. The surfaces were cut and polished within ~ 1º of the (111) and (110) orientations.

Despite the high purity of the single crystals used in this work, extensive cleaning was necessary to prepare atomically clean surfaces. This is because the low-level contaminants (sulfur, calcium, silicon, carbon, etc...) in the bulk single crystals have a lower surface free energy than the metal and segregate to the surface.

A clean single crystal surface can be prepared by removing these contaminants from the near surface region. This can be accomplished by Ar+ bombardment and cycles of heating in oxygen (1000 K in 5 x $10^{-7}$ Torr of $O_2$). The oxygen assists in the surface segregation by the formation of oxides as well as the removal of carbon and sulfur from the surface. In the case of silicon conatmination, it was necessary to sputter the surface as annealing in oxygen and/or vacuum are ineffective. The surfaces were then annealed in vacuum for 1-5 minutes at approximately 1000K to remove oxygen and to produce smooth, well-ordered planes of the particular metal surface cut.

[1] EBL Stavely Sensors, EBL2 type piezoceramic tubes 1.110 in o.d. x 0.5 in. long x 0.060 in. wall (approach tube). 0.125 in o.d. x 0.5 in. long x 0.020 in. wall (scan/offset tube). Note, it is cheaper to order piezos at at least twice the required length and cut them with a low speed diamond saw. Piezos should have a "wraparound" ( metallized on all surfaces, including ends) metallization with nickel.

[2] Eutectic Co., Flushing, NY. EutecRod 157. This is UHV compatible solder consisting of ~98% Ag, and contains no Cd, Zn, or low melting point metals, Acid flux must be used during soldering.

[3] Parker Seal Group, Lexington, KY. Viton can be used in these applications but it was found that S613-60 Silicone O-rings can operate under the same conditions and are better because they are somewhat softer than Viton.

[4] Actually two gold strips are reccomended since then the resistivity can be checked during the course of the sample approach to the tip to insure good contact with the sample holder.

[5] It should be noted that the support tube should be as free of scratches or asperities and as smooth as possible. Prior to anodization, it is reccomended that the aluminum tube be hand polished using microcloth with a slurry of aluminum powder and distilled water. This can produce a mirror finish with scratches < 1 $\mu$. Any imperfections prior to anodization will remain.

[6] The tip wires used in these experiments were 0.010-in.-diameter 80% Pt/Rh wire. These wires could be mechanically cut or electrochemically etched using a molten salt bath. It was found that having a higher percentage of Pt is preferable since the tip is harder and less prone to constant tip changes during the STM experiment.
Etching recipe: DC Voltage ≈ 2.5 V, Tip (+), Stainless steel electrode in salt mixture (-). Salt mixture: $NaNO_3$: NaCl = 4:1 ($KNO_3$:KCl = 4:1, may also be used). Melting point of salt bath ≈ 320° C. The current should be such that only very small bubbles are produced.

[7] 20 gauge hyponeedle, B-D Yale, Becton Dickinson & Co. Franklin Lakes, NJ 07417.

[8] The glue used is Epotec H61 ceramic single component epoxy. Epoxy Technology Inc., 14 Fortune Drive, Billerica, Mass. 01821. This epoxy requires some high temperature (~100-120° C for 2-3 hours) curing. This epoxy is available either as non-conducting (H61)or conducting (H31) silver epoxy. Do not use Torr Seal as it is not sufficiently strong and is not suitable for variable temperatures.

[9] California Fine Wire Co., Grover City, CA.

[10] These are 17 Series pins used in Amphenol D-shell electronic connectors.

[11] V. M. Hallmark, S. Chiang, J. F. Rabolt, J. D. Swalden, and R. J. Wilson, Phys. Rev. Lett. **59**, 2879 (1987).

[12] A. Stemmer and A. Engel, Ultramicroscopy, **V34**, 129 (1990).

[13] The piezoeletric transducers are capable of operating at pressures ranging up to 500+ atm before significant degradation occurs. For reference see H. H. A. Krueger and D. Berlincourt, J. Acoust. Soc. Am. **33**, 1339 (1961).

[14] Original design by J. Katz and M. Salmeron. Modified and sold commercially by RHK Technology, Inc. Rochester Hills, MI.

[15] Software developed by D. F. Ogletree. Available through RHK Technology, Inc., Rochester Hills, MI.

[16] Jotdraft Microseries etch resistant dry transfer tape, Datak Corp. 65 71st St., Guttenberg, N.J. 07093.

[17] Miccroshield, Tolber division Pyramid Plastics, Inc. a subsidiary of Michigan Chrome and Chemical Co. 220 W. 5th St. Hope, Arkansas 71801.

[18] Anodization and electroless nickel plating was carried out by the plating shop at LBL.

[19] Brushing the inertial approach tube with a slurry of Aquadag and acetone is generally sufficient. Aquadag may be obtained from Acheson Colloids Co. Port Huron, Mi.

[20] Varian Associates, Vacuum Products Division, Lexington, MA, 60 *L*/s triode ion pump.

[21] Pfeiffer Balzers, Hudson, NH, model TSH060/8290, 60 *L*/s.

[22] Research Incorporated, Minneapolis, MN, model 4085.

[23] Granville-Phillips Company, Santa Clara, CA, model 340.

[24] AMETEK Process and Analytical Instruments Division, Pittsburgh, PA. Dycor QMS model No. M200M.

[25] D. M. Zeglinski, D. F. Ogletree, T. P. Beebe, Jr., R. Q. Hwang, G. A. Somorjai, and M. B. Salmeron, Rev. Sci. Instrum. 61, 3769 (1990).

[26] Dupont Co. 0.50-in.-thick sheeting edged with 0.25-in.-thick open-cell foam weatherstrip tape, Maklanburg-Duncan Co. No. 1071-2016.

[27] T. Gritsch, D. Coulman, R.J. Behm, and G. Ertl, Phys. Rev. Lett. 63, 1086 (1989).

[28] D. Briggs, M.P. Seah, Practical Surface Analysis by Auger and X-ray Photoelectron Spectroscopy, Wiley, 1983, New York.

[29] G. Ertl, J. Kuppers, Low Energy Electrons and Surface chemistry, Verlag-Chemie, 1974, Germany.

[30] G. Ertl, J. Kuppers, Low Energy Electrons and Surface chemistry, Verlag-Chemie, 1974, Germany.

[31] M.A. Van Hove, S.Y. Tong, Surface Crystallography by LEED, Springer-Verlag, 1979, Berlin.

[32] Alpha Alumina Buehler Micropolish, 41 Waukegan Rd, Lake Bluff, IL 60044.

[33] Syntron model LP001 D, Syntron FMC Corp., Home City, Pa.

# CHAPTER 4

# ADSORBATE-INDUCED RESTRUCTURING OF PT(110)

## 4.1 Introduction

The nature of reconstructions of the (110) crystal face of platinum has been the subject of many experimental studies. The majority of these investigations were carried out in ultrahigh vacuum (UHV) environments. Low energy electron diffraction (LEED) experiments carried out on clean Pt(110) have shown the surface to be most stable in the (2x1) reconstructed arrangement [1]. A clean unreconstructed (1x1) surface can be formed, but is found to be less stable than the (2x1) surface. Ferrer and Bonzel [2] have also shown that exposing the clean (1x1) and (2x1) surfaces to hydrogen in vacuum does not change their respective morphologies. Adsorbing oxygen on Pt(110) has been shown to generate a wide range of (nx1) missing-row reconstructions, where n=2,3,5,7 [3,4]. Previous UHV studies have also shown that carbon monoxide will lift (2x1) missing-row reconstructions [5]. Impurities such as calcium and silicon have also been shown to stabilize missing-row reconstructions [6]. As a result, it is clear that adsorbates play crucial roles in the creation, stabilization, and lifting of missing-row reconstructions of the Pt(110) surface. Even so, our knowledge of the stable atomic-scale surface structure of the Pt(110) surface (and many others), while in atmospheric pressures of reactant gases, such as are used in catalytic reactions, is still rather limited. Recently, there has been some atomic-scale scanning tunneling microscopy (STM) work performed on the (110), (111), and (100) surfaces of platinum in ambient conditions; before and after heating in flowing oxygen, hydrogen, and air by Frohn et al [7]. These authors found that heating the Pt(110) crystal in 1 atm flowing oxygen at 1200 K for 2 h produced facet heights of several nanometers. However, after annealing in flowing hydrogen at 1200 K for 2 h, a

flatter surface containing some small scale structure is generated In this chapter, results will be presented from STM experiments carried out on the Pt(110) surface while under atmospheric pressures of oxygen, hydrogen, and carbon monoxide.

## 4.2 Experimental Procedure

Following cutting, orienting, and polishing the platinum (110) crystal, the sample was placed into a UHV chamber for cleaning. The UHV system is equipped with STM, low energy electron diffraction (LEED), and Auger electron spectroscopy (AES). This apparatus is currently being used for UHV STM experiments and has already been described in detail. The STM tips used throughout these experiments were mechanically cut Pt /40% Rh alloy wire, which has the advantage of being resistant to oxidation. The sample was cleaned by repeated cycles of argon ion sputtering, heating in 5 x $10^{-7}$ Torr of oxygen to 800 K, and annealing in vacuum. After the cleaning procedure, the sample was transferred in vacuum ($10^{-5}$ Torr) to the reaction chamber equipped with the HPSTM. Transferring back into the UHV chamber and analyzing by AES it was found that carbon is present on the surface, due to contamination in the limited vacuum of the transfer cell. Heating to 800 K in 5 x $10^{-6}$ Torr of oxygen, however, removed the carbon in all cases. Originally LEED showed the surface to have (2x1) periodicity. However, after numerous treatments in oxygen, the surface was converted to a very stable (3x1) structure. The (3x1) periodicity remained throughout the transfer and oxygen cleaning procedures. As the reaction cell is not equipped with surface sensitive analysis techniques except STM, it was assumed that by heating under the same conditions in the reaction cell (where the base pressure was in the $10^{-9}$ Torr range), as was done in the UHV chamber, the sample would be clean, excepting oxygen.

After removing the surface contamination (in the reactor cell) by heating in oxygen, the surface was introduced to atmospheric pressures by opening the leak valve to the desired gas and closing the gate valve to the ion pump. Analysis by a differentially pumped mass spectrometer showed that the most efficient method of switching from atmospheric pressures of one gas to another was by pumping the chamber with the turbomolecular pump to 1 x $10^{-6}$ Torr and then introducing the new gas. Since impurity levels in the compressed gas cylinders were not better than 1 ppm, it was not necessary to bake out the reaction cell before changing gases.

## 4.3 Results

### 4.3.1 The equilibrium structures of Pt(110) in $H_2$, CO and $O_2$.

After cleaning the sample in the reactor cell, the cell was brought up to 1 atmosphere of oxygen and imaged by STM. After evacuating with the turbomolecular pump, hydrogen was introduced and both the STM and sample were heated to 425 K for 5 hours. The sample was imaged before, during and after this heating treatment. Figure 4.1(a) is a topographic image taken in 1.6 atmospheres of hydrogen after the sample had cooled to room temperature. After this experiment, the chamber was again evacuated, and the sample imaged in 1 x $10^{-6}$ Torr of background hydrogen. Following this, the system was pressurized to 1 atmosphere of carbon monoxide and the STM and sample were heated to 425 K for approximately 4 hours. The sample was again imaged before, during and after this heating treatment. Figure 4.1(c) is a topographic image taken in 1 atmosphere of carbon monoxide after the sample had cooled to room temperature. The system was evacuated with the turbopump and the sample was imaged. Afterwards, the chamber was pressurized to 1 atmosphere of oxygen and the STM and sample were heated to 425 K for 5 hours. The sample was imaged prior to, during and after this heating treatment. Figure

4.1(b) is a topographic image taken in 1 atmosphere of oxygen after the sample had cooled to room temperature.

It is well known that platinum is perhaps the most versatile of all catalysts - operating on an extraordinarily wide range of reactions including oxidation-reduction and hydrogenation-dehydrogenation. The experiments described here were performed while taking advantage of this fact. In switching the reactor cell environment from oxygen to hydrogen, it is expected that any oxygen chemisorbed to the Pt(110) will subsequently react with the hydrogen to form water at room temperature. This has been known for some time and has even been used to titrate the exposed surface area of platinum [8]. From desorption studies of water on platinum and Pt(110) in particular, it is expected that by the time the reactor cell is pressurized to 1.6 atmospheres of hydrogen, any chemisorbed oxygen will have reacted and desorbed from the surface [9]. Likewise, hydrogen is known to desorb from Pt(110) at approximately 300 K. It has been shown that exposing a hydrogen covered Pt(110) surface to carbon monoxide, leads to a reduced binding energy of the hydrogen adatoms and, hence, a lower desorption temperature of hydrogen [10]. As a result, it is expected that in switching a surface from hydrogen to carbon monoxide and heating to 425 K in 1 atmosphere of carbon monoxide, any hydrogen on the surface will be replaced with carbon monoxide. It is also well known that Pt(110) is an excellent catalyst for oxidation of carbon monoxide [11]. One can expect that after switching the surface from carbon monoxide to oxygen and heating to 425 K in 1 atmosphere of oxygen for 5 hours, any chemisorbed carbon monoxide will react to form carbon dioxide and desorb from the surface, which will be saturated with oxygen. In the following sections the observed structures in equilibrium with each gas will be presented, in detail.

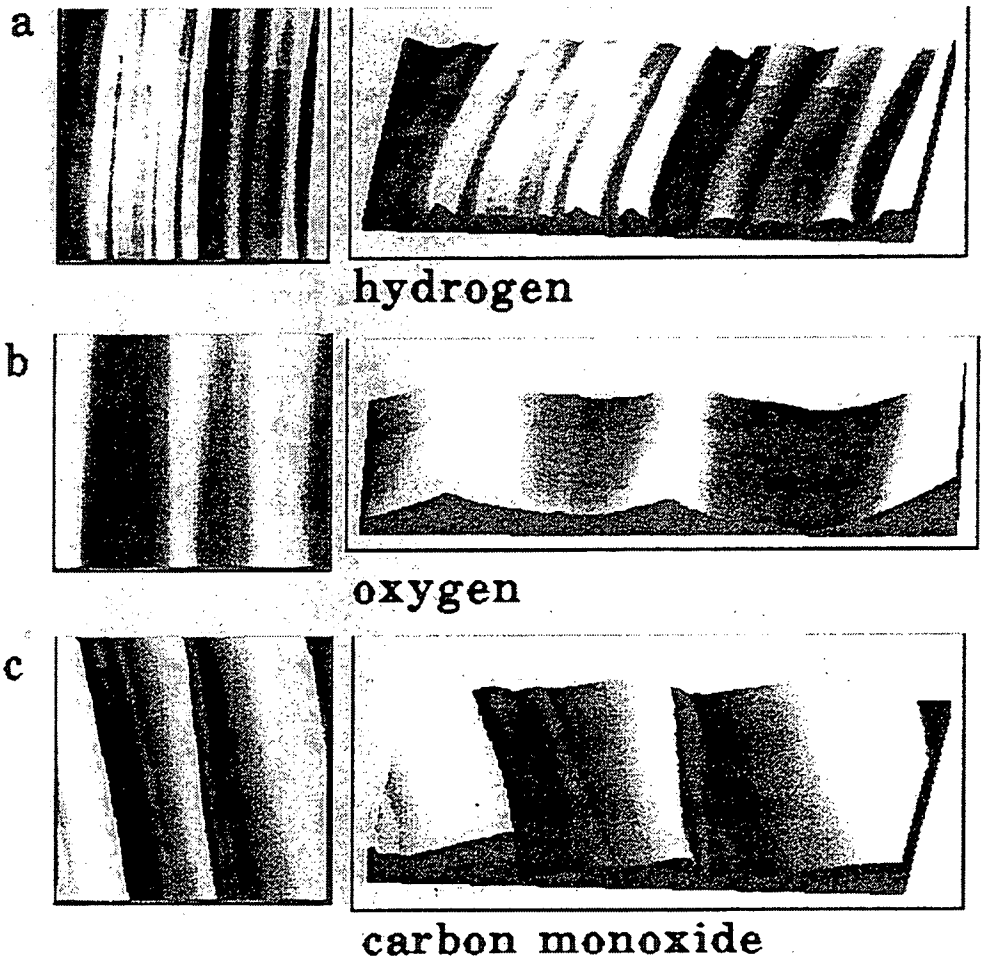


Figure 4.1. Topographic image of the Pt(110) surface in 1.6 atmospheres of hydrogen after heating to 425 K for 5 hours, showing (nx1) missing-row reconstructions randomly nested. Image size: 730 Å x 700 Å, vertical range $\triangle z$ = 10 Å. (b): Topographic image of the Pt(110) surface in 1 atmosphere of oxygen after heating to 425 K for 5 hours. Image size: 900 Å x 780 Å, $\triangle z$ = 25 Å. (c): Topographic image of the Pt(110) surface in 1 atmosphere of carbon monoxide after heating to 425 K for 4 hours. Image size: 770 Å x 740 Å, $\triangle z$ = 42 Å.

### 4.3.2 Hydrogen

The surface in hydrogen shows reconstructions of various sizes. The images consist of clearly separated parallel rows (hills) running for several hundreds of nanometers along the $[\bar{1}10]$ direction. The mean corrugation amplitudes across the channels range from to 0.3 - 0.5 Å in the (2x1) regions and 1.0 - 1.1 Å in the (3x1) regions. It was found that the distances between the maxima are always multiples of lattice spacings (except in the case of steps) and that there is a significant difference in the corrugation amplitudes of the different size reconstructions. From these two observations, one can conclude that the reconstructions must be of the missing-row type, since the asymmetric sawtooth and pairing-row type reconstructions require half-integer lattice spacings between their maxima [12]. While the corrugations of the (2x1) and (3x1) areas are always the same (within the error bar), the corrugation of the larger reconstructions often varied. After examining many different areas with domains of a specific reconstruction, it was found that the (4x1) has a corrugation of 2 Å and the (5x1) reconstruction has a corrugation of 3 Å. Careful investigation of large reconstructions with small corrugation amplitudes invariably showed the presence of monolayer steps within the channels. The images often show the surface as having nested reconstructions or areas with small domains of (2x1) or (3x1) reconstructions separated by larger reconstructions of various sizes and with no apparent order. Occasionally areas were found where one or two rows terminate abruptly and are continued by rows of a different periodicity as shown in figure 4.2(a). This figure shows the topography of a section exhibiting various typical features of the Pt(110) surface in hydrogen. It was possible to create an atomic model of the actual surface imaged by measuring both the row separation distances and the corrugation amplitudes. Considering the area of figure 4.2(a) outlined in white, this area was averaged with other

similar areas of the surface along the rows to eliminate noise, and thermal drift. This average area, shown in figure 4.2(b), was used to develop the atomic model (shown in figure 4.2(c)) of the area outlined in white in figure 4.2(a). The model shows more clearly the various (111) microfacets that are produced as a result of the varied (nx1) reconstructions.

It should be noted that the reconstructions were also stable before and during heating to 425 K for 5 hours. As well, the reconstructions were present after evacuating the reactor cell, just prior to introducing carbon monoxide.

Figure 4.2. (Following page) (a): Topographic image of the Pt(110) surface in 1.6 atmospheres of hydrogen after heating to 425 K for 5 hours, showing various sizes of (nx1) missing-row reconstructions and defects. Image size: 483 Å x 669 Å, $\triangle z$ = 15 Å. (b): Expanded area of the region outlined in white in (a), after averaging with other similar regions in the image. Image size: 305 Å x 10 Å. (c): Atomic model of the vertical profile as determined by measurement of lattice spacings and corrugation amplitudes of the reconstructions in (b).

a

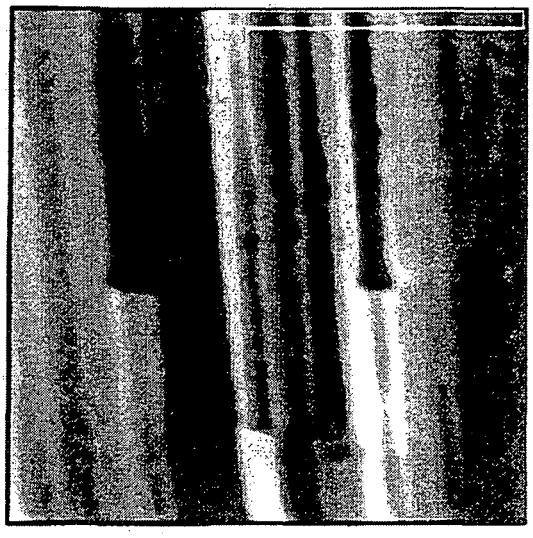

b

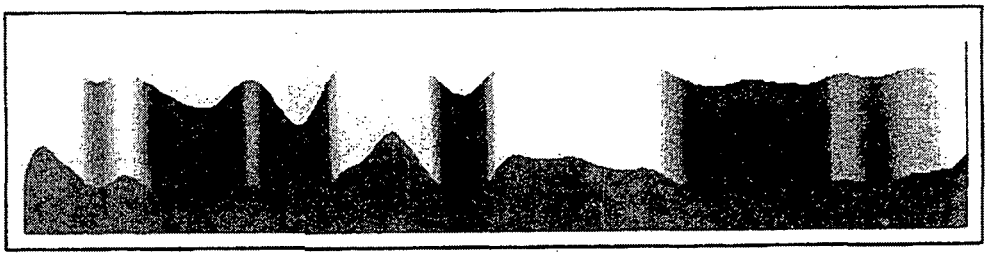

c

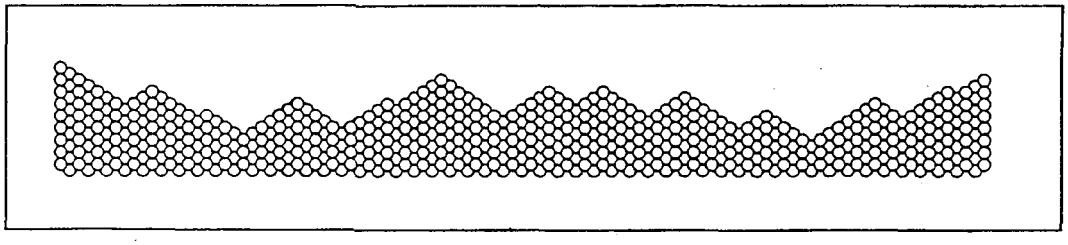

### 4.3.3 Oxygen

The surface in oxygen appears to be very different from the surface in hydrogen. Instead of the nested, small scale reconstructions, it was found that the surface is dominated by larger (100 - 300 Å) scale structures. It is likely that the larger hill and valley structure is due to enlarged (111) microfacets. For a model surface made up of (111) facets with periodicities of the scale observed in figure 4.1(a), one would expect to see a corrugation greater than 100 Å. However, these large corrugations were not observed, but rather the facets appear to be rounded, with much shallower valleys. This is likely to be the result of the tip shape being convoluted with the surface topography. Even so, the angles made by the facets are always larger than what one would expect for a surface with true (111) facets. This leads one to believe that the surface is actually comprised of enlarged (111) microfacets separated by steps which are not resolved because of tip convolution effects and the angle of the steps relative to the tip motion. If one considers a model of a reasonably sharp tip and a (110) surface made of (111) facets of various sizes, as shown in figure 4.3, the convolution effect is readily apparent. As a result, it is clear that it is possible to obtain good quality images of flat surfaces and yet have difficulty deducing the structures of moderately rough surfaces.

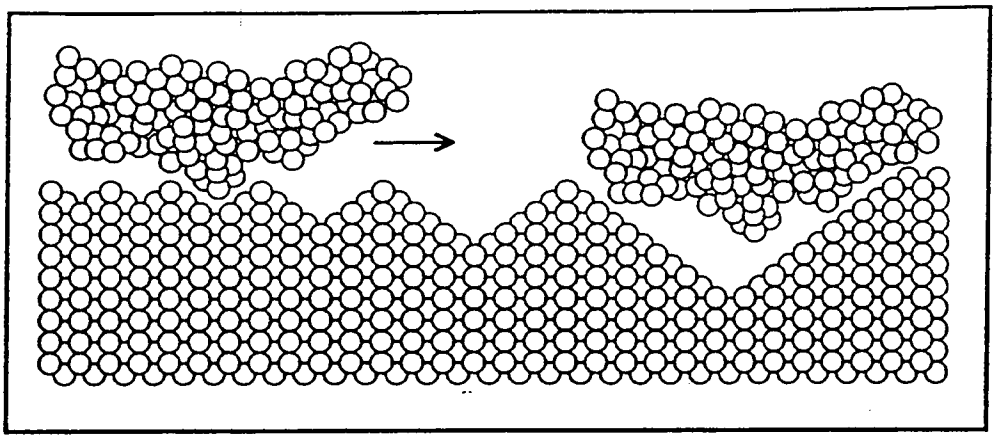

Figure 4.3. Model of tip and a (110) surface made of (111) microfacets of various sizes. For a reasonable tip geometry (~50 - 100 Å tip radius), it is apparent that the image topography may be significantly affected by tip-surface convolutions, especially as the facet size is increased.

### 4.3.4 Carbon monoxide

The surface in equilibrium with carbon monoxide is much different from either that in the presence of hydrogen or oxygen. On the scale of 1 Å to 30 Å, the surface appears to be smooth relative to the hydrogen case, showing no hints of missing-row reconstructions. The corrugation at this scale is typically within 0.3 Å . On a larger scale, features are observed, but of a much different nature than the surface in oxygen, appearing as though the surface has formed multiple height steps. This is in agreement with UHV studies, which show that carbon monoxide lifts missing-row reconstructions. In this case, it is expected that flat (1x1) terraces would be formed, separated by steps due to the displacement of platinum atoms to or from nearby terraces.

## 4.4 Discussion

### 4.4.1 Roughness comparisons

STM is an excellent tool to obtain local information, like atomic scale structure and surface roughness. However, one must be careful when describing the characteristics of an entire surface, using information obtained from small area images. Unfortunately, when carrying out the type of experiments described in the previous section, it is very difficult to be certain that one is examining the same areas under different conditions. Switching gases, heating and cooling inevitably cause disturbances in the STM experiment. One solution is to examine many different areas of the surface and compile statistics. A simple and effective way to do this with partially-ordered and disordered surfaces, is by comparing surface roughness measured from the STM images. Measurement of the geometric roughness of real systems has been rather limited. Recently, two methods

using STM have been developed to characterize rough surfaces at nanometer range and to determine the corresponding fractal dimension. The first method is based on area-perimeter determination of lakes or islands generated on STM digitized images and it has been applied to obtain the fractal dimensions of gold and platinum electrodeposits [13,14]. The second method is based on Fourier analysis of STM digitized images [15].

In this work, a somewhat simpler, modified method for three-dimensional image characterization is applied. The STM images acquired in these experiments are 256 x 256 matrices of data points that represent the height at a given position. Taking three neighboring points from the matrix and making them vertices of a triangle, one can calculate the area. By adding all these areas, it is possible to calculate the total surface area of the image. Dividing the surface image area by the scan area (or projected area), an estimate of the surface roughness is obtained. By changing the size of the triangles (the unit of measurement) and averaging neighboring data points into the vertices (thus reducing the weight of individual points), it is possible to observe how the surface roughness changes with scale, as shown in figure 4.4. The capability of observing the roughness change with scale provides additional information when comparing data sets. This is similar to the procedures described previously used to study the fractal nature of nanometer scale structures. Despite its simplicity, this method is particularly sensitive to sub-nanometer scale variances and is effective for comparing differences in atomic-scale reconstructions. Figure 4.4(a) shows the roughness versus scale (analysis area) for the three images shown in figure 4.1. As is shown, the surface in carbon monoxide appears to be the roughest of the three images. The surface in hydrogen has a significantly greater roughness on the small scale as compared to the surface in oxygen, however, on the larger scale, the surface in oxygen appears to be rougher. From the appearance of the STM images, one would expect that the surface in hydrogen would be rougher on the small scale than either the surface in oxygen or carbon monoxide. However, the image in

carbon monoxide has a corrugation amplitude of 42 Å, due to the multi-atomic steps, which is four times the corrugation of the image obtained in hydrogen and twice that of the image in oxygen. If the roughness calculation is carried out on a small area from each of these images (200 x 200 Å), which do not include steps or complete facets (in the case of oxygen), significant differences are observed (figure 4.4(b)). From this figure, the surface in hydrogen is much rougher on the small scale then it is in either carbon monoxide or oxygen. While the three images shown in figure 4.1 are representative of what is observed for the surface in the various environments, the plots in figure 4.4 primarily serve to show how the calculated roughness compares to what is found visually. This analysis technique can now be applied to a variety of images obtained in different environments and over different areas of the surface for a more analytical comparison.

In general, the roughness of the images in carbon monoxide varies significantly, due to the presence or absence of multiple height steps. The images of the surface in oxygen and hydrogen, however, are much easier to compare, as the features in these environments are consistent from image to image. As a result, it is possible to compile roughness plots of images obtained over various regions of the surface in these two environments and compare them directly (as shown in figure 4.5). From this composite plot of raw data points, it is clear that the surface in hydrogen is significantly rougher on the atomic scale than the surface in oxygen. This is due to the presence of the nested missing-row reconstructions in the hydrogen environment as compared to the large (111) microfacets in the oxygen environment.

Previous studies of oxygen on Pt(111) have shown that oxygen occupies exclusively the fcc three-fold hollow site [16]. It may be that the creation of fcc three-fold hollow sites (by forming enlarged (111) microfacets) is the driving force for this reconstruction. The surface in carbon monoxide however, does not show the small scale missing-row reconstructions but rather appears to have flat terraces separated by multiple height steps

and groups of steps. This is in agreement with UHV studies which show that carbon monoxide lifts missing-row reconstructions, generating flat (1x1) terraces. It is interesting to see that this behavior is still observed at atmospheric pressures, 9 to 12 orders of magnitude higher in pressure. Furthermore, the formation of multiple height steps and grouping of steps, indicates an attractive interaction. Finally, the fact that these surface structures are reversible upon switching between gas environments indicates that the surface is in a state of thermodynamic equilibrium.

While it is not possible to deduce from this data alone, mechanisms for these phenomena, further studies of this type will help bridge the gap that has separated until now UHV studies from catalytic and reactivity studies at normal industrial conditions.

Figure 4.4. (Following page) (a): Plot of the roughness versus scale (analysis area) for the three images shown in figure 4.1 (which are representative of what was observed for the surface in the three environments). In this plot, the surface in carbon monoxide appears to have a larger overall roughness. This is due to the presence of multiple height steps in the image. (b): Zooming in on a 200 Å x 200 Å area in each of the three images, which do not include steps (in the case of carbon monoxide) or complete facets (in the case of oxygen) and replotting the roughness versus scale provides additional information. From this figure, the surface in hydrogen is much rougher on the small scale than it is in either carbon monoxide or oxygen. This plot agrees with what is seen visually in figure 4.1.

a

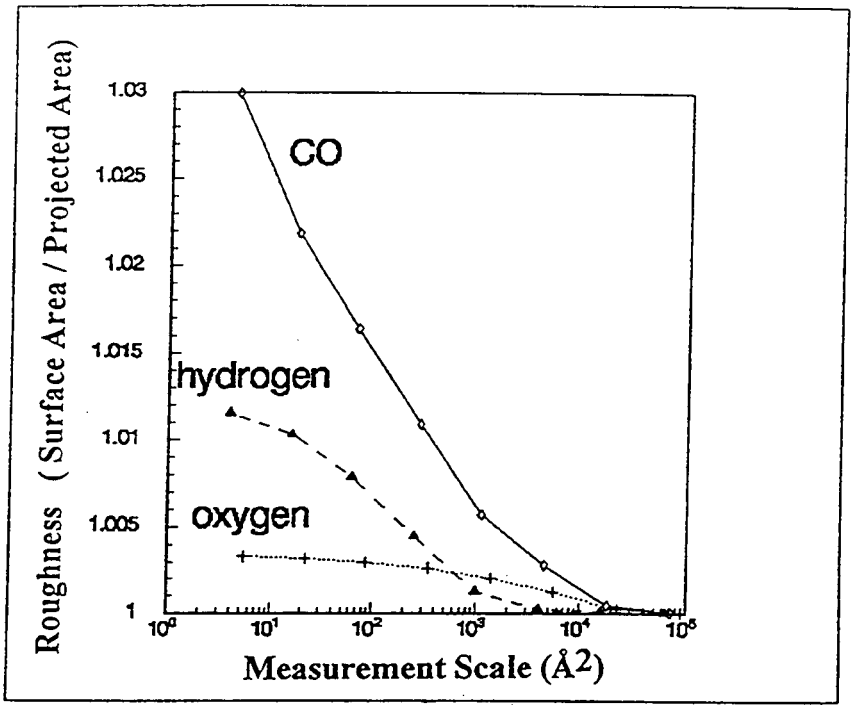
Roughness ( Surface Area / Projected Area)
1.03
1.025
1.02
1.015
1.01
1.005
1
CO
hydrogen
oxygen
$10^0$
$10^1$
$10^2$
$10^3$
$10^4$
$10^5$
Measurement Scale (Å2)

b

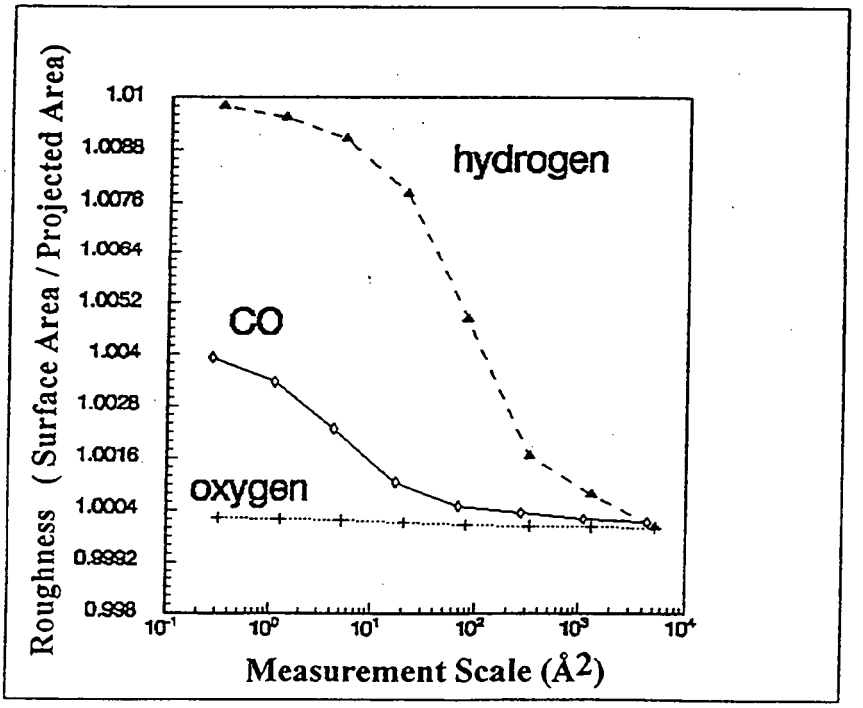
Roughness ( Surface Area / Projected Area)
1.01
1.0088
1.0076
1.0064
1.0052
1.004
1.0028
1.0016
1.0004
0.9992
0.998
hydrogen
CO
oxygen
$10^{-1}$
$10^0$
$10^1$
$10^2$
$10^3$
$10^4$
Measurement Scale (Å2)

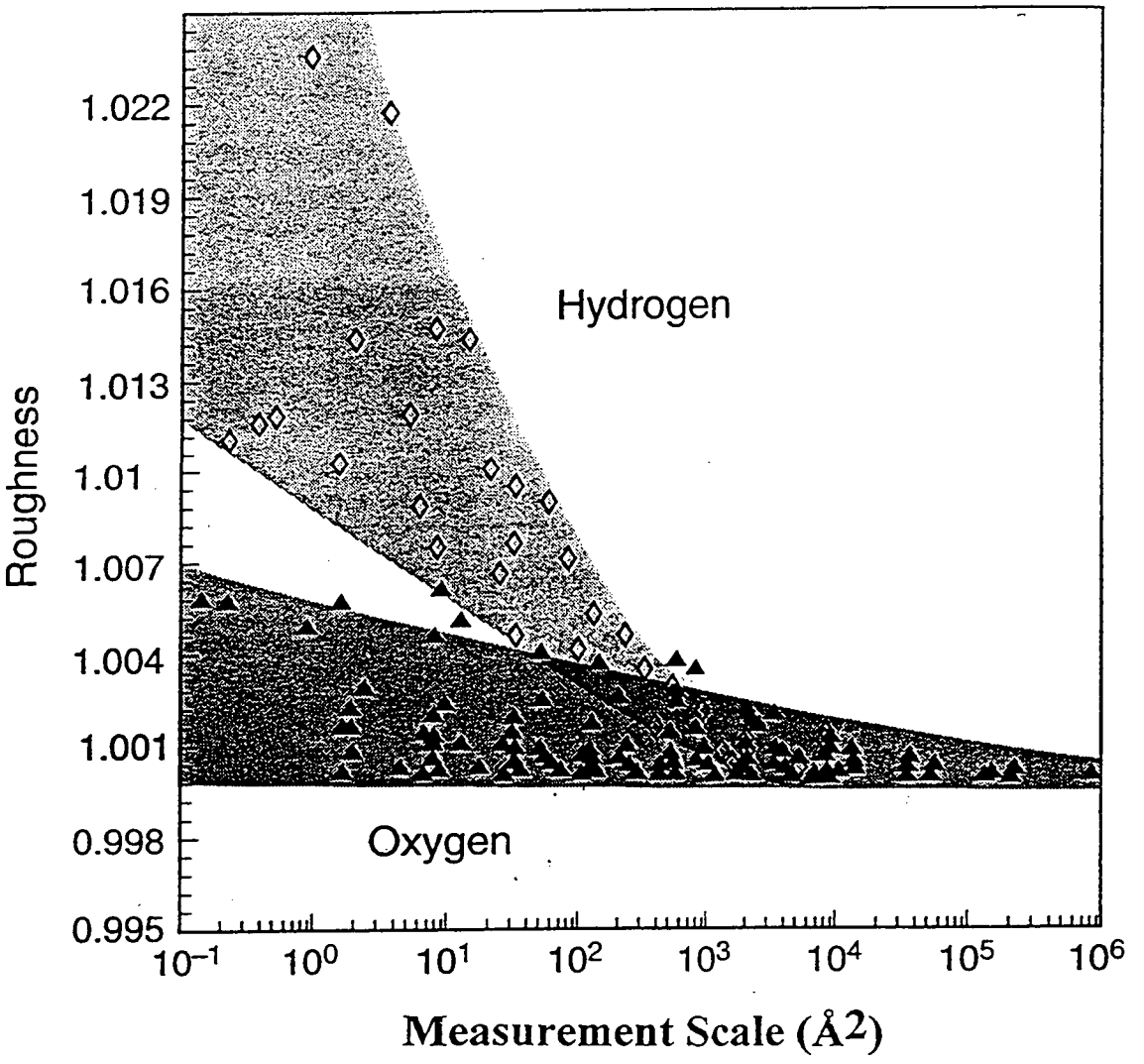


Figure 4.5 Composite (raw data) plot of the roughness (surface area / projected area) versus scale (analysis area) for 10 images obtained in hydrogen and 15 images obtained in oxygen. The images which make up this composite were obtained over various regions of the surface. From this plot, it is clear that the surface in hydrogen has significantly more small-scale structure than the surface in oxygen.

[1] P. Hofmann, S.R. Bare and D.A. King, Surf. Sci. **117,** 245, (1982).

[2] S. Ferrer and H.P. Bonzel, Surf. Sci. **119,** 234, (1982).

[3] R. Ducros and R.P. Merrill, Surf. Sci. **55**,227, (1976).

[4] M. Salmeron and G.A. Somorjai, Surf. Sci. **91,** 373, (1980).

[5] T. Gritsch, D. Coulman, R.J. Behm, and G. Ertl, Phys. Rev. Lett. **63**, 1086 (1989) and references therein.

[6] F. Masson and J.W. Rabalais, Surface Sci. **253,** 258, (1991).

[7] J. Frohn, U. Linke and K. Besoke, Prakt. Met. **26,** 518, (1989).

[8] (a) for a review up to 1980, see P.R. Norton, in : The Chemical Physics of Solid Surfaces and Heterogeneous Catalysis, Vol. 4, Eds. D.A. King and D.P. Woodruff (Elsevier, Amsterdam, 27, 1982).
(b) S. Ljungström, B. Kasemo, A. Rosén, T. Wahnström and E. Fridell, Surface Sci. **215**, 63, (1989), and references therein.

[9] J. Fusy and R. Ducros Surface Sci. **237,** 53, (1990), and references therein.

[10] J.R. Engstrom, W. Tsai, and W.H. Weinberg, J. Chem. Phys. **87,** 3104, (1987).

[11] M. Eiswirth and G. Ertl, Surface Sci. **177,** 90, (1986).

[12] H.P. Bonzel and S. Ferrer, Surface Sci. **118**, L263, (1982).

[13] J.M. Gómez-Rodríguez, A.M. Baró, and R.C. Salvarezza, J. Vac. Sci. Technol. B **9,** 495, (1991).

[14] J.M. Gómez-Rodríguez, A.M. Baró, L. Vázquez, R.C. Salvarezza, J.M. Vara and A.J. Arvía, J. Phys. Chem. **96,** 347, (1992).

[15] M.W. Mitchell and D.A. Bonnell, J. Mater. Res. **5**, 2244, (1990).

[16] K. Mortensen, C. Klink, F. Jensen, F. Besenbacher, and I. Stensgaard, Surface Science **220,** L701, (1989).

# CHAPTER 5

# UHV INVESTIGATIONS OF SULFUR ON PT(111)

## 5.1 Introduction

In order to prepare and maintain a clean surface for the HPSTM experiments, it is desirable to have a surface which can be protected during vacuum ( $<10^{-7}$ Torr) transfer from the UHV system to the HPSTM system. This is necessary because it is not possible to equip the high pressure reactor cell with surface instrumentation (aside from the STM) capable of checking surface cleanliness. One would therefore like to be able to clean the surface and then protect the surface prior to transfer, using an adsorbate that will passivate the surface, preventing adsorption of contaminants. Ideally, this passivating overlayer should be relatively easy to image with the STM, to insure the overlayer is still intact after transfer, and then easily removable once the transfer is complete.

For these reasons, sulfur was determined to be the ideal candidate for protection of the surface of interest, in this case Pt(111). Sulfur is well known to be an excellent poison of platinum under high pressure and temperature catalytic reaction conditions, strongly chemisorbing to the platinum and preventing further adsorption [1,2]. In particular, sulfur is known to block the adsorption of CO, one of the primary residual gases in the vacuum suitcase, on Pt at sulfur coverages above 0.25 monolayers [3,4]. From experiments involving the *in vacuo* transfer of the sulfur covered Pt(111) surface between the UHV system and the HPSTM system, it was found that the sulfur overlayer remained intact and ordered, and no contaminant adsorption occurred. Sulfur was also found to be relatively easy to image by STM as the ordered overlayers showed relatively large corrugations and

the sulfur atomic structure could be routinely resolved. Following transfer, the removal of the sulfur overlayer was carried out by mild heating in oxygen ($O_2$ pressures ~ 5 x $10^{-7}$ Torr or larger, and 300 °C) generating $SO_2$ which readily desorbed from the surface. This sulfur cleaning procedure was used in both UHV and HPSTM systems.

Finally, from the point of view of catalysis, the sulfur/platinum system is an interesting one, since the question of how sulfur poisons the platinum surface is still largely unresolved. For these reasons, some experiments were carried out in the UHV system and will be described in the following sections.

## 5.2 Sulfur Overlayer Structures

### 5.2.1 The Clean Pt(111) Surface

Fig. 5.1 shows the structure of the clean Pt(111) surface. The bulk crystal structure of platinum is fcc and the Pt(111) surface is a close packed face with triangular symmetry and a nearest neighbor distance of approximately 2.77 Å. Very slight ( $\leq$ 0.02 Å) variations in interlayer spacings have been observed by theoretical calculations based on LEED data [5]. The unreconstructed (111) surface of the fcc metals is considered to be particularly stable, however, as will be shown in chapter 6, the Pt(111) surface can undergo adsorbate-induced reconstructions.

The Pt(111) surface was cleaned by Ar+ bombardment and cycles of heating to 800° C in the presence of 5 x $10^{-7}$ Torr of oxygen and vacuum annealing to 800° C. Once the crystal was clean as verified by AES, it was exposed to $H_2S$ at 5 x $10^{-8}$ Torr for two to ten minutes while heating to approximately 700° C. $H_2S$ decomposes on the surface, leaving behind sulfur. After cooling the large scale ordering of the sulfur overlayer was determined with LEED, and the sulfur coverage determined with AES.

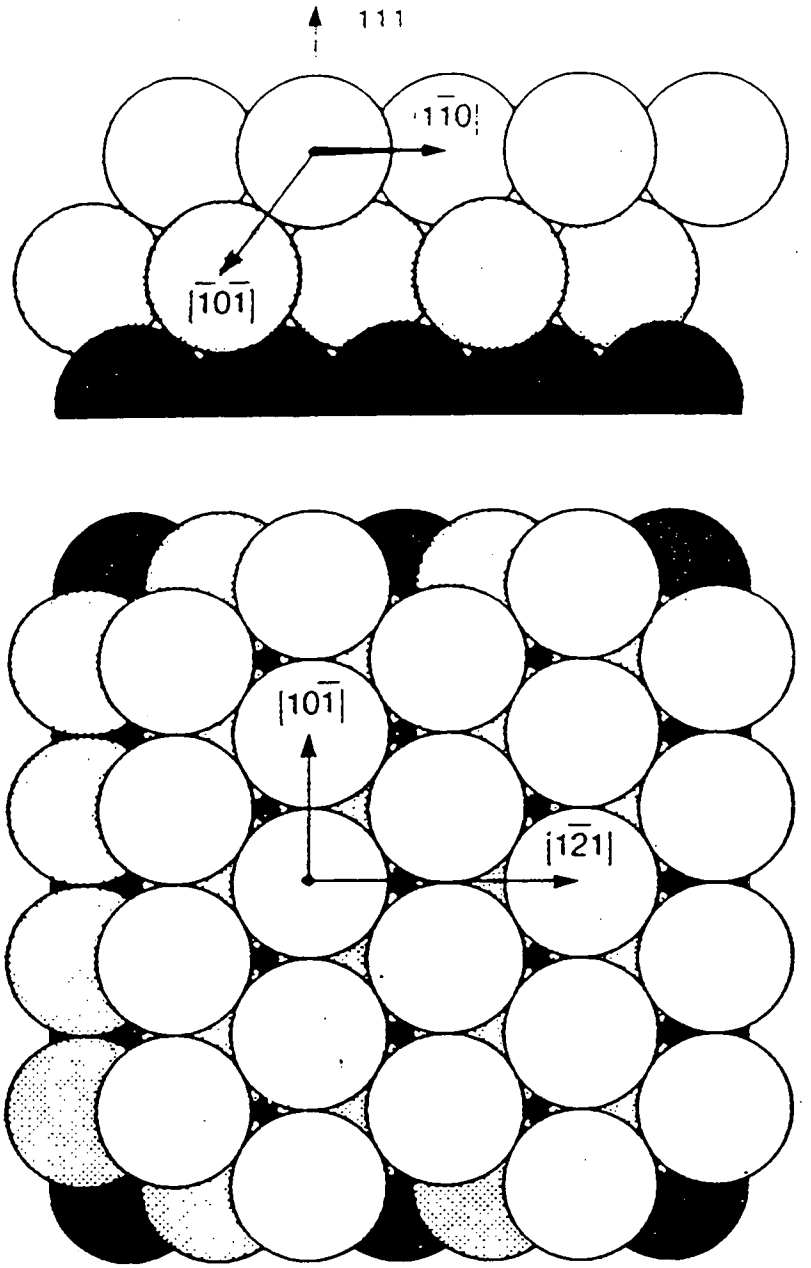


Figure 5.1. Schematic of clean Pt(111). The bulk crystal structure of platinum is fcc and the Pt(111) surface is a close packed face with triangular symmetry and a nearest neighbor distance of approximately 2.77 Å.

### 5.2.2 Low coverage ( $\theta \leq 0.25$ )

At low coverages ($\theta \leq 0.25$, where $\theta$ is the ratio of adsorbed sulfur atoms to first-layer platinum surface atoms) sulfur is known to produce a p(2x2) overlayer shown in Fig. 5.2 at room temperature [6]. STM images of the surface (Fig. 5.2) showed an array of maxima spaced at approximately 5.5 Å, consistent with a p(2x2) overlayer. Dynamical LEED calculations of sulfur on platinum have shown that at low coverages sulfur bonds at the highest coordination site [7]. On the Pt(111) surface this is the three-fold FCC hollow site.

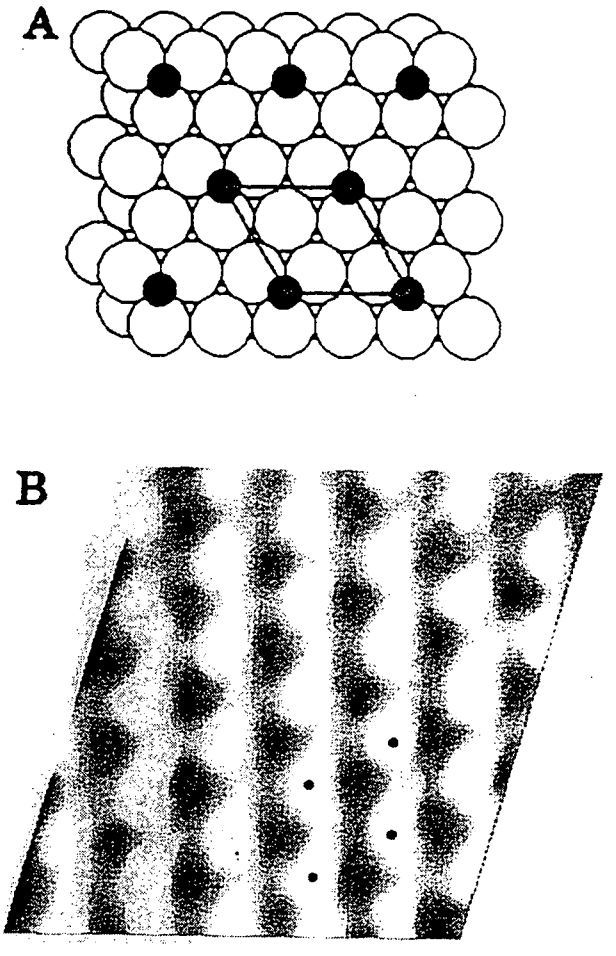


Figure 5.2.(a) Model of the p(2x2)sulfur overlayer structure on Pt(111). White circles represent the topmost layer of Pt atoms, the gray circles are the second Pt layer atoms and the black circles are sulfur atoms. The unit cell of the p(2x2) structure is marked in black.(b) Current mode STM image of the Pt(111)p(2x2)-sulfur structure. In the sulfur coverage range up to 0.25 monolayers, the STM images of the surface show an array of maxima spaced at approximately 5.5 Å, consistent with a p(2x2) overlayer.

### 5.2.3 The ($\sqrt{3}$ x $\sqrt{3}$ )R30º Phase

At coverages above 0.25 monolayers, sulfur forms the ($\sqrt{3}$ x $\sqrt{3}$)R30º overlayer shown in Fig. 5.3. A LEED analysis of the Pt(111)-($\sqrt{3}$ x $\sqrt{3}$)R30º-sulfur structure shows that sulfur bonds at the FCC site [8]. When completely covered with the overlayer, the sulfur coverage on Pt is 0.33 monolayers. STM images of the surface (Fig. 5.3) showed an array of maxima spaced at approximately 4.8 Å and rotated 30º with respect to the p(2x2) structure, consistent with a ($\sqrt{3}$ x $\sqrt{3}$)R30º overlayer.

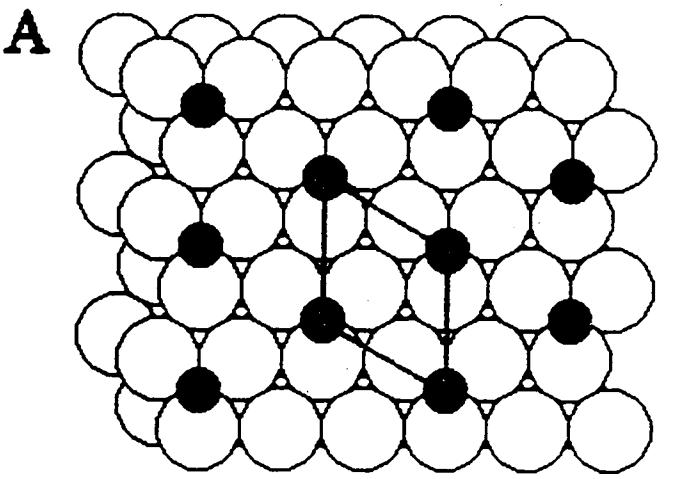


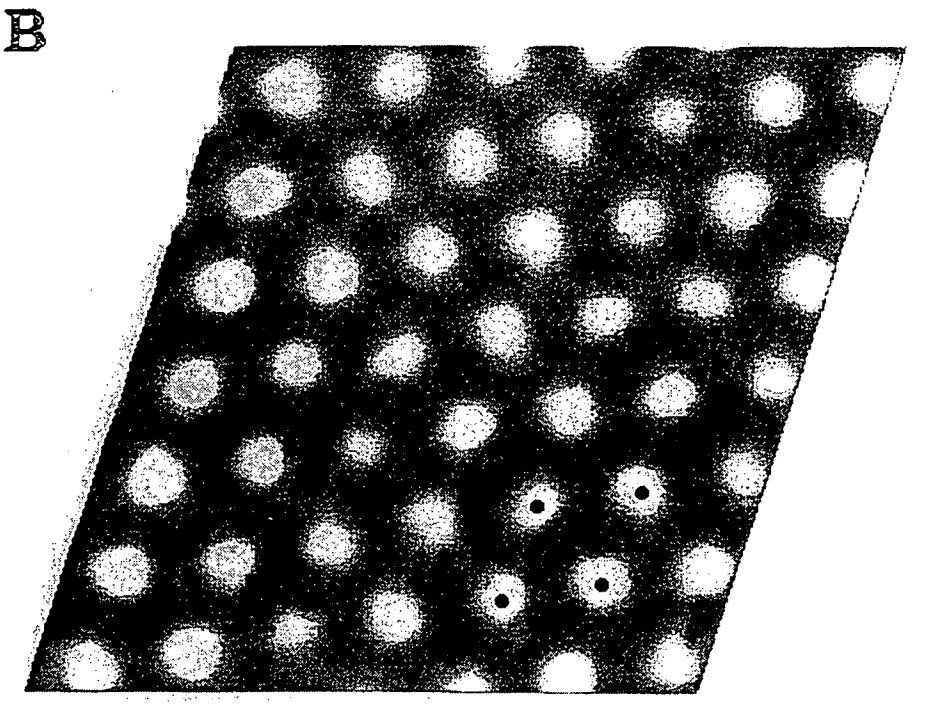


Figure 5.3. (a) Schematic and (b) current mode STM image of the Pt(111)($\sqrt{3}$ x $\sqrt{3}$)R30°-sulfur overlayer. For sulfur coverages ranging from 0.25 to 0.33 monolayers, the STM images of the surface show an array of maxima spaced at approximately 4.8 Å and rotated 30° with respect to the p(2x2) structure, consistent with a ($\sqrt{3}$X$\sqrt{3}$)R30° overlayer.

### 5.2.4 High coverage ( $\theta > 0.33$ )

It has been observed by LEED that sulfur can form an ordered structure having higher coverage than 0.33 monolayers [9] At temperatures below 100° C, the formation of a $\begin{vmatrix} 4 & -1 \\ -1 & 2 \end{vmatrix}$ structure is observed. This high coverage (~ 0.43 monolayer) structure cannot be formed with room temperature decomposition of $H_2S$ but only with an electrochemical sulfur source. This structure has three sulfur atoms per unit cell with a S-S distance of 3.94 Å (assuming a hexagonal arrangement of sulfur atoms) although the exact structure has yet to be determined. There are two other higher coverage phases that were reported by Heegemann, *et al.* Their structures were either undetermined or there was no long range order for LEED study.

## 5.3 STM tip-dependent image contrast of S/Pt(111) by controlled atom transfer

Sudden changes in the detailed appearance and corrugation of atomic-resolution STM images are commonly observed and are usually attributed to random changes in tip structure (gain or loss of atoms). These effects were observed during the course of imaging the Pt(111)($\sqrt{3}$ x $\sqrt{3}$)R30º-sulfur structure in a very controlled manner. Dramatic changes were observed in the corrugation upon controlled transfer of atoms between the tip and surface (as a result of pulsing the bias voltage). Such transfer of atoms between the tip and surface by bias pulsing has been reported previously [10]. After preparation of the Pt(111)($\sqrt{3}$ x $\sqrt{3}$)R30º-sulfur structure, the surface was imaged in UHV. A current mode STM image of the Pt(111)($\sqrt{3}$ x $\sqrt{3}$)R30º-sulfur structure is shown in Fig. 5.4(a). In this image, maxima corresponding to sulfur atoms separated by

$\sqrt{3}$ X the Pt-Pt distance are observed. A line profile from point a to point b shows the current corrugation is ~0.1 nA (Fig. 5.4(c)). After obtaining this image, a 0.7 V bias pulse was applied to three different areas of the image. The previous area was then imaged again (Fig. 5.4(b)). In this image, the sulfur atoms are much more clearly resolved, and the regions where the tip was pulsed show 6 to 10 missing sulfur atoms each. A line cross-section of Fig. 5.4(b) from point a' to point b' shows the corrugation to be greater than 1 nA (Fig. 5.4(d)).

A

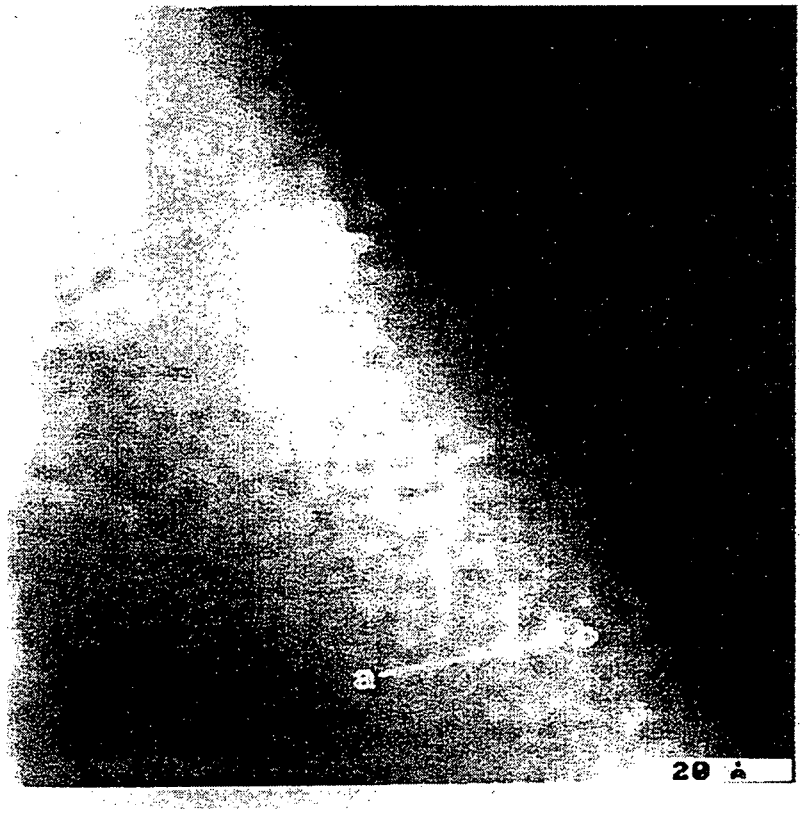


Figure 5.4.(a): Current mode STM image of Pt(111)($\sqrt{3}$ x $\sqrt{3}$)R30°-S. In this image, the sulfur atoms are resolved, however the corrugation is weak (approx. 0.1 nA) as shown in the line cross-section from point a to point b (Fig. 5.4(c)). A step runs from the top center to the bottom right of the image.

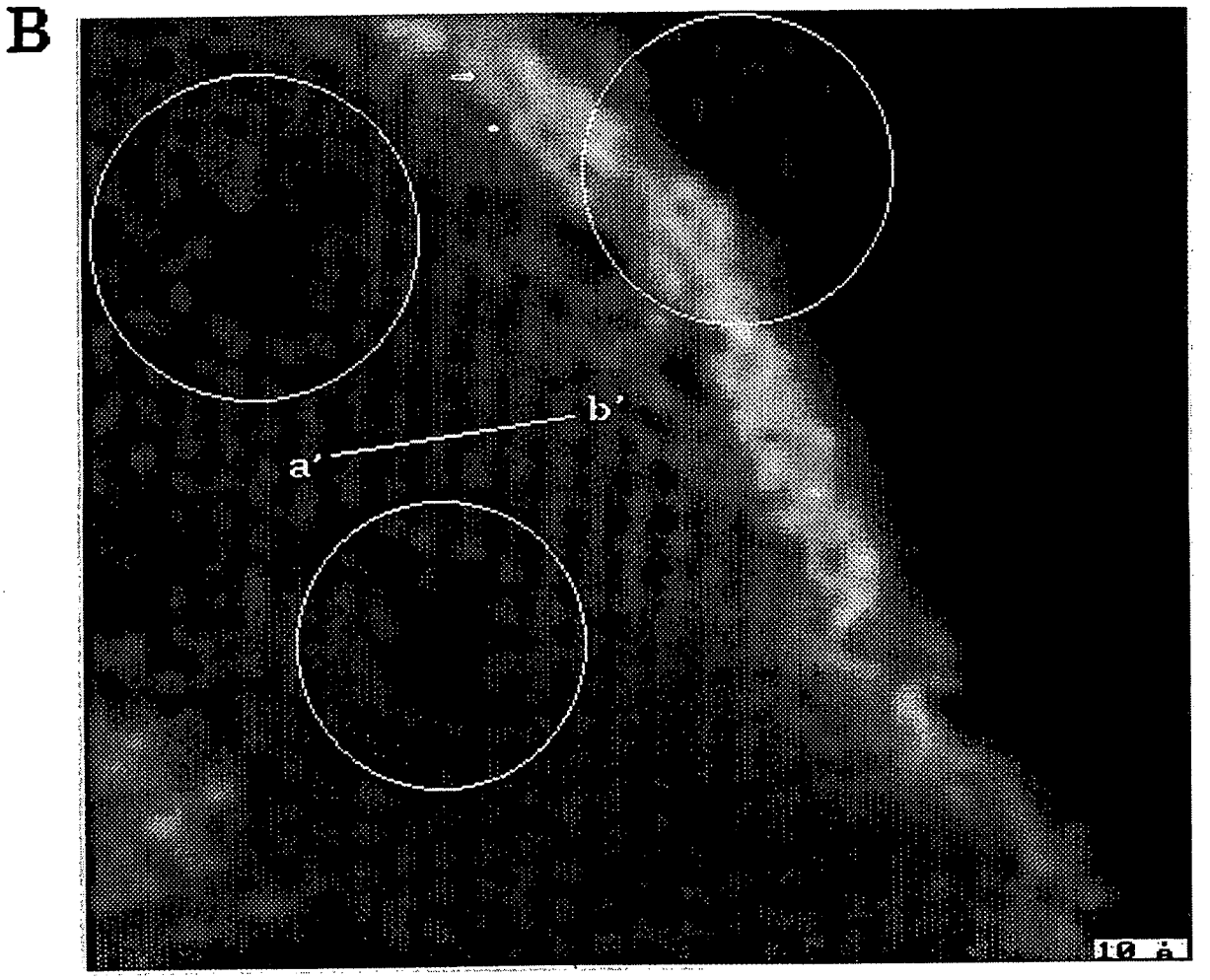


Figure 5.4.(b): Current mode STM image of the same area as (a) after applying a 0.7 V bias pulse in each of three different areas that removed 6 to 10 S atoms (circled). In this image, the sulfur atoms are clearly resolved and the three locations where the bias was pulsed show missing sulfur.

### 5.3.1 Electron Scattering Quantum Chemical (ESQC) method

To further understand the nature of the tip changes and to confirm the proposed transfer of S atoms from the surface to the tip, a calculation of the current profiles of the $(\sqrt{3} \times \sqrt{3})$R30°-sulfur structure were carried out using the Electron Scattering Quantum Chemical (ESQC) method [11,12]. In this approach, the tunneling gap is treated as a defect in a periodic bulk (tip and sample) across which electrons may propagate or be scattered back. The geometrical structure of the tip and surface is described atom by atom. The model system is comprised of two semi-infinite slabs which are generated by repetition in the z direction. One surface layer, the adsorbates and the tip consisting of a cluster are then inserted between them. The system has a finite lateral extension with lateral boundary conditions. The sample, adsorbate and tip are described by a linear combination of atomic orbitals. The description of the atoms in the bulk has been limited to 6s orbitals for simplicity, while a full spd basis set is used in the surface-adsorbate-tip part where the scattering phenomenon takes place. The energy dependent scattering matrix depends on the detailed structure of the tip, the (x,y, z) coordinates of the tip relative to the surface and the structure of the surface including atomic and molecular adsorbates. The semi-empirical Extended Hückel theory is used for the calculation of the Hamiltonian matrix elements on the chosen basis set, while all the overlap matrix elements are exactly calculated. It should be noted that none of the electronic parameters of the theory has been fitted to experimental STM images. The atomic exponents are obtained from Hartree Fock calculations on the atom while standard atomic energies are used. The gap resistance is derived from the scattering matrix with the Landauer formula using a zero bias voltage approximation. Previous studies using this theoretical approach have shown that the image structure is strongly dependent on the chemical identity of the terminating STM tip atom [13,14].

### 5.3.2 Results and Discussion of ESQC calculations for S/Pt(111)

The corrugations obtained after applying the theory to the sulfur/platinum case are shown by the dashed lines in Fig. 5.4(c) and (d) for tips terminated in Pt and S respectively. The observed changes in the corrugation of sulfur in these images can thus be explained by changes from the platinum-terminated to sulfur-terminated STM tips as shown by the good agreement with theoretically simulated STM corrugations. These results suggest that sulfur is indeed being transferred from the surface to the tip upon bias pulsing resulting in the dramatic changes in corrugation. The origin of the differences in corrugation between S and Pt tips can be qualitatively understood by considering the overlap between tip atom orbitals and the orbitals of the S atoms in the $(\sqrt{3} \times \sqrt{3})R30^{\circ}$-structure. The 6s external orbitals of Pt atoms extend farther out in space than the smaller S atom 3s and 3p orbitals. As a result of the more extended overlap, the topographic profiles, or the changes of current in constant height images show much smaller corrugation. From these experiments it was found to be possible to distinguish between two classes of single-atom tips: electronically large metal (Pt, Rh, W, or Re) atoms and smaller main group S or C atoms. Generally, only small quantitative differences were observed within each class. The ESQC method has previously been used in the case of S on Re(0001) [15]. The novelty of the experiments described here is the intentional removal of S atoms from the surface by pulsing and their transfer to the tip. Since this is done during the course of the same experiment, relatively quantitative comparisons between observed and calculated corrugations have been possible.

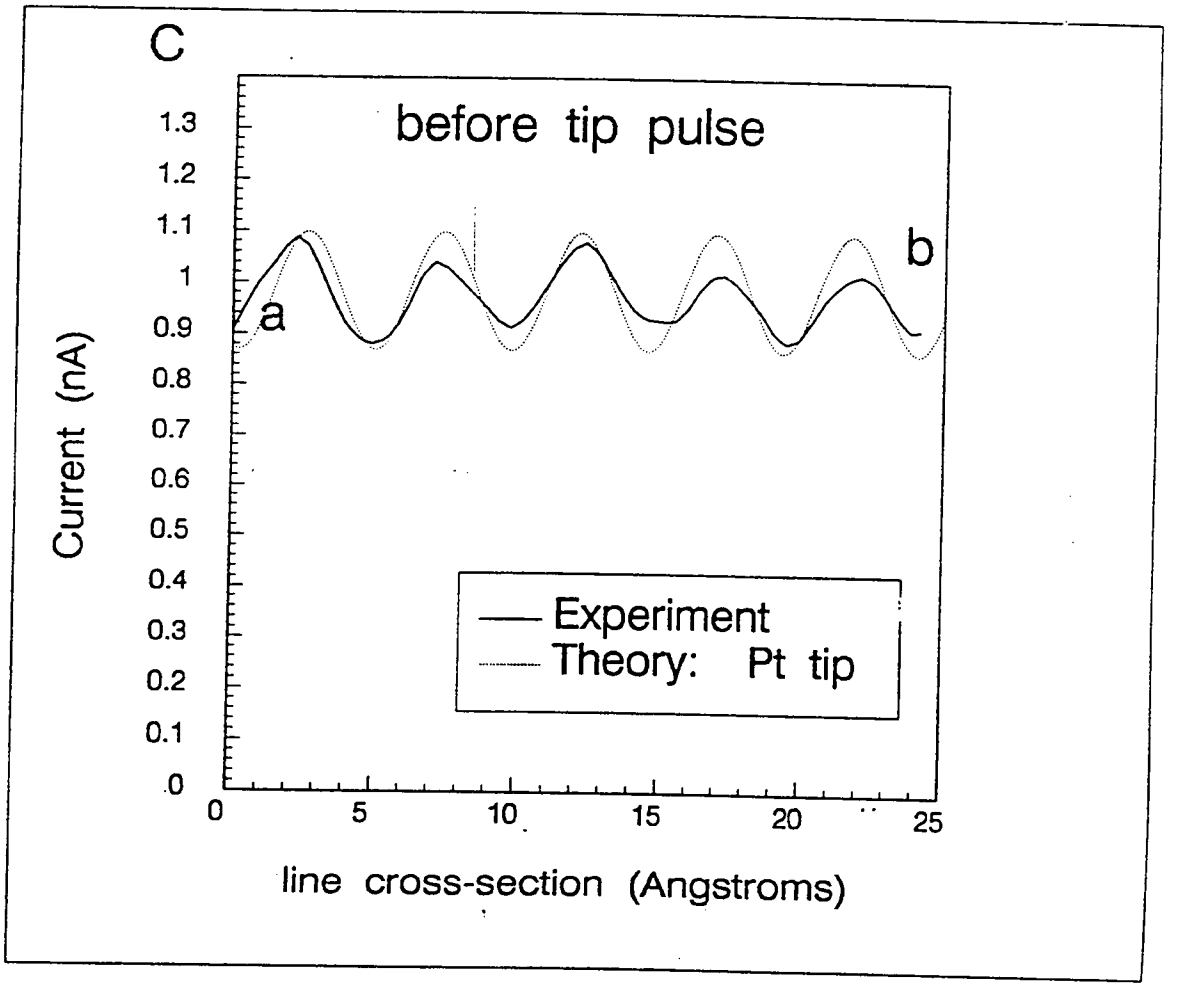


Figure 5.4.(c): Line cross-section of Fig. 5.4(a) from point a to point b, showing the corrugation to be ~0.1 nA. The dotted line shows the calculated corrugation profile for tips terminated in a single Pt atom.

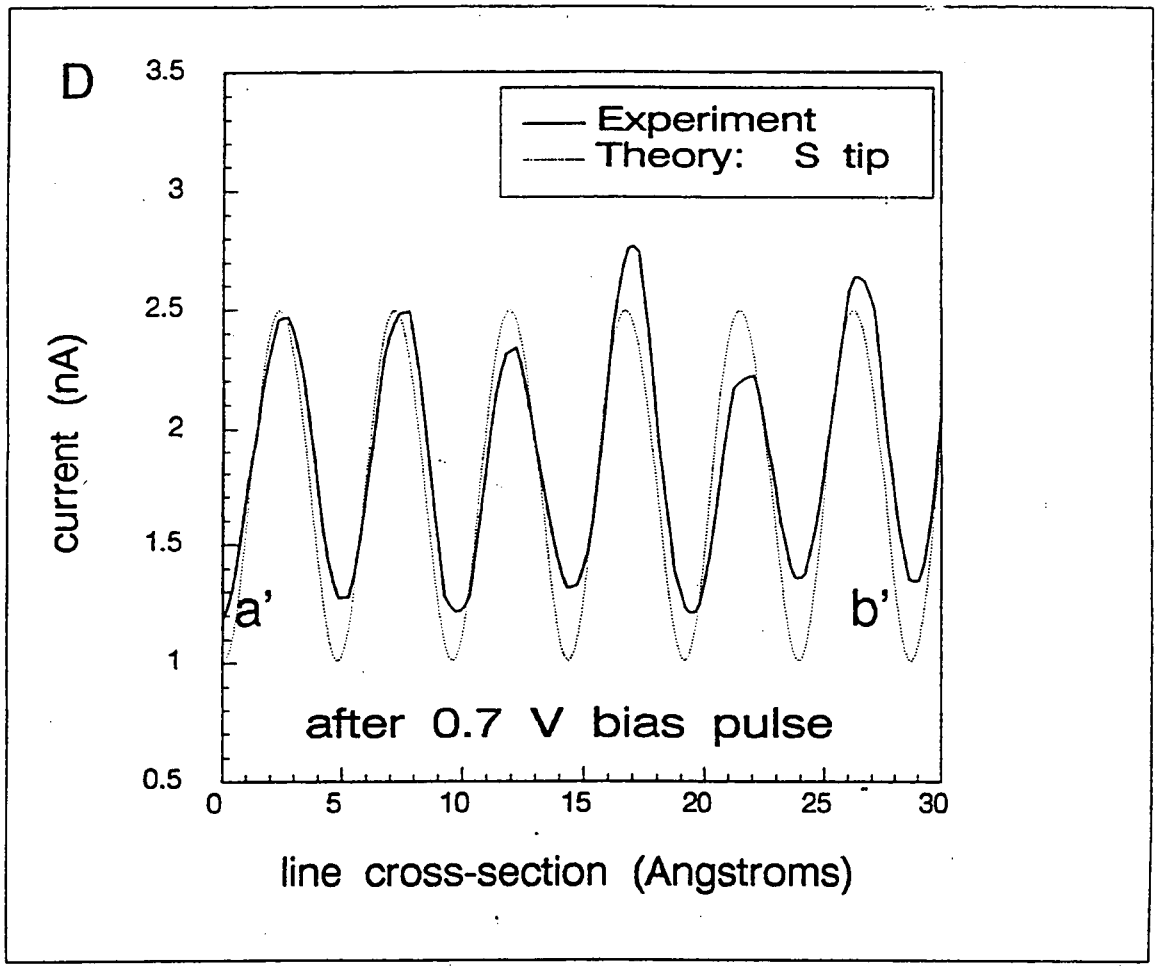


Figure 5.4.(d) Line cross-section of Fig. 5.4 (b) from point a' to point b', showing the corrugation to be greater than 1 nA. The dotted line shows the calculated corrugation profile for tips terminated in a single S atom.

### 5.3.3 Anisotropies in STM image contrast

The calculated images in the previous section all assumed that the STM tip was terminated with a single atom. After examination of images calculated using a tip terminated with a Pt, S, or C atom (see Fig. 5.5) it is clear that the general appearance of the images show a very similar ball-type contrast. In fact, the only way to tell these images apart is by analysis of their corrugations (Fig. 5.6). From hundreds of experiments on the $(\sqrt{3} \times \sqrt{3})R30^{\circ}$ sulfur structure, that two general classes of image corrugations were observed, 'low corrugation' ($\approx$ 0.1 Å) and 'high corrugation' ($\approx$ 0.4 Å). ESQC calculations with Pt, C, and S single-atom tip terminations showed two distinct ranges in corrugation that matched very well with what was observed experimentally, (see Fig. 5.6).

Over the course of numerous STM experiments on the $(\sqrt{3} \times \sqrt{3})R30^{\circ}$ sulfur structure, it became clear that the $(\sqrt{3} \times \sqrt{3})R30^{\circ}$ periodicity could be observed to have a wide variety of contrasts other than the simple ball-type structure (which is most commonly observed). Fig. 5.7 shows a compilation of some of the experimental images which clearly resolve the $(\sqrt{3} \times \sqrt{3})R30^{\circ}$ periodicity but have dramatically differing contrast mechanisms. In these images, the periodicities are no longer observed as ball-type structures but as hexagons, distorted crescents, and even asymmetric structures.

These novel image contrasts can be understood when considering the influence of the tip structures. It is likely that when the STM tip is terminated in two or more atoms whose distances from the surface are nearly the same, then both will contribute significantly to the image contrast. As a result, the image contrast is likely to be orientationally dependent on the multiple atom tip structure. For example a dimer atom tip is likely to produce an asymmetric image whose contrast is maximized when the sum of the tunneling channels from both terminal tip atoms is greatest. This type of image

convolution significantly complicates attempts at obtaining crystallographic information from STM images. Currently work is under progress using such theoretical tools as ESQC theory to deconvolute this information and ultimately extract structural information from experimental STM images. One example of a theoretical calculation for the ($\sqrt{3}$ x $\sqrt{3}$)R30º sulfur structure on Pt(111) is shown in Fig. 5.8. This calculation was made using a three-Pt atom tip termination and shows a significantly different image contrast compared to single-tip atom terminations.

Figure 5.5. (Following page) ESQC calculated images of the ($\sqrt{3}$ x $\sqrt{3}$)R30º sulfur structure using three different single atom tip-terminations (S, C, and Pt).

Image contrast: expt. vs. theory - ball structure of Pt(111)($\sqrt{3}$ x$\sqrt{3}$)R30° Sulfur.

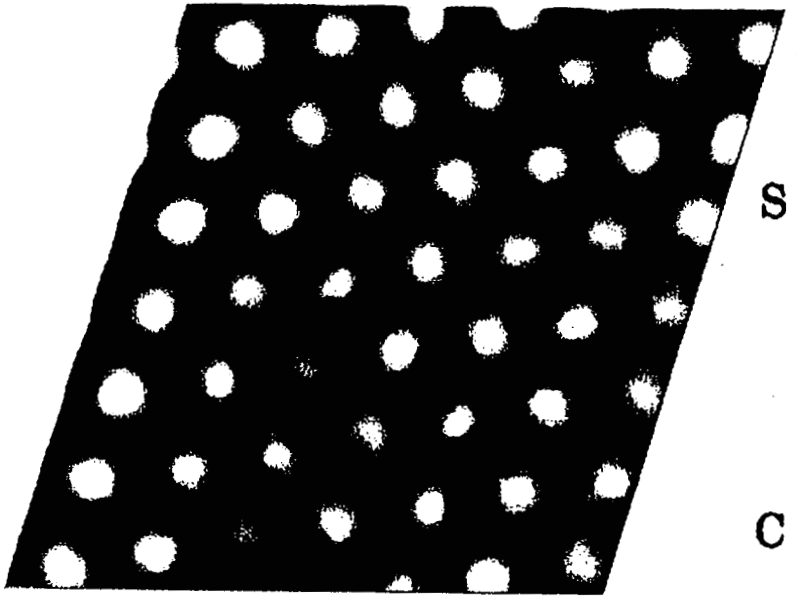

Experiment

Theory: single atom tips.

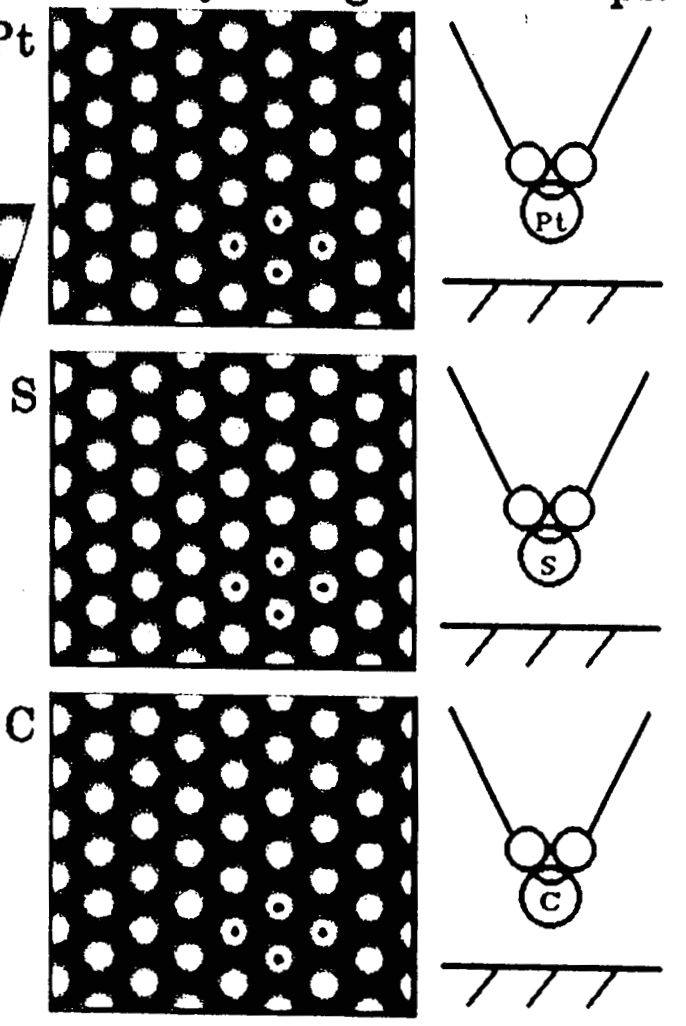

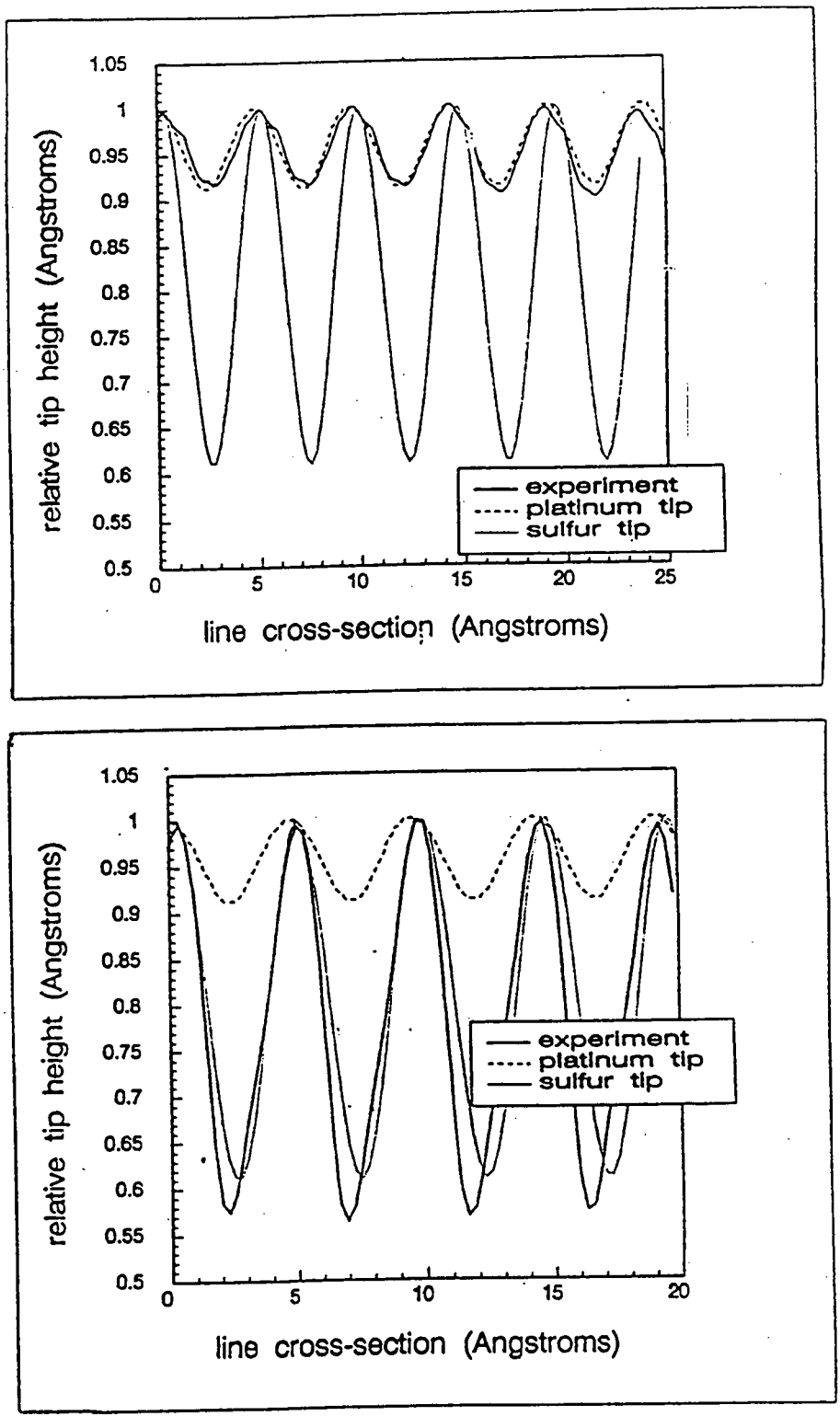


Figure 5.6. Comparison between experimental and calculated topographic corrugations for Pt(111)($\sqrt{3}$ x $\sqrt{3}$)R30° sulfur.

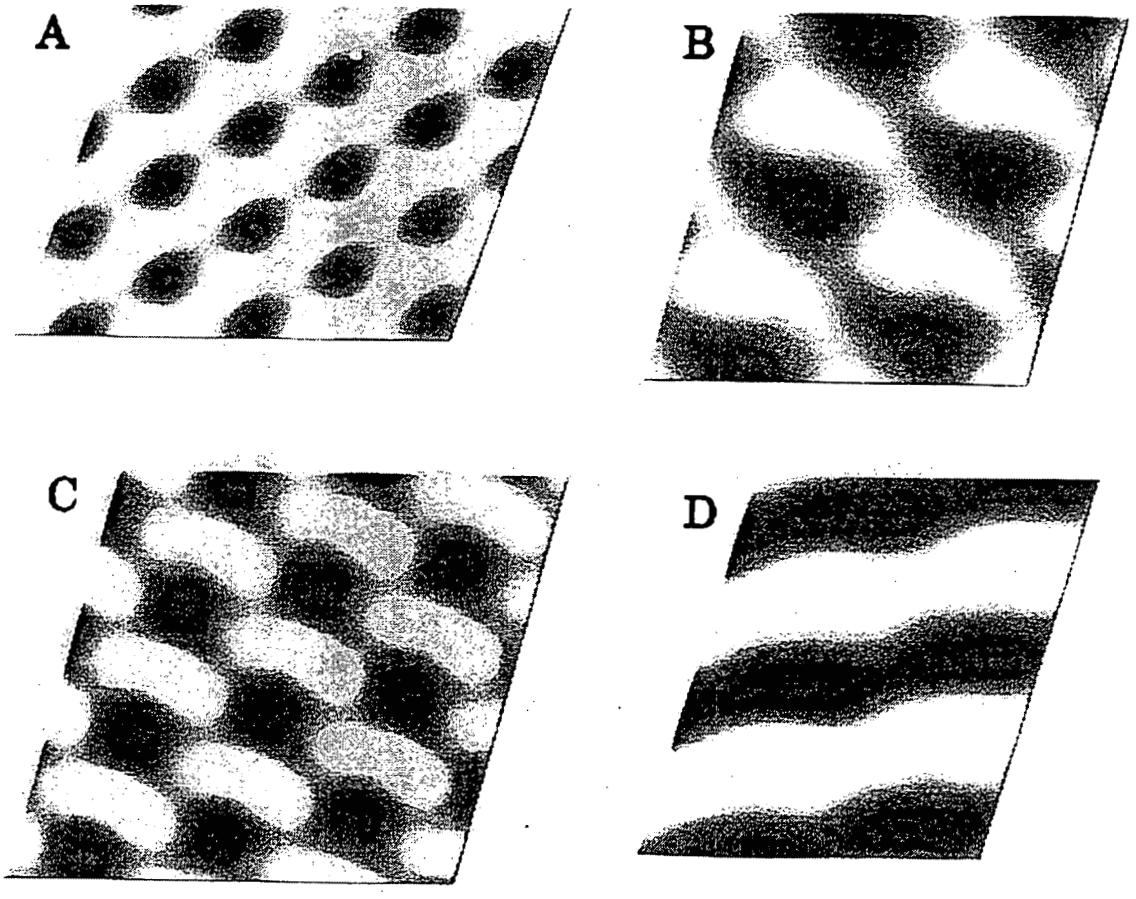


Figure 5.7. Compilation of some experimental contrasts for the ($\sqrt{3}$ x $\sqrt{3}$)R30º sulfur structure.

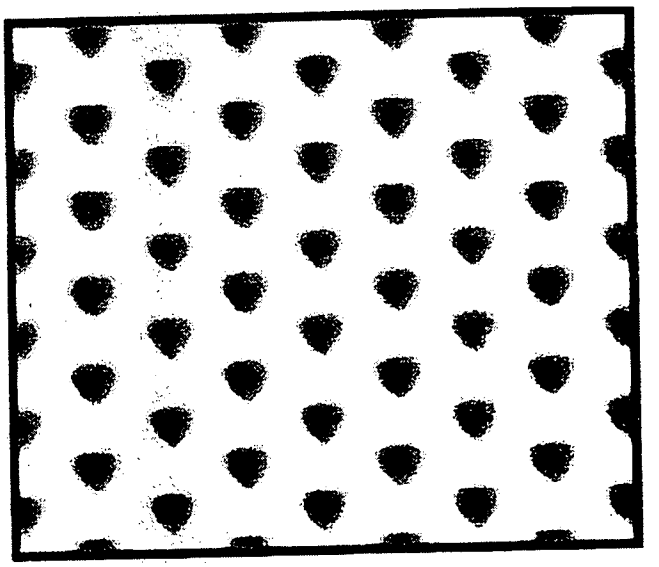

Figure 5.8. ESQC calculation for a three-Pt atom tip termination. This calculated image demonstrates the strong contrast dependence on the tip structure.

## 5.4 STM investigation of vacancy diffusion on Pt(111)

Understanding how atoms and molecules move around on surfaces is very important when attempting to answer even the most basic of questions related to surface chemistry and catalysis. The application of STM to study the diffusion of surface adatoms has been demonstrated recently [16,17,18,19]. In these studies, it has been shown that it is possible to directly observe the hopping of atoms in sequential images for systems where the surface diffusion is relatively slow. In cases where the diffusion rates are faster than the time between two images it has been shown to be possible to extract quantitative information from diffusion related 'noise' by use of a spatial correlation function [20,21].

The results described in this section show that it is also possible to monitor vacancy diffusion. This is done by measurements of changes of vacancies occurring in ordered adsorbate structures. This kind of information is of significant interest as the diffusion rates are likely to be different than the more common measurements of single atom diffusion rates as are carried out by such techniques as field emission (FEM) or field ion microscopy (FIM). The STM measurements described here are, in a sense, the inverse of the measurements made by FIM or FEM since what is measured in this case is the diffusion of vacancies within a sea of adsorbates. This measurement has an interesting property in that adsorbate-adsorbate interactions are inherently taken into account. As a result, this type of diffusion information is of significant interest in relating to surface chemical processes in terms of understanding how atoms and molecules diffuse around on surfaces which are covered with adsorbates.

In section 5.3, it was observed that 'holes' could be created in the sulfur overlayer by applying small bias voltage pulses. In image 5.4, the tip was pulsed in three different areas of the surface and the removal of sulfur atoms were detected upon subsequent scans. Following the hole structures with time, it was observed that they fill in. This is due to

diffusion of point defects from the holes to the edges of the terraces. In this image it was observed that the two holes located toward the top of the image filled in very rapidly. This is likely the result of their proximity to step edges (which opens the intriguing possibility of performing a systematic study of site specific diffusion). The hole in the bottom center of the image is more stable. A sequence of images taken over a time period of minutes show this hole is filling in (Fig. 5.9). By careful examination of several images of this hole one can estimate the rate the hole is being filled in and by applying an Arrhenius relation with a standard pre-exponential factor of $10^{13}$, a diffusion energy of ~ 0.89 eV is obtained. This value is comparable to previous studies of sulfur diffusion on metal surfaces [22,23].

Figure 5.9. (Following page) Sequence of current mode images of the bottom center hole created in Fig. 5.4. After a period of a few minutes, the hole is observed to have filled in significantly. By analysis of the rate of the hole filling, an estimation of the diffusion barrier can be obtained.

## Atomic-scale manipulation and adsorbate diffusion.

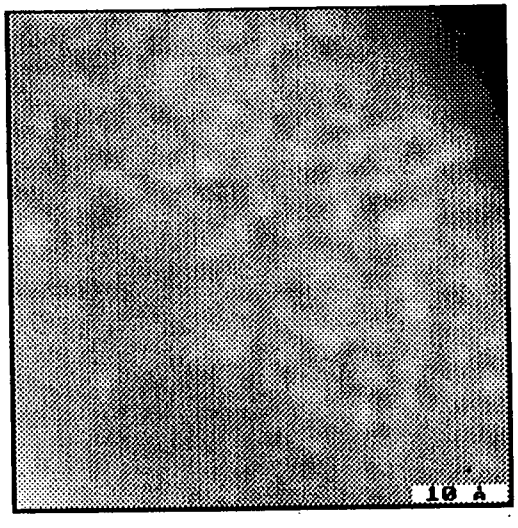


Before tip pulse

After 0.7 V pulse

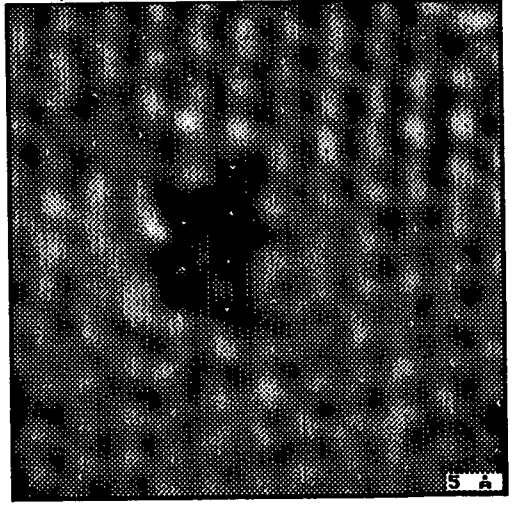


2 minutes later...

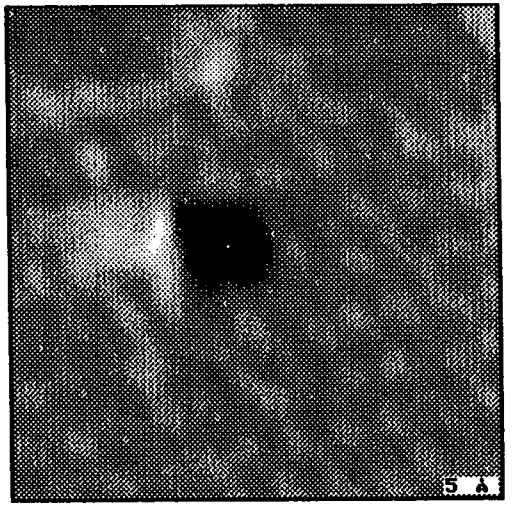

## 5.5 Coadsorbate-induced compression of sulfur overlayers on Pt(111) by CO

One of the puzzles of heterogeneous catalysis carried out on transition metal surfaces is that the active metal is usually covered with a strongly chemisorbed overlayer that does not participate in the catalytic turnover. During ammonia synthesis ($N_2 + 3H_2 \Rightarrow 2NH_3$) iron catalyst surfaces are covered by a monolayer of chemisorbed nitrogen [24]. During hydrocarbon dehydrogenation reactions (for example, cyclohexane $\Rightarrow$ benzene + $3H_2$) on platinum, the surface is covered by a carbonaceous deposit of CH or $C_2H$ stoichiometry [25]. Also, during the hydrodesulfurization of thiophene (thiophene $+2H_2 \Rightarrow$ butadiene + $H_2S$) the molybdenum or rhenium surfaces are covered by sulfur [26]. Isotope labeling studies of the atoms in the chemisorbed overlayer ($^{14}C$ and $^{35}S$) indicate that the molecules participating in the catalytic reaction turnover $10^4$ - $10^6$ times before the atoms in the topmost overlayer desorb. How is it possible that reactions characteristic to a given transition metal can occur while its surface is covered by atoms that do not participate in the reaction?

One mechanism which could explain this phenomenon is the temporary local displacement of the non-reactive adsorbate in order to accommodate the adsorption of the reactants. Once the catalytic reaction of these adsorbates is completed, the reaction products could desorb and allow the inert layer to re-expand, covering the surface. In this section evidence will be presented for such a mechanism with a model system composed of an inert chemisorbed layer of sulfur and a weakly bound adsorbate molecule of CO on the Pt(111) surface.

In these experiments it was observed that exposure of the lowest coverage ordered sulfur structure (p(2x2)) on Pt(111) to CO induces compression of the sulfur layer to a structure associated with a higher local coverage and CO chemisorbs in the holes created

in the sulfur layer. The reordering was observed by both a change in the LEED pattern and by real space STM imaging of the surface. After exposure to CO the new overlayer had $(\sqrt{3} \times \sqrt{3})R30^{\circ}$ symmetry. There was no increase in the amount of sulfur on the surface during this reordering. The overlayer could be returned to the original p(2x2) by annealing for several seconds at 600° C, during which the CO desorbed and sulfur atoms reoccupied the vacant metal sites.

### 5.5.1 CO adsorption on Pt(111)

CO adsorption on the Pt(111) surface has been the subject of many studies using a great variety of experimental methods. CO populates sequentially terminal and two-fold bridge sites and forms a diffuse $(\sqrt{3} \times \sqrt{3})R30^{\circ}$ LEED pattern for $T \leq 160$ K at CO coverages around 0.33 monolayer [27,28]. More recent studies show two complex and well ordered LEED patterns and an intermediate pattern at coverages of 0.17 and 0.33 monolayer with $T \approx 100$ K [29]. In the coverage range above 0.33 monolayer CO forms a c(4x2) pattern (0.50 monolayer), and a series of other complex LEED patterns at CO coverages ranging from 0.50 to 0.66 monolayer [30,31]. The adsorption energy of CO on Pt has been measured to be approximately 1 eV per molecule [32].

Because sulfur is known to block the adsorption of CO on Pt at coverages above 0.25 monolayers [33], the sulfur overlayer must be compressed in order for CO to adsorb.

### 5.5.2 LEED coadsorption results

After preparing the p(2x2) overlayer on the Pt(111) surface, a sharp p(2x2) LEED pattern is obtained as shown in Fig. 5.10(A). The crystal was then exposed to $1 \times 10^{-8}$ Torr of CO. Figure 5.10 (B-E) shows a time-lapsed series of LEED patterns while the surface is exposed to CO. (B) was taken after 5 minutes of exposure and shows dimming

of the p(2x2) spots. After 15 minutes, the $(\sqrt{3}X\sqrt{3})R30°$ spots begin to appear, coexisting with the p(2x2) spots, as shown in (C). Eventually, the p(2x2) spots disappear completely, and only the $(\sqrt{3}X\sqrt{3})R30°$ LEED pattern is observed ((D) -after 40 minutes). After about 65 minutes the $(\sqrt{3}X\sqrt{3})R30°$ pattern is very sharp (E). Annealing to 600° C restores the surface to its original p(2x2) structure as shown in (F). The sulfur coverage on the surface, as measured by AES, was unchanged during the transition. While CO is known to form a diffuse LEED pattern having a symmetry similar to the $(\sqrt{3}X\sqrt{3})R30°$ pattern at low temperatures, it is expected that because of the sharpness of the diffraction spots, the disappearance of the p(2x2) pattern, and STM images of the subsequent $(\sqrt{3}X\sqrt{3})R30°$ structure, only the rearrangement of the sulfur atoms on the surface is being observed. The time required for the transition depends on the sulfur coverage and CO pressure, with the longest times corresponding to coverages closest to a full quarter monolayer and lowest CO pressures.

Figure 5.10. (Following page) Evolution of the LEED pattern of the S covered Pt surface during exposure to 1 x $10^{-8}$ Torr of CO. A) Initial p(2x2) LEED pattern. B) after 5 minutes of exposure. C) after 15 minutes of exposure the $(\sqrt{3}X\sqrt{3})R30°$ spots begin to appear, coexisting with the p(2x2) spots. D) The LEED pattern after 40 minutes. E) after 65 minutes, the $(\sqrt{3}X\sqrt{3})R30°$ LEED pattern is very sharp. F) After annealing to 600° C for several seconds the CO desorbs and the original p(2x2) LEED pattern is observed.

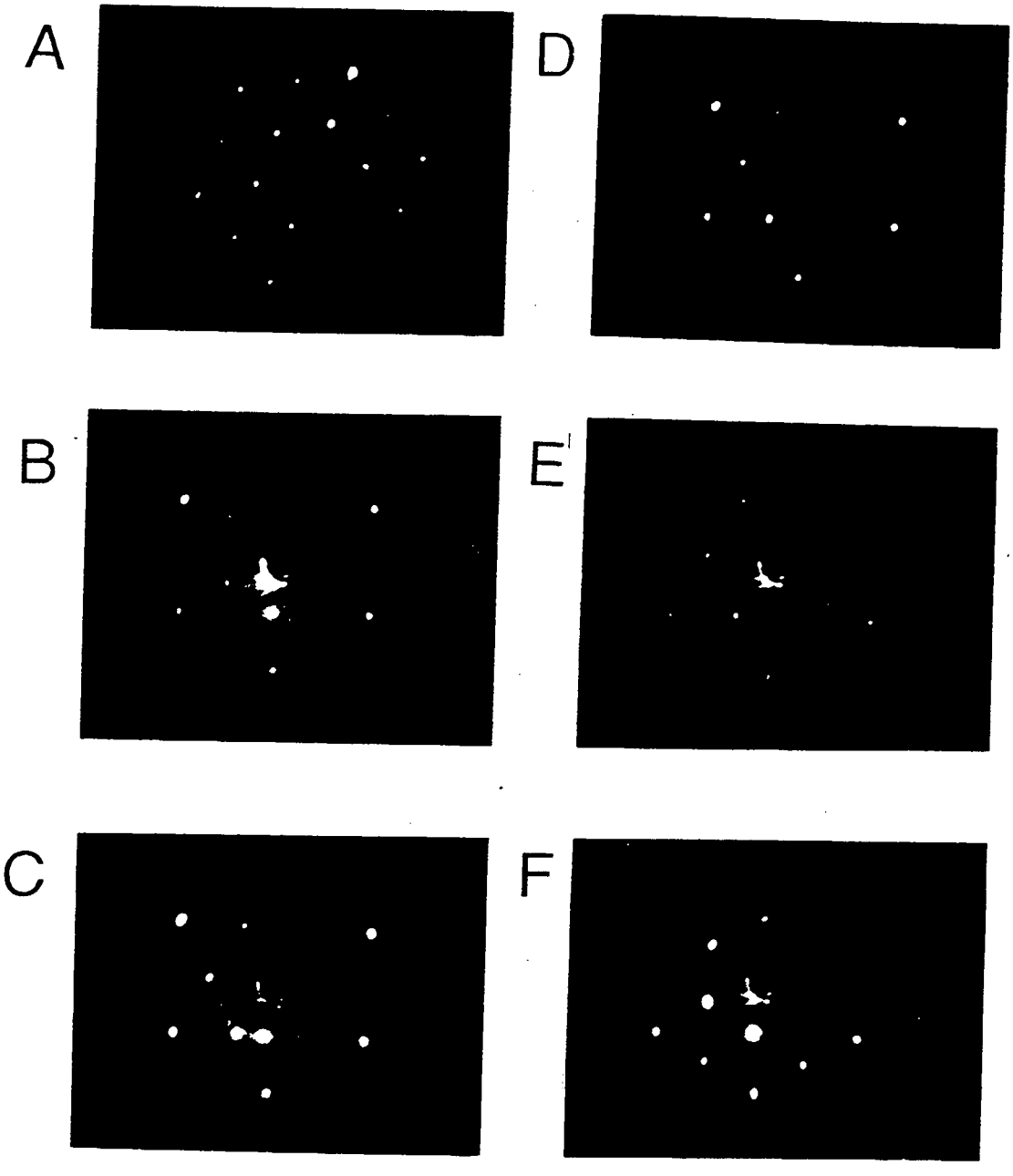
A
D
B
E
C
F

### 5.5.3 STM coadsorption results

The reordering of the sulfur due to CO adsorption was also studied by STM. After atomic resolution was obtained on the p(2x2) ordered surface, CO was leaked into the chamber and the surface imaged while it was exposed to CO. As has been reported by others, CO molecules were not resolved by the STM [34]. Despite this, the sulfur overlayer was clearly affected. Areas which were originally entirely of p(2x2) symmetry appeared to be either "clean" or dominated by small regions of p(2x2) order. Eventually, patches of the $(\sqrt{3}X\sqrt{3})R30°$ ordered sulfur structure were observed. Fig. 5.11 is an example of an area where islands of p(2x2) and $(\sqrt{3}X\sqrt{3})R30°$ order were observed to coexist.

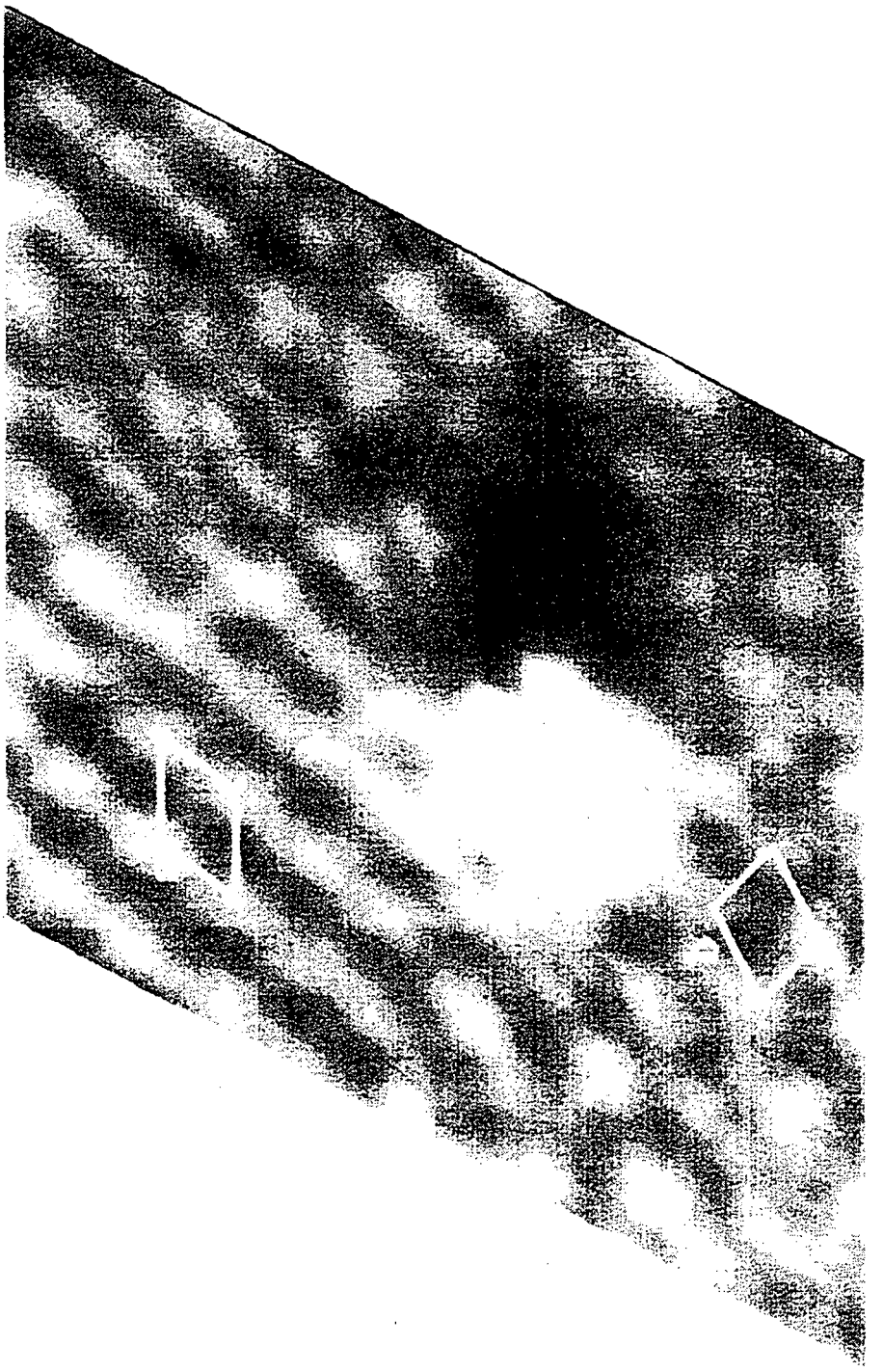

Figure 5.11. STM image showing the coexistence of the $(\sqrt{3}X\sqrt{3})R30°$ (unit cell 'a') and p(2x2) (unit cell 'b') ordered sulfur structures.

### 5.5.4 Discussion

From these experiments it was observed that the adsorption of CO on the metal surface occurred by the compression of the ordered sulfur overlayer. Because one of the two coadsorbed species (sulfur) forms ordered arrays, it was possible to monitor this process by STM and by LEED. The reverse process, the healing of the original overlayer by sulfur back-diffusion upon CO desorption, was also observed by LEED. If this phenomenon of adsorption of molecules by compression of adsorbates that are already present and perhaps chemically inert during surface reaction is generally valid, it could provide the mechanism by which molecules adsorb and react on transition metal surfaces that are crowded with inert adsorbates while they are subjected to the usual conditions used in metal catalysis. Clearly, both the mobility of the coadsorbates along the surface and their relative heats of adsorption must be of the proper magnitude for this phenomenon to occur at a given temperature. If one of the adsorbates is immobile because of high activation energies for surface diffusion, coadsorption cannot take place. This may happen when a carbonaceous overlayer present on platinum catalyst surfaces graphitizes. Intralayer carbon-carbon bonds create large chemical units (graphite islands or partially hydrogenated structures) that immobilize the overlayer. In this circumstance the catalyst is "poisoned", a well known effect in heterogeneous catalysis. If one of the coadsorbates has a low heat of adsorption, the thermodynamic driving force is absent, thus preventing hole creation in the adsorbed overlayer to produce adsorption sites. The adsorption energy of one adsorbate must be sufficient to overcome the self-repulsion of the other adsorbate in order for it to be compressed into a more compact layer. One also expects the interaction between the two coadsorbates to play a role in the coadsorbate-induced compression phenomenon. Regardless of whether this interaction is attractive or

repulsive, it is usually an order of magnitude smaller than the heats of adsorption to the metal for most chemisorbed atoms or molecules.

Similar effects of the interaction between adsorbates and coadsorbed CO have been observed in the case of p(2x2) Se on Pt(111) [35]. In this system CO coadsorption compressed the selenium into a higher coverage structure. These authors report that they did not find the same effect for S on Pt(111). However, the work was done at temperatures (T < 220 K) at which the reordering would have been quite slow.

## 5.6 An *in situ* STM determination of a kinetic pathway for the coadsorbate-induced compression of sulfur by CO on Pt(111)

STM can be used to study the interactions between adsorbates on surfaces by coadsorbing different species. As described in the previous section, when CO is coadsorbed with sulfur on Pt(111), the sulfur is compressed into ordered structures of higher local coverage. The steps leading to this compression were observed with both STM and LEED. This section presents *in situ* STM evidence suggesting the mechanism by which sulfur is compressed by coadsorbed CO on Pt(111). In this mechanism, sulfur is displaced by CO from the p(2x2) site to the next nearest fcc hollow site. This displacement initiates a chain reaction by which one-dimensional rows of sulfur atoms separated by $\sqrt{3}$ X the Pt-Pt distance are created. The formation of sulfur chains generates new sites for CO adsorption by which the compression phenomenon is further propagated.

Site competition and lateral interactions between adsorbates is one of the key mechanisms affecting chemical reactions on surfaces and in catalysis. Experiments carried out in this laboratory have recently demonstrated the compressibility of ordered sulfur overlayers on Pt(111) and Re(0001) by coadsorbed CO [36]. In spite of its strong binding to the surface, S can be displaced by much more weakly bound CO, if the sulfur coverage

is below saturation. The reason for this is the strong repulsive interactions between S and CO and by the relatively weak diffusion energy barrier of S (< 1 eV) that can be compensated by the CO adsorption energy (≈ 1 eV).

In this section the process of S compression by CO on Pt(111) is examined in detail. Scanning Tunneling Microscopy (STM) is the technique of choice for these studies as it provides information on surfaces without long range order, allowing insight to the mechanism by which the coadsorbate-induced compression phenomenon occurs for the S and CO on Pt(111) system.

### 5.6.1 STM Results

After atomic resolution was attained on a p(2x2) ordered surface, CO was leaked into the chamber at a pressure of $1X10^{-8}$ Torr and the surface imaged while exposed to CO. Figure 5.12 shows a constant height mode STM image of the Pt(111)(2x2)-sulfur surface while in $1X10^{-8}$ Torr CO. A step runs diagonally from the top left to the bottom right of the image. The image was obtained shortly after the surface was exposed to CO and shows a significant lack of long-range two-dimensional order, however the sulfur atoms are still clearly resolved and are separated by either $\sqrt{3}$ or 2 times the Pt-Pt lattice distance of 2.77 Å. Fast Fourier Transform (FFT) analysis of the image shows the presence of both (2x2) and $(\sqrt{3}X\sqrt{3})R30°$ structures. Occasional patches of p(2x2) order are observed (a unit cell of one such patch is highlighted in the right side of the image). One very interesting feature is the formation of rows of atoms having $\sqrt{3}$ periodicity which are observed to run approximately normal to the step on both terraces in this particular image (see arrow direction in Figure 5.12). In many areas along with these rows, periodic arrays of holes are also observed. A close-up view of one such region is shown in Figure 5.13. These hole arrays tend to form along either side of the rows forming a structure similar to a honeycomb (an example of this is outlined by the box in the middle right of the image).

As more CO is adsorbed, S is pushed and forms ordered $(\sqrt{3}X\sqrt{3})R30°$ structures that are stabilized preferentially near the top edges of the terraces. This is shown in figure 5.14. It is interesting to note that we did not observe sulfur aggregation along the bottom of a step edge. The apparent "empty" space created by this aggregation and seen in Fig. 5.14, however, is too large to account for the compression from the p(2x2) to the $(\sqrt{3}X\sqrt{3})R30°$. STM observations of sulfur diffusing at room temperature on Re(0001) [37] have shown that regions where the diffusion events are occurring appear to be void

of structure (within the background noise of intermittent spikes due to atoms diffusing under the tip). It is likely then that these structureless regions are in fact covered with fast diffusing CO and S that cannot be imaged at our scanning rate (~ 10 Hz). Figure 5.15 was obtained after approximately one hour of exposure to CO. At this point, the sulfur appears to be well ordered and forms exclusively a $(\sqrt{3}X\sqrt{3})R30°$ structure. In this image, a region of $(\sqrt{3}X\sqrt{3})R30°$-sulfur is observed which contains several domains separated by anti-phase boundaries.

Figure 5.12. (Following page) A constant height mode STM image of the Pt(111)(2x2)-sulfur surface while in $1X10^{-8}$ Torr CO. A step runs diagonally from the top left to the bottom right of the image. The image was obtained shortly after the surface was exposed to CO and shows a significant lack of long-range two-dimensional order, however the sulfur atoms are still clearly resolved and are separated by either $\sqrt{3}$ or 2 times the Pt-Pt lattice distance of 2.77Å. FFT analysis of the image shows the presence of both (2x2) and $(\sqrt{3}X\sqrt{3})R30°$ structures. Occasional patches of p(2x2) order are observed (a p(2x2) island with unit cell is circled). One very interesting feature is the formation of rows of atoms having $\sqrt{3}$ periodicity which are observed to run normal to the step on both terraces in this particular image (highlighted by arrow). In many areas along these rows periodic arrays of holes are observed. Image size: 140 Å x 200 Å.

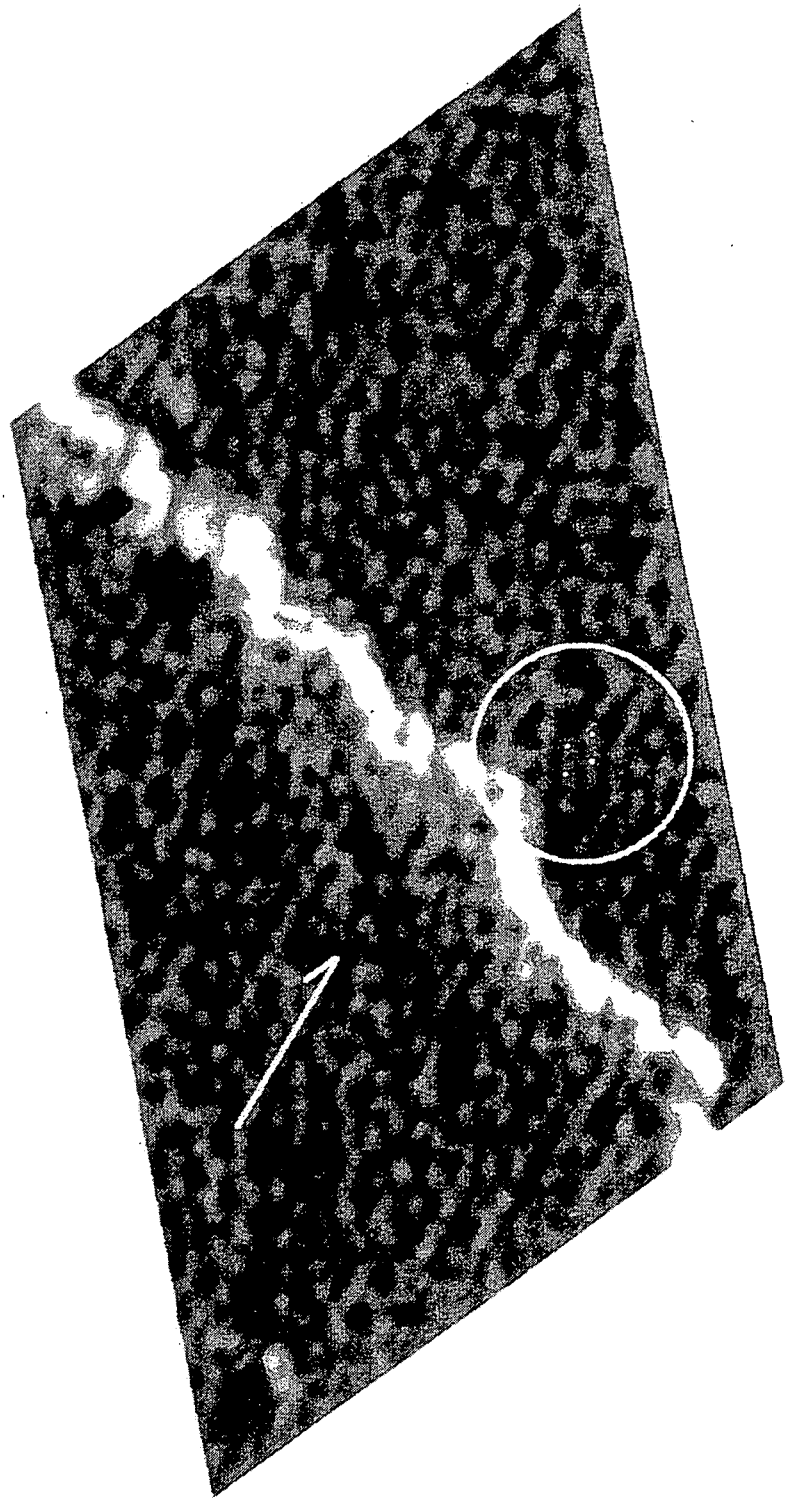

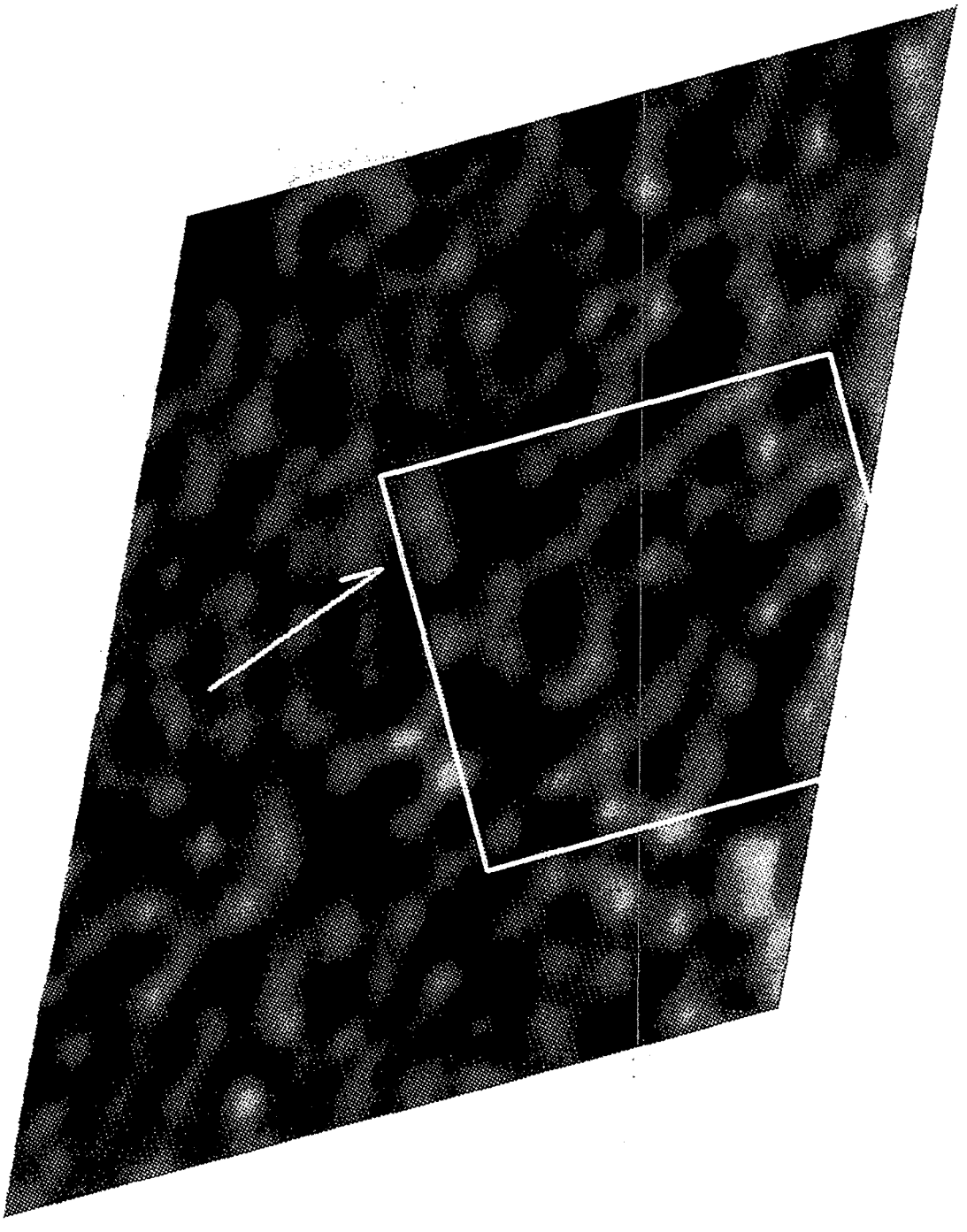

Figure 5.13. STM image showing the periodic arrays of holes neighboring the one-dimensional rows. These arrays of holes tend to form along either side of the rows of sulfur atoms forming a structure similar to a honeycomb (an example of this is outlined by the box). The $(\sqrt{3}X\sqrt{3})R30°$ lattice direction is indicated by the arrow. Image size: 65 Å x 76 Å.

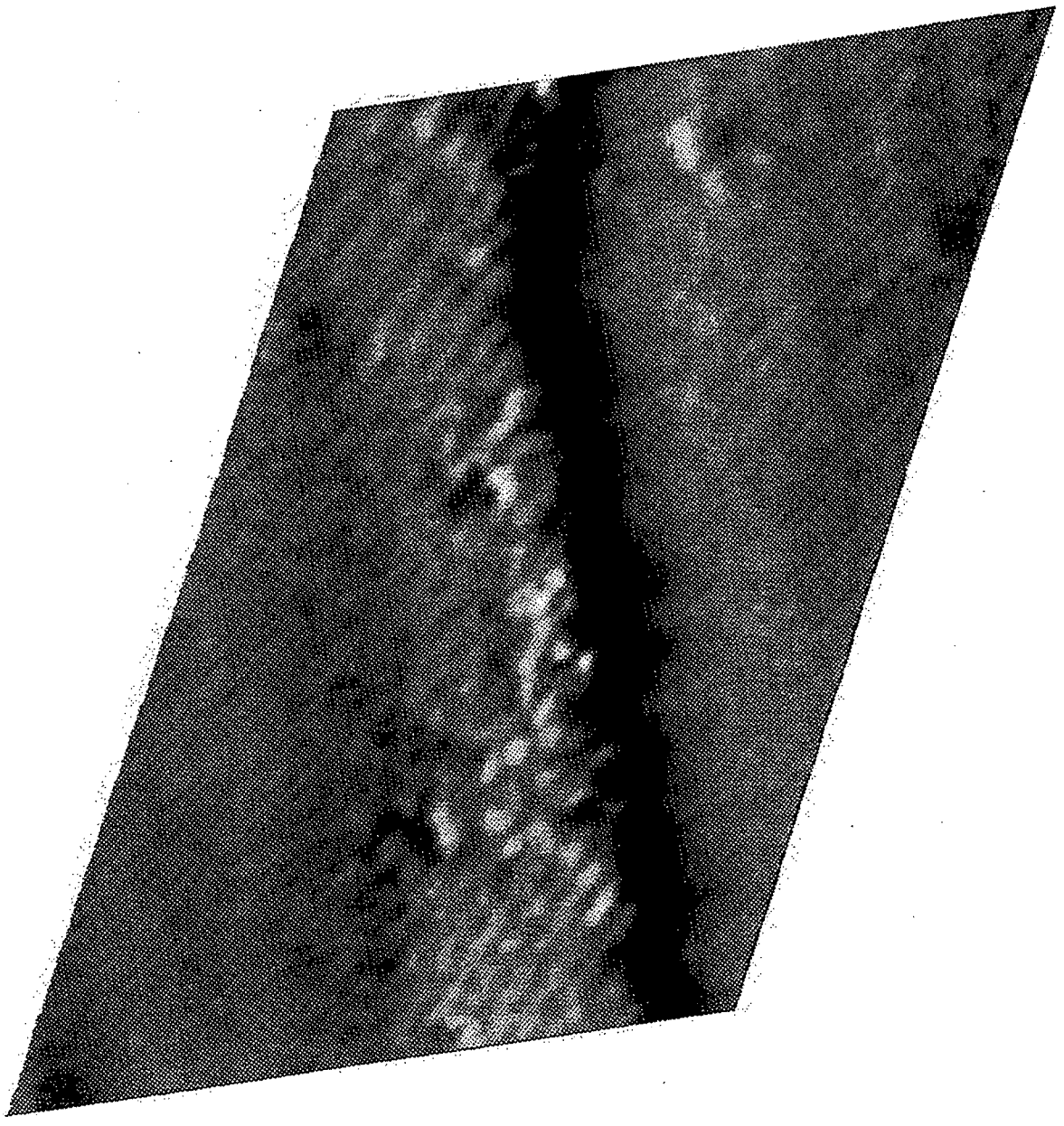

Figure 5.14. STM image showing that as CO is adsorbed S is pushed and forms ordered $(\sqrt{3}X\sqrt{3})R30°$ structures that are stabilized preferentially near the top edges of the terraces. It is interesting to note that we did not observe sulfur aggregation along the bottom of a step edge. It is likely that these structureless regions are in fact covered with fast diffusing CO and S that cannot be imaged at our scanning rate (~ 10 Hz). Image size: 124 Å x 111 Å.

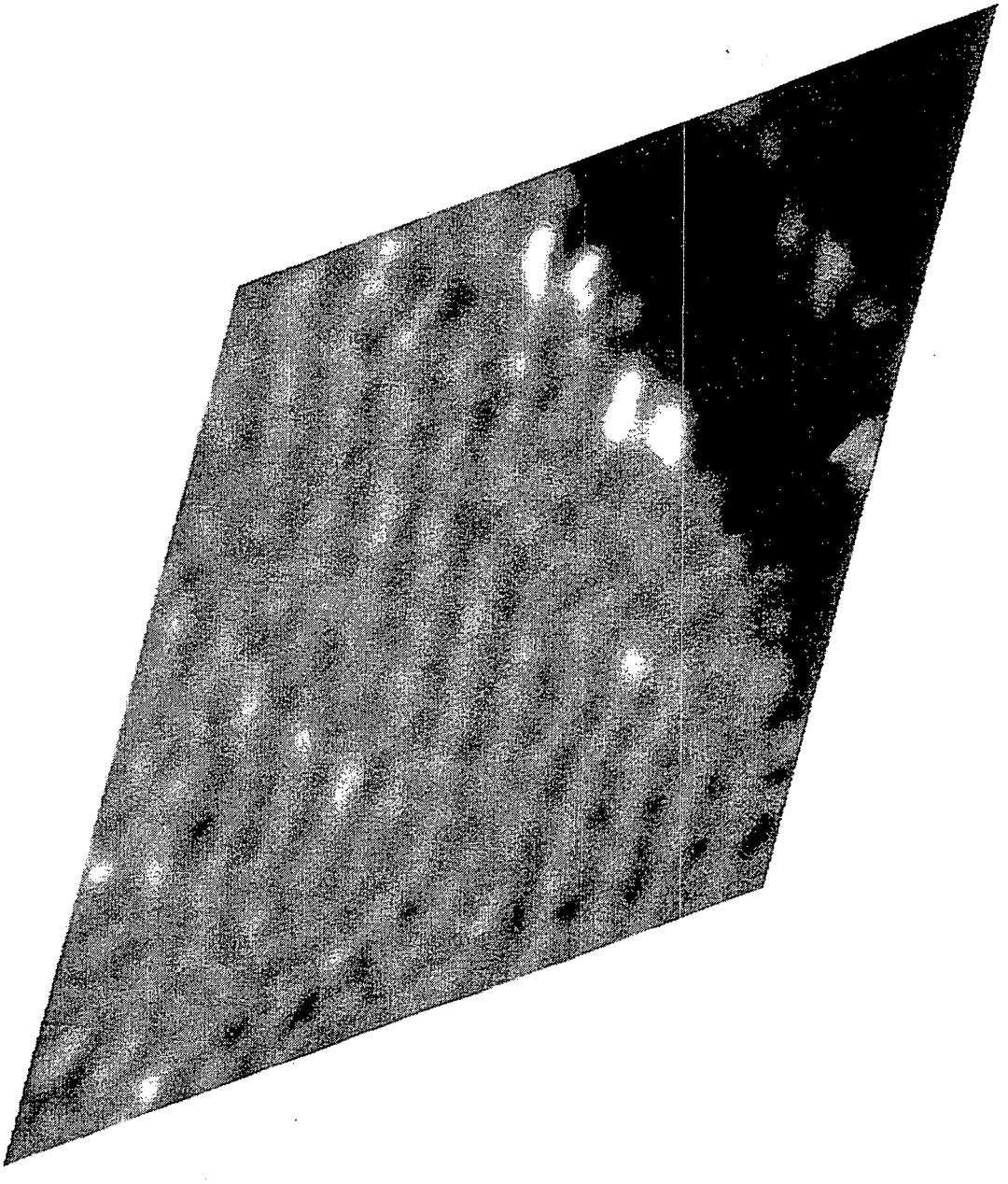

Figure 5.15. STM image obtained after approximately one hour of exposure to CO. At this point, the sulfur appears to be well ordered and forms exclusively a $(\sqrt{3}X\sqrt{3})R30°$ structure. In this image, a region of $(\sqrt{3}X\sqrt{3})R30°$-sulfur is observed which contains several domains separated by anti-phase boundaries. Image size: 63 Å x 60 Å.

### 5.6.2 Discussion

It is probable that the CO adsorbs initially on areas of the surface where sulfur is not present (i.e. defects, domain boundaries, steps, etc...). Eventually, the p(2x2) sulfur overlayer is disrupted, generating new sites for CO adsorption. With increasing coverage of CO the sulfur begins to form large domains having $(\sqrt{3}X\sqrt{3})R30°$ order. The compression phenomenon is reversible, such that upon annealing to desorb the CO the sulfur overlayer 'reheals' and the original p(2x2) structure is regenerated.

Analysis of the STM images obtained while the sulfur was undergoing compression allows one to understand the kinetic pathways by which this phenomenon occurs. From figure 5.12 it is clear that the original p(2x2) overlayer is converted at least initially to one-dimensional domains of $(\sqrt{3}X\sqrt{3})R30°$ order. It is likely that this is the result of sulfur diffusion events occurring near CO adsorbates. From the fact that these coadsorbates segregate, we conclude that the S - CO interaction is repulsive in relation to S-S or CO-CO interactions. As a result, sulfur localized around an adsorbed CO molecule can shift from its p(2x2) site to the next fcc hollow site away from the CO. In doing so, this sulfur atom is now occupying the site at the $\sqrt{3}$ position in relation to its two second-nearest S neighbors. However, it is separated only by a single Pt lattice distance from its first-nearest S neighbor. In this event the nearest neighbor sulfur atom is also repelled and subsequently displaced to the next fcc site which has the same arrangement of sulfur neighbors as the original displaced sulfur atom. This process of sulfur displacement is then repeated as a chain reaction, "zipping-up" the p(2x2) domain (see Figure 5.16(a)). The resulting structure consists of sulfur atoms which are arranged in a one-dimensional row with $\sqrt{3}$ periodicity and surrounded by sulfur having p(2x2) order (see Figure 5.16(b)). In this geometry, sulfur cells having a distorted pentagonal symmetry are created (Fig. 5.16(b)). The geometry of these vacancies is similar to the

holes observed in the experimental images (Fig. 5.13) near the one-dimensional rows of sulfur atoms. Within these vacancies, both bridge and top sites become available for further CO adsorption. It is interesting to note that the one-dimensional rows are often comprised of ten or more sulfur atoms, indicating that by this mechanism a single CO molecule can create ten or more new CO adsorption sites.

Once the compression phenomena are completed, ordered $(\sqrt{3}X\sqrt{3})R30°$ domains are formed near the top of the step edges. This can be explained by assuming that CO adsorption starts preferentially at the bottom of step edges and sulfur is pushed away from there to create more CO sites. The larger S-CO repulsion (as compared with CO-CO or S-S) explains the expansion of the CO regions and the formation of the S domains at the terrace edges near the top of the steps.

Figure 5.16. (Following page) Models showing the mechanism of sulfur overlayer compression by CO. (a) In this mechanism, sulfur localized around a CO molecule can shift from its p(2x2) site to the next nearest fcc hollow site. In doing so, this sulfur atom is now occupying the site at the $\sqrt{3}$ position in relation to its two second-nearest S neighbors. In this event the first-nearest neighbor sulfur atom is also repelled and subsequently displaced to the next fcc site which has the same arrangement of sulfur neighbors as the original displaced sulfur atom. This displacement initiates a chain reaction by which one-dimensional rows of sulfur atoms having $\sqrt{3}$ periodicity are created. (b) The one-dimensional rows are surrounded by sulfur having p(2x2) order. In this geometry, sulfur cells having a distorted pentagonal symmetry are created (as outlined in gray). The geometry of these vacancies is similar to the holes observed in the experimental images (figures 5.12 and 5.13) near the one-dimensional rows of sulfur atoms. Within these vacancies, both bridge and top sites become available for further CO adsorption.

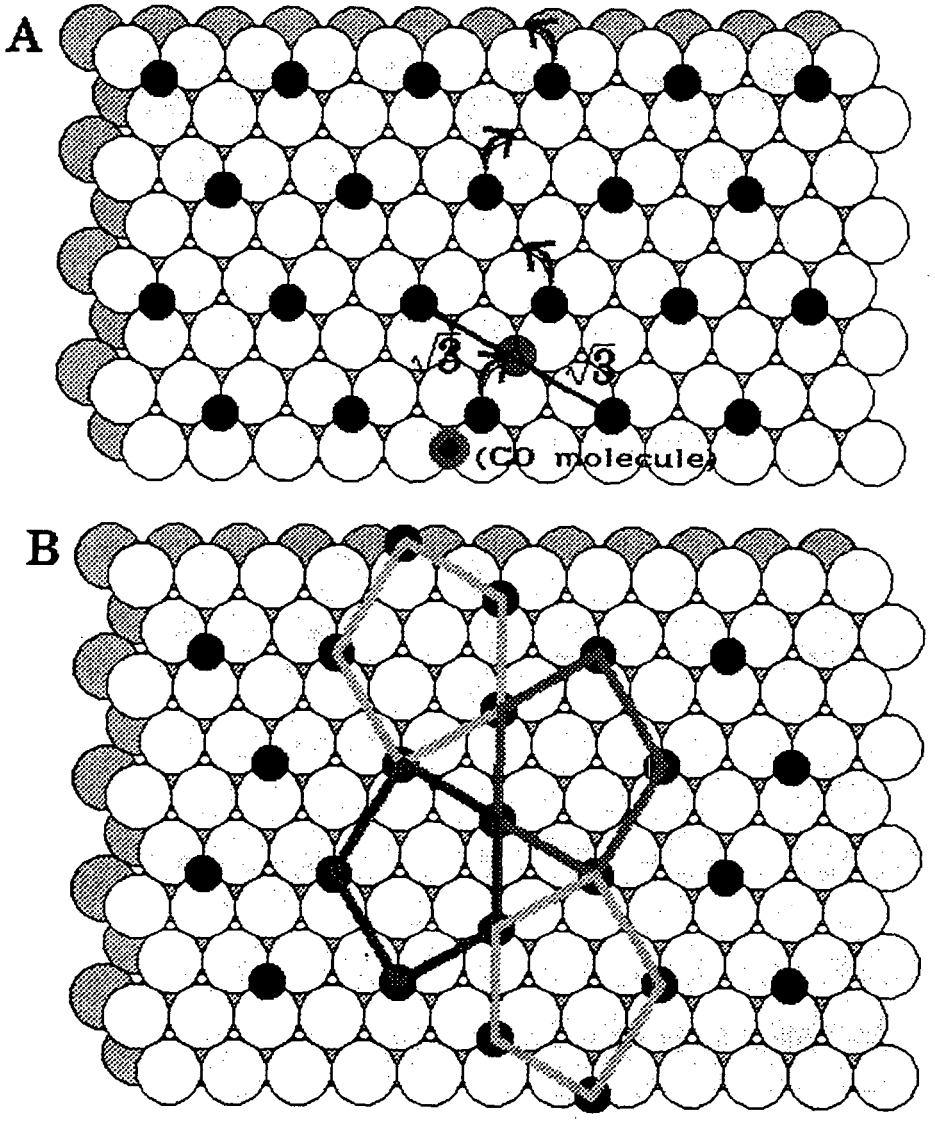
A
√3
√3
(CO molecule)
B

[1] B.C. Gates, J.R. Katzer, G.C.A. Schuit, Chemistry of Catalytic Processes, McGraw-Hill, NY, 1979.

[2] C.N. Satterfield, Heterogeneous Catalysis in Practice, McGraw-Hill, NY, 1980.

[3] M. Kiskinova, A. Szabo, and J.T. Yates, Surface Sci. **226,** 237, (1990).

[4] D.G. Kelly, A.J. Gellman, M. Salmeron, G.A. Somorjai, V. Maurice, M. Huber and J. Oudar, Surface Sci. **204**, 1, (1988).

[5] J.M. MacLauren, J. B. Pendry, P.J. Rous, D.K. Saldin, G.A. Somorjai, M. A. Van Hove, and D. D. Vvedensky, A Handbook of Surface Structures, D. Reidel Publishing Co., Holland, (1987).

[6] W. Heegemann, E. Bechtold and K. Hayek, Proc. 2nd International Conference on Solid Surfaces, 185 (1974).

[7] N. Materer, M.A. Van Hove and G.A. Somorjai, unpublished results.

[8] K. Hayek, H. Glassl, A. Gutmann, H. Leonhard, M. Prutton, S.P. Tear, and M.R. Welton-Cook, Surface Sci. **152**, 419, (1985).

[9] K. Hayek, H. Glassl, A. Gutmann, H. Leonhard, M. Prutton, S.P. Tear, and M.R. Welton-Cook, Surface Sci. **152**, 419 (1985).

[10] D.M. Eigler, C.P. Lutz and W.E. Rudge, Nature **352**, 600, (1991), and references therein.

[11] P. Sautet and C. Joachim, Phys. Rev. B **38**, 12238, (1988).

[12] P. Sautet, O. Eisenstein and E. Canadell, Chem. Mater. **1**, 225 (1989).

[13] P. Sautet and C. Joachim, Ultramicroscopy **42**, 115, (1992).

[14] J.C. Dunphy, D.F. Ogletree, M.B. Salmeron, P. Sautet, M.-L. Bocquet and C. Joachim, Ultramicroscopy, **42-44**, 490, (1992).

[15] J.C. Dunphy, D.F. Ogletree, M.B. Salmeron, P. Sautet, M.-L. Bocquet and C. Joachim, Ultramicroscopy, **42-44**, 490, (1992).

[16] F. Jensen, F. Besenbacher, E. Lægsgaard, and I. Stensgaard, Phys. Rev. B **42**, 9206 (1990).

[17] R.M. Feenstra, A.J. Slavin, G.A. Held, and M.A. Lutz, Phys. Rev. Lett. **66**, 3257 (1991).

[18] A. Feltz, A.U. Memmert, and R.J. Behm, Chem. Phys. Lett, **192**, 271 (1992).

[19] E. Ganz, S.K. Theiss, I.S. Hwang, and J. Golovchenko, Phys. Rev. Lett. **68**, 1567 (1992).

[20] J.C. Dunphy, P. Sautet, D.F. Ogletree, O. Dabbousi, and M.B. Salmeron, Phys. Rev. B, **47**, 2320 (1993).

[21] J.C. Dunphy, P. Sautet, D.F. Ogletree, and M.B. Salmeron, J. Vac. Sci. Technol. A., **11**, 2145, (1993).

[22] J.C. Dunphy, P. Sautet, D.F. Ogletree, O. Dabbousi, and M.B. Salmeron, Phys. Rev. B, **47**, 2320 (1993).

[23] J.C. Dunphy, P. Sautet, D.F. Ogletree, and M.B. Salmeron, J. Vac. Sci. Technol. A., **11**, 2145, (1993).

[24] D.R. Strongin and G.A. Somorjai, J. of Catal. **118**, 99, (1989).

[25] S.M. Davis, F. Zaera, and G.A. Somorjai, J. of Catal. **77**, 439, (1982).

[26] M.E. Bussell, A.J. Gellman, and G.A. Somorjai, Catal. Lett., **1**, 195, (1988).

[27] H. Steininger, S. Lehwald and H. Ibach, Surface Sci. **123**, 645, (1982).

[28] H. Hopster and H. Ibach, Surface Sci. **77**, 109 (1978).

[29] B. Poelsema, R.L. Palmer and G. Comsa, Surface Sci. **123**, 152 (1982): Surface Sci. **136**, 1, (1983).

[30] M. Tüshaus, E. Schweizer, P. Hollins and A.M. Bradshaw, J. Electron Spectrosc. Rel. Phenom. **44**, 305, (1987), and references therein.

[31] N.R. Avery, J. Chem. Phys. **74**, 4202, (1981).

[32] G. Ertl, M. Neumann, and K.M. Streit, Surface Sci. **64**, 393, (1977).

[33] M. Kiskinova, A. Szabo, and J.T. Yates, Surface Sci. **226**, 237, (1990).

[34] T. Gritsch, D. Coulman, R.J. Behm, and G. Ertl, Physical Review Letters, **63**, 1086 (1989).

[35] M. Kiskinova, A. Szabo, and J. T. Yates, Vacuum, **41**, 82, (1990).

[36] J.C. Dunphy, B.J. McIntyre, J. Gomez, D.F. Ogletree, G.A. Somorjai, and M.B. Salmeron, to be published.

[37] J.C. Dunphy, P. Sautet, D.F. Ogletree, O. Dabboussie, and M. Salmeron, Phys. Rev. B, **41 (4)**, 2320, (1993).

# CHAPTER 6

# ADSORBATE-INDUCED RECONSTRUCTION OF PT(111)

## 6.1 Introduction

The (111) surfaces of fcc metals are considered to be particularly stable with Au(111) thought to be the only exception [1]. Recently, it was discovered that Pt(111) can also undergo reconstructions under special conditions [2]. Sandy *et al.* found that Pt(111) will reconstruct at temperatures above 1330 K, but that below this temperature the unreconstructed phase is stable. Bott *et al.* found that the reconstructed surface of Pt(111) is stabilized down to 400 K when in the presence of a super-saturated Pt gas-phase environment [3]. In the work described in this chapter, it was found that the coadsorption of sulfur and carbon monoxide can induce the reconstruction of Pt(111) at room temperature. As described in the previous chapter, when CO is coadsorbed with sulfur on Pt(111), the sulfur is compressed into ordered structures of higher local coverage. The steps leading to this compression were observed with both STM and LEED. This chapter presents *in situ* STM evidence which suggests a mechanism for this coadsorbate-induced reconstruction.

The reconstructed structure of Au has been investigated by various methods and discussed in detail recently by Barth, *et al.* [4]. They found that the reconstructed surface can be described by a 'stacking-fault-domain' model involving periodic transitions from fcc to hcp stacking of top-layer atoms. The transition regions separating the hcp and fcc domains appear as bright double parallel lines 27 Å apart. The lines run along the $[11\bar{2}]$ direction and each pair of lines contains an extra row of atoms which results in a local uniaxial contraction in the $[1\bar{1}0]$ direction. These double lines form a superstructure with

a lattice constant of 63 Å (22 x 2.884Å) in the $[1\bar{1}0]$ direction. The line pairs do not cross but bend ±120° every 250 Å, forming a zig-zag pattern. The termination of the lines occurs in well-ordered, U-shaped connections of neighboring lines. In this manner, the hcp and fcc domains are fully separated by the transition regions.

Bott, *et al.* found that the reconstruction of the Pt(111) surface corresponds very closely to the reconstructed Au(111) surface. They observed that the double lines and the U-turns are qualitatively and quantitatively equivalent to those found on the Au(111) surface. However, they did observe that (unlike the reconstructed Au(111) surface), on the Pt(111) reconstructed surface, the double lines cross, forming network structures.

The reason behind most metal surface reconstructions is a very simple one. Surface atoms have fewer nearest neighbors than the atoms in the bulk. As a result, the surface energy may be reduced by having shorter bond lengths within the surface plane. In a recent theoretical study by Needs, et al [5], it was observed that there are three main effects which are involved in determining the stability of the reconstructed phases of the (111) surfaces of Pt, Ir, Al, and Au:

1. The tendency of these surfaces to have shorter bond lengths (i.e. higher surface density).

2. The energy changes associated with transferring atoms to or from the surface layer in order to increase its density.

3. The reduced bonding energy to the substrate of a compressed reconstructed layer which is at least partially incommensurate.

Clearly (1) is the driving force of the reconstruction where (2) and (3) are responsible for stabilizing the unreconstructed phase. In their work, Needs, *et al.* found that the (111) surfaces of Ir, Pt, and Au are all close to an instability towards adding atoms to the surface.

## 6.2 Experiment

The experiments were performed in an ultrahigh vacuum chamber. The Pt(111) surface was cleaned by Ar+ bombardment and cycles of heating to 800º C in the presence of 5 x $10^{-7}$ Torr of oxygen and vacuum annealing to 800º C. Once the crystal was clean as verified by AES, it was exposed to $H_2S$ at 5 x $10^{-8}$ Torr for two to ten minutes while heating to approximately 700º C. $H_2S$ decomposes on the surface, leaving behind sulfur. After cooling the large scale ordering of the sulfur overlayer was determined with LEED, and the sulfur coverage determined with AES. After atomic resolution was attained on a p(2x2) ordered surface, CO was leaked into the chamber at a pressure of $1X10^{-6}$ Torr and the surface imaged while exposed to CO. Figure 6.1 shows a constant height mode STM image of the Pt(111)(2x2)-sulfur surface while in $1X10^{-6}$ Torr CO. In this image the Pt atoms are clearly resolved. as are distortions of the surface. These undulations are separated by approximately 23 Å and their structures are identical to the small scale atomically resolved images obtained by Bott, *et al.* Also observed are the ±120° angles which the transition regions have been previously reported to have every 250 Å. From topographic images obtained of these reconstructed regions (see Fig. 6.2), it was observed that the transition regions have corrugations up to 1 Å, while the atomic corrugation was observed to be 0.25 ±0.05 Å. These corrugations are slightly larger than reported by Bott, *et al.* however this is not surprising as it is likely that these images were obtained with a sulfur-terminated STM tip which has been observed to result in corrugation increases for this system by as much as a factor of 10. Fig. 6.3 shows a reconstructed region of the surface coinciding with nearby islands of ordered $(\sqrt{3}X\sqrt{3})R30°$-sulfur. It should be noted here that sulfur was never observed to adsorb on the reconstructed regions. Rather, the reconstructed regions are expected to be covered with carbon

monoxide which is not resolved because of its rapid diffusion on the surface. In this and many other images, it was observed that the reconstructions are often located at the bottoms of step edges. Fig. 6.4 shows this quite clearly. In this image it appears that the middle step may have in fact recessed at the location of the reconstruction. The large bumps on the terraces are sulfur atoms in the $(\sqrt{3}X\sqrt{3})R30°$ geometry.

The reconstructed Pt surface appears to be very sensitive to STM tip conditions since tip effects are commonly observed. in Fig. 6.5, the atomic structure is resolved as bumps, however at the bottom of the image the bumps become holes. Occasionally, other unusual tip effects are observed. In Fig. 6.6 a set of images is shown which demonstrates that the contrast of the atomic features can also depend on the direction in which the tip is scanned over the surface. In this figure, the left and right image pages were acquired simultaneously while the tip was rastered in the left and right directions, respectively. In images "b" and "b' ", for example, it is clearly observed that the bottom third of the left page "b" shows the atomic structure resolved as bumps while the same region of the right page "b' " shows the atomic features as holes (and similarly for "a" and "a' "). It is likely that in these experiments, the tip is scanning over the surface at slightly different heights in the forward and reverse directions (due to capacitance effects in the fast uni-polar scan geometry). These effects were not observed when acquiring in slower scanning, topographic mode images. However, these results point out a very significant contrast dependence on tip height which may be possible to model using the ESQC approach described in the previous chapter.

Figure 6.1. (Following page) Current mode STM image of the initial Pt(111)(2x2)-sulfur covered surface in 1 x $10^{-6}$ Torr CO. At the point the sulfur has been compressed to the $(\sqrt{3}X\sqrt{3})R30°$ structure and regions void of sulfur are clearly observed where CO is present. This image shows a region of the surface where CO has adsorbed and pushed sulfur away. The bumps represent the reconstructed Pt(111) atomic structure. The undulations observed are transition regions between the fcc and hcp domains. These transition regions form double lines which are separated by approximately 23 Å and zig-zag at ±120° angles every 250 Å. The white rectangle shows a unit cell for the reconstruction. The regions labeled fcc and hcp are done so arbitrarily but according to the convention that the hcp structure is less stable and is generally found to form smaller domains which occupy the region between two transition lines. The individual rows of Pt atoms are found to be somewhat non-linear. This is believed to be the result of their shift between fcc and hcp positions. The 2-D Fast Fourier Transform (FFT) pattern in the upper left corner of the figure shows the hexagonal order of the surface. Measuring the spacing of the maxima in this pattern shows the atomic structure has an average spacing of approximately 2.65 Å, which agrees well with the lattice spacing observed for the reconstructed Pt(111) surface by Bott, *et al.*

# Reconstructed Pt(111)

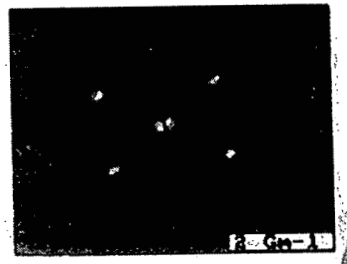

4% increase in
Pt atom density

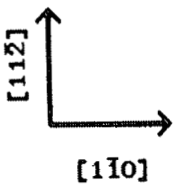


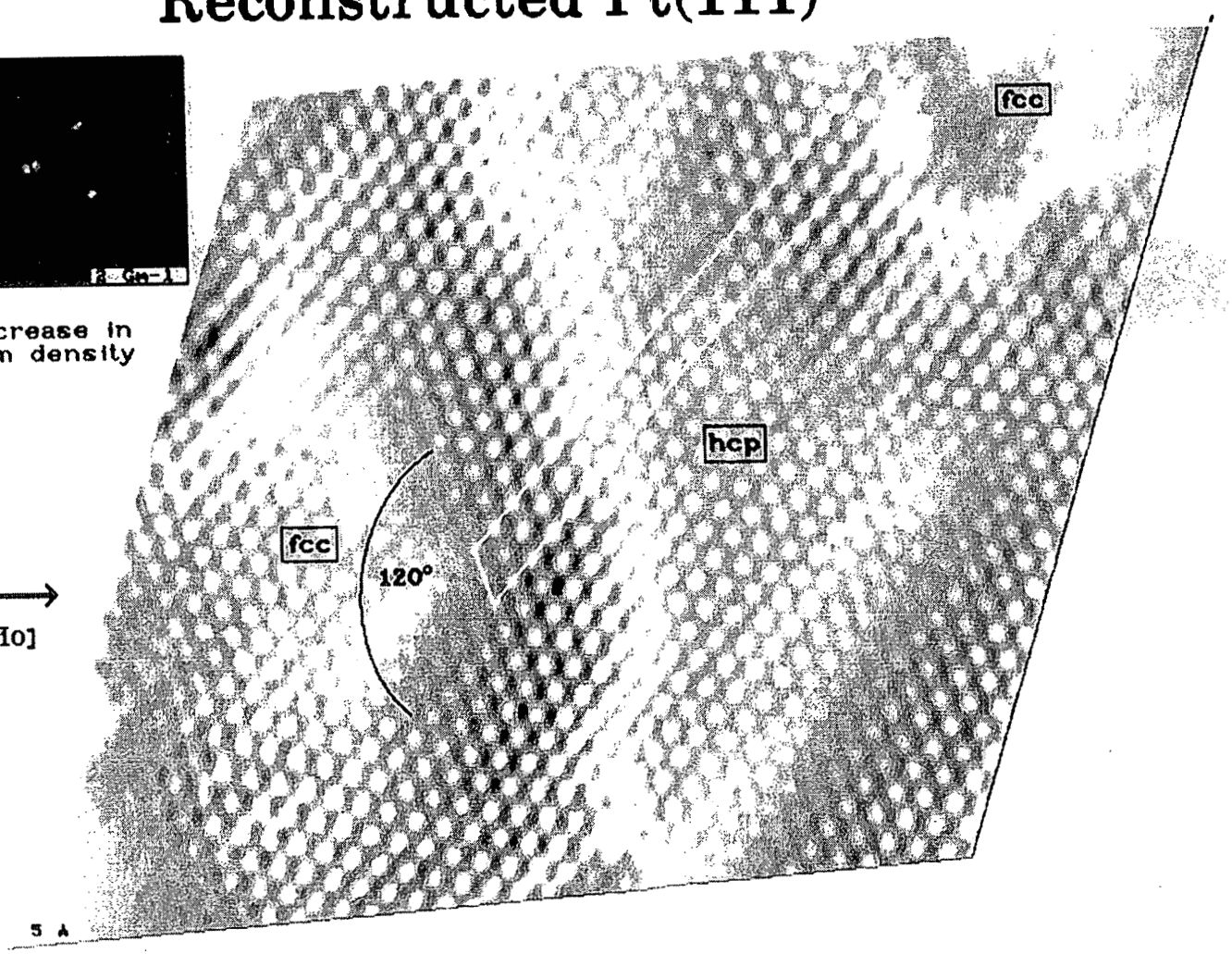

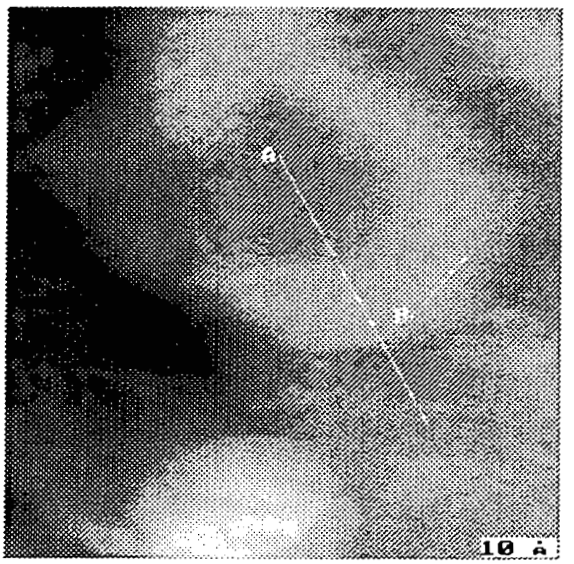


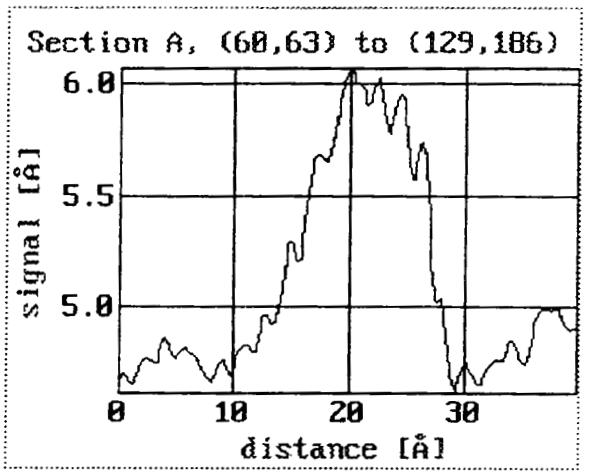


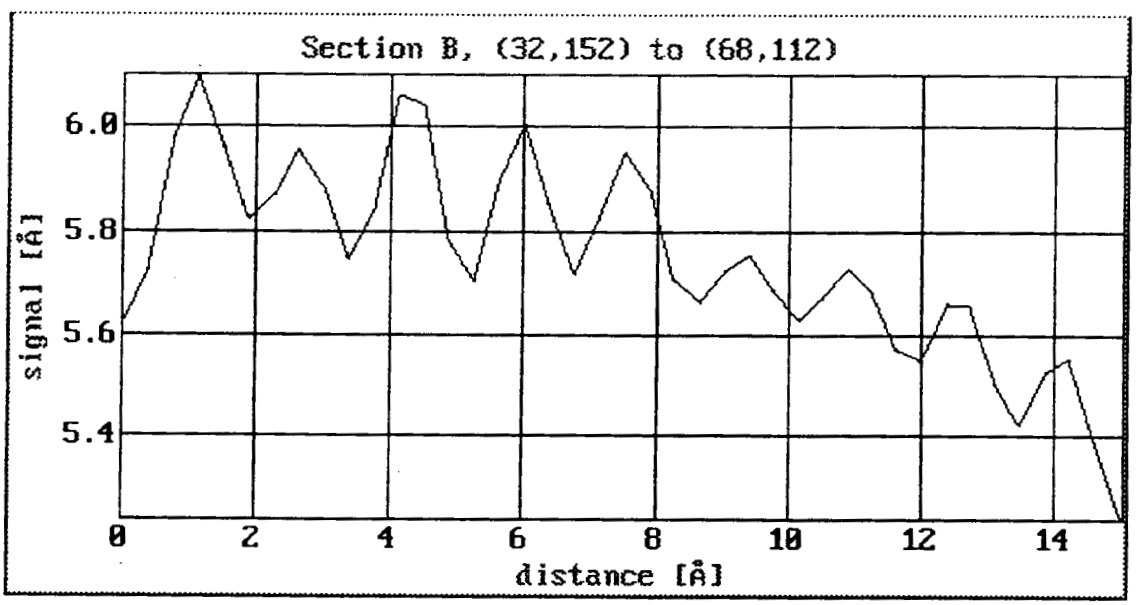


Figure 6.2. Topographic mode STM image of a reconstructed region of the Pt(111) surface. The transition regions (line cross-section 'A') were observed to have corrugations up to 1 Å, while the atomic corrugation (line cross-section 'B') was found to be 0.25 ± 0.05 Å.

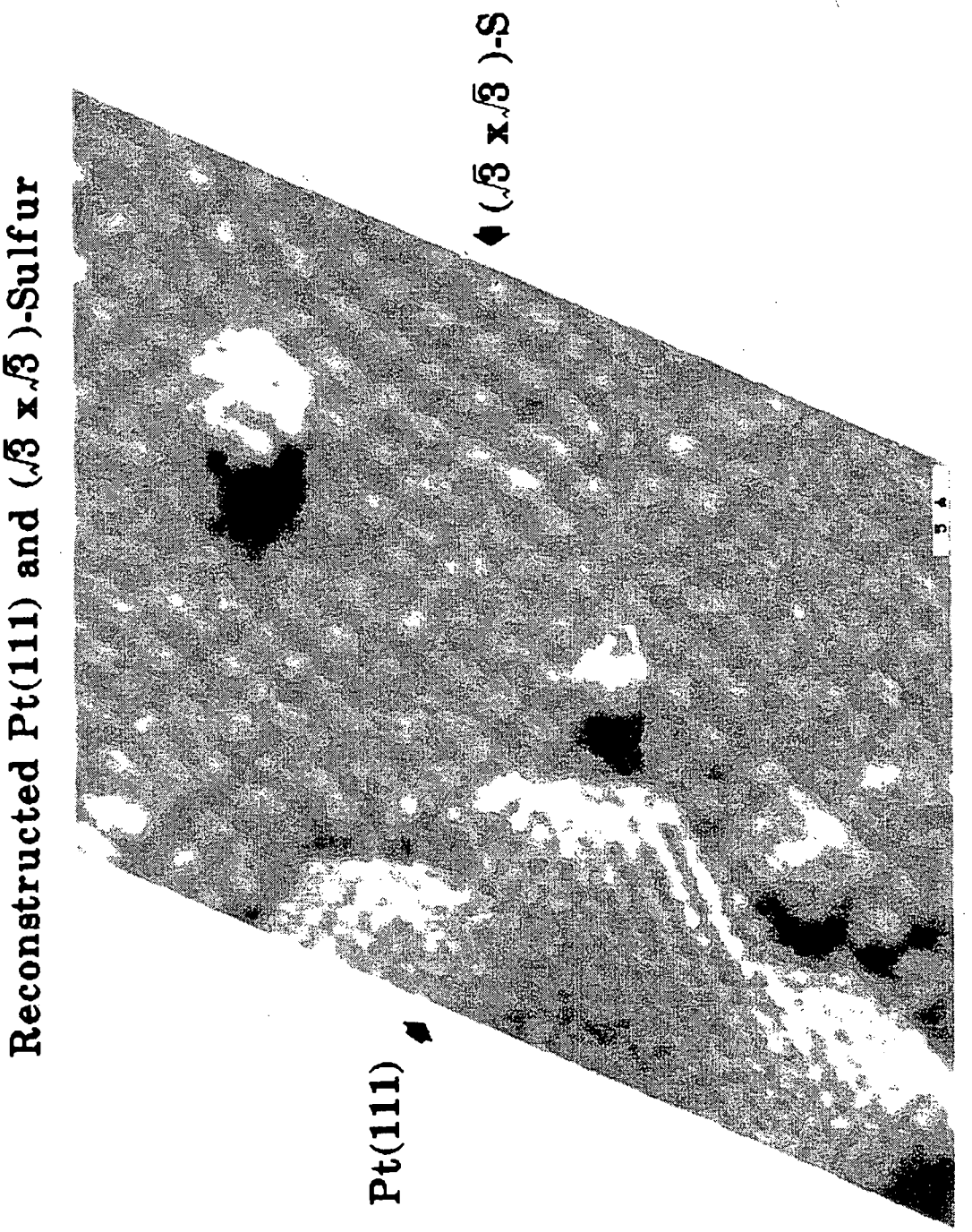


Figure 6.3. Reconstructed Pt(111) (on left side of image) surface coinciding with islands of ordered $(\sqrt{3}X\sqrt{3})R30°$-sulfur. Occasionally raised islands such as the one in the upper right of the image are observed but their presence is not yet understood.

Figure 6.4. Reconstructed region of the surface coinciding with 3 nearby Pt terraces. The regions of reconstructed Pt were observed at the bottoms of step edges.

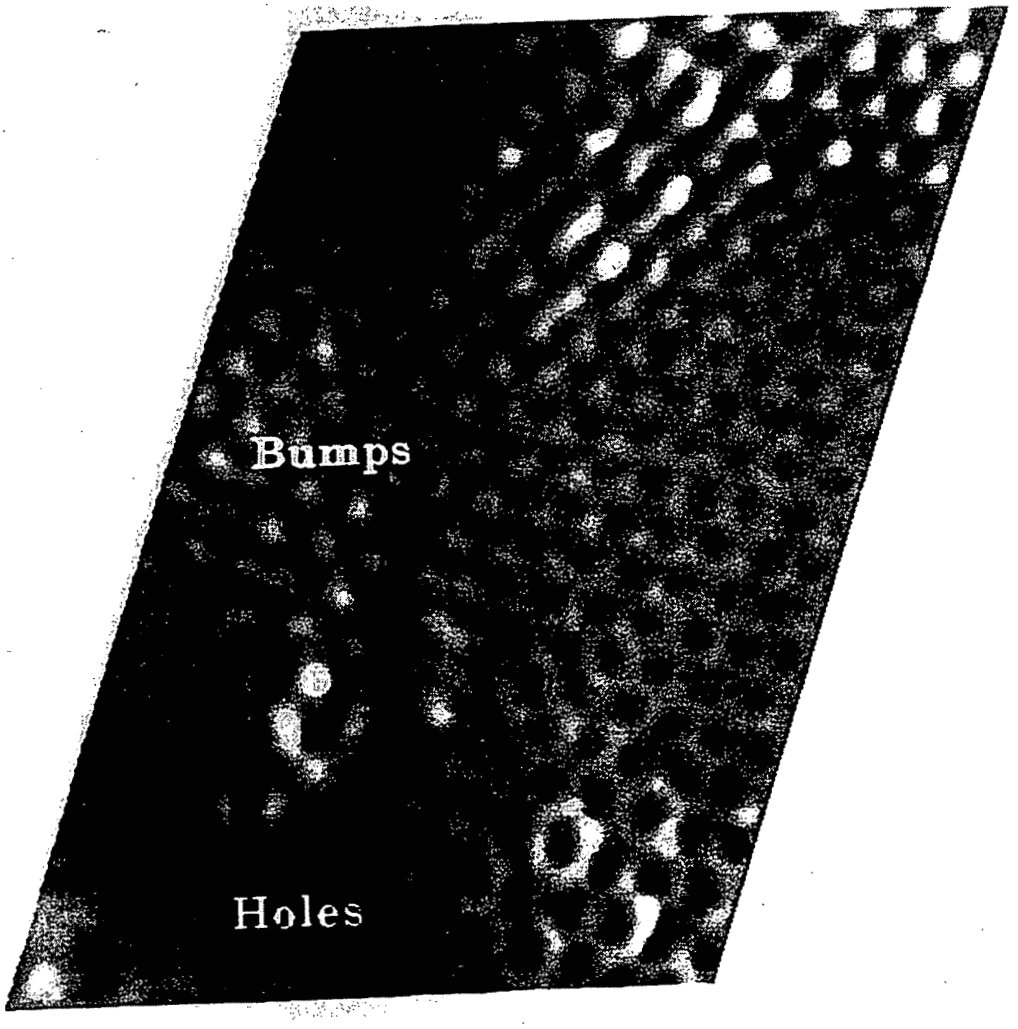


Figure 6.5. Current mode STM image showing contrast changes. The upper part of the image shows the atomic structure as bumps, however, at the bottom of the image the atomic registry is resolved as holes.

Figure 6.6. (Following page) Two sets of current mode STM images demonstrating contrast reversal. In this figure, the left and right image pages were acquired simultaneously while the tip was rastered in the left and right directions, respectively. Image "a" was aquired while the tip was scanned to the right while "a' " was obtained of the same area with the tip scanned to the left, (and similarly with "b" and "b' "). It is likely that in these experiments, the tip is scanning over the surface at slightly different heights in the forward and reverse directions (due to capacitance effects in the fast uni-polar scan geometry). These effects were not observed when acquiring in slower scanning, topographic mode images. However, these results point out a very significant contrast dependence on tip height which may be possible to model using the ESQC approach described in the previous chapter.

# Contrast Reversal

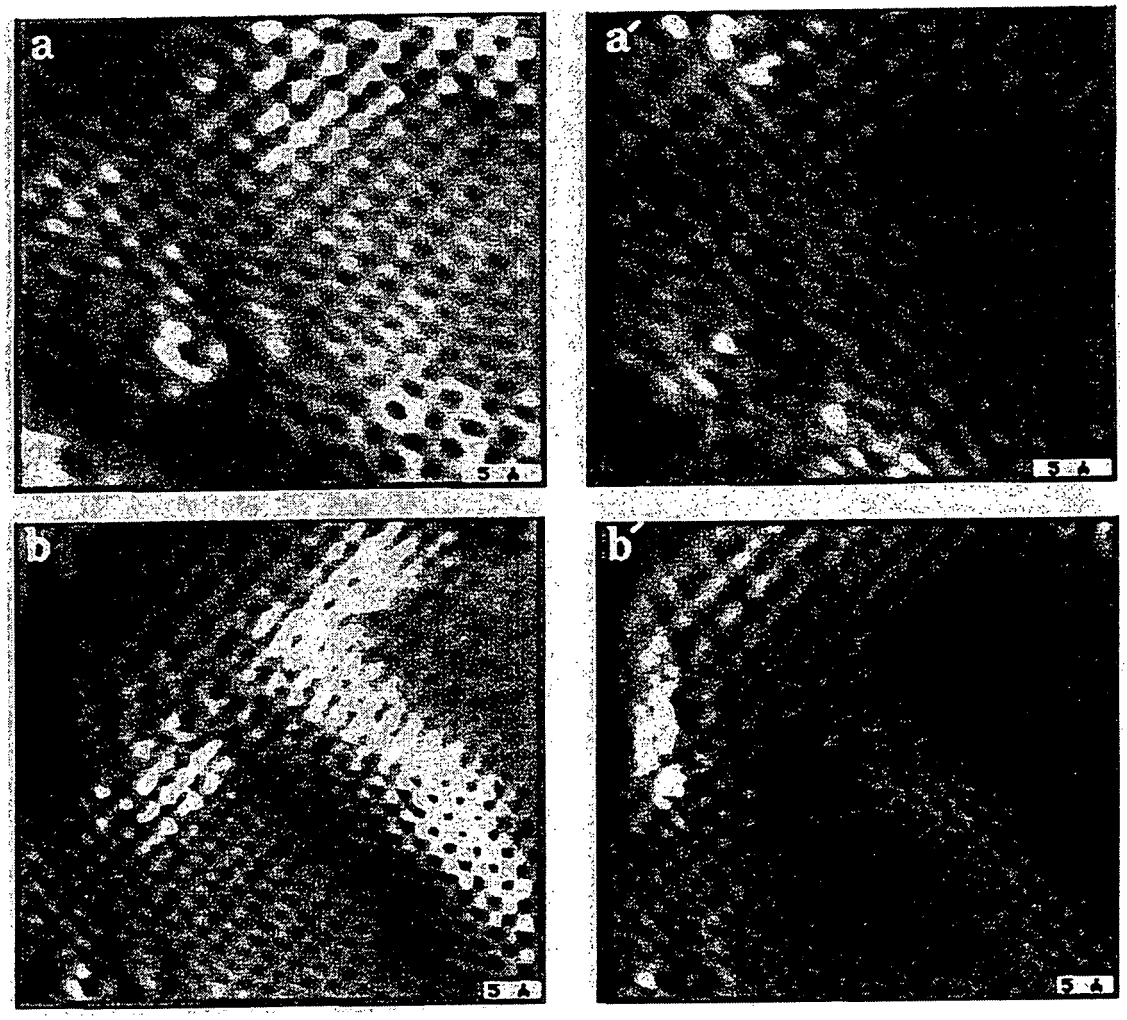

## 6.3 Discussion

It should be mentioned that to the author's knowledge, this is the first example of a coadsorbate-induced reconstruction. From experiments on the clean surface in the same CO pressures the reconstructions were never observed to occur. The reconstructions were also never observed after the surface was exposed to sulfur. It is clear that the presence of both adsorbates is necessary for the reconstruction to occur.

The stabilization of the reconstructed Pt surface at room temperature by the coadsorption of sulfur and CO reported here can be understood within the findings of Needs, *et al.* In this mechanism, sulfur is anisotropically compressed by CO. This anisotropic compression was observed to occur when CO pushes sulfur to the tops of step edges. It has been shown previously that for stepped Pt(111), sulfur will cause step doubling of the surface [6]. Lanzillotto, *et al.* found that when a Pt-6(111)x(100) surface, (steps with 6 atom wide terraces having (111) orientation), is exposed to sulfur the initially monatomic height steps will come together to form double height steps. While step doubling was not observed here for the vicinal Pt(111) surface, this may be the result of larger terrace widths and uniform sulfur coverages. In the event of anisotropic compression, it is likely that new surface energetics arise which favor the formation of multiple height steps. In the course of step doubling, Pt likely undergoes a reconstruction which involves 2-D Pt atom evaporation from steps. It is also expected that step edges are likely to be covered with adsorbates which may reduce their capacity to act as sinks for adatom diffusion. This situation of a 2-D Pt adatom lattice gas on the surface is similar to the conditions in which Bott, *et al.* observed the Pt reconstructed phase to be stabilized under homoepitaxial growth of Pt on Pt(111). A schematic of this proposed mechanism is shown in Fig. 6.7. Under these conditions the energy factor (2) described by Needs, *et al.* which arises from the energy changes associated with transferring atoms to the surface to

increase the density is affected. This factor which helps to stabilize the unreconstructed phase is significantly reduced and thus the energetics are swung in the favor of reconstruction.

These results demonstrate for the first time the adsorbate-induced reconstruction of an fcc(111) metal surface. Also for the first time, the reconstructed Pt(111) surface phase was observed to be stabilized down to room temperature. And finally, because it was necessary for both sulfur and CO to be present to cause the reconstruction, it is also the first example of a coadsorbate-induced reconstruction.

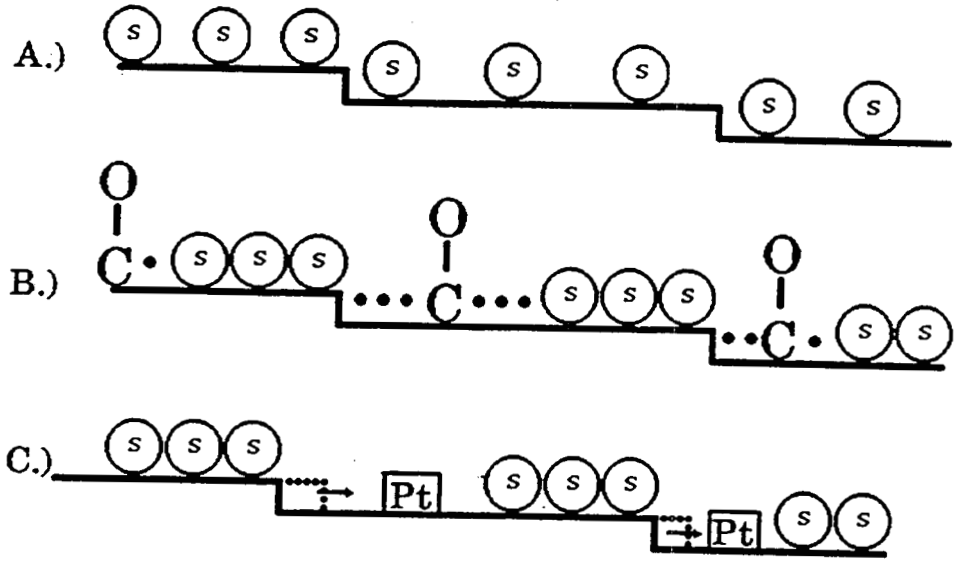


Figure 6.7. Schematic of the proposed mechanism for the coadsorbate-induced reconstruction of Pt(111). In this mechanism, the sulfur initial adsorbs uniformly over the surface (A.). After exposure to CO, the sulfur is compressed anisotropically from the step bottoms to the terrace edges (B.). The "free" step-bottoms can now "emit" Pt atoms to the clean terrace (perhaps this 2-D evaporation is enhanced by the presence of S on the tops of the steps) (C.). The resulting condition of a 2-D Pt adatom lattice gas on the surface stabilizes the Pt(111) reconstruction as observed by Bott, *et al.*

[1] J.V. Barth, H. Brune, G. Ertl, and R.J. Behm, Phys. Rev. B, **42**, 9307 (1990).

[2] A.R. Sandy, S.G.J. Mochrie, D.M. Zehner, G. Grübel, K.G. Huang, and Doon Gibbs, Phys. Rev. Lett. **68**, 2192, (1992).

[3] M. Bott, M. Hohage, T. Michely, and G. Comsa, Phys. Rev. Lett. **70**, 1489 (1993).

[4] J.V. Barth, H. Brune, G. Ertl, and R.J. Behm, Phys. Rev. B, **42**, 9307 (1990).

[5] R.J. Needs, M.J. Godfrey, and M. Mansfield, Surf. Sci. **242**, 215, (1991).

[6] A.M. Lanzillotto and S.L. Bernasek, J. Chem. Phys. **84**, 3553 (1986).

# CHAPTER 7

# HPSTM INVESTIGATIONS OF HYDROCARBONS ON PT(111)

## 7.1 Introduction

The stability of hydrocarbons on catalyst surfaces while under reaction conditions and the subsequent process of coking of the catalysts upon decomposition are subjects of major interest to the catalysis industry [1,2,3]. The intermediate hydrocarbon decomposition products are of interest in catalysis as it is thought that certain forms of "carbidic" carbon may play active roles in catalytic processes while graphitic carbon is generally thought to act as a poison [4]. The metal component of hydrocarbon reforming catalysts plays an important role as a source of reactive hydrogen atoms. It is also known that active hydrocarbon catalysts are covered with monolayer amounts of strongly-bound hydrocarbon species which inhibit hydrogen adsorption and dissociation [5]. So an important question arises as to how molecules can be actively catalyzed on such a surface. Do the carbidic species play a role? It has been suggested that they may be involved in the hydrogen transfer from the surface to the reactive intermediates [6]. In any case it is important to understand what morphologies these carbidic species have and whether their structures change with environment. This kind of information is readily obtainable from *in situ* HPSTM studies.

Light alkenes (ethylene, propylene, butadiene,...) have been often used as models for hydrogenation-dehydrogenation reactions in surface science and catalysis studies [7,8,9,10]. In particular, studies of interactions between Pt(111) and these molecules have focused on many aspects such as the identity of the molecular adsorbates as a function of temperature, kinetics of the reactions and catalytic reactivity [11,12,13,14,15,16,17,18].

In this chapter, results from HPSTM studies of the chemistry of propylene on Pt(111) will be discussed. Propylene readily adsorbs on the surface of Pt under these conditions and forms ordered structures of propylidyne ($\equiv C\text{-}CH_2\text{-}CH_3$) that have been studied in the past in detail [19]. Figure 7.1 reviews some of the structural aspects of the adsorption and decomposition of propylene on Pt(111) in UHV as determined by HREELS and LEED studies [20]. At temperatures up to 200 K, propylene adsorbs intact with the C=C-C bond axis parallel to the Pt(111) surface. At temperatures above 200K propylene ($C_3H_6$) converts irreversibly to propylidyne ($C_3H_5$) by loss of hydrogen. The C-C-C bond axis is perpendicular to the surface. The propylidyne species is stable on the Pt(111) surface at temperatures up to 450 K. Above 450 K the propylidyne species undergoes C-C bond scission and further loss of hydrogen forming ethylidyne and carbonyl species. Above 500 K more hydrogen is lost and the surface is characterized as having carbonaceous species of CH and $C_2H$ stoichiometry. Above 550K, the surface hydrocarbons appear to form longer chains having wide-ranging stoichiometries and have thus been described as "polymeric". Above 900K, the carbonaceous species form graphite.

Variable temperature UHV STM studies have also observed this dehydrogenation/decomposition process for ethylene on Pt(111) [21]. In this study, the authors observed that upon heating to 500 K, the ethylidyne covered sample showed the surface to be uniformly covered with carbon containing particles approximately 10-15 Å in diameter. Annealing the carbon particle covered surface to higher temperatures results in the formation of graphite islands which eventually accumulate at the Pt steps and lead to step pinning.

With the HPSTM, the stability of propylene on Pt(111) and the morphology of decomposition products as a function of atmospheric environment (hydrogen, $H_2$/propylene, and CO) and sample temperature (300K - 900K) has been investigated.

Clusters of carbonaceous material were formed as a result of various decomposition pathways. The clusters and cluster aggregates were observed to form regular patterns whose size and shape depended on decomposition environment and temperature.

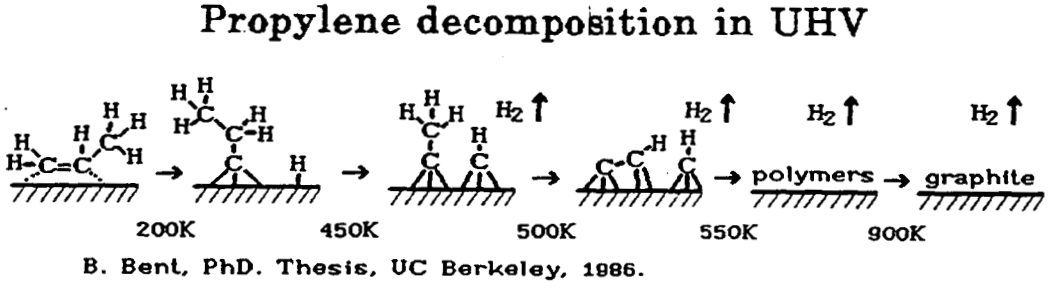


Figure 7.1. Schematic of thermal decomposition of propylene on Pt(111) in UHV as determined by HREELS and LEED studies. At temperatures up to 200 K, propylene adsorbs intact with the C=C-C bond axis parallel to the Pt(111) surface. At temperatures above 200 K propylene converts irreversibly to propylidyne by a loss of hydrogen. The C-C-C bond axis is perpendicular to the surface. The propylidyne species undergoes C-C bond scission and further loss of hydrogen forming ethylidyne and carbonyl species at temperatures above 450 K. Above 500 K more hydrogen is lost and the surface is characterized as having carbonaceous species of CH and $C_2H$ stoichiometry. Above 550 K, the surface hydrocarbons appear to form longer chains having wide-ranging stoichiometries and have thus been described as "polymeric". Above 900K, the carbonaceous species form graphite.

## 7.2 UHV STM studies of propylene decomposition

STM images of the clean Pt(111) surface and room temperature propylene covered surface show straight monatomic-height steps with approximately 150 Å terrace widths (see Fig. 7.2). The propylene covered surface was obtained by exposing the initially clean surface to approximately 100 Langmuir of pure propylene. This exposure is known to produce a saturation coverage of 0.25 monolayers [22]. The individual propylene molecules were not resolved at room temperature. As shown by previous STM studies of a similar molecule (ethylidyne, ≡C-CH3) by Land *et al.*, at room temperature the mobility of the adsorbed molecules on the Pt(111) surface is too large such that no atomic resolution STM images could be obtained [23].

Annealing the propylene covered surface to 500° C decomposes the propylene, and leaves C residues that form islands 30-50 Å in diameter and 1-2 Å in height, as shown in Fig. 7.3(a-c). The particles appear to be more or less uniformly distributed over the surface. These particles appear to be slightly larger in average diameter relative to the clusters observed for similar annealing temperatures of ethylene by Land *et al.* It should be noted that the individual particles are much larger than those expected for individual carbon atoms or even small carbon clusters. Clearly the existence of such large carbonaceous particles indicates that new C-C bonds are being formed as the propylidyne is dehydrogenated. The heights of the clusters are observed have a bimodal height distribution. The highest fragments are observed to be approximately one monatomic Pt step height (2.27 Å), while the shorter fragments have a height that is about 1/2 of a monatomic Pt step height. It is not clear how this quantized height distribution relates to the actual cluster composition, however, in consideration of C-C and Pt-C bond lengths, it seems that the clusters are not likely to be more than two atoms high. The role of the

electronic effects which are inherent to the STM experiment are of course also present which makes any interpretation beyond general approximations quite difficult.

It is also apparent that after annealing the steps are no longer straight. Small scale images show that there is some carbonaceous growth at the step edges. It appears that the carbonaceous fragments have significant carbonyl (Pt-C bonding) character as they are observed to be very stable on the surface, hindering the 2D-evaporation of Pt atoms from the Pt step to the terrace, causing pinning of the steps, and resulting in greatly increased surface kink densities (step roughening). It is interesting to note that Land *et al.* did not observe step pinning until annealing to 1200 K. This temperature is well above the temperature required for the formation of graphite. It may be that the lower temperature step pinning observed in this work occurred because the surface has a significantly higher step density and therefore different surface energetics. Another possibility is that the roughening is due to a carbon induced rearrangement of the Pt atoms at the step and the carbidic species formed from the propylene decomposition have a higher proclivity to Pt step-atom rearrangement.

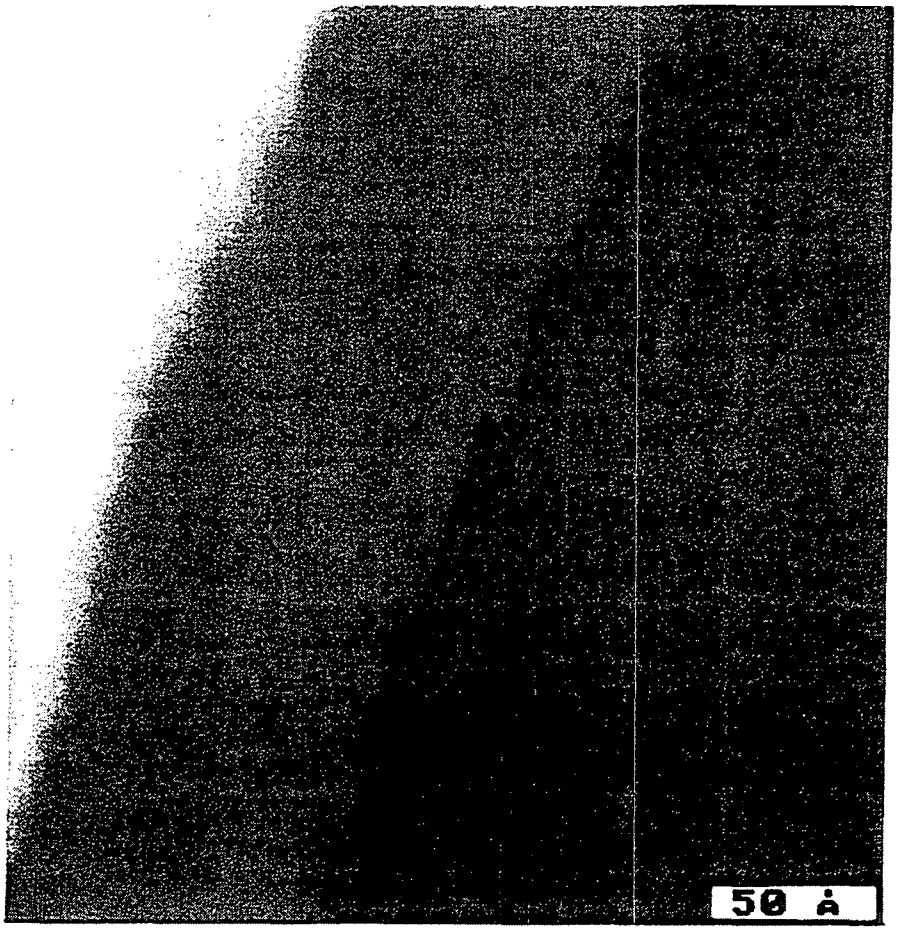


Figure 7.2. STM image of the room temperature propylene covered surface. Straight monatomic-height steps with approximately 150 Å terrace widths are observed, which is identical to the clean surface. The propylidyne molecules are too mobile at room temperature to be resolved with the relatively slow scanning STM tip.

Figure 7.3. (Following page) STM image in UHV after annealing the propylene covered surface to 500° C. (A) Carbonaceous clusters of approximately 30 - 50 Å in diameter are observed to be more or less uniformly distributed over the surface. Large scale images show a dramatic increase in the step kink density. (B and C) Smaller scale STM image of the hydrocarbon clusters. The aggregation of carbonaceous species at the step edges is widely observed and results in the pinning of the Pt steps.

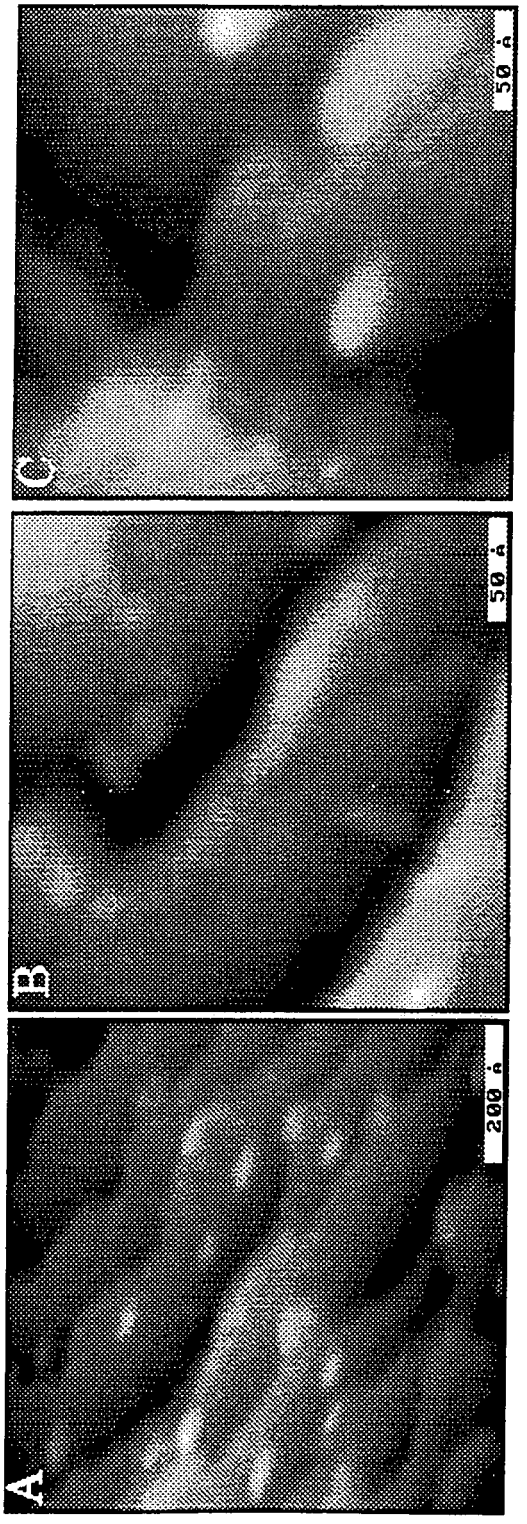
A
200 Å
B
50 Å
C
50 Å

## 7.3 Decomposition of propylene under catalytic reaction conditions

After preparation of the Pt(111) surface in UHV, the Pt surface was protected from contamination by adsorbing a sacrificial monolayer of sulfur that formed a $(\sqrt{3} \times \sqrt{3})R30^{\circ}$ ordered structure. The sample was transferred to the reactor cell in a small transfer chamber at $10^{-6}$ Torr pressure. Once in the cell the protective S layer was imaged with the HPSTM (see Fig. 7.4) and then removed by heating in a pure oxygen pressure of 1 atm. The oxygen was pumped down to $10^{-5}$ Torr and a mixture of propylene (10%) and $H_2$(90%) was admitted to the chamber with the sample at RT. A schematic of the sample preparation is shown in Fig. 7.5.

The STM images show the surface consisting of flat and featureless terraces and monatomic height steps that are also characteristic of the clean Pt(111) (see Fig. 7.6). It should be noted that under these conditions, the Pt surface will catalyze the hydrogenation of propylene to propane[24]. While the reactants and products were not detected in these experiments, it is expected that the STM measurements were carried out while the surface was catalytically hydrogenating propylene.

With the infrared-spot heater it was possible to anneal the surface while in this atmospheric pressure. It was found that the propylene did not decompose to form carbonaceous clusters until after annealing to 400° C. This is approximately 250° C higher temperature than necessary to form carbonaceous clusters in UHV or non-hydrogen containing environments (such as pure propylene or carbon monoxide). This indicates that the dehydrogenation/decomposition is inhibited by the presence of atmospheric pressures of hydrogen. This is likely due to the carbonaceous species being hydrogenated and desorbed as methane, in accordance with IR studies under similar conditions). Fig. 7.7 was taken after annealing the surface to 500° C. These images show

20-30 Å particles in elongated aggregates (200Å x 75Å). The diagonal lines running across the images are monatomic height steps. The elongated nature of the aggregates is not understood, but could be due to coadsorbate (hydrogen and/or propylene) interactions which force the hydrocarbons to the edges of adsorbate islands.

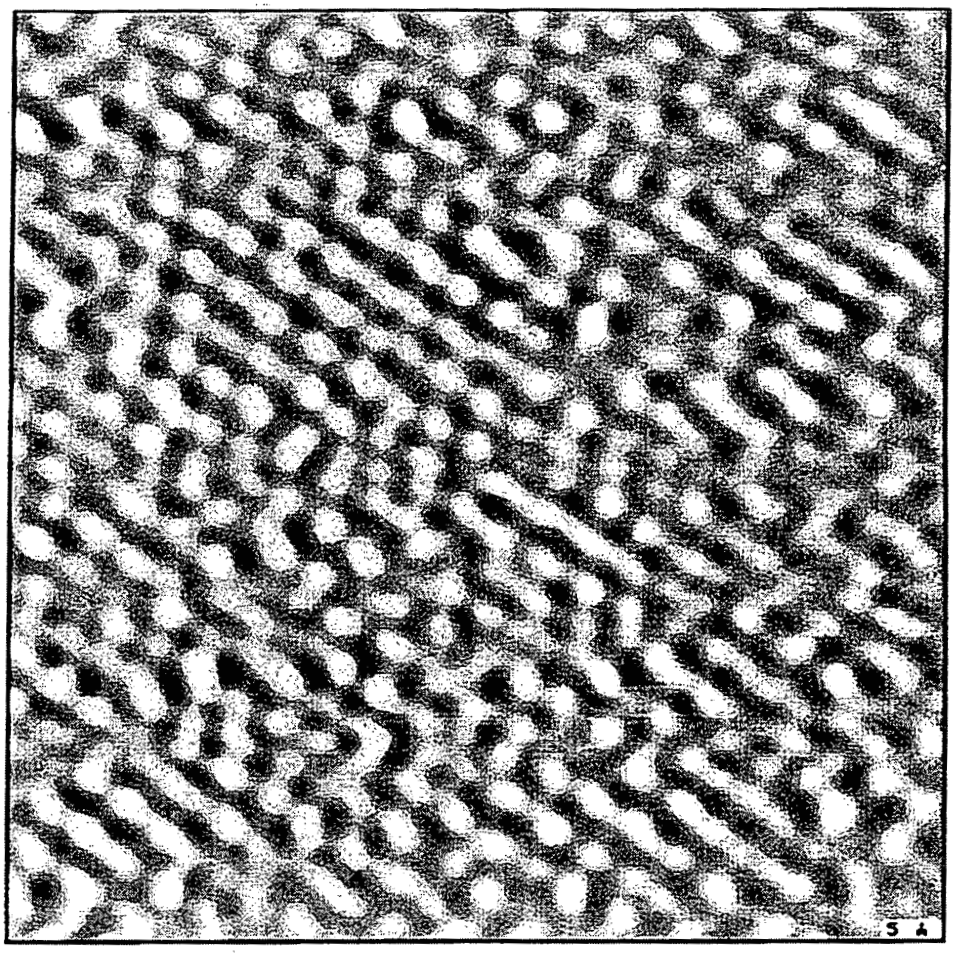


Figure 7.4. Current mode STM image of the Pt(111)($\sqrt{3}$ x $\sqrt{3}$)R30°-sulfur structure after *in vacuo* transfer from the UHV chamber to the HPSTM system. This sacrificial sulfur overlayer is removed by annealing in oxygen.

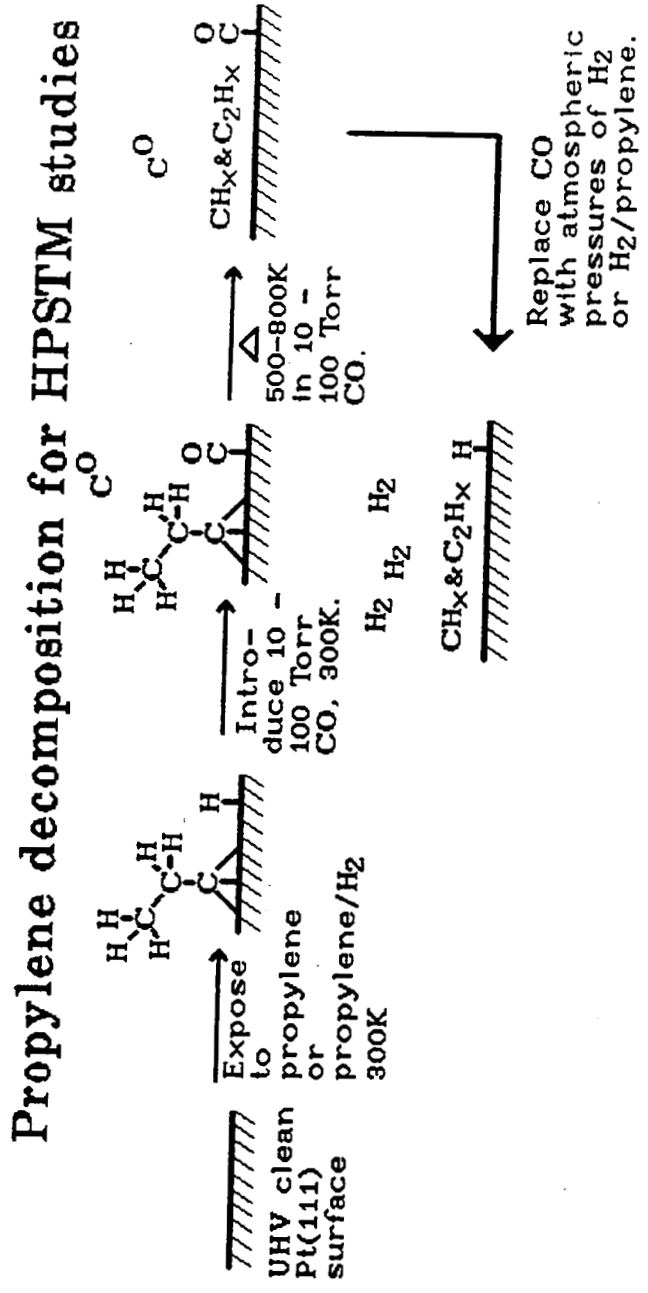


Figure 7.5. Schematic of the sample preparation in the HPSTM. After vacuum transfer, the sulfur overlayer is removed by annealing in oxygen. The oxygen is then removed by exposure to hydrogen environments. This surface is exposed to propylene environments and then the decomposition experiments are carried out from this point (depending on the environment and annealing temperature of interest).

Figure 7.6. (Following page) Topographic mode STM images of the Pt(111) surface in atmospheric pressures of a 90% hydrogen/propylene mixture at room temperature. In general, this surface shows flat and featureless terraces and monatomic height steps that are also characteristic of the clean Pt(111) surface. Under these conditions, it is expected that the Pt surface is catalyzing the hydrogenation of propylene to propane. A) The crossing steps in this image are at 60º relative to one another (along close-packed directions). B) This image shows numerous step terminations, giving the terraces a 'rod-like' appearance. A closer view of these step terminations is shown in C. D-F show close-up views of the surface which at the atomic-scale appears to be clean.

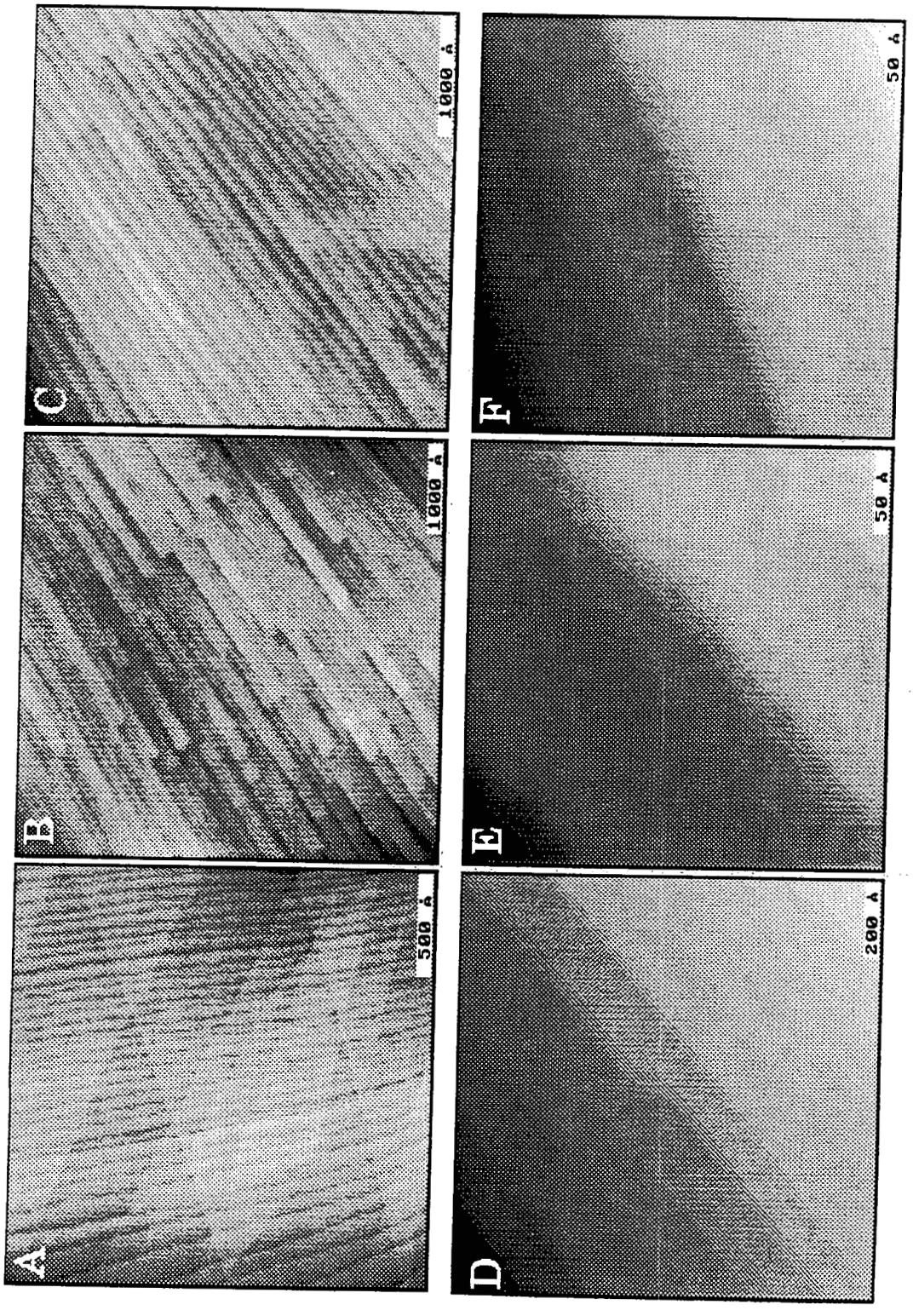
A
500 Å
B
1000 Å
C
1000 Å
D
200 Å
E
50 Å
F
50 Å

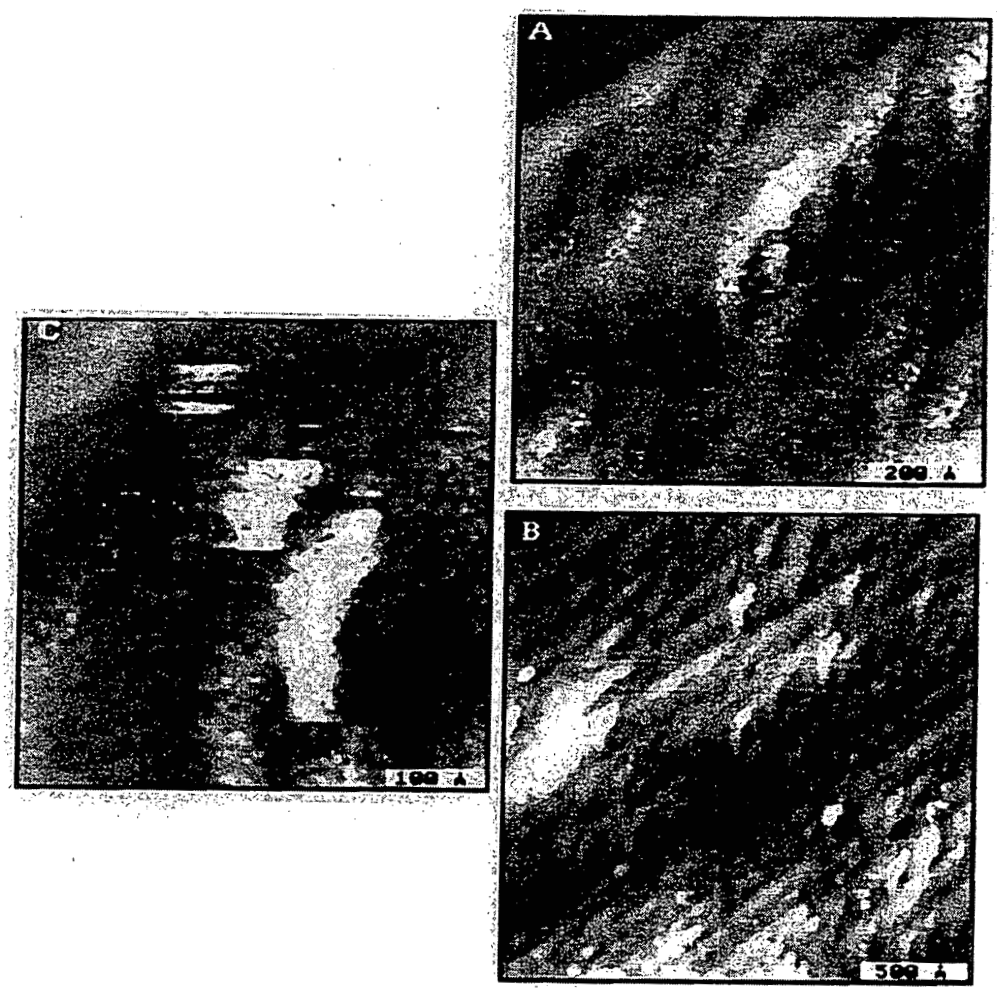


Figure 7.7. Topographic mode image after annealing the surface to 800 K in the atmospheric pressure of 90% hydrogen/propylene. The images show 20-30 Å particles in elongated aggregates (200Å x 75Å). A.) Large scale image, the diagonal lines running across the image are monatomic height steps.

## 7.4 Decomposition of propylene in carbon monoxide

Along with temperature dependence, it is also important to know whether the shapes of the clusters is dependent on the gas environment.

Following the sample preparation described in the previous section, after the Pt sample was exposed to the atmospheric pressure of the propylene/$H_2$ mixture at room temperature the chamber was pumped down and the cell was backfilled with pure carbon monoxide. The carbon monoxide was pre-purified by leaking in only the vapor from a liquid nitrogen-cooled manifold which contained an activated charcoal filter. This was done in order to prevent the introduction of iron carbonyls from the gas cylinder. Using this method the chamber was backfilled to pressures of approximately 0.1 atm. The stability of the propylene in this CO environment was then examined as a function of temperature.

Annealing the surface to 175° C resulted in the formation of decomposition products having a very unusual morphology (see Fig. 7.8(A)). The carbonaceous clusters formed crescent and overlapping crescent (star) clusters with overall dimensions of approximately 300 Å. these structures appear to be sensitive to steps as they all have the same orientation and the middle of the crescent extends out to the top of the step edge. this morphology might be explained by the presence of islands of carbon monoxide which do not intermix with the carbonaceous species but rather force them to cluster between the CO islands, as depicted schematically in Fig. 7.8.

It is also observed that these carbonaceous species have a high degree of mobility on the Pt surface. Removing the CO background pressure and replacing it with 1 atm. of $H_2$/propylene, the crescent-shaped islands are no longer observed (see Fig. 7.8(B)). In this environment, the decomposition products appear to have adopted a random morphology.

After annealing to higher temperatures (300° C), the carbonaceous species form circular islands, which have the same diameter as the terrace width (= 150 Å) and generally have a vertical corrugation of one monatomic step height (see Fig. 7.9). These islands appear to have some internal structure which indicates that the islands are not completely uniform in composition (i.e. have varying C/H ratios). These clusters are relatively stable on the surface as their structures do not noticeably vary after switching the CO environment to $H_2$/propylene.

Annealing to higher temperatures causes further loss of hydrogen and the clusters become smaller and more compact. This is evident in Fig. 7.10 which shows the clusters after annealing to 400° C (A) and 500° C (B).

It is clear that annealing in the CO environment results in the loss of hydrogen from the surface and produces carbonaceous clusters that are due to polymerization of the hydrocarbon fragments. It is interesting to note that there was no observed change in the step structure when annealing to the same temperature in CO as was done in UHV described in section 7.2. This seems to indicate either that the decomposition species are different or that perhaps the higher coverage of carbonaceous species on the surface inhibits the 2-D evaporation of Pt atoms from the step edges to the terraces.

Figure 7.8. (Following page) (A) After annealing to ~ 475 K, carbonaceous clusters were formed which have crescent and overlapping crescent (star) cluster morphologies. These clusters were observed to have overall dimensions of appproximately 300 Å and were sensitive to steps as they were found to have the same relative orientation, with the ends of the crescent initiating at the bottom of a step edge and the middle of the crescent extending out to the edge of the terrace. (B) The morphology of the crescent shaped clusters was observed to change when the CO environment was replaced with the 90% hydrogen/propylene mixture. In this environment, the decomposition products appear to have adopted a random morphology. Schematic representation of the proposed mechanism for the formation of the crescent shaped clusters under low temperature (~475 K) decompositions in CO environments. In this model, the CO is proposed to form islands which do not intermix with the carbonaceous species, but rather force them to cluster between the CO islands.

# $C_xH_y$ fragments on Pt(111)

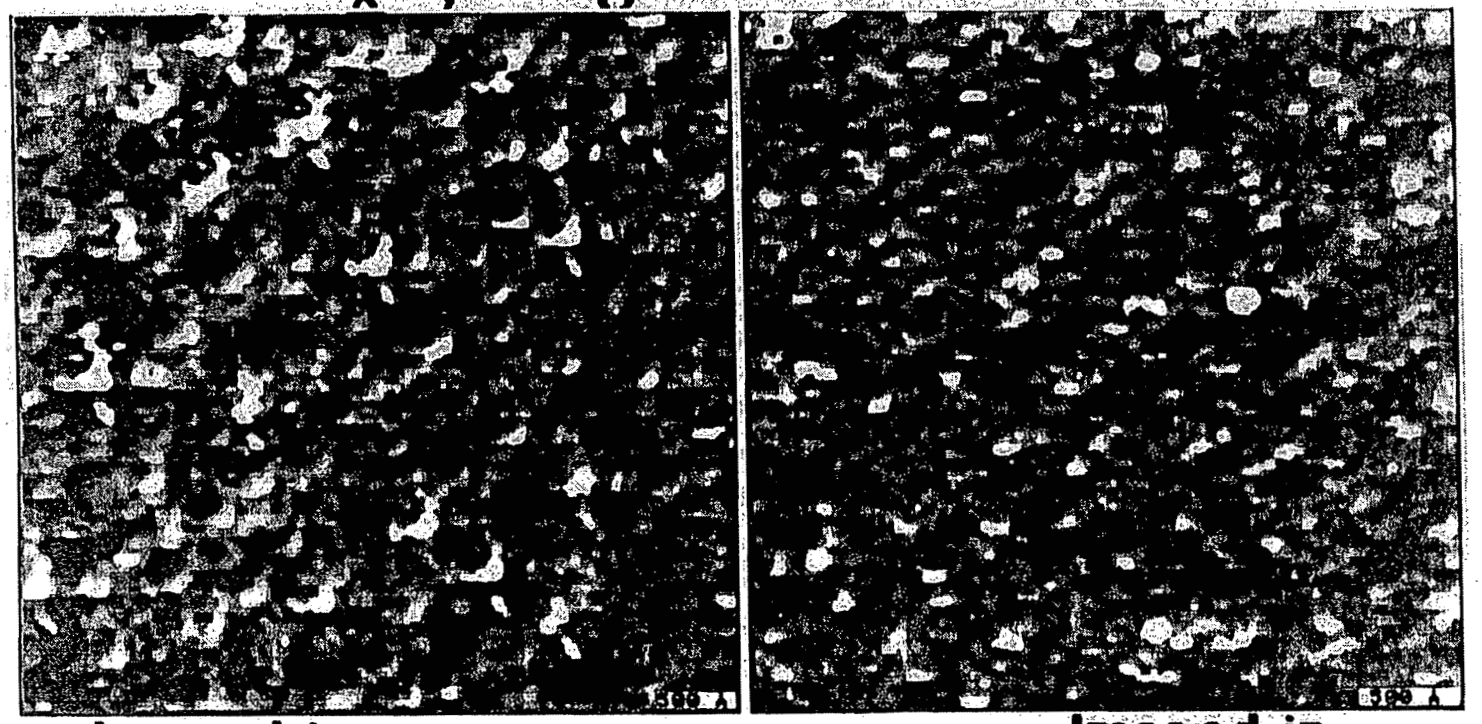

Imaged in
1 atm of CO

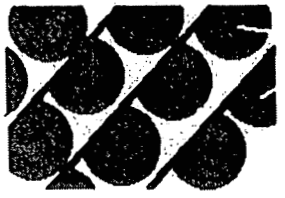

Imaged in
1 atm $H_2$ + $C_3H_6$

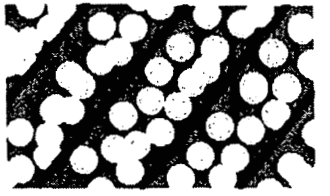

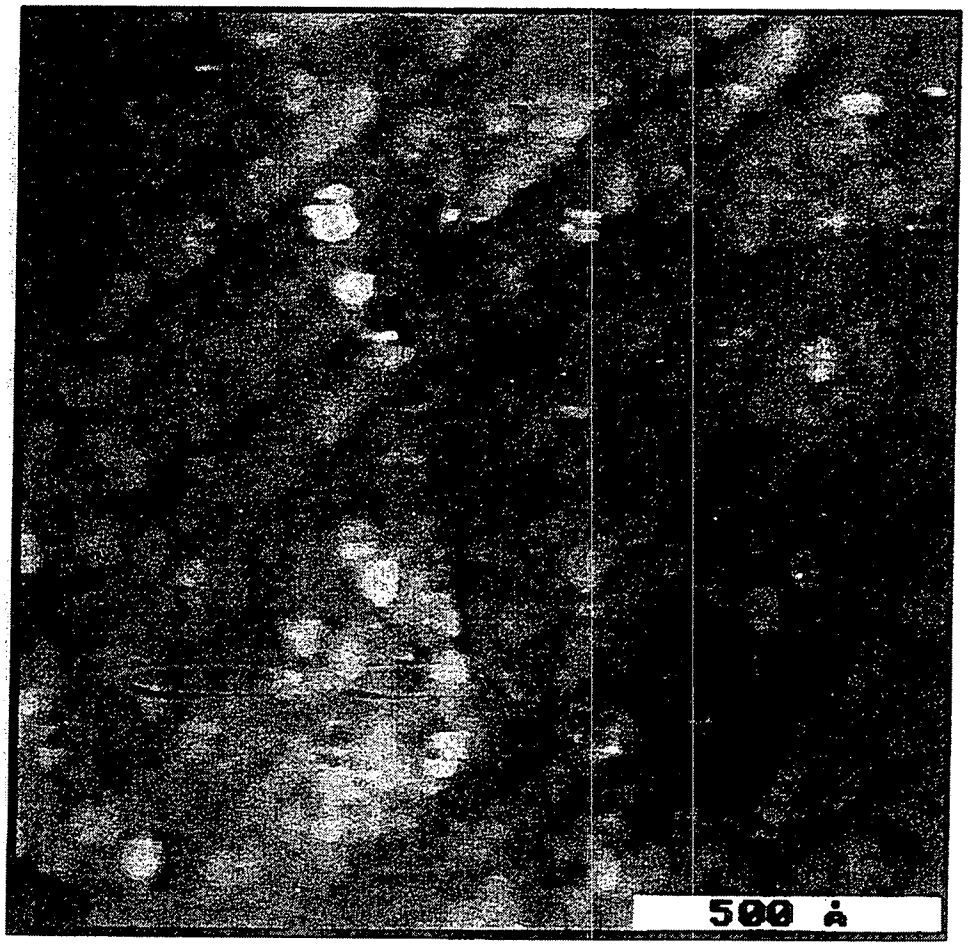


Figure 7.9. Annealing to 600 K in CO causes the hydrocarbons to form circular islands, which have the same diameter as the terrace width (≈ 150 Å) and generally have a vertical corrugation of one monatomic step height.

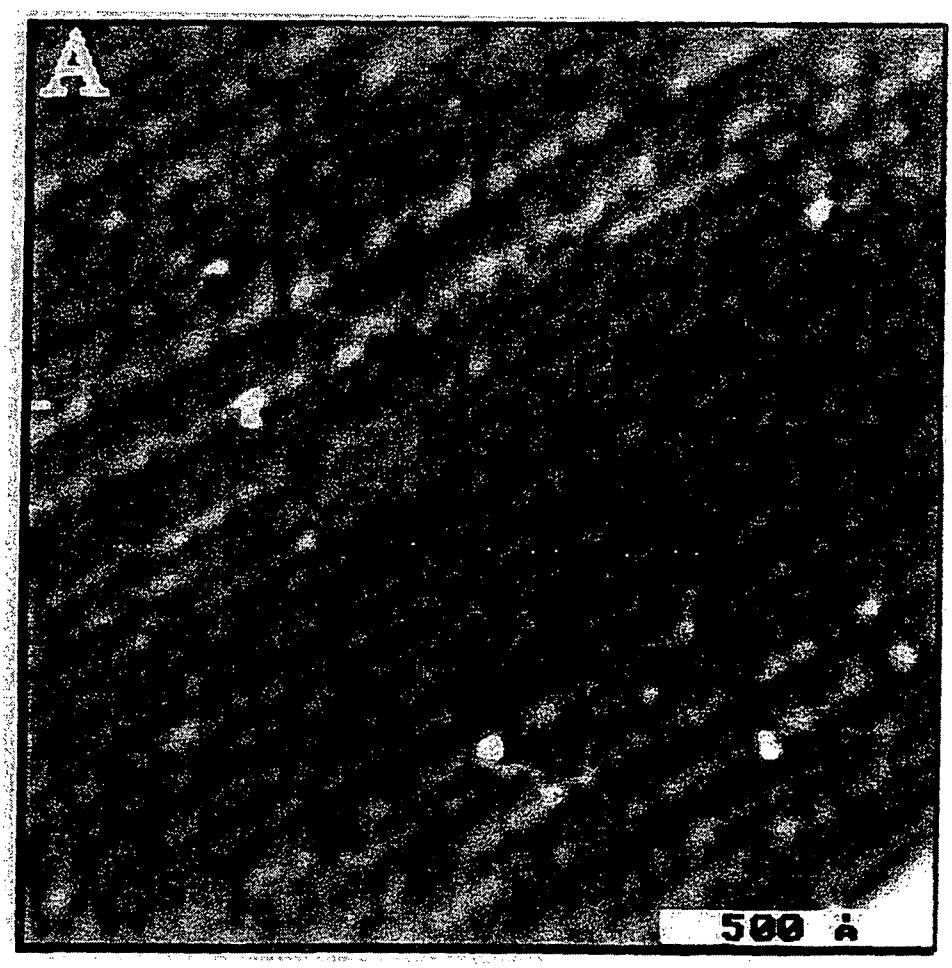


Figure 7.10. (A) Annealing to higher temperatures (700K) and (800K in Fig. B, on the following page) results in the further loss of hydrogen and the clusters become smaller and more compact, and decorate the terraces more regularly.

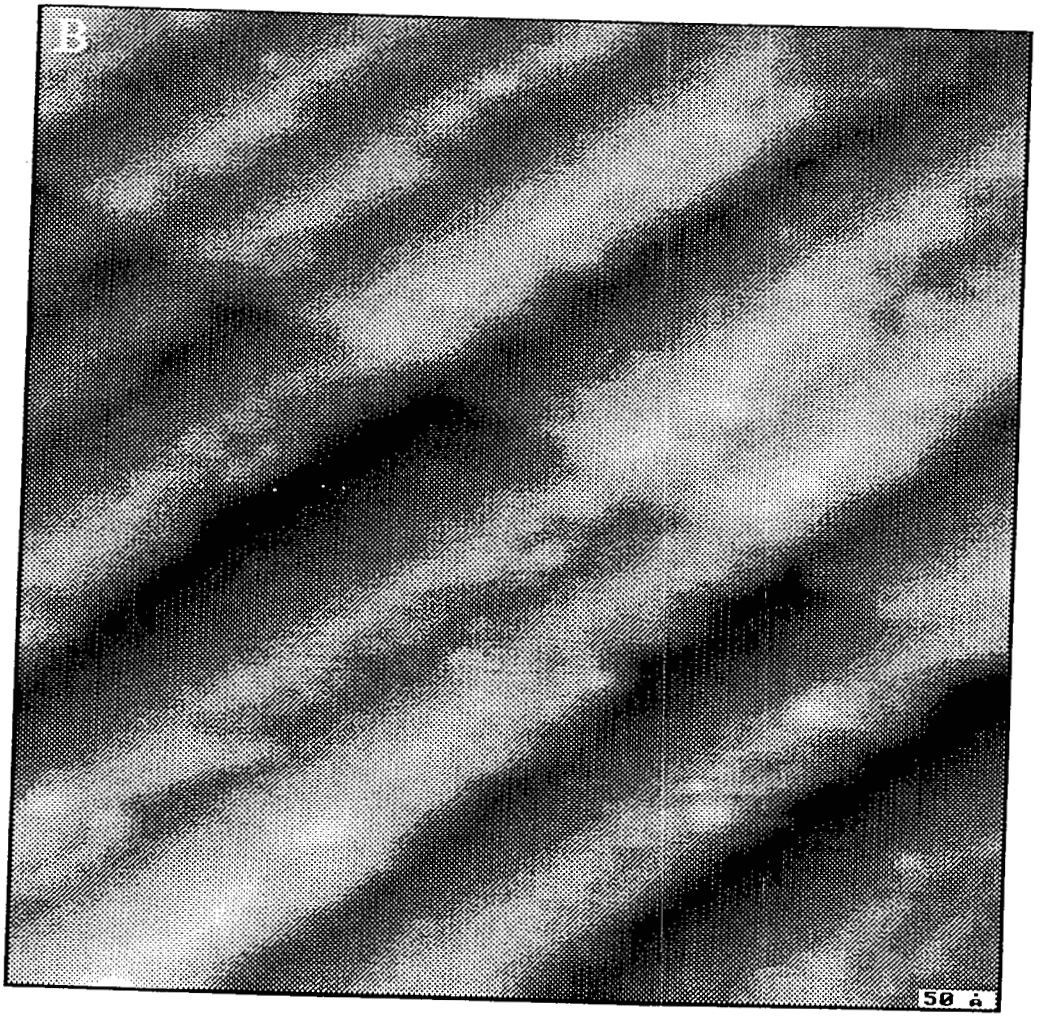
B
50 Å

## 7.5 Disproportionation

After annealing the surface in CO to 500° C, the CO was replaced with 25 Torr of hydrogen. The islands appear to be stable, however, upon annealing in hydrogen, the clusters change dramatically. After annealing to 600° C in hydrogen the surface appears to be clean. Under these conditions it is expected that the carbonaceous species should be largely hydrogenated and desorbed as methane. However, occasionally structures were observed on this surface which are very large (~ 200 Å diameter) but which appear to have a uniform morphology (see Fig. 7.11). In Fig. 7.11 aggregates of these clusters are observed to form "nanoflowers". The "flowers" are due to multiple tip effects, however, the small sub-units which make up the petals of the flower are observed individually over various areas of the surface and appear to be the result of agglomeration of hydrocarbons on the surface.

Previous IR studies [25] of annealing Pt surfaces which are covered with hydrocarbons in hydrogen environments have shown that a "disproportionation reaction" occurs. Shahid, *et al.* found that annealing platinum with preadsorbed propylene in vacuum above 430 K leads to the breakdown of the initially adsorbed species to give ethylidyne, implying C-C bond-breaking and an increasingly alkenyl-type dehydrogenated surface species, in agreement with previous UHV studies. They also observed that the addition of atmospheric pressures of $H_2$ at room temperature to the species from the adsorbed propylene leads largely to the removal of the surface species as propane and the residual surface species are alkyl in nature. Heating in the hydrogen environment to > 450 K causes these alkyl species to be largely removed as methane but the spectra of the remaining surface alkyl species show the presence of lengthened hydrocarbon chains. This disproportionation process was observed by following both the $CH_3$ and $CH_2$ IR stretch signals. They showed that the amount of $CH_3$ on the surface dramatically decreased while

the $CH_2$ signal increased. It was proposed that the terminal methyl groups are being hydrogenated and desorbed as methane while the remaining alkyl type hydrocarbons on the surface are significantly increasing their chain lengths.

It appears likely that under the conditions of the STM experiment, the carbon clusters are simultaneously being hydrogenated and forming longer chain polymers. It is interesting to note the uniformity of the subunits on the surface, which appear to have random orientations yet very uniform geometries.


Figure 7.11. After annealing the surface in CO to 800 K, the CO was replaced with 25 Torr of hydrogen. Annealing to 900 K in hydrogen produces a surface which appears to be free of clusters except for occasional regions where large clusters were observed to form. Aggregates of these clusters are observed here forming "nanoflowers". The "flowers" in this image are the result of multiple tip effects, however, the small sub-units which make up the petals of the flower are observed individually over various areas of the surface and appear to be the result of agglomeration of hydrocarbons on the surface, possibly due to a disproportionation process as proposed previously from IR studies.

## 7.6 Summary

The experiments described in this chapter have produced a number of significant new observations about the surface chemistry of hydrocarbons on Pt(111). These observations are summarized below.

The stability of propylene on Pt(111) and the morphology of decomposition products as a function of environment (UHV, and atmospheric pressures of hydrogen, $H_2$/propylene, and CO) and sample temperature (300K-900K) was investigated *in situ*, with the HPSTM. Clusters of carbonaceous material were formed as a result of various decomposition pathways. The cluster and cluster aggregates were observed to form regular patterns whose size and shape depended on decomposition environment and temperature.

UHV studies of the decomposition of propylene show that the dehydrogenation of propylene on Pt(111) at temperatures of 800 K leads to the formation of large two dimensional carbonaceous clusters on the surface with mono- or diatomic height. The particles are dispersed uniformly over the surface following the step and terrace geometry of the substrate. These particles were observed to cause step pinning. This varies significantly with previous studies by Land, *et al.* in which step pinning for ethylene decomposition was not observed until annealing to much higher (>1200 K) temperatures.

STM measurements were carried out on the initially clean Pt(111) surface while in atmospheric pressures of $H_2$/propylene mixtures. This is the first time STM experiments have been carried out on a surface while exposed to an atmospheric pressure of reactant gases in which the sample is expected to be catalytically active. In this environment the catalyst surface was observed to be stable on a mesoscopic scale, (i.e. there was no large

scale restructuring of the surface or formation of carbonaceous clusters characteristic of hydrocarbon decomposition).

With regards to the decomposition of propylene in hydrogen containing environments, it was observed that the temperature necessary to form carbonaceous aggregates is significantly higher (~250° C) than in non-hydrogen containing environments. This demonstrates the likelihood that for lower temperatures, the 'carbidic' carbon which is thought to play a significant role in catalytic reactions is likely to be comprised of individual carbon atoms, $C_2$ or $C_3$ species in hydrogen-rich environments but small agglomerates (which was observed to be the stable form in vacuum or non-hydrogen environments) in hydrogen-lean catalytic reactions.

The decomposition of propylene in atmospheric pressures of carbon monoxide showed dramatic differences relative to the hydrogen environments. Carbonaceous clusters were observed to form at temperatures characteristic of UHV environments. The clusters appeared differently to those observed in UHV, however, in that the coverage appeared to be significantly higher in the CO environment. This is likely due to the possibility that the equilibrium coverage of propylene on the Pt surface in atmospheric exposures is much higher than the 0.25 monolayer saturation coverage in UHV. (Note: It was observed that in accordance with numerous UHV studies, the CO did not decompose on the Pt surface even after annealing the clean sample in atmospheric pressures of CO). The morphology of the low temperature decomposition clusters were observed to depend on the environment. This is proposed to be the result of lateral interactions between coadsorbates and appears to play a very significant role for the creation of regions of the transition metal surface which are free of carbonaceous clusters and may therefore be active for catalysis. These results indicate that the stable forms of the carbonaceous clusters generated under hydrogen-free environments are flat (1-2 atom height) clusters whose sizes depend on the degree of decomposition (they become smaller and more

uniform as the decomposition temperature is increased). As a result, it is likely that these species play a very different role in catalytic reactions than the carbon present in hydrogen environments.

Finally, it was observed that the Pt(111) surface was stable under all of the atmospheric pressure conditions. The hydrocarbon clusters were observed to conform to the underlying transition metal catalyst surface structure. It may be that the surface is stabilized by high coverages of the decomposition products since the only occurrence of significant reconstruction of steps occurred in lower coverage UHV decomposition conditions.

[1] J. Barbier, Catalyst Deactivation, B. Delmon and G.F. Froment (Editors), Elsevier Science Publishers, B. V., Amsterdam, 1987.

[2] P. G. Menon, J. of Molec. Catalysis, **59**, 207 (1990).

[3] J. Barbier, G. Corro, Y. Zhang, J. P. Bournville, and J. P. Franck, Appl, Catalysis, **16**, 169 (1985).

[4] S.M. Davis and G.A. Somorjai: The Chemical Physics of Solid Surfaces and Heterogeneous Catalysis, Vol. 4, D.A. King and D.P. Woodruff eds. (Elsevier, Amsterdam, 1983).

[5] S.M. Davis, F. Zaera and G.A. Somorjai, J. Catal. **77**, 439 (1982), and references therein.

[6] S.J. Thomson and G.J. Webb, J. Chem. Soc., Chem. Commun. (1976) 526.

[7] J. Horiuti, K. Miyahara, Hydrogenation of Ethylene of Metallic Catalysts, NSRDS-NBS, **13** (1968).

[8] P.H. Otero-Schipper, W.A. Wachter, J.B. Butt, R.L. Burwell, Jr., and J.B. Cohen, J. Catal. **50**, 494 (1977).

[9] S.M. Davis and G.A. Somorjai, J. Catal. **65**, 78 (1980).

[10] C.P. Khulbe and R.S. Mann, Proc. 6th Int. Congr. Catal., Lond., 447 (1976).

[11] J.L. Gland, F. Zaera, D.A. Fischer, R.G. Carr, E.B. Kollin, Chem. Phys. Lett. **151**, 227 (1988).

[12] R.J. Koestner, J. Stöhr, J.L. Gland, J.A. Horsley, Chem. Phys. Lett. **105**, 333, (1984).

[13] L.L. Kesmodel, L.H. Dubois, G.A. Somorjai, J. Chem. Phys. **70**, 2180 (1979).

[14] P.C. Stair, G.A. Somorjai, J. Chem. Phys. **66(5)**, 2036, (1977).

[15] G.A. Somorjai, Surf. Sci. **242**, 481 (1991).

[16] G.A. Somorjai, M.A. Van Hove, B.E. Bent, J. Phys. Chem. **92**, 973 (1988).

[17] M. Salmeron, G.A. Somorjai, J. Phys. Chem., **86**, 341 (1982).

[18] R.J. Koestner, J.C. Frost, P.C. Stair, M.A. Van Hove, G.A. Somorjai, Surf. Sci. **116**, 85 (1982).

[19] For a few references describing structural observations of propylidyne, see: M. Salmeron and G.A. Somorjai, J. Phys. Chem. **86,** 341, (1982) 341. R.J. Koestner, M.A. Van Hove and G.A. Somorjai, J. Phys. Chem. **87**, 203, (1983). R. J. Koestner, J.C. Frost, P.C. Stair, M.A. Van Hove and G.A. Somorjai, Surf. Sci. **85** , 116, (1982). K.M. Ogle, J.R. Creighton, S. Akhter and J.M. White, Surf. Sci. **169**, 246, (1986). N.R. Avery and N. Sheppard, Proc. R. Soc. Lond. A **405**, 1, (1986).

[20] B.E. Bent, Ph.D. Thesis, 1986.

[21] T.A. Land, T. Michely, R.J. Behm, J.C. Hemminger, and G. Comsa, J. Chem. Phys. **97(9)**, 6774 (1992).

[22] R.J. Koestner, J.C. Frost, P.C. Stair, M.A. Van Hove and G.A. Somorjai, Surf. Sci. **116**, 85 (1982).

[23] T.A. Land, T. Michely, R.J. Behm, J.C. Hemminger, G. Comsa, J. Chem. Phys. **97**, 6774 (1992).

[24] P.H. Otero-Schipper, W.A. Wachter, J.B. Butt, R.L. Burwell, Jr., and J.B. Cohen, J. Catal. **50**, 494 (1977).

[25] G. Shahid and N. Sheppard, Spectrochimica Acta, **46**, 999 (1990).

# CHAPTER 8

# STM TIP-INDUCED CATALYSIS

## 8.1 Introduction

In the previous chapters it was demonstrated that through the development of the HPSTM it is possible to elucidate *in situ*, the atomic structure of catalyst surfaces in the course of a chemical reaction in real conditions. A logical extrapolation and refinement of this concept is to see if, in addition to atomic resolution images, the tip of the STM can act catalytically to induce surface reactions with atomic spatial resolution. A precursor to this idea is to be found in the numerous experiments carried out to pattern the surface and to manipulate atoms using the STM tip [1].

In this chapter evidence is presented which shows for the first time the chemical activity of a platinum STM tip that catalyzes with nanometer spatial resolution the rehydrogenation and re-oxidation of carbonaceous species on the surface of Pt(111). The tips used were made of Pt(80%)-Rh(20%) wires and had an apex radius of approximately 100 Å or less, as estimated from measurements of atomic step heights and widths. The samples were prepared as described in the previous chapter for the generation of carbonaceous clusters in atmospheric pressures of carbon monoxide. After UHV sample preparation and *in vacuo* transfer to the HPSTM, the sulfur protective layer was removed and a mixture of propylene (10%) and $H_2$(90%) was admitted to the chamber with the sample at RT. Carbonaceous clusters on the surface were formed by heating in a vacuum (after pumping the propylene - $H_2$ gas mixture) or after backfilling the cell with pure CO. A discussion of this process and the resulting clusters formed is provided in the previous chapter.

## 8.2 STM tip catalysis in hydrogen environments

The STM tip-induced catalysis was first observed to occur in atmospheric pressures of propylene (10%) and $H_2$ (90%). To observe the tip induced catalysis, the cell was filled up to one atmosphere of the propylene (10%)-$H_2$ (90%) mixture and maintained at RT. The surface is uniformly covered with carbonaceous clusters as shown in Fig. 8.1. The reaction was observed to take place on this surface only when the tip is "activated" by pulses of several tenths of a volt. This is shown in Fig. 8.2. In the upper third of the image, the characteristic clusters formed by the previous heating of the propylene layer to 550 K are observed, aligned following the direction of the step edges. A pulse was applied at the position labeled "p" and produced the 15 Å elevation in this position that indicates material being transferred from the tip to the substrate by the pulse. Below this line, as the tip continues to scan, the clusters have been removed. If the tip is immediately moved to a fresh new area while it remains active, all the clusters are again removed from the area scanned as shown in Fig. 8.3. Eventually, the activity of the tip decays (its "lifetime" being of the order of minutes), presumably by hydrocarbon contamination that prevents $H_2$ adsorption and dissociation at the apex. It is in this deactivated state that the image in Fig. 8.4 was obtained after the central square was imaged first while the tip was active (Fig. 8.3). The step structure clearly indicates that these two images are of the same area. Catalytic activity can be restored once more by additional pulses to remove contaminant material as shown in the sequence of images in Fig. 8.4. In the first image (8.4(a)), a large area covered by clusters is observed (see expanded area), together with a large feature marked "f" in the upper right corner. The feature appears double due to a double tip apex. The tip was catalytically inactive during this entire image acquisition. Immediately afterward, the tip was pulsed near the center of the same area. The two bumps in the center of Fig. 8.4(b) are the result of the two pulses applied. The active tip obtained is used to image the same area as shown in 8.4(b). All the clusters are removed

in the top part of the image (see expanded area). The large feature f is also being thinned out (its height is reduced in half after passage of the active tip). The tip is suddenly turned off or deactivated at a point in the line marked by the arrows. For this reason the clusters in the region below remain intact. This process of activation-deactivation can be followed and continued many times. A further activation pulse, whose marks are seen on the right edge of Fig. 8.4(c), produces again a very active tip that removes all clusters in the area, including the large feature, as seen in this image. Only the marks in the center "$P_1$", (due to the first activation pulses), and on the right side "$P_2$" (due to the second series of pulses) remain. The bump at position f in the upper right area also remain from the large feature in Fig. 8.4(a) and (b). This indicates that these bumps are made of chemically inactive materials that cannot be rehydrogenated by the tip.

It was observed that the hydrocarbons which surround an area were extremely stable as a region could be imaged hours later with no discernible back-diffusion of clusters into the area initially cleaned by the tip. Since the gas environment is a mixture of hydrogen and propylene, this 'apparently clean' area is expected to be covered by a layer of propylidyne.

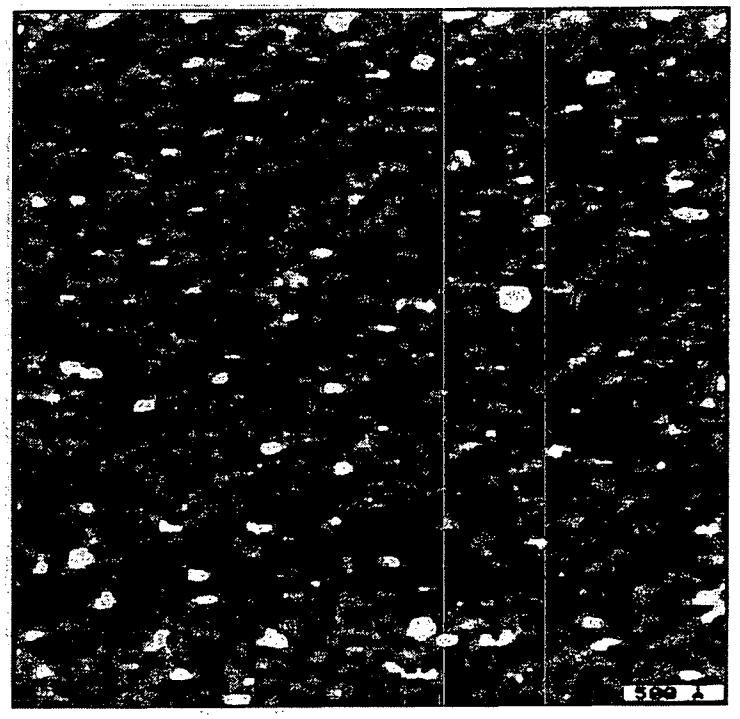

Figure 8.1. STM image of a Pt(111) surface covered with hydrocarbon species generated by exposure to propylene gas. Images taken in constant height mode at 0.1 V bias and 1.3 nA current. After heating the adsorbed propylidyne to 500 K, clusters form by polymerization of the $C_xH_y$ fragments, randomly decorating the terraces.

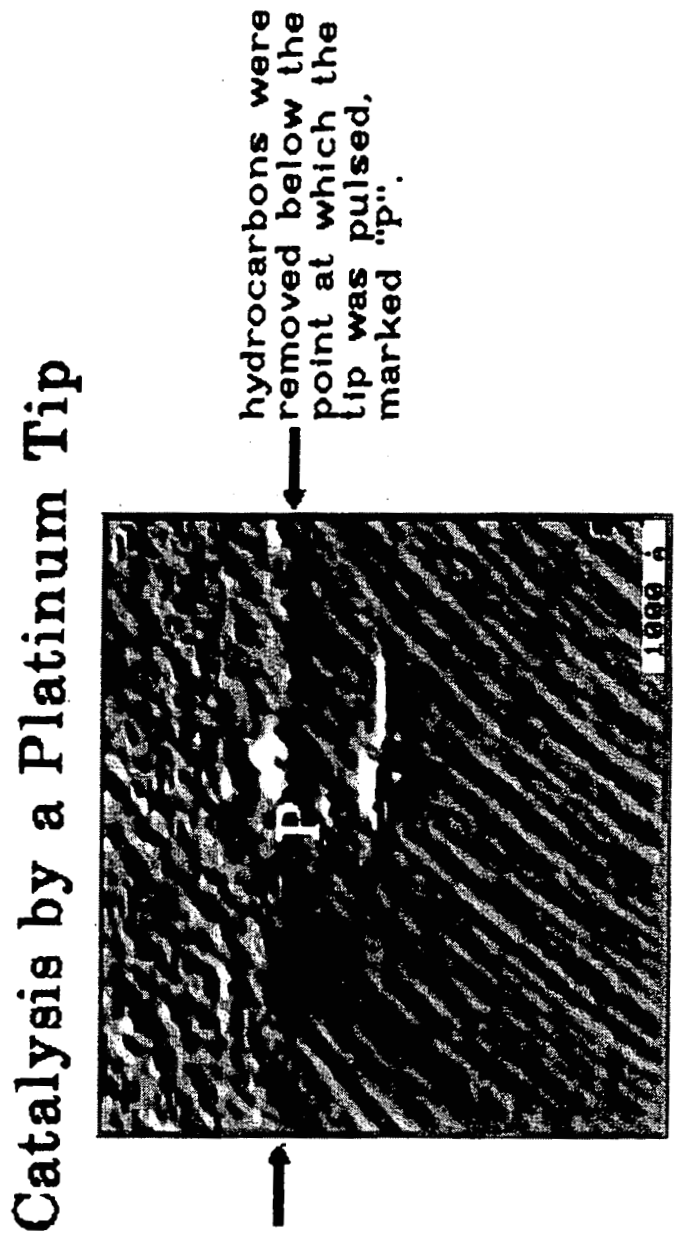


Figure 8.2. The catalytic action of the STM Pt tip is illustrated in this image corresponding to a surface covered by carbonaceous clusters as in Fig. 8.1. Imaging is done in one atmospheric pressure of a mixture of propylene (10%) and $H_2$ (90%) and at RT. In this image carbon clusters are imaged in the top 1/3 of the image while the tip was inactive. A voltage pulse of 0.9 V was applied at the position marked 'p', leaving a mound of material 15 Å in height. This process produces a chemically active Pt tip that catalyzes the removal of all clusters from the remaining 2/3 of the image. Only the lines corresponding to the steps are visible.

Figure 8.3. (Following page) (a) Area which is initially covered with carbonaceous clusters. (b) After activating the tip in a different location, the area shown in (a) was scanned. The carbonaceous clusters are entirely removed from this area, and only monatomic Pt steps are observed. (c) After tip deactivation, a slightly larger image was taken of this same area. The region where the hydrocarbons were removed is clearly visible as are the carbonaceous clusters in the surrounding area. During the course of hundreds of experiments, the build up of 'piles' of clusters was *never* observed. As shown in (c) the edges of the square show no evidence of clusters piling up.

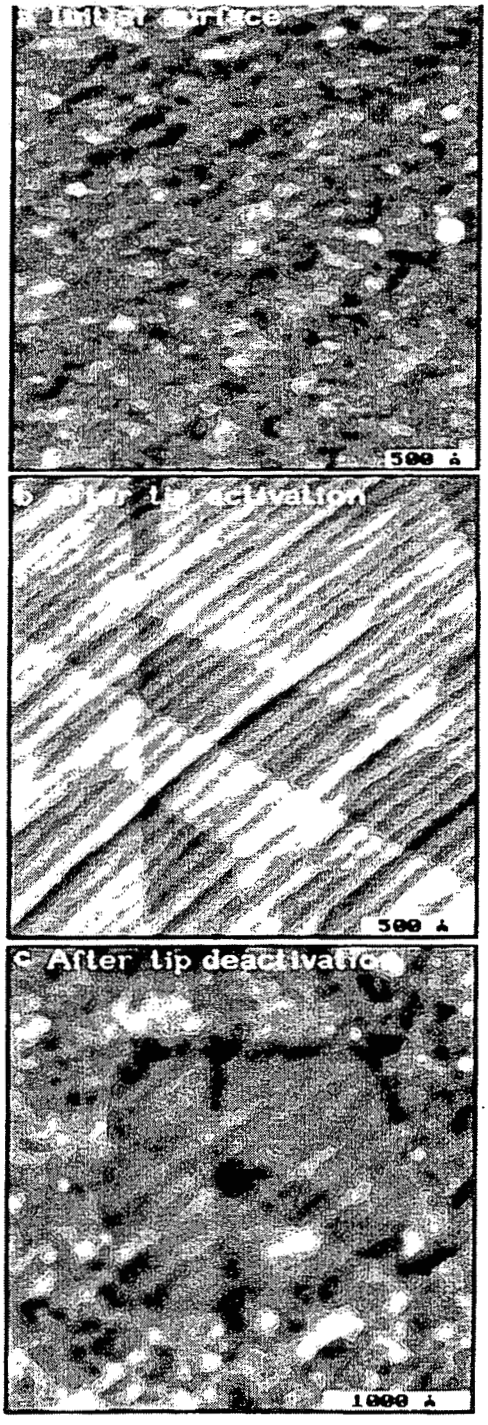
500 Å
500 Å
1000 Å

Figure 8.4. (Following page) Experiments illustrating the switching of the tip between catalytically active and inactive states. In (a) a 5,000 x 5,000 Å image is obtained with an inactive tip. As seen in the expanded area in the right-hand side (a'), the surface is covered by clusters as in figure 1(b). A large feature marked f is observed on the upper right side that serves as a marker. It appears double (f and f ') due to a double apex tip. After image acquisition, two pulses of 0.9 V were applied while the tip was positioned near the center of the area. These pulses produced the bumps marked by $P_1$ in (B). The tip is activated by these pulses and in a new scan (b), it catalyzes the removal of all clusters from the top 1/3 of the area, as well as the thinning of structure f (its height is reduced in half after this scan). At the line marked by the arrows the tip suddenly becomes inactive and no cluster removal occurs in the bottom 2/3 of the image. See expanded area (b') on the right. Two new pulses (at position marked $P_2$ in (c)) restore once more the activity of the tip and the subsequent scan removes all carbonaceous clusters, including the large feature f, where a bump remains that is probably made of chemically inert material.

# Catalysis by active Pt tips

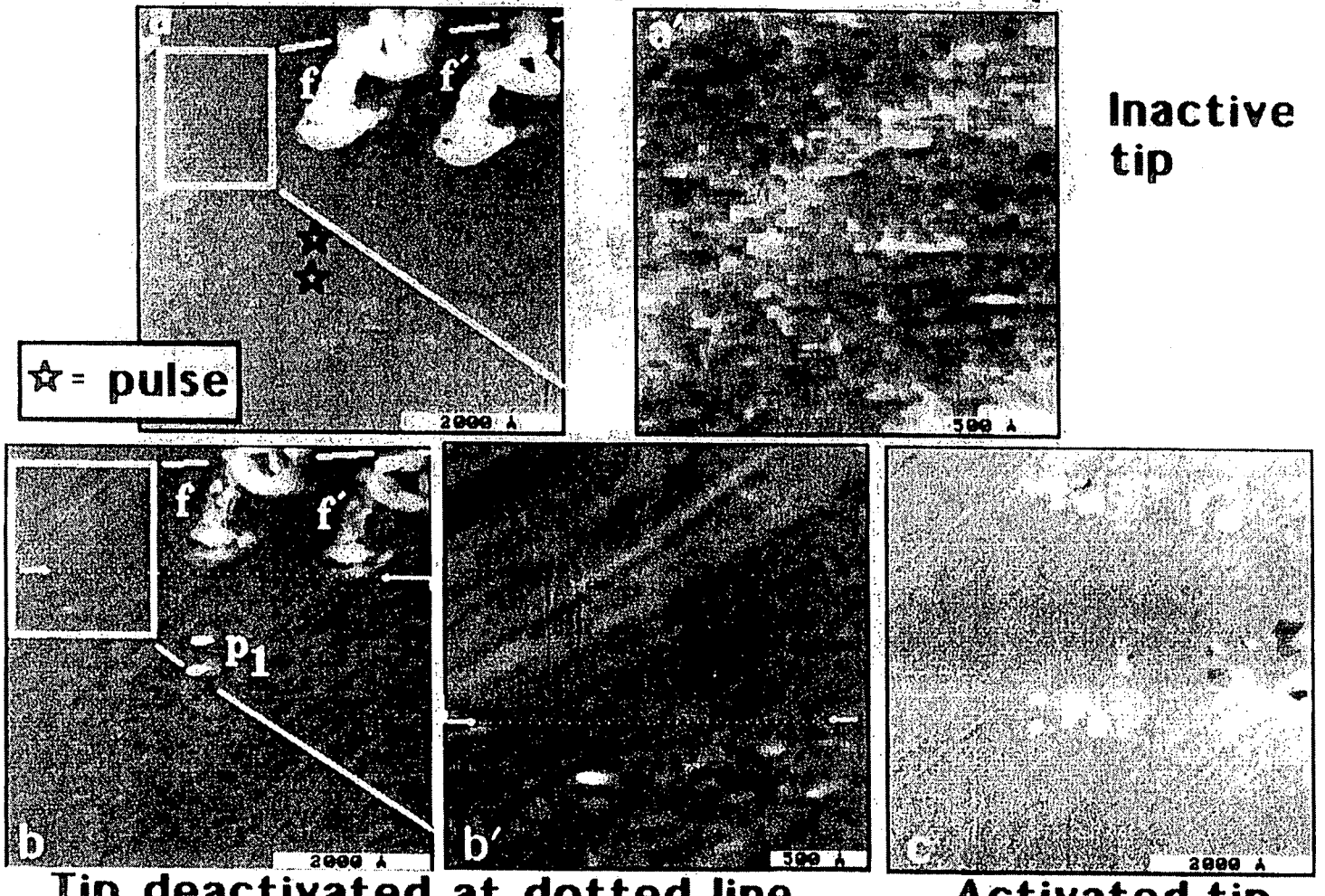

## 8.3 STM tip catalysis in oxygen environments

One of the questions that arises from the results described in the previous section is whether or not the catalytic effect will only occur in hydrogen environments. It was found that in numerous experiments carried out in UHV and atmospheric pressures of carbon monoxide the tip catalysis never occurred. At this point it was proposed that the catalytic effect was the result of STM tip-induced hydrogenolysis of the carbonaceous clusters, generating smaller hydrocarbon fragments which have sufficient mobility on the surface to be 'invisible' to the STM.

The oxidation of hydrocarbons on Pt is widely acknowledged to have lower activation barriers than hydrogenolysis of similar species [2]. The activation energy for hydrogenolysis is typically of the order of 50 - 80 Kcal/mol whereas the activation energy for oxidation is approximately 15 Kcal/mol. Similarly, both oxygen and hydrogen readily dissociatively chemisorb on Pt at room temperature [3]. From this perspective, it might be expected that if it is possible for STM tip-induced hydrogenolysis to occur, then STM tip-induced oxidation is also very likely and may occur even more readily.

To check this, the sample was prepared and the tip catalysis was observed in the hydrogen environment. Afterward, the hydrogen containing atmosphere was pumped away and the chamber was backfilled with pure oxygen. Once back in tunneling range and observing the hydrocarbon clusters (see Fig. 8.5(a)), the tip was pulsed and the same area was imaged repeatedly (Fig. 8.5(b). In this image, the removal of the hydrocarbons was clearly observed. This removal was observed many times and although there was never a case where all hydrocarbon clusters were removed from a region, it was not possible to say whether the hydrocarbons were removed more or less easily in an oxygen atmosphere compared to in hydrogen environments. It was observed, however, that once the tip was 'activated' in an oxygen atmosphere that it tended to remain active longer than when in an

atmospheric pressure of propylene/hydrogen. It is not yet clear, however, whether the tip lifetime in the propylene/hydrogen environment is due to the presence of propylene in the background.

Figure 8.5. (Following page) The catalytic action of the STM Pt tip is illustrated in these two images. (a) This is the surface prior to bias pulsing and clearly shows the surface having an extremely high coverage of hydrocarbons, most of which are removed after repeated scans with the activated tip, as shown in (b). (b) was obtained after ten scans of the area shown in (a).

# Tip-Induced Catalysis in Oxygen.

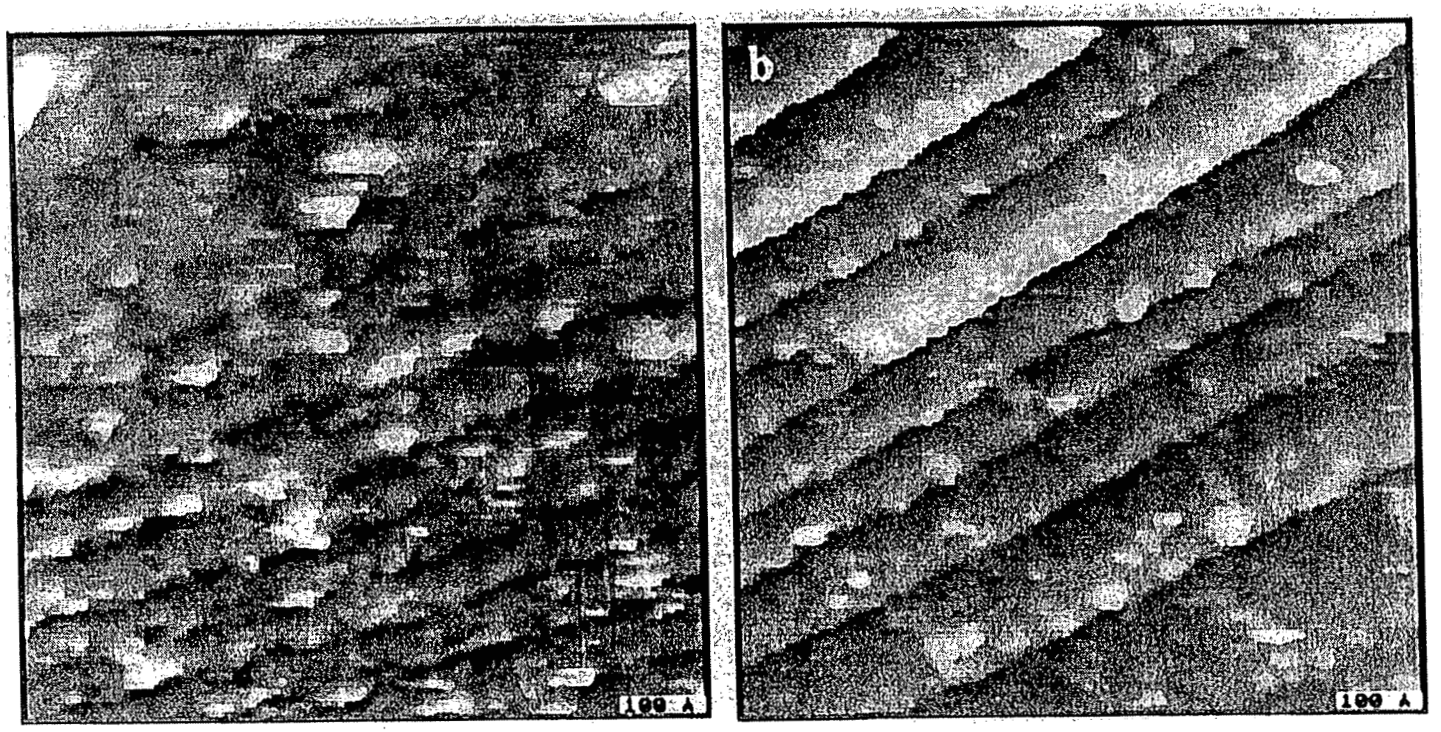


Before tip pulse

After tip pulse

## 8.4 Tip catalysis 'cluster by cluster'

It was mentioned in the previous chapter that the carbonaceous clusters were observed to have a bimodal height distribution of ~1.2 Å and 2.3 Å. An example of an STM image with clusters having the two different heights is shown in Fig. 8.6. The cursor line 'a' shows a 'low' cluster having a height of about 1/2 a Pt monatomic step and the cursor line 'b' shows a 'high' cluster having a vertical corrugation of approximately 1 Pt monatomic step height. This has been observed previously for the decomposition of ethylene and was proposed to be due to the formation of 1 and 2-carbon atom high clusters on the surface [4].

During the course of investigating the properties of STM tip-induced catalysis it was observed that the rate of the removal of the hydrocarbon clusters was dependent on the conditions of their formation. In general it was found that to remove hydrocarbon clusters that formed by propylene decomposition at higher temperatures required more STM scans (longer tip residence times) than to remove clusters that were formed at lower temperatures. Similarly, hydrocarbon clusters which were formed at very high annealing temperatures (> 800 K) were not removed at all. At this temperature, the degree of dehydrogenation is very large and graphitic clusters are produced that are much more difficult to rehydrogenate at RT.

By forming carbonaceous clusters at moderate annealing temperatures (≈ 500 K), it was found to be possible to remove them with the STM tip in a more controlled 'cluster by cluster' fashion. An example of this is shown in the series of images in Fig. 8.7. In this series, individual clusters and fractions of clusters are removed one at a time. Careful analysis of which clusters are removed in several image sequences shows that both the 'high' and the 'low' clusters are removed with equal efficiency and that the 'high' clusters

are completely removed as opposed to being converted into 'low' clusters. A distribution of the removal of 'high' and 'low' clusters is shown in Fig. 8.8

It was also observed that there was no dependence on cluster location on the surface. The clusters were removed with approximately equal efficiency on the middle of a terrace or at the bottom or top of a step edge. Fig. 8.9 shows two series of images taken in different areas where two clusters were observed prior to bias pulsing and after one of the clusters was removed, leaving the other undisturbed.

Figure 8.6. (Following page) STM image showing 'low' and 'high' clusters. (a) line cursor profile showing a 'low' cluster having a height of approximately 1/2 a monatomic Pt step height. (b) a line cursor profile showing a cluster which has a height of approximately 1 Pt monatomic step height. Throughout these experiments, a bimodal height distribution of the clusters was observed.

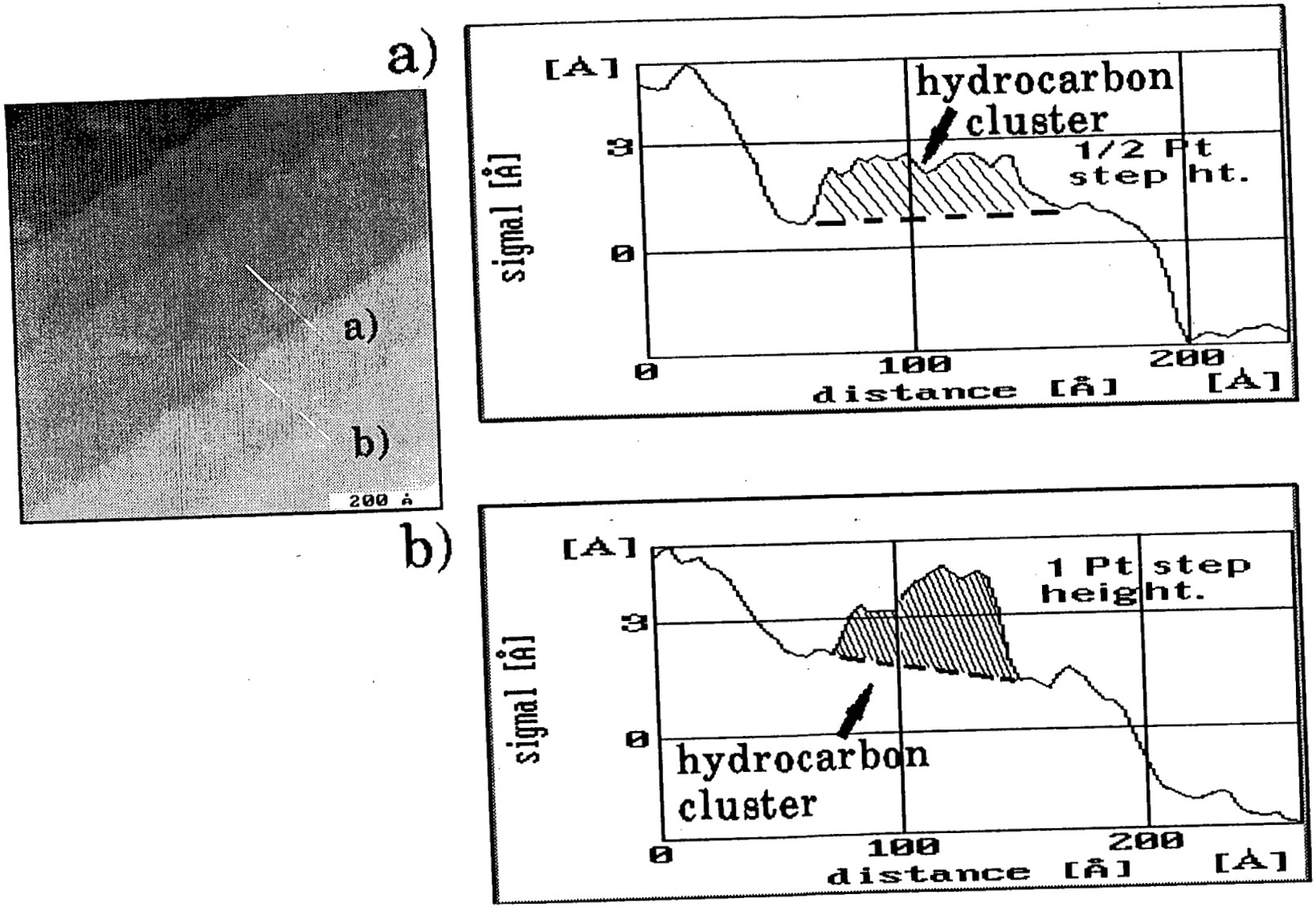
a)
a)
b)
200 Å
[A]
hydrocarbon
cluster
1/2 Pt
step ht.
signal [Å]
3
0
0
100
200
distance [Å]
[A]
b)
[A]
1 Pt step
height.
signal [Å]
3
0
hydrocarbon
cluster
0
100
200
distance [Å]
[A]

Figure 8.7. (Following page) Series of STM images showing the removal of individual or parts of individual clusters. The circles mark clusters which were at least partially removed in subsequent images.

# Catalysis by STM Tip: 'Cluster by Cluster'

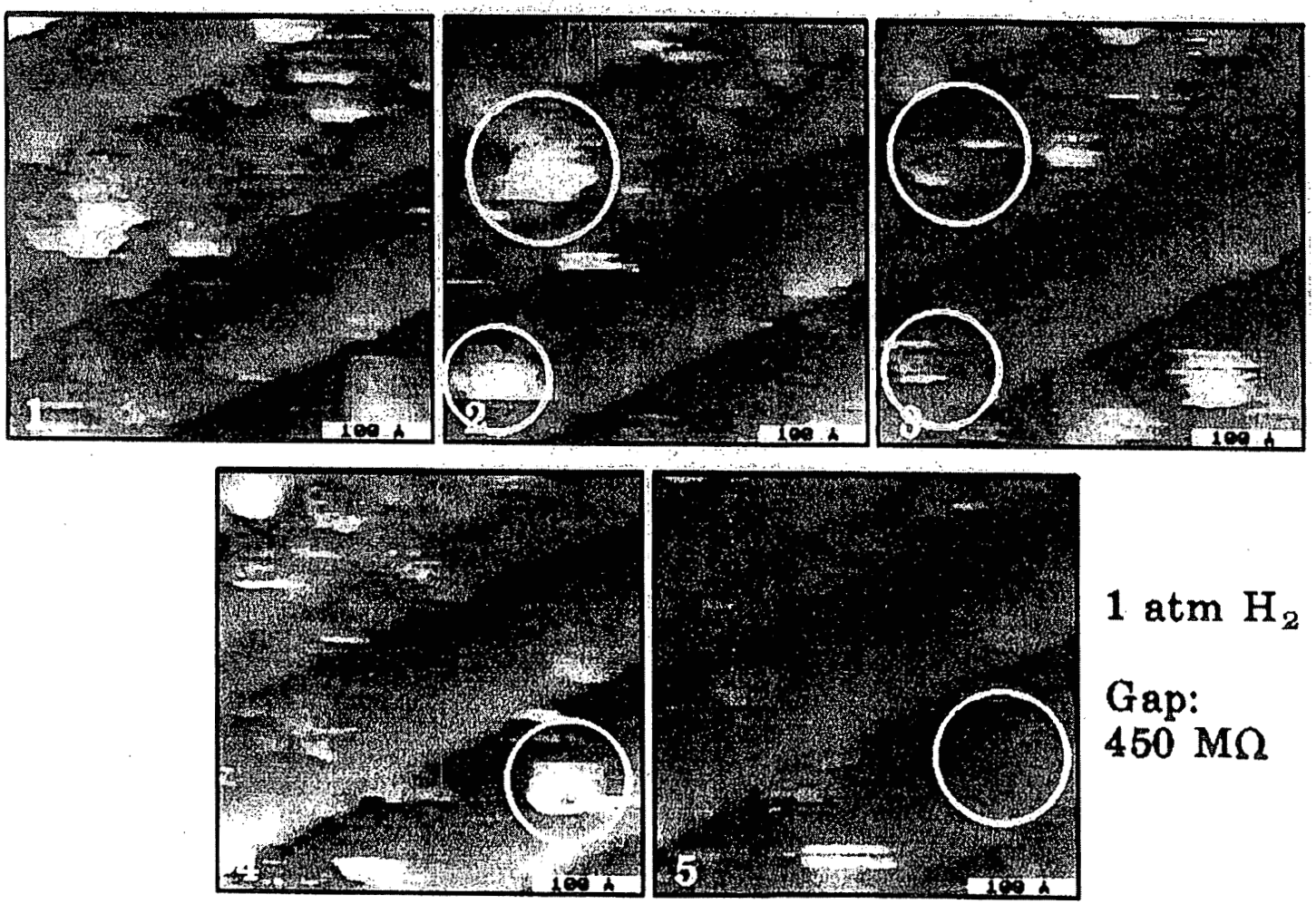


1 atm $H_2$

Gap:
450 MΩ

Figure 8.8. (Following page) The efficiency for removal of the clusters as a function of their height was investigated to determine whether a preference exists for the removal of one type of cluster over another. After analyzing image sequences, a compilation of the removal of approximately 50 low and 50 high clusters was obtained and their distributions are plotted here. From these results, there was no evidence for preferential removal of low or high clusters. Also, the high clusters tended to be entirely removed as there was only one case observed where a high cluster appeared to be converted to a low cluster.

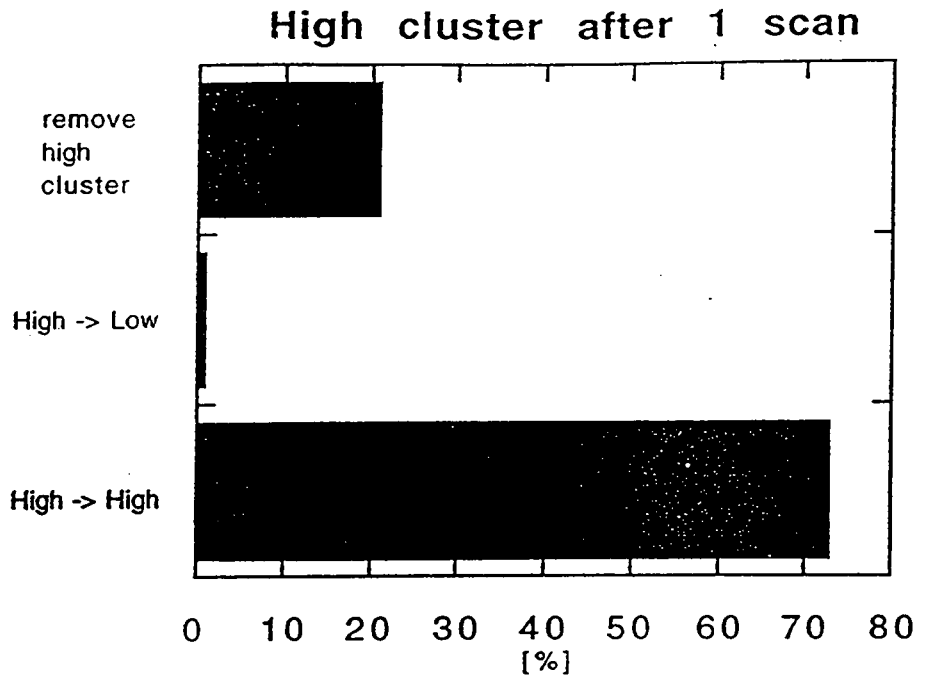
High cluster after 1 scan
remove high cluster
High -> Low
High -> High
0 10 20 30 40 50 60 70 80
[%]

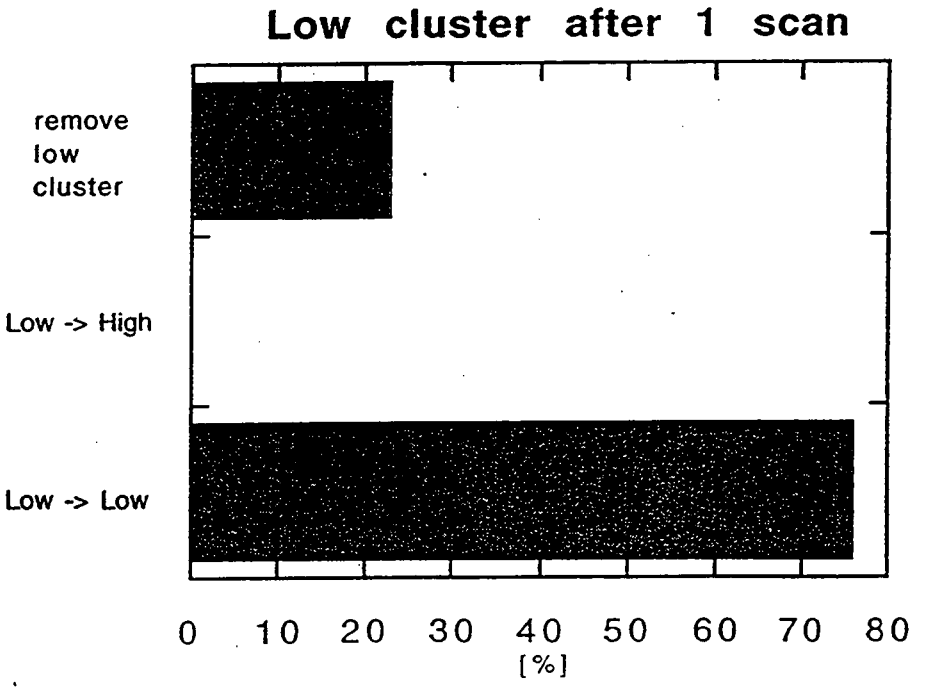
Low cluster after 1 scan
remove low cluster
Low -> High
Low -> Low
0 10 20 30 40 50 60 70 80
[%]

Figure 8.9. (Following page) Two series of images showing close-up views of regions where two clusters were located and after tip activation only one of the clusters remained. The clusters marked with a circle disappear where the clusters marked with a rectangle remain on the surface after bias pulsing. In both these cases the clusters were removed from the bottom of the step edge however, in general, there was no cluster location dependence observed for the efficiency of their removal.

before pulse

after pulse

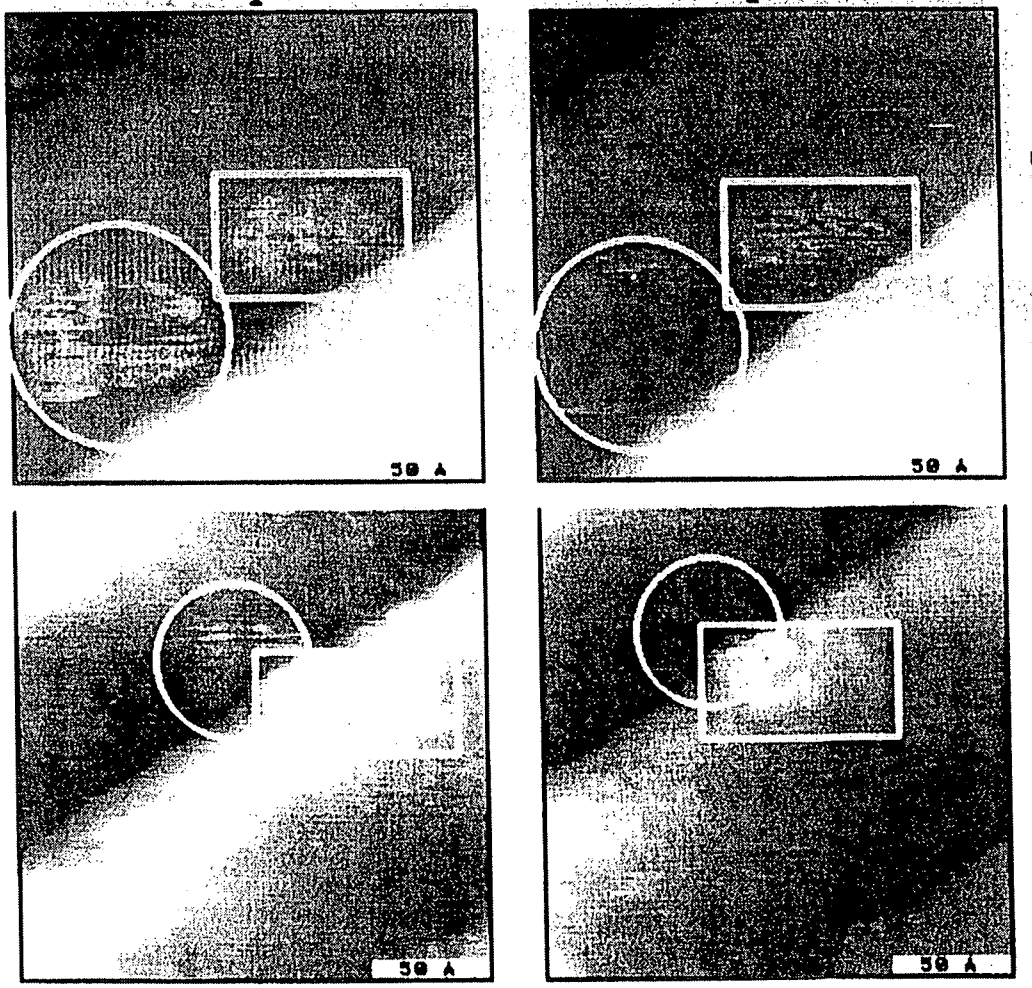


Tip Catalysis on single Hydro-carbon Clusters on Pt(111)

## 8.5 Tip composition dependencies

To further understand the role of the STM tip in the catalysis effect, the Pt STM tip was replaced with a gold tip and the experiments in hydrogen and oxygen were repeated. In switching to a gold STM tip it is possible to investigate the possibilities of mechanical effects as well as to separate the importance of having a source of oxygen or hydrogen atoms vs. oxygen or hydrogen molecules.

Fig. 8.10 shows a series of STM images obtained with the gold STM tip. Fig. 8.10(a) was obtained in vacuum and shows the CxHy fragments on the Pt(111) surface. After filling the chamber with 1 atm. of the hydrogen/propylene mixture and pulsing the tip Fig. 8.10(b) was obtained. It was found that the hydrocarbon clusters were not removed after bias pulsing in any case with the gold tip. This inactivity was also observed in the oxygen environment (Fig. 8.10(c)).

The experiments with the gold tip showed significant dependencies on the tunneling gap conditions. The hydrocarbon species were only observed with very high tunneling currents and low bias voltages (interestingly, these were the exact conditions that were found to most likely cause the removal of the clusters with the Pt tips as will be discussed in the next section).

It is interesting to note that in the course of imaging with the Au tips, significant distortions of the STM images were very common. In these cases the steps appear to be distorted at the edges of the images. These distortions may be caused by mechanical interactions between the tip and surface, causing the tip to rotate slightly as its direction is reversed. This may be due to a part of the tip which is closer to the surface but is insulating and therefore is being pushed against the surface so that a conducting part of the tip is able to be within tunneling range. If this is the case, then it is an interesting result

that the tip can be in physical contact with the surface and yet the carbonaceous clusters remain unaffected.

Finally, it can be concluded from the gold tip experiments that it is necessary that hydrogen or oxygen atoms be present in order for the tip-induced catalysis to occur, (since gold does not dissociate hydrogen or oxygen molecules).

Figure 8.10. (Following page) (a) STM image of the carbonaceous cluster covered surface obtained with a gold tip in vacuum ($10^{-6}$ Torr). (b) Topographic image obtained after multiple tip pulsing and scans of the same area showing no indication of cluster removal. (c) Similar case to (b) but in an atmosphere of oxygen.

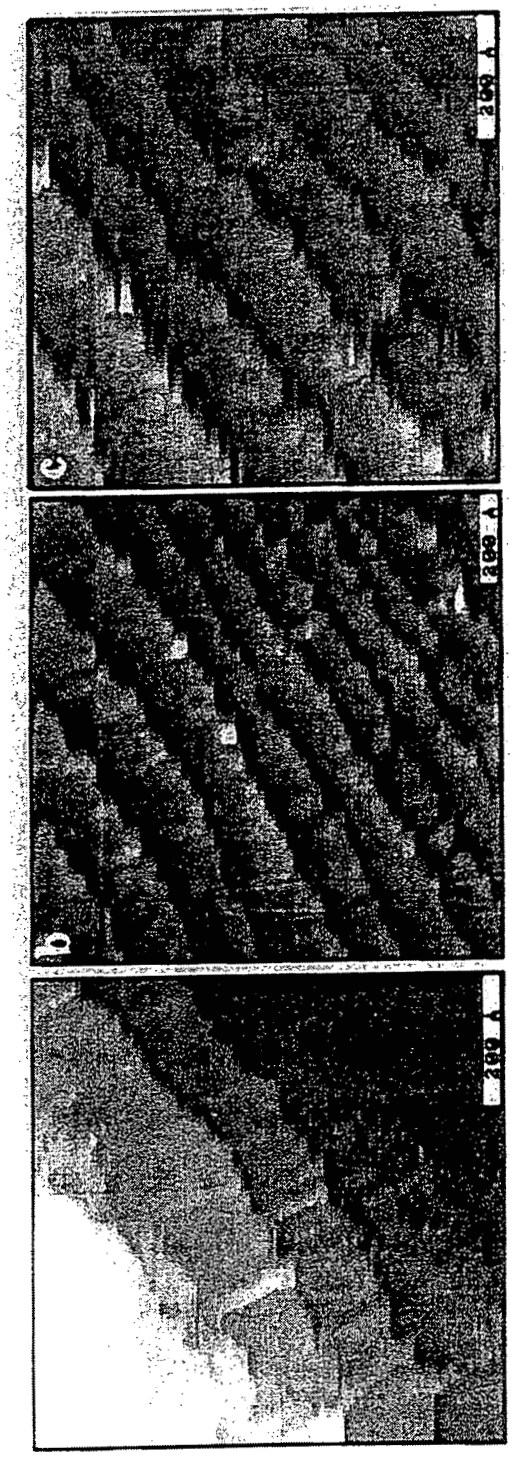
c
b
Vacuum
1 Atm. $H_2$
1 Atm. $O_2$

## 8.6 Tunneling gap dependence

How are oxygen and hydrogen atoms transferred from the STM tip to the $C_xH_y$ species on the surface? In attempt to elucidate the mechanism for the tip-induced catalysis, the effects of tunneling current, bias voltage and gap resistance was investigated. The understanding of which of these effects are important is extremely useful in developing a mechanism for the tip-induced catalysis effect. For example, if it is observed that the bias voltage is important then it is likely that the catalysis involves a field evaporation or perhaps a field-induced dissociation of the chemical bonds. In fact, the field evaporation of hydrogen from a Pt STM tip to a surface (Si(111)-7x7) has been observed previously [5]. Kuramochi, *et al.* found that by performing STM experiments in $1 \times 10^{-7}$ Torr of hydrogen they were able to field evaporate hydrogen atoms from the end of their Pt STM tip by applying sufficiently high (3.5 V) bias voltages. On the other hand, if the gap resistance appears to be the predominant parameter, then it is likely that the atom transfer from the tip to the surface is governed by a proximity effect.

In attempt to understand which effects predominate, experiments were carried out with Pt tips in both hydrogen and oxygen environments. In these series of experiments, the tunneling conditions were varied systematically and the resulting efficiency of hydrocarbon cluster removal was investigated. Fig. 8.11 shows a series of STM images obtained in atmospheric pressures of hydrogen/propylene under different tunneling currents and bias voltages but while maintaining a constant gap resistance. In these three sets of images there was no discernible difference in the STM tips ability to remove the clusters. This indicates that there is no observable field effect under the range of tunneling conditions which we are able to operate. This is not surprising as the fields applied are still approximately an order of magnitude too low for field evaporation or field induced dissociation to occur.

The final parameter to investigate is the role of the gap resistance. Fig. 8.12 shows three series of STM images which were obtained while maintaining a constant bias voltage but varying the tunneling current. While it is true that the field also varies in this experiment, it is not varying significantly, and previous studies of field evaporation and dissociation show that the conditions in this experiment are at least an order of magnitude too low to significantly affect electronic orbitals of atoms and molecules [6]. It was observed that the hydrocarbon clusters were most efficiently removed in the series of experiments where the tunneling current was highest (gap resistance was lowest). This was found to be the case also when the current was kept constant and the bias voltage was varied (both in oxygen and hydrogen environments).

To further demonstrate the importance of gap resistance in the tip catalysis effect, the resistance was varied while STM images were being acquired. In Fig. 8.13(a) the STM image was initiated with a gap resistance of 350 MΩ. Approximately one-third of the way down the image the gap resistance was reduced to 50 MΩ. At this point (denoted by an arrow) the removal of the carbonaceous clusters was clearly more efficient. In Fig. 8.13(b) the gap resistance was varied three times, generating bands of clusters at high gap resistances and clean bands in the regions where the tip was scanned at low gap resistances. This effect was also observed in oxygen environments (see Fig. 8.14(a and b)).

These results clearly indicate that the hydrogen and oxygen atoms are transferred from the STM tip to the molecules on the surface as a result of the tips proximity to the surface. Estimates of the STM tip to metal surface distance are approximately 5 - 10 Å for the tunneling conditions used. In this case it is likely that the STM tip is in Van der Waals contact with the carbonaceous clusters and thus the transfer of the atoms from the tip appears to be more efficient as the tip to sample distance is reduced and this overlap is enhanced.

Figure 8.11. (Following page) Three series of STM images which were obtained in the hydrogen/propylene atmosphere while investigating the role of tunneling conditions for tip catalysis. It was observed that there was no noticeable change in the ability of the tip to remove the clusters simply by changing the tunneling current or bias voltage while maintaining a constant gap resistance.

## Tip Catalysis at constant Gap (100 MΩ)

I=0.5nA
U=.05V

I=1.0nA
U=0.1V

I=2.0nA
U=0.2V

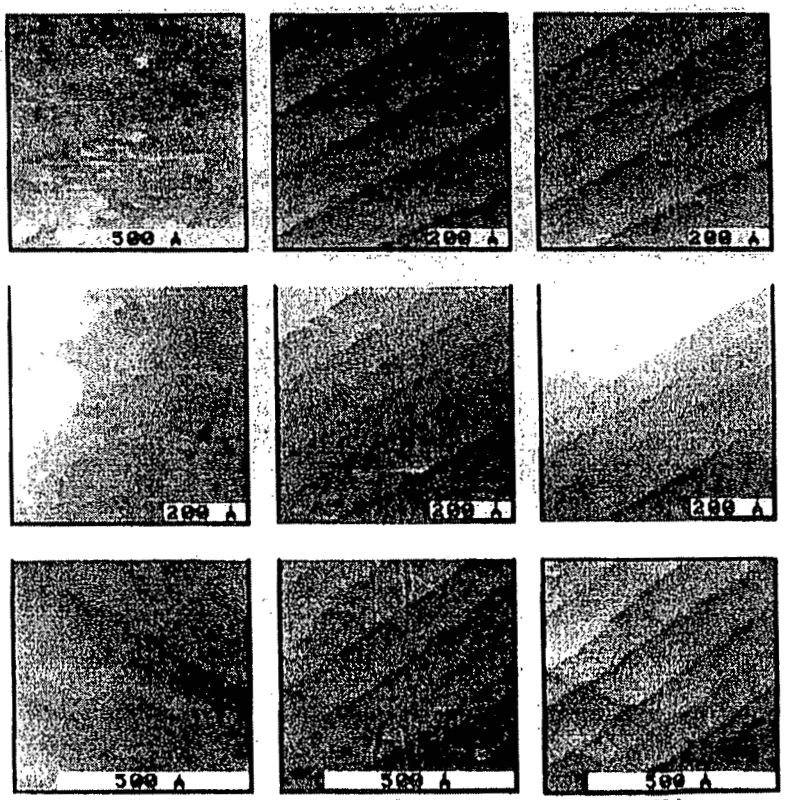


before 1. after 2.after

1 atm $H_2$
$C_xH_y$/Pt(111)

Figure 8.12. (Following page) Three series of STM images obtained in the hydrogen/propylene atmosphere investigating the effect of varying the tunneling current while maintaining a constant bias voltage. In these experiments it was found that the tip catalysis was enhanced in cases where the tunneling current was increased (reduced gap resistances).

## Tip Catalysis at Different Tunneling Current

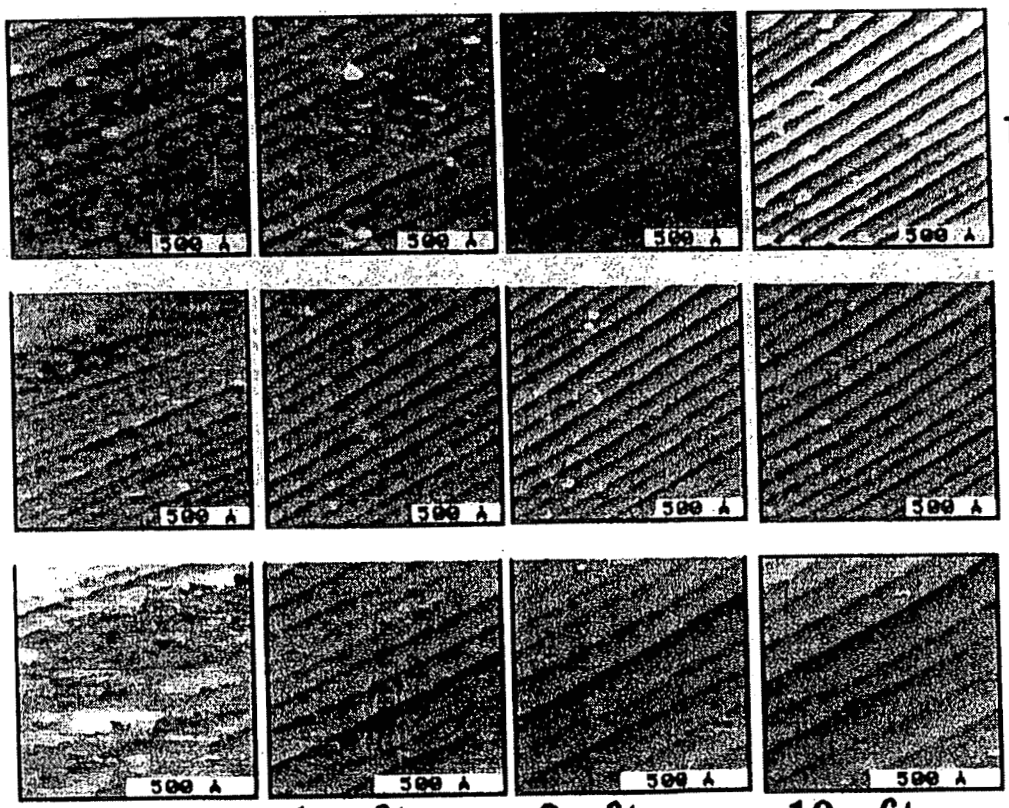

Figure 8.13. (Following page) In order to further investigate the role of varying the gap resistance, the resistance was varied in the course of imaging. (a) In this image the gap resistance was reduced from 350 MΩ to 50 MΩ approximately 1/3 of the way down the image. Above this point the hydrocarbons were partially removed while below this point they were completely removed from the surface. (b) In this image, the resistance was varied twice as indicated at the points on the right side. The bands of hydrocarbons are clearly observed in the areas where the gap resistance was large while the areas which were imaged with a small gap resistance were clearly much more efficient at removing the hydrocarbons.

# Tip Catalysis at Different Gap Resistances

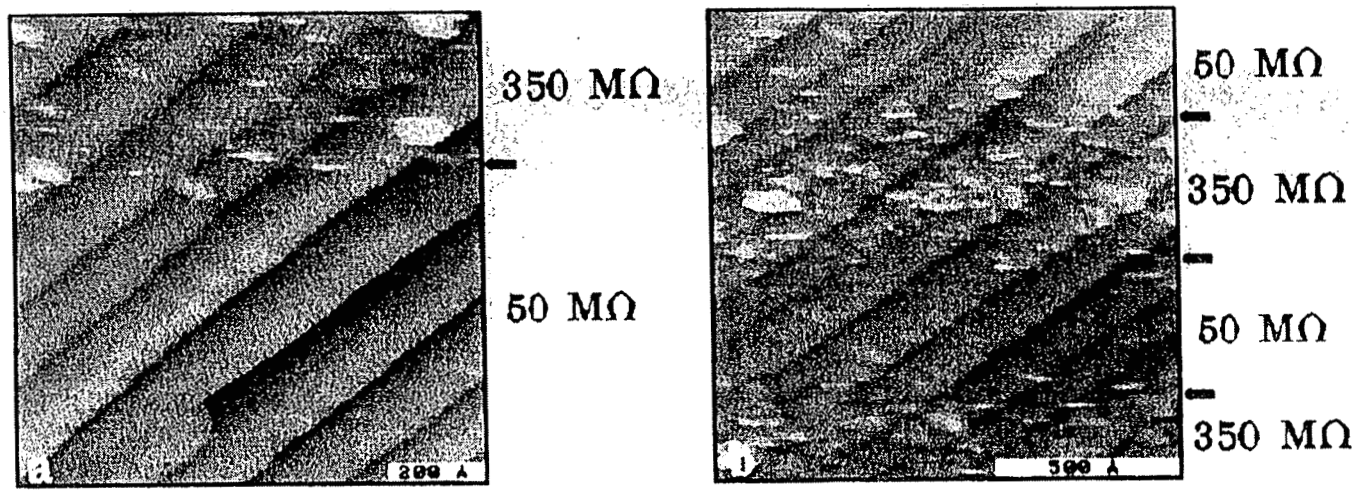


Hydrocarbons/Pt(111) in 1 atm $H_2$

Figure 8.14. (Following page) The same experiment as described in Fig. 8.13 was carried out in the oxygen environment. As shown by the markers on the sides of the two images, there is a distinct dependence on the efficiency of the tip to remove the clusters on the gap resistance.

## Catalysis at different Gap resistances

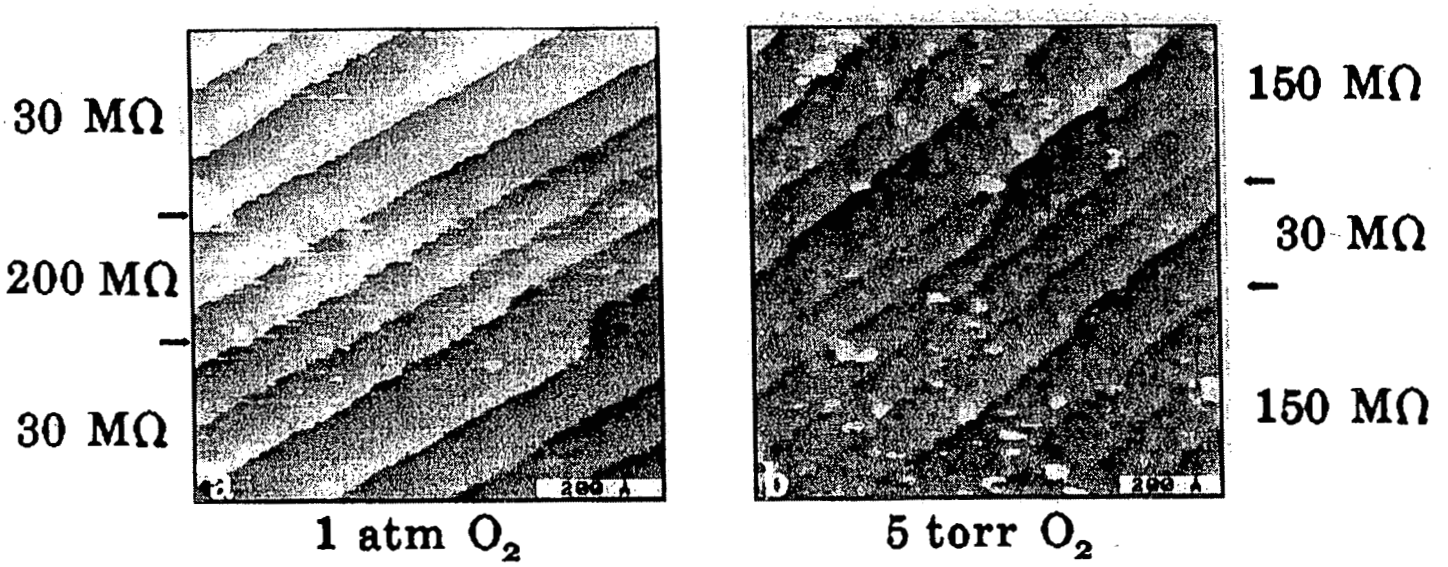

## 8.7 Pressure dependence of the tip catalysis

Finally, the influence of reactant gas pressure was investigated. Once the tip catalysis was initiated in atmospheric pressures of hydrogen or oxygen, the chamber was pumped down to interval pressures and the tip catalysis was reinitiated. In both the hydrogen and oxygen environments it was observed that the ability of the tip to remove carbonaceous clusters was reduced with pressure. In the case of hydrogen, it was observed that the tip catalysis stopped altogether somewhere in the pressure range of 0.5 Torr - 5 Torr. The oxygen environment proved to be able to remove hydrocarbon clusters at pressures down to $5 \times 10^{-3}$ Torr. A series of images obtained in various oxygen pressures is shown in Fig. 8.15. From the pressure experiments, it appears that perhaps the oxygen environment is somewhat more efficient at removing the hydrocarbon clusters than the hydrogen containing environment.

After examining the number of scans required to remove approximately 80% of the hydrocarbons clusters in an area as a function of hydrogen and oxygen gas pressures, a plot was made which shows that the amount of removed material appears to be logarithmically dependent on the gas pressure (see Fig. 8.16).

The question now arises as to why the catalytic action of the tip should have such a dramatic pressure dependence. It seems unlikely that even in the $10^{-3}$ Torr range there should be a noticeable lack of dissociatively chemisorbed oxygen or hydrogen atoms on the tip. One has to remember, however, that it is expected that the STM tip is on the average, blunt compared to the actual mini-tip which is involved in the tunneling effect. As a result of the bluntness, there could be a significant diffusion limited effect for the dissociatively chemisorbed hydrogen or oxygen atoms to reach the mini-tip involved in the catalysis.

Figure 8.15. (Following page) In these experiments the role of reactant gas pressure on the efficiency of the tip catalysis was investigated. This figure shows a series of images obtained in various oxygen pressures. It was observed that as the reactant gas pressure was reduced it was necessary to scan the tip over the surface more times in order to remove the clusters. In general, in 1 atmosphere of oxygen or hydrogen, it was observed that almost all of the clusters could be removed with a single scan. However, at pressures ranging from $1x10^{-3}$ to 10 Torr, 10 or more scans were required to remove similar amounts of hydrocarbon clusters.

# Catalysis at different Oxygen Pressures

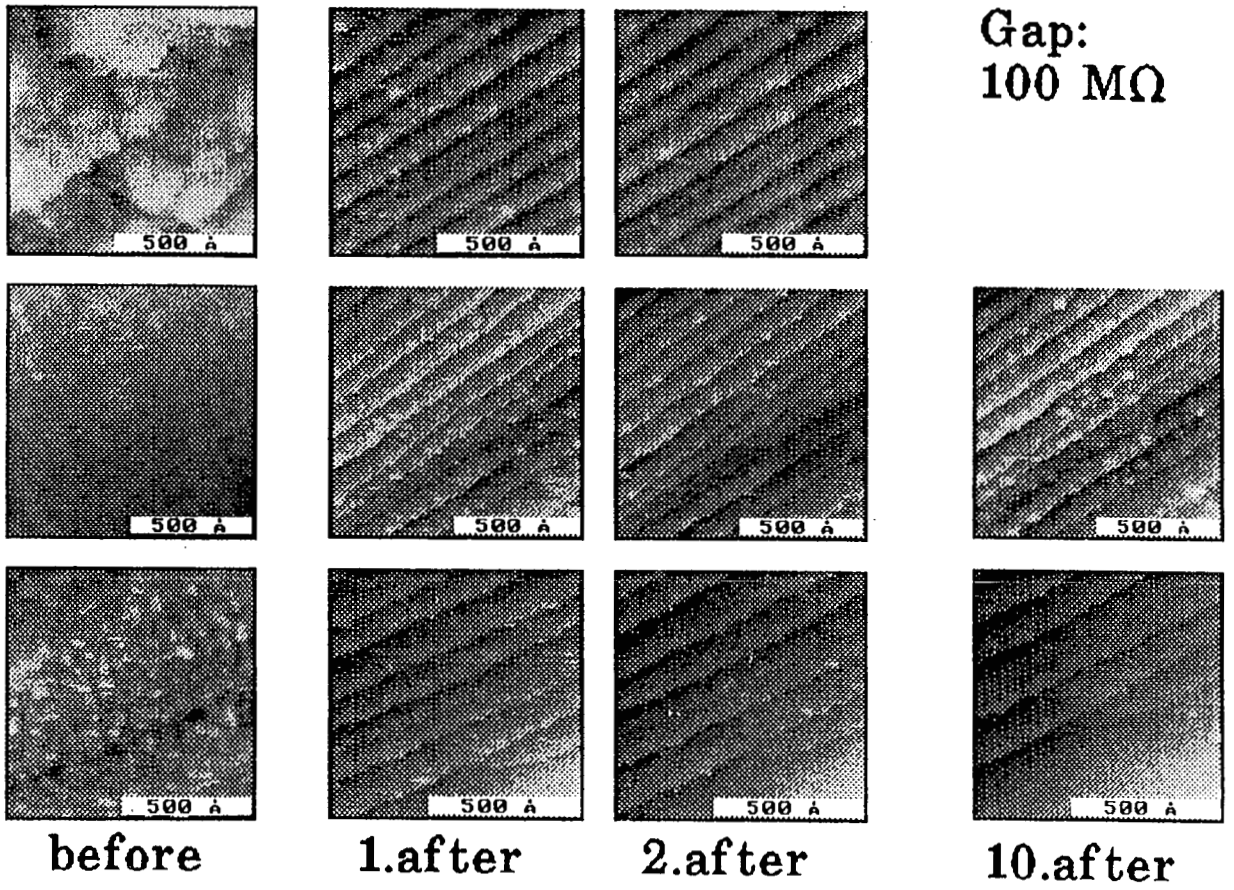

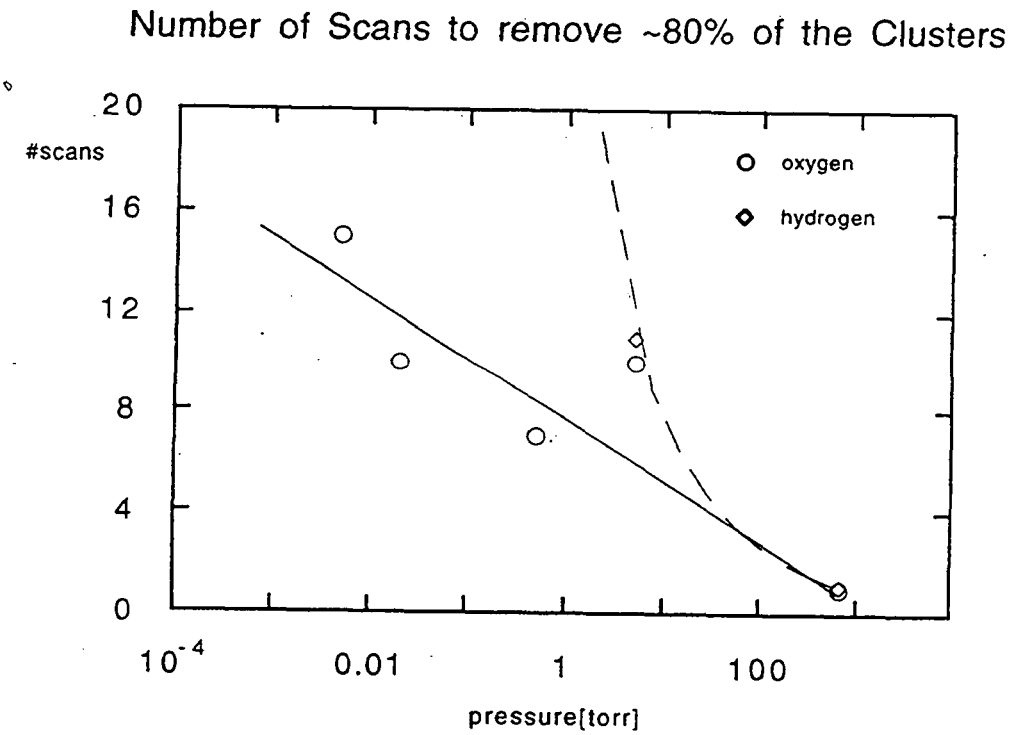


Figure 8.16. After examining the number of scans required to remove approximately 80% of the hydrocarbon clusters in an area as a function of hydrogen and oxygen gas pressures, a plot was made which shows that the amount of removed material appears to be logarithmically dependent on the gas pressure. In the case of hydrogen/propylene mixtures it was observed that the catalysis effect did not occur at pressures below 0.5 Torr.

## 8.8 Dependence of Removal Rate on Decomposition Temperature

From hundreds of experiments investigating the tip catalysis effect, it was observed that the ability of the tip to remove the hydrocarbon clusters was inversely dependent on the degree to which the clusters were decomposed on the surface. For experiments on hydrocarbon clusters which were formed by annealing to temperatures greater than 600 K, no tip catalysis was observed. This is expected to be due to the fact that at higher decomposition temperatures the carbonaceous clusters are becoming more graphitic and thus less easily catalyzed. Indeed, even within the range of low temperature hydrocarbon decomposition, variances were observed in the efficiency of the tip-induced catalysis. From these results, however, it is difficult to further deconvolute variances in the tip conditions with the degree of decomposition of the hydrocarbon clusters.

## 8.9 Proposed model for tip catalysis

It is proposed here that the catalytic action by the active tip, which is presumably clean Pt, consists of atomizing $H_2$ and $O_2$ from the gas phase and hydrolyzing and oxidizing C bonds of the clusters under it. The mechanism by which the hydrogen transfer occurs appears to be a local proximity effect. Once reacted, the hydrocarbon fragments produced from the cluster are either desorbed or remain on the surface but are sufficiently small to diffuse quickly over the surface and remain invisible to the STM. This could be due to desorption as well but from simple energetic arguments appears to be less likely. A schematic of this proposed mechanism is shown in Fig. 8.17.

To ascertain the proposed catalytic action of the STM tip, experiments were performed to investigate the effects of tunneling conditions, gas pressure, gas environments of oxygen, carbon monoxide, and vacuum, switching from a platinum to a

gold STM tip, and annealing the hydrocarbons at higher temperatures. No cluster removal was observed by the tip under any condition of tip pulsing when in vacuum, when in a CO environment, after high temperature hydrocarbon decomposition, or when using a gold STM tip. So, the clean tip produced by pulsing cannot remove the clusters in the absence of hydrogen or oxygen. One can dismiss also the possibility of the tip mechanically removing or displacing the clusters since large areas (>5000 Å on a side), were cleaned of clusters by an active tip without visible deposits of material being observed at the edges of the empty areas or when using a gold tip which appears to be in mechanical contact with the surface and the hydrocarbons. After returning over one hour later to areas where clusters were reacted away, it was observed that the areas remain "clean", in other words, there was no discernible back-diffusion of the clusters. Such accumulation following mechanical removal has been observed previously by others [7].

The present results clearly demonstrate the local catalytic activity of the STM tip, and suggest a wealth of other experiments that can provide deep insights into the nature of the atomic scale structure and kinetics of the catalytic action. It is still not clear at this time, what is the exact mechanism by which the H or O is activated by the tip and transferred to the carbonaceous fragments. It is known that both hydrogen and oxygen readily dissociate over platinum (hydrogen dissociates at temperatures below 300K as shown by $H_2$-$D_2$ exchange studies [8]). Since the residence time of the tip over the area occupied by one cluster is of the order of milliseconds at these scanning speeds, it is clear that the turnover frequency of the H or O transfer reaction from the tip is approximately $2x10^3$ (sec·Pt site)$^{-1}$ (assuming the atoms are being transferred from a single Pt atom on the STM tip).

In regards to the hydrogenolysis process, this tip-induced catalysis is about an order of magnitude higher than that expected from comparable studies of hydrogenation of ethylene and propylene under similar conditions [9] and several orders of magnitude higher than hydrogenolysis of CxHy species [10]. However, these differences are not

surprising as it is not necessary for these molecules to be completely hydrogenated and removed from the surface in order for them to be unobservable by the STM. Isotope exchange reactions of hydrocarbons with deuterium gas on Pt(111) have shown that the exchange kinetics at low conversions displayed zero activation energy, a first order dependence on $D_2$ pressure, and a strong negative-order dependence on the surface coverage by strongly bound carbonaceous species [11-12]. This negative-order dependence arises from the inhibition of dissociative chemisorption of deuterium molecules by the carbonaceous deposits. It was found that the rate of dissociative deuterium chemisorption on the platinum surfaces that are partially covered by strongly chemisorbed carbonaceous species controlled the overall exchange kinetics. From these observations, it could be argued that in this case, the STM tip may be acting as a source of activated hydrogen, eliminating the need for a site for dissociative hydrogen chemisorption on the surface and as a result significantly increasing the rate of conversion of the hydrocarbon clusters.

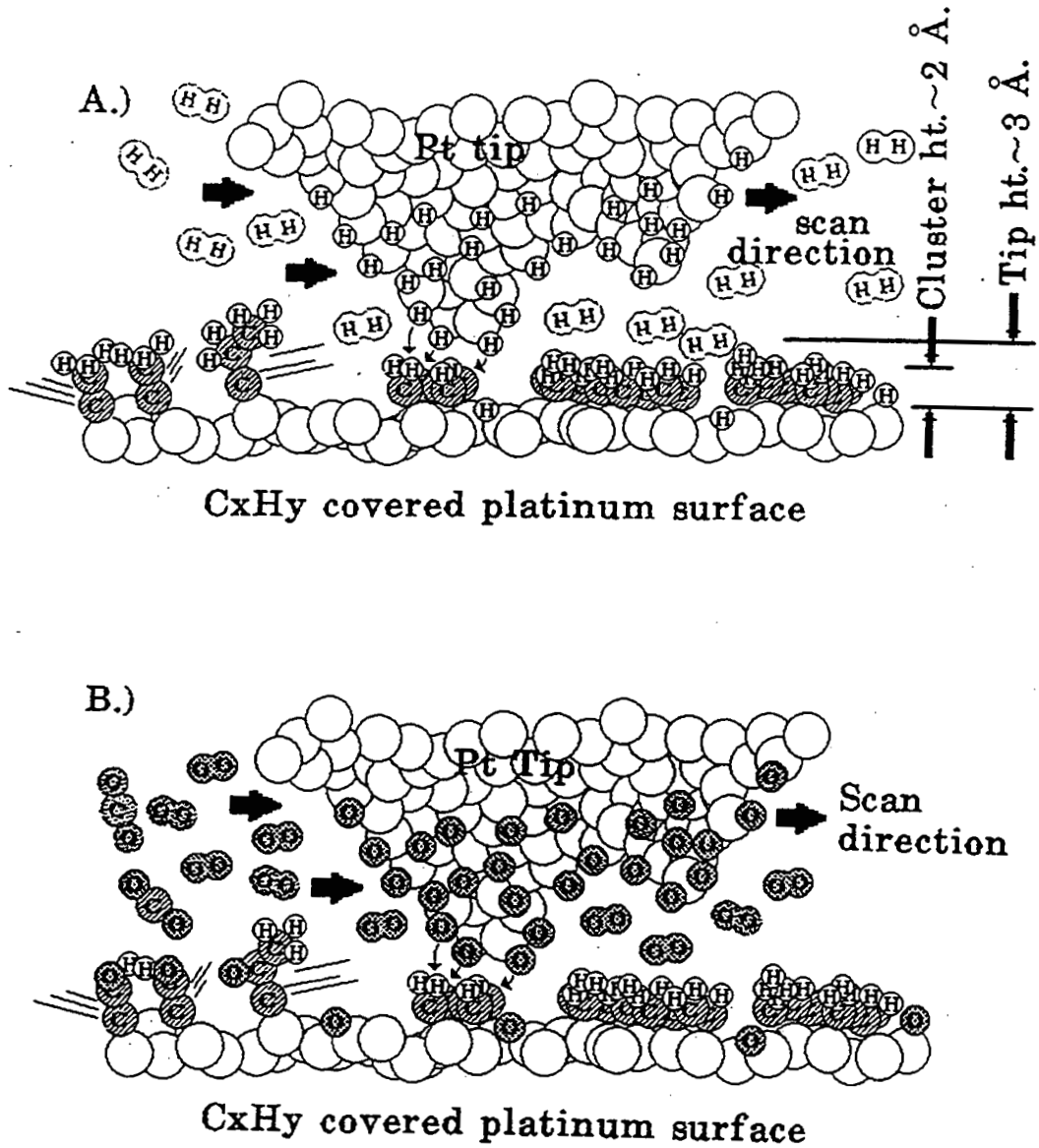


Figure 8.17. Cartoon of the proposed mechanism for tip-induced catalysis. It is proposed here that the catalytic action by the active tip, which is presumably clean Pt, consists of atomizing $H_2$ and $O_2$ from the gas phase and hydrolyzing and oxidizing C bonds of the clusters under it. The mechanism by which the hydrogen transfer occurs appears to be a local proximity effect. Once reacted, the hydrocarbon fragments produced from the cluster are either desorbed or remain on the surface but are sufficiently small to diffuse quickly over the surface and remain invisible to the STM. This could be due to desorption as well but from simple energetic arguments appears to be less likely.

## 8.10 Summary

The platinum tip of a Scanning Tunneling Microscope that operates inside an atmospheric pressure chemical reactor cell, has been used to locally rehydrogenate and oxidize carbonaceous fragments deposited on the surface of Pt(111). The carbon fragments were produced by partial dehydrogenation of propylene. The reactant gas environment inside the cell consisted of a mixture of pure $O_2$ or a mixture of $CH_3CHCH_2$ (10%) and $H_2$(90%) at 300K. The Pt tip acted as a catalyst after activation by short voltage pulses. In this active state the clusters in the area scanned by the tip were reacted away with very high spatial resolution.

In order to further ascertain the catalytic effect observed in the hydrogen environment a number of experiments were carried out. These experiments were designed to investigate the dependence of the catalytic effect on various parameters including; tunneling gap conditions, reactant gas composition, reactant gas pressure, and STM tip composition.

These first results demonstrating the catalytic action of the STM tip open the way for very exciting experiments and applications- from gaining insights to fundamental questions of catalysis and surface reactions by allowing the study of the local catalytic activity of surface sites and defects that can only be studied at present in an average way with the more conventional tools and methods, to creating chemical templates with atomic precision.

[1] Ph. Avouris, NATO ASI Series, Series E, Applied Sciences, No. 239, Atomic and Nanometer-scale Modification of Materials: Fundamentals and Applications, Ph. Avouris, ed., Dororecht; Boston; Kluwer Academic Publishers, 1993.

[2] J.M. Thomas and W.J. Thomas, "Introduction to the Principles of Heterogeneous Catalysis", Academic Press, London, New York, 1967.

[3] K. Christmann, G. Ertl, and T. Pignet, Surf. Sci. **54**, 365 (1976). F.P. Netzer and G. Kneringer, Surf. Sci. **51**, 526 (1975). S. Ferrer and J.P. Bonzel, Surf. Sci. **119**, 234 (1982). B.Lang, R.W. Joyner, and G.A. Somorjai, Surf. Sci. **30**, 454 (1972).

[4] T.A. Land, T. Michely, R.J. Behm, J.C. Hemminger, G. Comsa, J. Chem. Phys. **97**, 6774 (1992).

[5] H. Kuramochi, H. Uchida, and M. Aono, Phys. Rev. Lett., in press.

[6] H.J. Kreuzer, NATO ASI Series, Series E, Applied Sciences, No. 239, Atomic and Nanometer-scale Modification of Materials: Fundamentals and Applications, Ph. Avouris, ed., Dororecht; Boston; Kluwer Academic Publishers, 1993.

[7] T.A. Jung, A. Moser, H.J. Hug, D. Brobechk, R. Hofer, H.R. Hofer, H.R. Hidber, and U.D. Schwarz, Ultramicroscopy, **42-44**, 1446, (1992), and references therein.

[8] M. Salmeron, R. Gale, and G.A. Somorjai, Phys. Rev. Lett. **38**, 1027 (1977).

[9] F. Zaera and G. A. Somorjai, J. of Am. Chem. Soc. **106**, 2288 (1984).

[10] J.H. Sinfelt, Catalysis Lett. **9**, 159 (1991).

[11] S. M. Davis and G.A. Somorjai, J. Phys. Chem. **87**, 1545 (1983).

[12] B.E. Koel, B.E. Bent, and G.A. Somorjai, Surf. Sci. **146**, 211 (1984).

# CHAPTER 9

# CONCLUDING REMARKS

## 9.1 Summary of Experimental Results

The experimental results presented in this thesis have shown that through the use of a specialized STM developed in the course of this thesis (see chapter 2), STM measurements can provide very useful information about the nature of surfaces and their adsorbates while exposed to environmental pressures of reactant gases.

After initial testing, experiments were carried out to investigate the stability of (Pt(110)) under high pressures of hydrogen, oxygen, and carbon monoxide (see chapter 4). In these studies it was observed that the surface structure was sensitive to atmospheric pressures of reactant gases. In the case of the oxygen environment, the Pt(110) surface formed microfacets opening up (111) planes for oxygen adsorption, whereas in the CO environment surface reconstructions would be lifted, forming a (1x1) Pt(110) surface. In hydrogen atmospheres, small scale ((nx1), where n=2-7) missing-row reconstructions were observed.

*In situ* UHV and high vacuum experiments were carried out for sulfur on Pt(111) (see chapter 5). In these studies, atomically resolved images of ordered sulfur overlayers were obtained and compared to complimentary LEED studies. The STM image contrast of the sulfur atoms was investigated and compared to theoretical calculations using the Electron Scattering Quantum Chemical (ESQC) method. In these comparisons, the contrasts and corrugations obtained experimentally were found to agree very well with calculations using different STM tip terminations. In the end, it was found to be possible

to distinguish between two classes of single atom tip terminations (C and S) and (Pt). These results were confirmed experimentally by transferring atoms in a controlled manner between the surface and the tip and observing the resulting changes in the STM image corrugation. These studies showed that it was also possible to observe diffusion of vacancies within sulfur islands on the Pt(111) surface. By observing sequential STM images, it was possible to observe 'atom or hole hopping' and by measuring the rate of hole filling, an estimate of the diffusion barrier was obtained. Coadsorption experiments with sulfur and CO showed that CO could reversibly compress the sulfur to structures having higher local coverage. *In situ* STM measurements of this coadsorbate-induced compression provided a kinetic pathway by which the sulfur is displaced in a one-dimensional 'chain' of atoms, opening up new sites for further CO adsorption and compression. This type of information on the lateral interaction of coadsorbates could aid in the development of models for catalytic reactions which are known to occur on surfaces which are covered with stagnant overlayers.

STM investigations of the CO/S/Pt(111) system in high pressures of CO ($1x10^{-6}$ Torr) showed that the Pt substrate undergoes a 'stacking-fault-domain' reconstruction involving periodic transitions from fcc to hcp stacking of top-layer atoms (see chapter 6). This reconstruction is similar to what has been observed for Au(111) and for Pt(111) at temperatures above 400 K in high vapor pressures of Pt. These results are the first which show this reconstruction of Pt can be stabilized at room temperature. Also, because it was found to be necessary for both sulfur and CO to be present to cause the reconstruction, it is also the first example of a coadsorbate-induced reconstruction.

In chapter 7, the stability of propylene on Pt(111) and the morphology of decomposition products as a function of environment (UHV, atmospheric pressures of hydrogen, $H_2$/propylene, and CO) and sample temperature (300K-900K) was investigated

*in situ*, with the HPSTM. Results from these studies produced a number of significant new observations about the surface chemistry of hydrocarbons on Pt(111).

Clusters of carbonaceous material were formed as a result of various decomposition pathways. The cluster and cluster aggregates were observed to form regular patterns whose size and shape depended on decomposition environment and temperature.

UHV studies of the decomposition of propylene show that the dehydrogenation of propylene on Pt(111) at temperatures of 800 K leads to the formation of large two dimensional carbonaceous clusters on the surface with mono- or diatomic height. The particles are dispersed uniformly over the surface following the step and terrace geometry of the substrate. These particles were observed to cause step pinning.

STM measurements were carried out on the initially clean Pt(111) surface while in atmospheric pressures of $H_2$/propylene mixtures. This is the first time STM experiments have been carried out on a surface while exposed to an atmospheric pressure of reactant gases in which the sample is expected to be catalytically active. In this environment the catalyst surface was observed to be stable on a mesoscopic scale, (i.e. there was no large scale restructuring of the surface or formation of carbonaceous clusters characteristic of hydrocarbon decomposition).

With regards to the decomposition of propylene in hydrogen containing environments, it was observed that the temperature necessary to form carbonaceous aggregates is significantly higher (~250° C) than in non-hydrogen containing environments. This demonstrates the likelihood that for lower temperatures, the 'carbidic' carbon which is thought to play a significant role in catalytic reactions is likely to be comprised of individual carbon atoms, $C_2$ or $C_3$ species in hydrogen-rich environments but small agglomerates (which was observed to be the stable form in vacuum or non-hydrogen environments) in hydrogen-lean catalytic reactions.

The decomposition of propylene in atmospheric pressures of carbon monoxide showed dramatic differences relative to the hydrogen environments. Carbonaceous clusters were observed to form at temperatures characteristic of UHV environments. The clusters in the CO environment appeared to have a significantly higher coverage than those observed in UHV. This is likely due to the possibility that the equilibrium coverage of propylene on the Pt surface in atmospheric exposures is much higher than the 0.25 monolayer saturation coverage in UHV. (Note: It was observed that in accordance with numerous UHV studies, the CO did not decompose on the Pt surface even after annealing the clean sample in atmospheric pressures of CO). The morphology of the low temperature decomposition clusters were observed to depend on the environment. This is proposed to be the result of lateral interactions between coadsorbates and appears to play a very significant role for the creation of regions of the transition metal surface which are free of carbonaceous clusters and may therefore be active for catalysis. These results indicate that the stable forms of the carbonaceous clusters generated under hydrogen-free environments are flat (1-2 atom height) clusters whose sizes depend on the degree of decomposition (they become smaller and more uniform as the decomposition temperature is increased). As a result, it is likely that these species play a very different role in catalytic reactions than the carbon present in hydrogen environments.

Finally, it was observed that the Pt(111) surface was stable under all of the atmospheric pressure conditions. The hydrocarbon clusters were observed to conform to the underlying transition metal catalyst surface structure. It may be that the surface is stabilized by high coverages of the decomposition products since the only occurrence of significant reconstruction of steps occurred in lower coverage UHV decomposition conditions.

Finally, in chapter 8, results are presented which show how the platinum tip of the HPSTM was used to locally rehydrogenate and oxidize carbonaceous clusters deposited

on the surface of Pt(111). The Pt tip acted as a catalyst after activation by short voltage pulses. In this active state the clusters in the area scanned by the tip were reacted away with very high spatial resolution.

In order to further ascertain the catalytic effect observed in the hydrogen environment a number of experiments were carried out. These experiments were designed to investigate the dependence of the catalytic effect on various parameters including; tunneling gap conditions, reactant gas composition, reactant gas pressure, and STM tip composition. It was observed that the tip-induced catalysis was logarithmically dependent on reactant gas pressure, and was dependent on the tip proximity to the surface. The catalytic effect was not observed when the Pt tip was replaced by a gold tip, indicating the necessity for hydrogen or oxygen atoms to be present. From these experiments, a model was proposed where the tip acts as a source of hydrogen or oxygen atoms which are then transferred to the carbonaceous clusters when the tip comes into proximity

These first results demonstrating the catalytic action of the STM tip open the way for very exciting experiments and applications- from gaining insights to fundamental questions of catalysis and surface reactions by allowing the study of the local catalytic activity of surface sites and defects that can only be studied at present in an average way with the more conventional tools and methods, to performing chemical lithography with atomic precision.

## 9.2 Recommendations for Future Research Directions

Using STM to study model catalyst surfaces under high pressure reaction conditions began only 4 years ago. This thesis presents the first results, and serves as a survey of a few of the directions for future research. From these initial experiments, the prospects for future work are very exciting.

Obviously the tip-induced chemistry effect should be further investigated. In particular, it would be very interesting to attempt to react away atomic or molecular adsorbates which could be resolved with the STM. The oxidation of sulfur to $SO_2$ is a likely candidate as is the hydrogenation of larger hydrocarbons (benzene or larger) which are expected to have lower diffusion rates and should be possible to obtain molecularly resolved images. The possibility of performing site specific reaction studies on catalytic systems which are known to be structure sensitive is extremely appealing. Other possible experiments include replacing the substrate with something other than Pt to investigate the degree to which the tip is able to catalyze a reaction when the substrate is not catalytically active.

Aside from tip-induced reactions, there is a wealth of possible catalytic systems which are available for investigation with the HPSTM. The key is to decide on systems in which the HPSTM is likely to be able to provide a maximum amount of information. At the moment, it appears that candidates include reactions which involve larger molecules or molecules and atoms with relatively slow diffusion rates which can be resolved with the STM. For *in situ* studies, the temperatures should be below 150° C although with the infrared spot heater, higher temperature experiments can be carried out in conditions very close to *in situ*. The 150° C temperature limit is certainly not the theoretical upper limit for atmospheric pressure STM studies. By using piezoceramics with higher Curie

temperatures (such as quartz) and using materials which are better able to withstand high temperature reaction conditions it is certainly possible to perform STM measurements at temperatures which are well within the realm of most industrial catalytic reaction conditions.

The work in this thesis demonstrates that there are also some very interesting processes occurring in UHV and high vacuum environments which would be very exciting to pursue. Coadsorbate systems and adsorbate-adsorbate interactions are problems which are directly addressable by STM experiments and are of significant interest to the catalysis community. In particular, the systematic STM and LEED investigation of dipole-dipole interactions of coadsorbates would be particularly useful. Finally, the experiments described in chapter 6 which demonstrate the possibility for coadsorbate-induced restructuring of even the most stable of metal surfaces is a dramatic demonstration of how 'flexible' surfaces can be in chemisorptive environments. A systematic study of this and similar systems would be very useful in helping to bridge the pressure gap that has separated UHV studies from catalytic and reactivity studies at normal industrial conditions.